UNIVERSIDAD COMPLUTENSE DE MADRID

FACULTAD DE CIENCIAS GEOLÓGICAS

TESIS DOCTORAL

Geoquímica de emanaciones difusas y termografía en sistemas volcánicos: implicaciones para la exploración geotérmica y la vigilancia volcánica en Canarias

Geochemistry of diffuse degassing and thermal imaging in volcanic systems: implications for geothermal exploration and volcano monitoring in the Canary Islands

MEMORIA PARA OPTAR AL GRADO DE DOCTOR

PRESENTADA POR

Fátima Rodríguez García

Directores

Nemesio M. Pérez Rodríguez
Pedro A. Hernández Pérez
Eleazar Padrón González

Madrid, 2016

Universidad Complutense de Madrid (UCM)

Facultad de Ciencias Geológicas

GEOQUÍMICA DE EMANACIONES DIFUSAS Y TERMOGRAFÍA EN SISTEMAS VOLCÁNICOS: IMPLICACIONES PARA LA EXPLORACIÓN GEOTÉRMICA Y LA VIGILANCIA VOLCÁNICA EN CANARIAS

Geochemistry of diffuse degassing and thermal imaging in volcanic systems: implications for geothermal exploration and volcano monitoring in the Canary Islands

TESIS DOCTORAL

Fátima Rodríguez García

Instituto Volcanológico de Canarias (INVOLCAN)

Tenerife, Islas Canarias

D. Nemesio Miguel Pérez Rodríguez, doctor por la Universidad de La Laguna, D. Pedro Antonio Hernández Pérez, doctor por La Universidad Autónoma de Madrid, D. Eleazar Padrón González, doctor por la Universidad de La Laguna y D. Eumenio Ancochea Soto, doctor por La Universidad Complutense de Madrid.

HACEN CONSTAR:

Que Fátima Rodríguez García, licenciada en Ciencias Geológicas por la Universidad Complutense de Madrid, ha realizado bajo nuestra supervisión, la presente memoria titulada "Geoquímica de emanaciones difusas y termografía en sistemas volcánicos: Implicaciones para la exploración geotérmica y la vigilancia volcánica en Canarias", para optar al grado de Doctor en Ciencias Geológicas. Además autorizamos a que esta tesis sea presentada en la modalidad de compendio de publicaciones.

Y para que así conste y surtan los efectos oportunos en cumplimiento de las disposiciones vigentes, extendemos este certificado en Granadilla de Abona a 6 de Julio de 2015.

Dr. Nemesio M. Pérez Rodríguez
Director de la División de Medio Ambiente-
Instituto Tecnológico y de Energías Renovables (ITER). Instituto Volcanológico de Canarias (INVOLCAN).
Codirector

Dr. Pedro A. Hernández Pérez
Investigador de la Agencia Insular de Energía de Tenerife (AIET).
Instituto Volcanológico de Canarias (INVOLCAN).
Codirector

Dr. Eleazar Padrón González
Investigador de la División de Medio Ambiente-
Instituto Tecnológico y de Energías Renovables (ITER)
Instituto Volcanológico de Canarias (INVOLCAN).
Codirector

V. B. Dr. Eumenio Ancochea Soto
Facultad de Ciencias Geológicas
Departamento de Petrología y Geoquímica
Universidad Complutense de Madrid
Tutor

GEOQUÍMICA DE EMANACIONES DIFUSAS Y TERMOGRAFÍA EN SISTEMAS VOLCÁNICOS: IMPLICACIONES PARA LA EXPLORACIÓN GEOTÉRMICA Y LA VIGILANCIA VOLCÁNICA EN CANARIAS

AUTOR DE LA TESIS:

Fátima Rodríguez García

Licenciada en Geología
Instituto Volcanológico de Canarias (INVOLCAN)
Tenerife, Islas Canarias

DIRECTORES:

Dr. Nemesio M. Pérez Rodríguez (ITER-INVOLCAN)
Dr. Pedro A. Hernández Pérez (AIET-INVOLCAN)
Dr. Eleazar Padrón González (ITER-INVOLCAN)

TUTOR:

Dr. Eumenio Ancochea Soto (UCM)

TESIS DOCTORAL POR COMPENDIO DE PUBLICACIONES
REMITIDA PARA EL GRADO DE DOCTOR EN LA
UNIVERSIDAD COMPLUTENSE DE MADRID

Madrid
Julio, 2015

Los siguientes proyectos han colaborado en la financiación de esta tesis doctoral:

- ✓ GEOTHERCAN (IPT-2011-1186-920000), co-financiado por el Ministerio de Economía y Competitividad (MINECO) con fondos FEDER, GEOHELIO (PTQ-12-05661) y TIMANFAYA (CGL2008-06345), todos dentro del Plan Nacional 2008-2011 de I+D+I.
- ✓ MAKAVOL (MAC/3/C161), ALERTA y ALERTA II (INTERREG IIIB Azores-Canarias-Madeira) del programa de Cooperación Transnacional de la Unión Europea.
- ✓ ProID20100158, ProID20100160 y PI2001/025, del Gobierno de Canarias.

Agradecimientos

En primer lugar quiero agradecer enormemente al Dr. Nemesio M. Pérez, director de esta tesis, la oportunidad que me brindó en 2008 de poder trabajar con él y con su magnífico grupo de trabajo en el apasionante mundo de la volcanología. Nemesio gracias por creer en mí, por tus consejos, por todo el tiempo dedicado, por tu paciencia, por todo. Muchas gracias.

En segundo lugar, dar las gracias muy especialmente al Dr. Pedro A. Hernández y al Dr. Eleazar Padrón, co-directores de la tesis. Vuestro asesoramiento y correcciones han mejorado notablemente este trabajo. Muchas gracias también por estar mano a mano conmigo en el proceso de escritura de los artículos, sin los cuales no hubiera sido posible esta tesis.

Gracias al Dr. Eumenio Ancochea, por realizar las labores de tutoría de la tesis.

Mi agradecimiento a todos los co-autores de los trabajos presentados que han hecho posible la realización de esta tesis doctoral. En especial a la gente de la Universidad de Barcelona: Juanjo Ledo, Pilar Queralt, Alex Marcuello, Fabián Bellmunt y Perla Piña-Varas. Gracias Perla por todo tu trabajo y esfuerzo en el artículo de *Garehagua*. Gracias también a Raúl Hidalgo y Rayco Marrero por sus críticas constructivas en la fase de escritura de los artículos. Un especial agradecimiento al Dr. Hirochika Sumino, del Geochemical Research Center–University of Tokyo, por la realización de los análisis de isótopos de He. Así como a los co-autores Keisuke Nagao, Kenji Notsu, Antonio Ramos, Antonio Márquez, Roberto Quevedo, Dina López, Ángel Rodríguez y Letizia Spampinato.

Dar también las gracias a diversas instituciones/organismos por ayudarnos con la logística del trabajo: A los Cabildos insulares de La Palma y El Hierro y en especial al Cabildo Insular de Tenerife, por apostar por la creación del Instituto Volcanológico de Canarias (INVOLCAN), al Ayuntamiento de Fuencaliente de La Palma, a la comunidad de regantes del pozo de Amargavinos de La Palma, al Ayuntamiento de Guía de Isora, al Parque Nacional de Timanfaya, al Parque Nacional de Las Cañadas del Teide, a la Unidad de helicópteros de la Guardia Civil en Canarias y por último y no por ello menos importante, al Centro Coordinador de Emergencias y Seguridad (CECOI) y a la comunidad de aguas de San Simón de El Hierro.

Mi especial agradecimiento a todos mis compañeros de la División de Medioambiente, porque sin vosotros nada de esto hubiera sido posible: Gladys, gracias por preocuparte siempre y aconsejarme durante todo este tiempo; María, gracias por ayudarme con los formatos y maquetación de la tesis; Germán, gracias por enseñarme el mejor método del mundo, el "*German method*"; Pepe, gracias por tus consejos "gratis"; Samara, gracias por todas las risas que nos hemos echado juntas, sobre todo en tantos momentos de estrés que hemos compartido;

David, gracias por tus consejos y enseñanzas sobre todo en mis primeros años en el grupo con nuestro programa educativo. No puedo olvidarme de todos aquellos compañeros con los que coincidí durante alguna etapa de este camino: Dácil, Rayco, Marga, Gabi, Isabel, Cristina, Íñigo, Mª Dolores, María, Cayetano y Mar. Gracias a todos por todo, por los grandes favores y los pequeños detalles, por haberme hecho sentir como en familia.

Quiero agradecer también a todos los compañeros del resto de departamentos del Instituto Tecnológico y de Energías Renovables. Ha sido un placer trabajar con vosotros.

A todos los estudiantes, tanto de universidades españolas como extranjeras, y voluntarios que me han acompañado en los trabajos de campo y en los análisis de laboratorio. Especialmente a Alba, Alberto, Alejandro, Alessia, Cynthia, Daniel, Rocío, David Mani, David Nieto, Diego, Isaac, Melchor, Mimi, Nando, Pablo, Paula, Raquel, Rayco, Rubén, Verónica… y a todos los que haya podido olvidar. Sin vosotros el campo no hubiera sido igual de divertido!

Gracias a todas aquellas personas que en algún momento u otro han formado parte de mi vida, porque de todos he aprendido cosas. A todos los amigos que alguna vez me dijeron "¿cómo llevas la tesis? Ánimo, ya queda menos!": Nely, Miguel, Meri, Rayco, Ruymán, Xiomara, Alberto, Irene, Víctor, Cristina, Amalia... A mis amigas y compañeras de la Facultad, Itzi, Patri y Vero con quien comparto la pasión por la geología. Así como a Esther, mi compi de geología de Talavera.

Gracias a mis "hermanas": Bea, Cris, Leti y Noe, por su apoyo incondicional. A pesar de la distancia siempre he sentido que os tengo muy cerca.

Gracias especialmente a Ceci, por estar a mi lado, por escucharme y por darme ánimos cuando los he necesitado.

A mi familia, pero muy especialmente a mis padres, Ramón y Mª Carmen, que siempre están ahí para lo que haga falta, por preocuparse por mí, por aconsejarme… No existen palabras para expresar todo mi amor y agradecimiento.

Por último, solamente citar una frase de un poeta inglés, que se me quedó grabada hace tiempo y ahora me viene "al pelo": si A. Tennyson decía que "*somos una parte de todo aquello que encontramos en nuestro camino*", entonces yo soy un poquito de cada uno de todos vosotros. Gracias de corazón.

Fátima Rodríguez García

Dedicatoria:

A mis ángeles de la guarda,
mis abuelos, Ángel y Josefa
y Mariano y Ascensión,
a quienes me hubiera gustado
poder enseñarles esta tesis

Summary

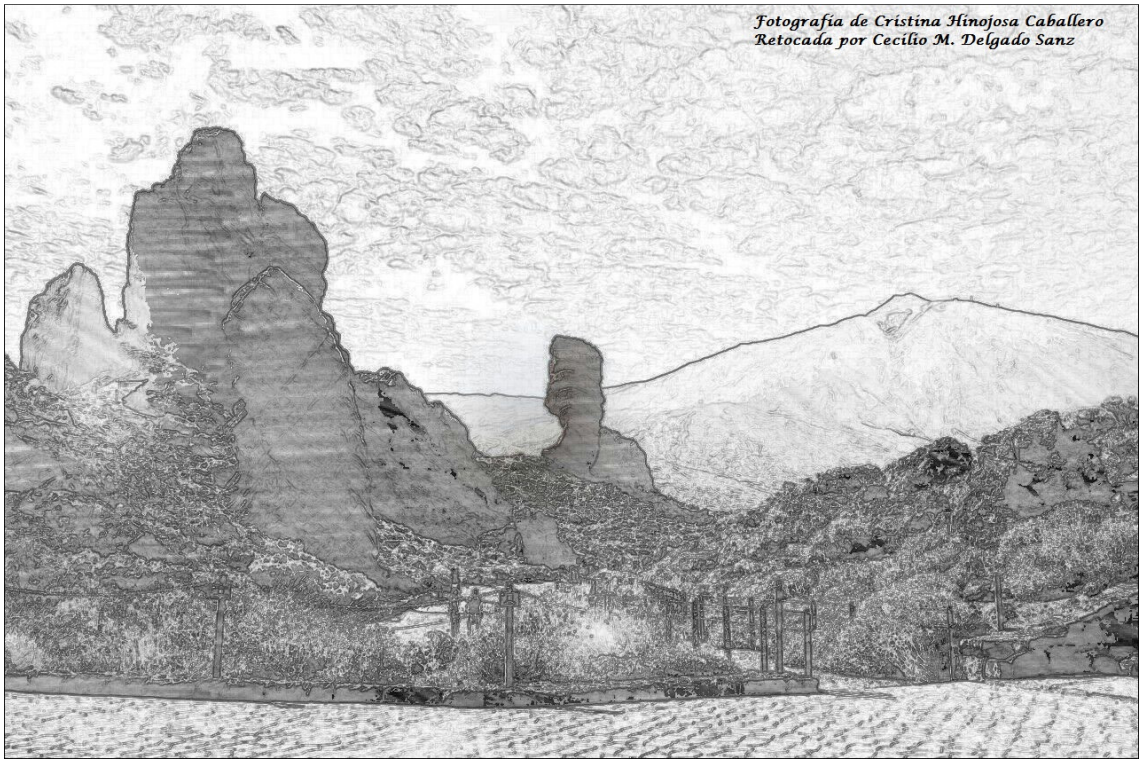

CONTENTS

List of Figures

List of Tables

Abstract

In the present Ph.D. Thesis, entitled “Geochemistry of diffuse degassing and thermal imaging in volcanic systems: implications for geothermal exploration and volcano monitoring in the Canary Islands”, the use of soil gas emission studies, together with other geophysical methods as magnetotelluric and infrared (IR) thermal surveys, are evaluated as useful techniques for volcano monitoring and geothermal exploration. Canary Islands were the case study to achieve this objective, because Holocene volcanic activity has occurred on all islands except La Gomera, with historic activity having been on Tenerife, La Palma, Lanzarote and El Hierro. The entire Canarian Archipelago can be considered a volcanically active area and its volcanic risk is now higher than 40 years ago as a result of the actual higher levels of population and socio-economic value exposure to the volcanic hazards present on the territory. In the recent history of the Canary Islands, there have been few efforts to take advantage of the benefits of the Canary Islands volcanism, as would be the development of geothermal energy, although the archipelago is the only Spanish territory with potential high enthalpy geothermal resources due to its volcanic nature and recent volcanic activity. Therefore, greater efforts are needed to develop the geothermal energy in the Canaries and to improve the early warning system of future volcanic reactivation processes. Hence, this Ph.D. Thesis aims (i) to reduce the negative impacts of volcanism on Canary Islands through an advance in the understanding of the dynamics of volcanic gas emissions as a powerful technique for volcano monitoring purposes, and (ii) to promote the development of geothermal energy through an advance in the understanding of geothermal resources that might exist in the subsurface of the Canary Islands.

Owing to their high mobility within the Earth's crust, volcanic gases act as efficient indicators of magmatic rising and offer to the scientific community working in volcano monitoring effective tools to reduce the uncertainty inherent to the early warning signals of volcanic unrest episodes. In geothermal exploration, gas geochemistry studies are particularly useful to study physico-chemical and thermal conditions in the geothermal reservoir at depth and to detect enhanced vertical permeability areas related to high temperature hydrothermal activity. In the case of volcano monitoring, measurements of volcanic gas emission help to

evaluate the state of the volcano and to anticipate the eruption, because before the eruption onset, volcanoes show significative changes in the chemical composition and/or the fluxes of the volcanic gases emitted. In the last decades, the developments of theoretical models and analytical instrumentation applied to volcano monitoring have contributed greatly to provide multi-disciplinary volcano monitoring techniques. The use of infrared thermal cameras for volcano monitoring is a good example. Thermal imaging data, especially when used together with other monitoring techniques such as seismicity, GPS measurements, and volcanic gas emissions, helps to determine the nature of potential volcanic hazard. Within the geochemical methods in volcano monitoring and geothermal exploration, diffuse degassing studies have revealed that volcanic areas release large amounts of gas as non-visible, diffuse degassing form, during both repose and active periods. Discrete surveys of diffuse degassing covering large areas of the volcano have provided important precursory increases of the emission rate prior to volcanic eruption or accompanying injection of fresh magma into volcanic systems. They have become also a powerful tool in geothermal exploration, since mapping soil gas enrichments relative to background concentrations and/or their fluxes is useful in delineating main upflow regions and areas of increased subsurface permeability related to high temperature hydrothermal activity at depth. These studies are particularly necessary to discover new geothermal systems where the resources are either hidden or lie at great depths.

To achieve the objectives of this Ph.D. Thesis, several studies have been carried out in the different study areas performing hundreds of in situ measurements and laboratory analysis of different geophysical and geochemical parameters. The sampling sites were selected based on their accessibility and geological criteria. Studies of geothermal exploration performed in this research work were carried out in several research permits defined by five mining licenses in Tenerife and Gran Canaria islands. Regarding volcano monitoring, an extensive survey was performed in Timanfaya, Lanzarote Island, including analysis of several chemical species of the soil gas and their isotopic composition and temperature. The most active basaltic volcano of the Canaries, Cumbre Vieja volcano in La Palma Island, was investigated through different soil CO_2 efflux surveys carried out in 13 years. This study was complemented by the analysis of the isotopic composition of helium (He) released in the only known visible gas emission site occurring in La Palma island, a CO_2-rich bubbling cold spring that exists inside Taburiente caldera. As no visible emanations occur at the surface environment of El Hierro, diffuse degassing studies have become the most useful geochemical tool to monitor the volcanic activity in this volcanic island. El Hierro Island experienced a seismic-volcanic crisis from July 2011 culminating with an underwater eruption on October 12, 2011. This eruption has been the first in the history of Canary Islands to be monitored from a multidisciplinary approach and a unique opportunity to study the role of volcanic gases during periods of volcanic unrest in

oceanic islands like the Canaries. The studies at El Hierro Island were focused in He emission and thermal imaging surveys. The ideal characteristics of the He as geochemical tracer that minimize the interaction of this noble gas on its movement toward the earth's surface were demonstrated during this volcanic unrest. Furthermore, the temporal evolution of the eruption and the total magma volume emitted, were investigated for the first time by means of helicopter IR-thermal surveys.

Through the research activities presented here, the following results and conclusions have been obtained. Regarding geothermal exploration, joint geochemical and geophysical methods have helped to define the most appropriate areas that are susceptible of more detailed research to minimize the uncertainty for the location of a future geothermal exploratory drilling. Combining the overall information shown in this work it was possible to obtain weighting tools to sort five different study areas in terms of their relative potential of finding geothermal resources. In this context the southern and western volcanic-rift of Tenerife seemed to show the highest geothermal potential of the five mining licenses studied. Soil gas surveys in the southern volcanic-rift of Tenerife provided useful information about the mechanisms of uprising of deep-seated gases and helped finding vertical permeability structures that favour leakage of endogenous gases from the volcano-geothermal system. A 3-D resistivity model showed a geoelectrical distribution typical of a high-temperature geothermal system with a low resistivity layer, interpreted as an impermeable clay cap located roughly at 1,500 meters depth. The inverse correlation between the thickness of this clay alteration cap and enrichments of non-reactive gases as He, suggests the presence of permeability discontinuities in the study area since the uprising of volcano-geothermal gases towards the surface is less hindered where lower thickness of the clay alteration cap is present.

Soil gas prospecting in Timanfaya volcanic system (Lanzarote Island) showed a composition characterized by atmospheric air slightly polluted by deep-seated He emissions, CO_2 degassed from a cooling magma body and biogenic CO_2. Important emission rates of He were measured along the main eruptive fissure of the 1730–36 eruption of Timanfaya volcano. The presence of deep He and CO_2 make the main eruptive fissure of Timanfaya volcano an ideal site for volcano monitoring. Diffuse emission surveys carried out at Cumbre Vieja volcano (the most active volcanic system of the Canaries) have shown that this volcano releases deep-seated CO_2 diffusively at several sites along the southern coast of the volcano, although biological processes such as degradation of organic matter are the main source of CO_2 at Cumbre Vieja. Only ~4% of the total diffuse CO_2 output should be considered to be released from a deep source during volcanic quiescence periods from the southern part of Cumbre Vieja. Significant increases in the CO_2 emission rate from the volcano were observed in 2011 and 2013, which might be related to inputs of deep-seated CO_2 that occurred a year in advance.

The patterns of He release observed at El Hierro Island during the 2011-2012 submarine eruption and the correlations with seismic energy, provide significant insight on the build up and release of subterranean gas pressure, migration of fracture-controlled gas release, and precursory potential of inert gases, such as He, particularly regarding the timing of gas release with respect to the onset of seismic activity. The results clearly show the critical role that He can play in the prediction of major volcanic events and the importance of continuous monitoring of this gas in active volcanic regions, mainly when magma migrates aseismically, i.e., silently, toward the surface. This submarine eruption was also an excellent opportunity to test the usefulness of aerial thermal images to reconstruct the temporal evolution of the eruption and to estimate the total magma volume emitted during the submarine eruption. This technique has proven to be an easy method to use, efficient and reliable in producing results during a volcanic crisis, and relatively inexpensive when compared to bathymetric surveys.

Resumen

En la presente tesis doctoral, titulada "Geoquímica de emanaciones difusas y termografía en sistemas volcánicos: implicaciones para la exploración geotérmica y la vigilancia volcánica en Canarias", se ha evaluado el uso conjunto de técnicas geoquímicas (prospecciones geoquímicas de gases y volátiles en el ambiente superficial del suelo) y geofísicas (campañas de exploración magnetotelúrica y estudio de imágenes térmicas) como herramientas para la monitorización volcánica y la exploración geotérmica. Las Islas Canarias fueron el marco de estudio elegido para lograr este objetivo, debido a que en dichas islas ha habido actividad volcánica holocénica (a excepción de La Gomera), habiéndose registrado erupciones históricas en las islas de Tenerife, La Palma, Lanzarote y El Hierro. El archipiélago canario en su conjunto se puede considerar como un área volcánicamente activa, siendo el riesgo volcánico hoy día mayor que hace 40 años, como resultado de un drástico aumento poblacional y socio-económico, expuesto a los peligros volcánicos inherentes a la naturaleza volcánica del archipiélago. En la historia reciente de las Islas Canarias existe una carencia de esfuerzos para la explotación de uno de los beneficios del fenómeno volcánico, como podría ser el desarrollo de la energía geotérmica: Canarias es la única región del territorio nacional con recursos geotérmicos de alta temperatura como consecuencia de la presencia de un volcanismo activo. Por lo tanto, es necesario un mayor esfuerzo para desarrollar la energía geotérmica en Canarias y mejorar los sistemas de detección de señales de alerta ante futuros procesos de reactivación volcánica. Este trabajo de tesis doctoral persigue (i) reducir los impactos negativos de la actividad volcánica en las islas Canarias a través de un avance en la comprensión de la dinámica de las emisiones de gases volcánicos como una poderosa técnica de vigilancia volcánica y (ii) promover el desarrollo de la energía geotérmica a través un avance en el conocimiento de los recursos geotérmicos que pudieran existir en el subsuelo de las Islas Canarias.

Debido a su gran movilidad en la corteza terrestre, los gases volcánicos actúan como potentes indicadores de movimientos de magma en el interior de la Tierra y ofrecen a la comunidad científica que trabaja en el campo de la vigilancia volcánica, una herramienta efectiva para reducir la incertidumbre en la predicción de señales de alerta tempranas ante

episodios de reactivación volcánica. En exploración geotérmica, los estudios de geoquímica de gases son particularmente útiles para estudiar las condiciones físico-químicas de reservorios geotermales en profundidad y para detectar zonas de mayor permeabilidad relacionadas con la actividad hidrotermal de alta temperatura. En el caso de la vigilancia volcánica, la prospección de gases y volátiles del suelo ayuda a evaluar el estado de actividad volcánica y en último término, anticipar una erupción, ya que antes de que esta ocurra, los volcanes muestras cambios significativos en la composición química y/o los flujos de gases emitidos. En las últimas décadas, el desarrollo de modelos teóricos e instrumentación analítica aplicada a la vigilancia volcánica ha contribuido a desarrollar sistemas de vigilancia multidisciplinares. El uso de cámaras térmicas con fines de vigilancia volcánica es un buen ejemplo. Las imágenes térmicas, especialmente usadas junto con otras técnicas como la sismicidad, la geodesia y las emisiones de gases, ayudan a determinar la naturaleza de los potenciales peligros volcánicos. Dentro del estudio de los métodos geoquímicos en vigilancia volcánica y exploración geotérmica, los estudios de desgasificación difusa han señalado que los volcanes emiten grandes cantidades de gases de forma no visible (o difusa), tanto en periodos activos como en periodos de reposo. Los estudios de prospección geoquímica de gases en el ambiente superficial del suelo han mostrado incrementos en los valores de emisión en sistemas volcánicos antes de una erupción o acompañando la inyección de magma en profundidad. De la misma forma, son una herramienta poderosa en la exploración geotérmica, ya que los enriquecimientos relativos con respecto a concentraciones normales y/o sus flujos sirven para definir zonas de permeabilidad vertical que favorecen el ascenso de fluidos hidrotermales en profundidad. Estos estudios son particularmente útiles cuando no existen manifestaciones de gases visibles en superficie y es necesaria una búsqueda de recursos que se encuentran "escondidos" y/o a grandes profundidades.

Para lograr los objetivos de esta tesis doctoral, se han realizado múltiples estudios en distintas áreas, desarrollándose cientos de medidas *in situ* y análisis en laboratorio de distintos parámetros geofísicos y geoquímicos. Los puntos de muestreo fueron seleccionados en base a criterios geológicos y de accesibilidad. Los estudios de exploración geotérmica de este trabajo se desarrollaron en 5 permisos de investigación en las islas de Tenerife y Gran Canaria. Se llevaron a cabo estudios de geoquímica de emanaciones difusas así como estudios de magnetotelúrica. En cuanto a vigilancia volcánica, se desarrolló una extensa campaña en el área volcánica de Timanfaya (Lanzarote), incluyendo análisis de diversas especies químicas de gas del suelo y su composición isotópica y temperatura. El volcán basáltico más activo de canarias, el volcán de Cumbre Vieja en La Palma, fue objeto de investigación mediante campañas de emisiones difusas de CO_2 durante 13 años. Este estudio se complementó con los análisis

isotópicos de helio en la única manifestación de gases visible de la isla (el burbujeo de Dos Aguas dentro de la Caldera de Taburiente).

La no existencia de manifestaciones visibles de gases en la isla de El Hierro convierte los estudios de desgasificación difusa en una herramienta geoquímica útil para monitorizar la actividad volcánica en esta isla. La isla de El Hierro experimentó una crisis sismo-volcánica desde julio de 2011 que culminó con una erupción submarina el 12 de octubre de 2011. Esta erupción ha sido la primera en la historia de Canarias en ser monitorizada desde un enfoque multidisciplinar y una oportunidad única para estudiar el papel de los gases volcánicos durante un periodo de actividad volcánica en islas oceánicas como las Islas Canarias. Los estudios en la isla de El Hierro se han centrado en la emisión difusa de helio en el área emergida de la isla y la toma de imágenes térmicas de la superficie del mar afectado por la erupción submarina. Las características ideales del helio como trazador geoquímico que reducen al mínimo la interacción de este gas noble en su movimiento hacia la superficie de la tierra, se demostraron durante esta reactivación volcánica. Por otra parte, la evolución temporal de la erupción y el volumen de magma total emitido, se investigaron por primera vez a través de imágenes térmicas tomadas desde un helicóptero.

A través de los estudios de investigación presentados en este trabajo de tesis doctoral, se han obtenidos los siguientes resultados y conclusiones. En cuanto a exploración geotérmica, se han definido áreas susceptibles de investigaciones más detalladas para minimizar la incertidumbre en la ubicación de futuros sondeos exploratorios en busca del recurso geotérmico. Combinando la información generada fue posible obtener herramientas de ponderación para ordenar las cinco áreas de estudio en términos de potencial geotérmico relativo. En este contexto, el permiso de exploración situado en la dorsal sur de la isla de Tenerife mostró el potencial geotérmico más alto de las cinco licencias mineras estudiadas. Los estudios de gases del suelo en esta área proporcionaron información útil sobre los mecanismos de ascenso de gases profundos y ayudaron a encontrar estructuras de permeabilidad vertical que favorecen la migración hacia la superficie de los gases de origen endógeno desde el sistema volcánico-geotermal. Un modelo de resistividad 3-D mostró una distribución geoeléctrica típica de un sistema geotérmico de alta temperatura con una zona de baja resistividad, interpretada como una capa de arcilla impermeable situada aproximadamente a unos 1.500 metros de profundidad. La correlación inversa entre el espesor de esta capa de alteración y los enriquecimientos relativos de gases no reactivos como el helio, sugiere la presencia de discontinuidades de permeabilidad en la zona de estudio, siendo el ascenso de gases hacia la superficie menos obstaculizado cuanto menor es el espesor de la capa de alteración presente.

La prospección de gases del suelo en Timanfaya (Lanzarote) mostró una composición caracterizada por aire atmosférico ligeramente contaminado por emisiones de helio profundas

con una pequeña fracción de CO_2 procedente de un cuerpo magmático en enfriamiento. Se midieron tasas de emisión de helio importantes a lo largo de la principal fisura eruptiva de la erupción de Timanfaya de 1730-1736. La presencia de helio y CO_2 profundo convierten a la fisura eruptiva principal del volcán de Timanfaya en un sitio ideal para la vigilancia volcánica. Los estudios de emisión difusa de flujo de CO_2 en el volcán Cumbre Vieja (el sistema volcánico más activo de las Canarias) han demostrado que este volcán emite CO_2 de origen profundo en varios puntos a lo largo de la dorsal sur del volcán, siendo los procesos biológicos (degradación de la materia orgánica) su principal fuente de emisión. Sólo alrededor del ~4% de la emisión de CO_2 de forma difusa en superficie en Cumbre Vieja durante periodos de calma volcánica puede ser considerado de origen endógeno. Aumentos significativos en la tasa de emisión de CO_2 del volcán fueron observados en 2011 y 2013, lo que podría estar relacionado con mayores aportes de CO_2 magmático que ocurrieron con un año de antelación.

Los patrones de desgasificación de helio observados en la isla de El Hierro durante la erupción submarina de 2011-2012 y las correlaciones con la energía sísmica, proporcionaron información importante sobre la acumulación y liberación de presión de gases desde la corteza terrestre, la desgasificación y su relación con las características volcano-estructurales y el uso de gases nobles, tales como helio, como potenciales precursores de actividad volcánica. Los resultados muestran claramente el papel fundamental que el helio puede desempeñar en la predicción de eventos volcánicos y la importancia de la monitorización continua de este gas en las regiones volcánicas activas, sobre todo cuando el magma migra asísmicamente hacia la superficie. Esta erupción submarina fue también una excelente oportunidad para poner a prueba la utilidad de las imágenes térmicas aéreas como herramienta para reconstruir la evolución temporal de la erupción y estimar el volumen de magma total emitido durante la misma. Esta técnica ha demostrado ser un método fácil, eficaz y fiable en la producción de resultados durante una crisis volcánica. Es, además, una técnica relativamente barata en comparación con las campañas batimétricas.

Introduction

1. Introduction

1.1. Diffuse degassing in volcanic systems

Many studies on volcanic gas emissions report that, even during repose periods, volcanoes release large amounts of gases from both visible (fumaroles, solfataras, plumes) and non-visible emanations (diffuse degassing) from the flanks of the volcano (Baubron et al. 1990; Allard et al. 1991; Chiodini et al. 1996; Gerlach et al. 2001; Salazar et al. 2001; Hernández et al. 2001a and b, 2003, 2006, 2012; Padrón et al. 2012a; Burton et al. 2013; Pérez et al. 2013). Non-visible emanations have been termed "diffuse", because it is invisible and can take place over wide areas (Figure 1.1). Diffuse emanations of volcanic gases consist essentially of CO_2, associated with rare gases as He, H_2 and ^{222}Rn (Allard 1992). Diffuse CO_2 degassing from both volcanic and tectonic structures is a large contributor to the global geological CO_2 emission (Pérez et al. 2011; Burton et al. 2013). At dormant volcanoes, diffuse degassing can even be the dominant process of gas release (Mori et al. 2001; Fridriksson et al. 2006; Padrón et al. 2012b). Considering the two types of volcanic gas release, Notsu et al. (2006) proposed a five-stage evolutionary model for the release of volcanic gas. According to this model, as magma rises into the subsurface, diffuse degassing begins to increase before plume degassing shows obvious signs of volcanic reactivation (Figure 1.2). Diffuse degassing studies are particularly useful for volcano monitoring in those volcanic areas where there are no visible volcanic-hydrothermal gas emissions. Discrete surveys of diffuse degassing covering large areas have provided important precursory increases of the emission rate prior to volcanic eruption or accompanying injection of fresh magma into volcanic systems (Hernández et al. 2001a; Arpa et al. 2013; Granieri et al. 2006). These surveys have become also a powerful tool in geothermal exploration (Bertrami et al. 1990; Finlayson 1992; Fridriksson et al. 2006; Voltattorni et al. 2010; Hanson et al. 2014; Jolie et al. 2015). Mapping soil gas enrichments relative to background concentrations and/or their fluxes is useful in delineating main upflow regions (Figure 1.3) and areas of increased subsurface permeability related to high temperature hydrothermal activity at depth (Fridriksson et al. 2006; Chiodini et al. 2007; Hernández et al. 2012; Barberi et al. 2013; Hanson et al. 2014; Jolie et al. 2015). These studies are particularly necessary to discover new geothermal systems where the resources are either hidden or lie at great depths (Hanson et al. 2014).

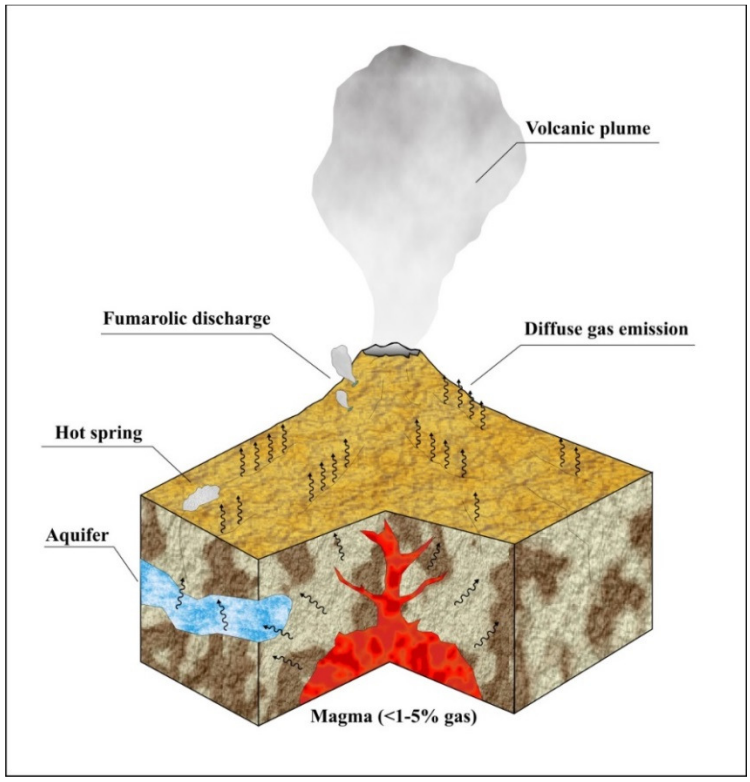

Figure 1.1. *Different types of volcanic gas emission*

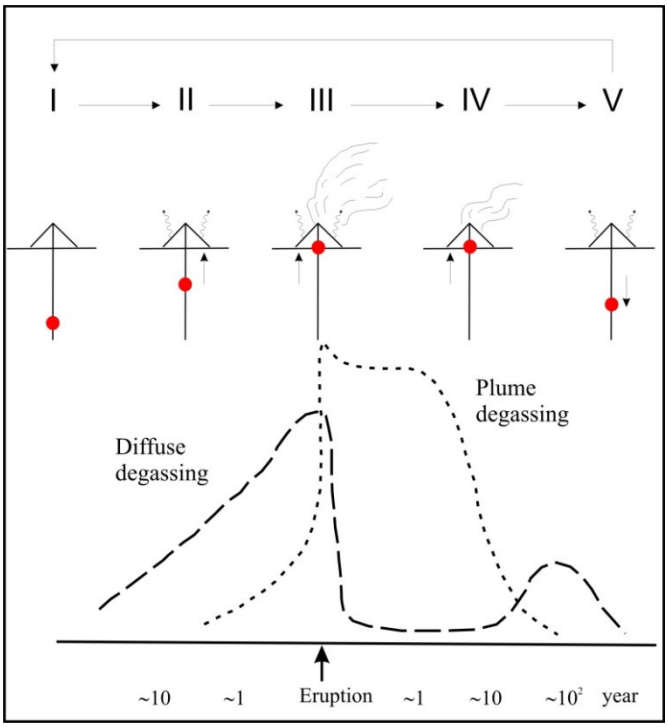

Figure 1.2. *Schematic illustration showing an evolutionary model of gas release from volcanoes. Solid red circle is magma rising and descending along the vent. Emission patterns of both diffuse and plume degassing are roughly illustrated as two broken lines. Time scale of horizontal axis is tentatively indicated in case the recurrence time of eruption is 10^2~10^3 year (Notsu et al. 2006)*

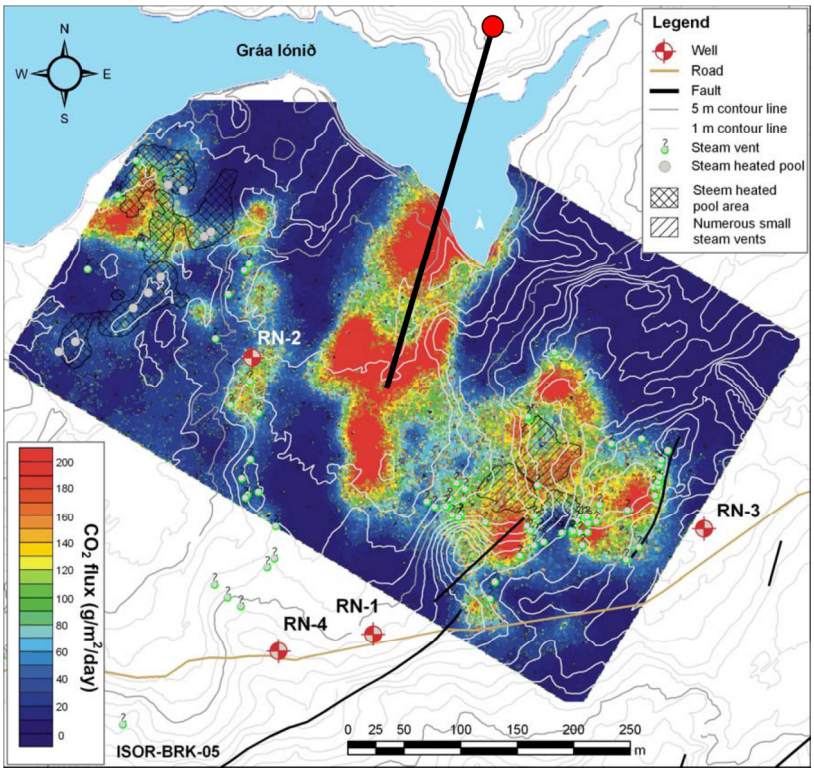

Figure 1.3. *Results of diffuse CO_2 emission survey at Reykjanes geothermal field, Iceland. (Fridriksson et al. 2006)*

1.2. Thermal energy released in volcanic systems

The study of heat fluxes in active volcanic areas provides a fundamental contribution to understanding volcanic processes, and to volcanic hazard assessment and risk management (Spampinato et al. 2011). Thermal data, especially in combination with geophysical and geochemical signals, have proved to be useful precursors of eruption onsets (Oppenheimer 1998; Andronico et al. 2005; Hernández et al. 2007). Recent research have demonstrated that thermal energy released at volcanoes through the surface condensation of volcanic-hydrothermal steam is much higher than the elastic energy released by seismic shocks, conductive heat transfer and the energy of ground deformations caused by volcanic unrest episodes (Figure 1.4; Chiodini et al. 2001). Thermal imaging data, especially when used together with other monitoring techniques such as seismicity, GPS measurements, and volcanic gas emissions, helps to determine the nature of potential volcanic hazards, since it distinguish lava flows of different age and concealed lava tubes' path. Several authors have developed a routine for volcano monitoring at Kilauea (Hawaii, Patrick et al. 2014), Etna and Stromboli (Italy), and other volcanoes (Spampinato et al. 2011).

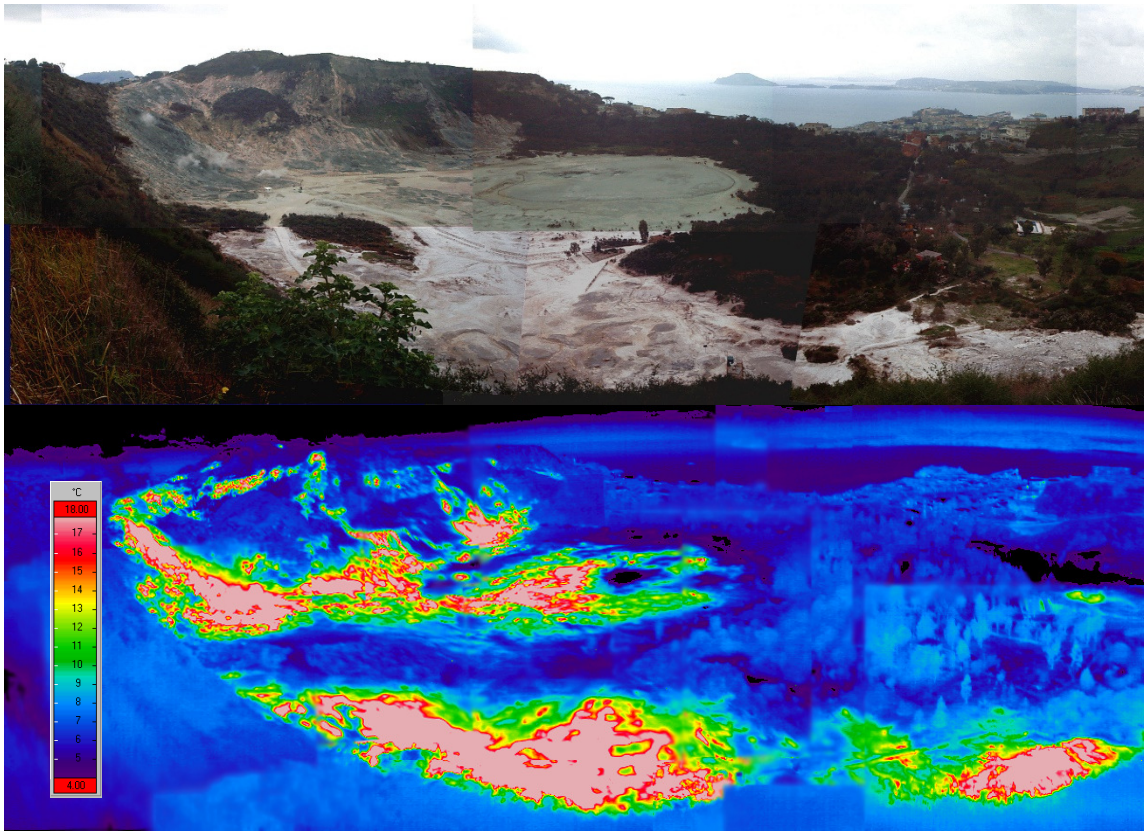

Figure 1.4. *Visual and thermal image of Solfatara di Pozzuoli caldera, Italy. (Chiodini et al. 2001)*

1.3. Magnetotelluric studies in volcanic systems

Magnetotelluric (MT) data give valuable information regarding the presence of fluids, partial melt or conducting anomalies at different levels of the crust and upper mantle. It also provides first order structure and physico-chemical state (temperature, fluids, melts) of the subsurface. Magnetotelluric surveys have been used to image volcanic edifices and processes inside them (Ogawa et al. 1999; Garcia and Jones 2010; Spichak et al. 2013; Piña-Varas et al. 2014 and 2015), as volcano monitoring technique (Manzella and Zaja 2006; Aizawa et al. 2009) and for geothermal exploration (Piña-Varas et al. 2014). Many of geothermal exploration studies have imaged low resistivity structures associated with hydrothermal fluid circulation, clay and/or with partial melting. In geothermal areas, MT can be used to delineate the low resistivity structures that usually correspond to the smectite clay ring that typically exists around a geothermal resource (Figure 1.5).

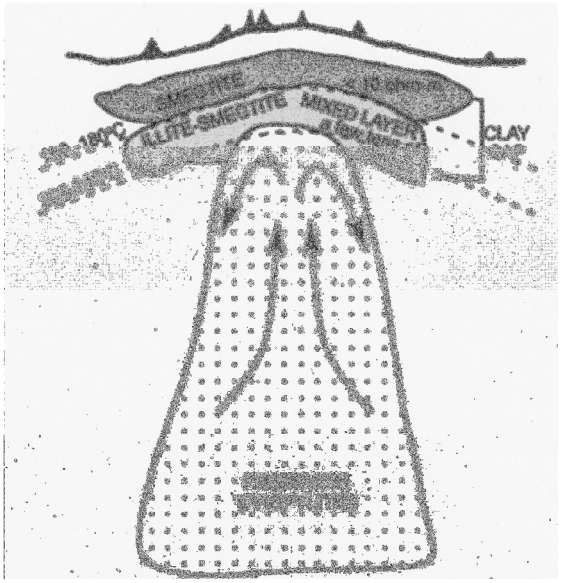

Figure 1.5. *Scheme of a generalised geothermal system (Johnston et al. 1992)*

1.4. Volcanic risk and geothermal exploration in the Canary Islands

The Canary Islands are the only region of Spain where there is active volcanism. Holocene volcanic activity has occurred on all islands except La Gomera with historic activity having been on Tenerife, La Palma, Lanzarote and El Hierro. This last experienced the last volcanic eruption of the Canaries, a submarine eruption that took place between October 12, 2011 and March 5, 2012 off the south coast of El Hierro Island (Figure 1.6). The entire Canarian Archipelago can be considered a volcanically active area (Schmincke and Sumita, 2010). In fact, the Canaries are the most active volcanic island group among Atlantic volcanic islands, next to Iceland and Azores. It should be highlighted that volcanic risk in the Canary Islands is now higher than 40 years ago as a result of the actual higher levels of population and socio-economic value exposure to the volcanic hazards present on the territory (Figure 1.7; Pérez and Hernández 2008).

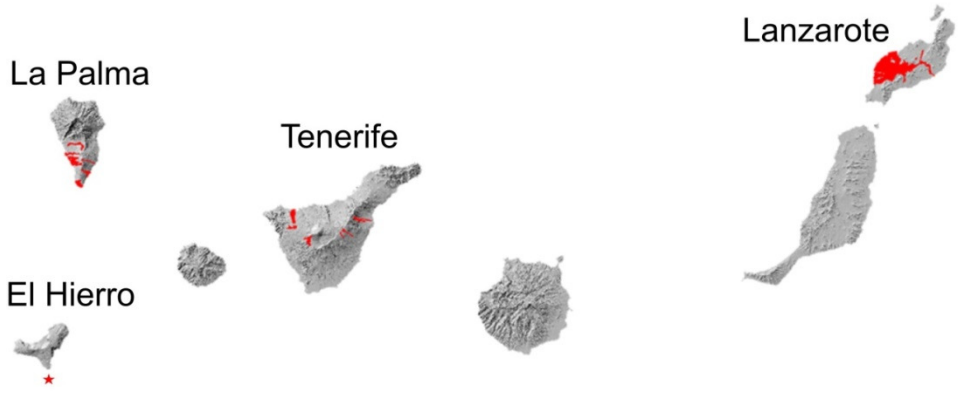

Figure 1.6. *The Canary Islands map showing areas covered by lava flows during historic eruptions (post 1,500 BC). The location of the 2011-2012 submarine eruption off the south coast of El Hierro is shown by a red star*

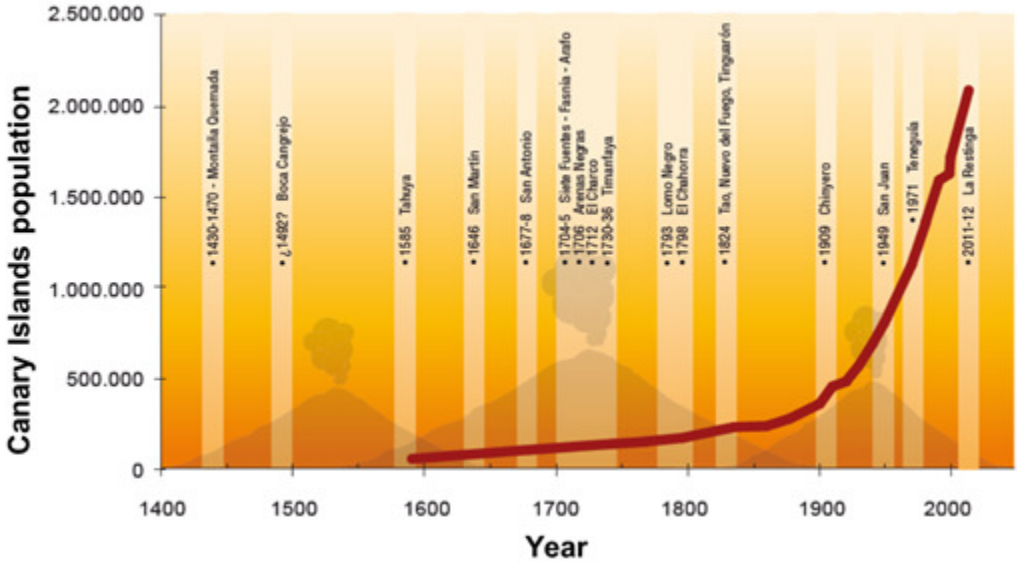

Figure 1.7. *Graph showing historical eruptions in the Canary Islands (post 1,500 BC), together with the evolution of the population of the Canary Islands*

During the International Decade for Natural Disaster Reduction (1990-1999) the scientific and political international community did perform an intense analysis and assessment on the impact of natural disasters that has served to define and recommend the materialization of various actions to reduce the risk of natural hazards including that associated to the volcanic phenomenon. The major actions that had been recommended by the Internal Association of Volcanology and Chemistry of the Earth's Interior (IAVCEI) and the United Nations Organization (UNESCO) to reduce volcanic risk are: (1) to elaborate volcanic hazards mapping, (2) to establish a multidisciplinary approach for volcano monitoring, constantly being updated with technological development, in order to optimize the system for early warning of future eruptions and (3) to develop emergency plans for volcanic risk. The aim of volcanic surveillance is to improve and optimize the early warning system of future volcanic unrest episodes. This monitoring includes geochemical, geophysical and geodetical parameters. The multidisciplinary character of volcano monitoring lies on performing not only continuous monitoring with permanent instruments, but also comprises discrete (non continuous) measurements or surveys.

The Canary Islands archipelago, owing to its recent volcanism, is the only Spanish territory with potential high enthalpy geothermal resources (European Commission 1999). However, very few efforts have been made to develop the potential geothermal energy resources in the archipelago. From the 1970's to the 1990's, the Spanish Geological Survey (IGME, http://www.igme.es) performed an intense research on geothermal resources in the country,

including studies at Lanzarote, Gran Canaria, Tenerife and La Palma islands in the Canaries: geochemical and isotopic analysis of hydrothermal discharges (fumaroles) of Teide volcano, volcano-structural and magnetotelluric studies at Las Cañadas caldera and groundwater hydrochemistry studies (IGME 1977; 1979; 1993a, b, c, d, e, f, g and h; Albert-Beltrán et al. 1990; Valentín et al. 1990). As a result of these exploratory studies, one exploratory drilling in Tenerife and two in Gran Canaria were performed with unsatisfactory results (IGME 1993h). Recently the interest in the development of geothermal energy in the Canaries has increased again, mainly through the efforts of a private company (Petratherm; http://www.petratherm.com.au) and Cabildo Insular de Tenerife through the Instituto Tecnológico y de Energías Renovables (ITER).

1.5. Objectives of this study

The final objective of this Ph.D. Thesis is to assess the use of diffuse emission and soil gas prospecting techniques for geothermal exploration and volcano monitoring purposes in the Canary Archipelago; additionally, we aim to evaluate the use and application of surface thermography for volcano monitoring in shallow submarine eruptions. To achieve this goal, several surveys have been carried out in different systems in the islands of Tenerife, Gran Canaria, Lanzarote, La Palma and El Hierro, this last during a volcanic unrest episode. The following specific objectives have been identified:

- To reduce the uncertainty in the selection of an area with the highest geothermal potential by means of diffuse He and H_2 degassing.
- To evaluate the joint use of soil gas prospecting and magnetotelluric techniques to better characterize the existence of hidden geothermal reservoirs.
- To investigate the relationship between soil gas concentrations and the volcano-tectonic structures.
- To study the relationship between total diffuse CO_2 output to the atmosphere by volcanoes and the level of volcanic activity.
- To evaluate the use of diffuse He studies for the prediction of volcanic events.
- To estimate magma emission rates from shallow submarine eruptions by means of thermal imaging.

These specific objectives are listed on the research papers published in Science Citation Index Journals, which comprise this Ph.D. Thesis:

a) Diffuse helium and hydrogen degassing to reveal hidden geothermal resources in oceanic volcanic islands: The Canarian Archipelago case study – Surveys in Geophysics (2015).

b) Surface geochemical and geophysical studies for geothermal exploration at the sourthern volcanic rift zone of Tenerife, Canary Islands, Spain – Geothermics (2015).

c) Soil gas geochemistry in relation to eruptive fissures on Timanfaya volcano, Lanzarote Island (Canary Islands, Spain) – Journal of Volcanology and Geothermal Research (2013).

d) Dynamics of diffuse carbon dioxide emissions from Cumbre Vieja volcano, La Palma, Canary Islands – Bulletin of Volcanology (2015).

e) Diffusive helium emissions as a precursory sign of volcanic unrest – Geology (2013).

f) Magma emission rates from shallow submarine eruptions using airborne thermal imaging – Remote sensing of environment (2014).

Methodology

2. Methodology

2.1. Soil gas sampling and in-situ measurements

To achieve the objectives of this Ph.D. Thesis, several studies have been carried out in the different study areas performing hundreds of in situ measurements and laboratory analysis of different geophysical and geochemical parameters. The sampling sites were selected based on their accessibility and geological criteria. In the next lines the studied areas and the sampling sites locations will be described.

Studies of geothermal exploration performed in this research work were carried out in several research permits defined by five mining licenses (Figure 2.1); four in Tenerife (*Abeque, Berolo, Garehagua* and *Guayafanta* mining licenses) and one in Gran Canaria (*Atidama* mining license).

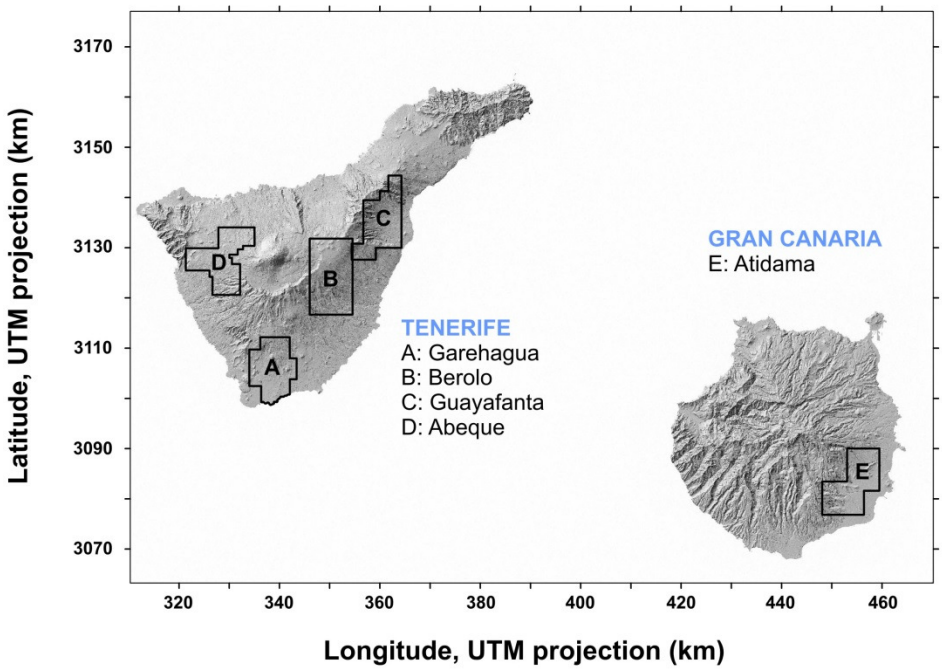

Figure 2.1. *Location of the different mining licenses studied in this Ph.D. Thesis with geothermal exploration purposes*

Soil gas samples for chemical analysis were collected at 557, 577, 600, 406 and 541 sites selected in *Garehagua, Berolo, Atidama*, *Abeque* and *Guayafanta*, respectively (Figure 2.2). Studies for geothermal exploration were focused mainly in nonreactive and/or highly mobile gases such as He and H_2 in the five mining licenses depicted in Figure 2.2. A more detailed study that comprises geochemical and geophysical studies (soil CO_2 and H_2S diffuse effluxes, soil ^{222}Rn activity, soil He, H_2, N_2, CO_2 and O_2, H_2S concentrations, isotopic composition of soil CO_2 and magnetotelluric) was carried out in *Garehagua* mining area.

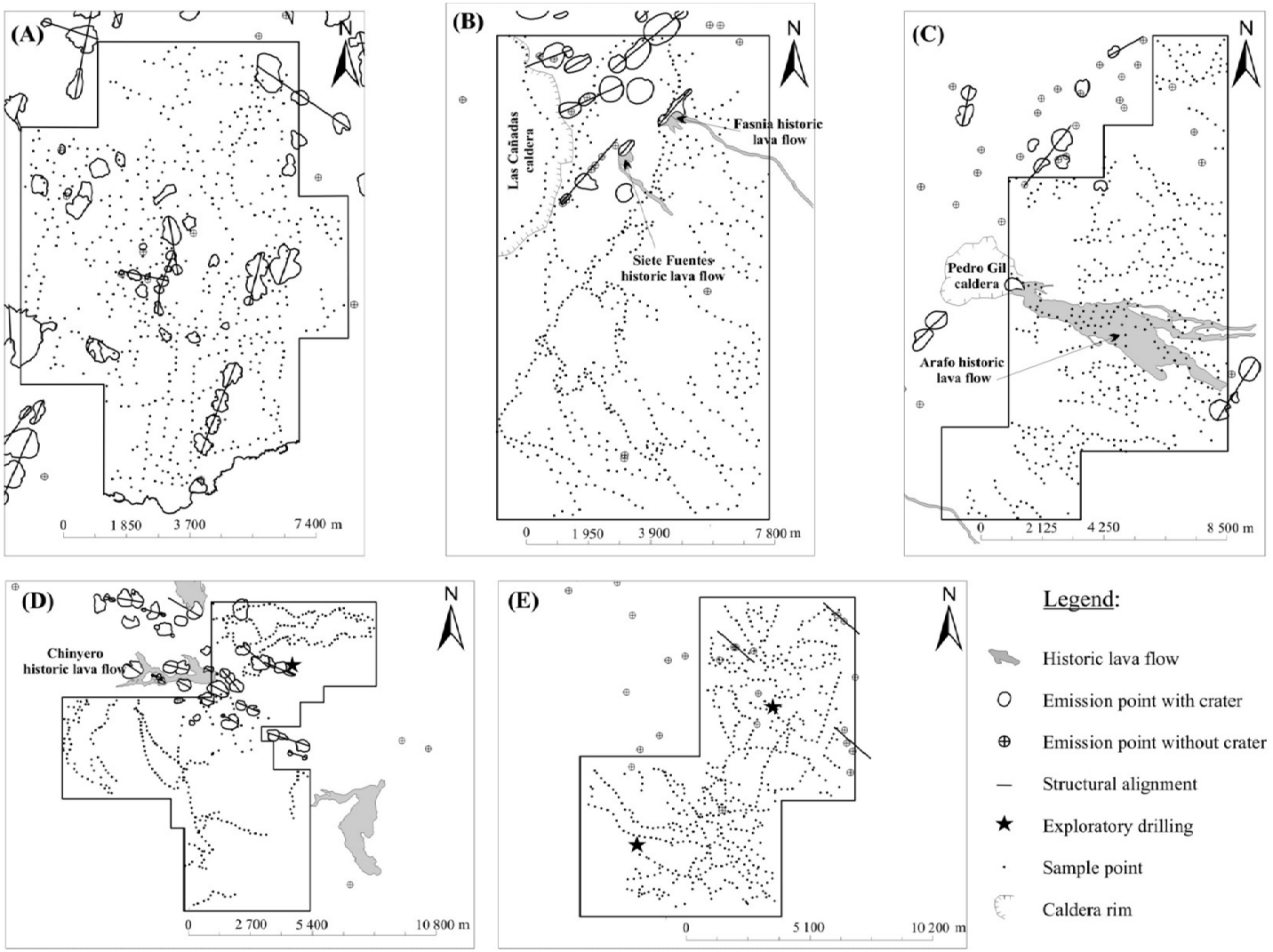

Figure 2.2. *Volcano-structural map and sample sites location of (A) Garehagua, (B) Berolo, (C) Guayafanta, (D) Abeque and (E) Atidama mining licenses. Surfaces covered by historic lava-flows are also displayed. Stars indicate the location of the exploratory drillings carried out in Tenerife and Gran Canaria by IGME (IGME 1993h)*

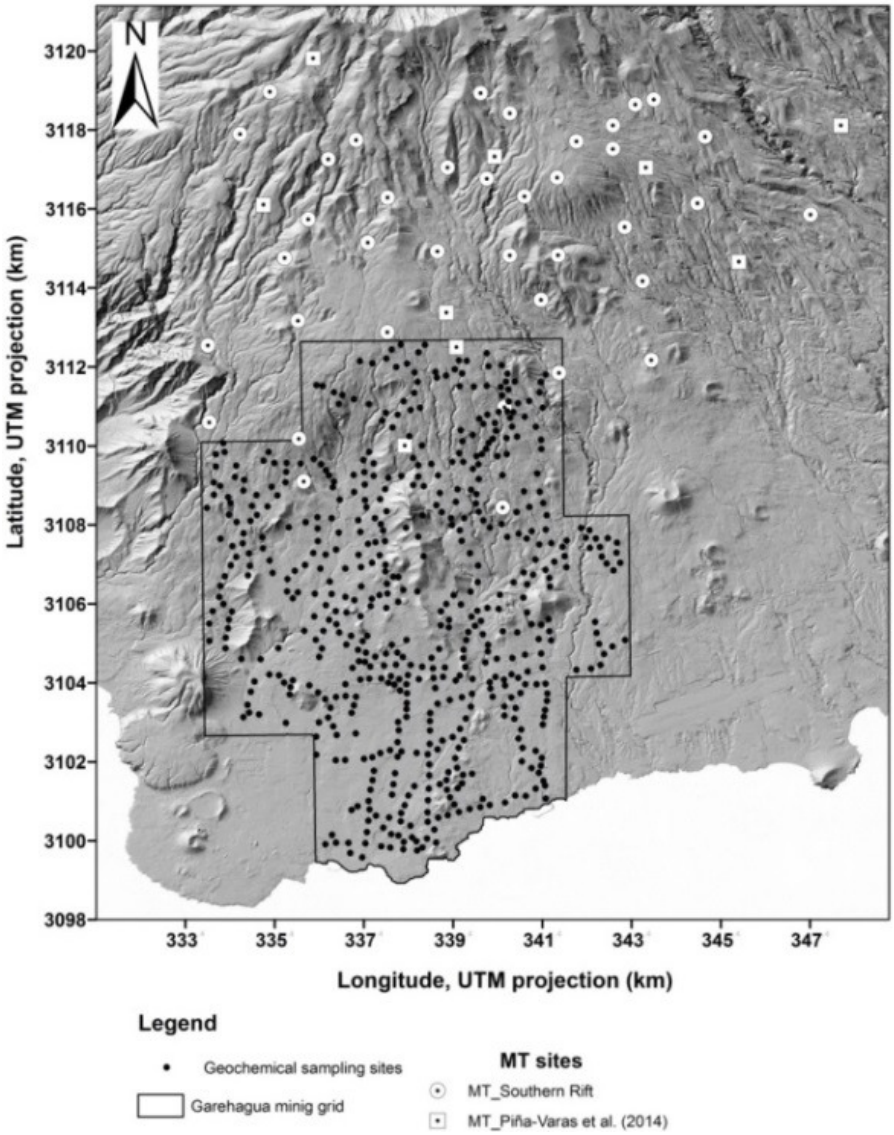

Figure 2.3. *Location of sampling points selected for geochemical analysis (solid black circles) and MT stations (white circles). The location of the MT stations reported by Piña-Varas et al. (2014) are shown as white squares*

In the MT study of *Garehagua*, 47 sites were chosen from different field surveys; 9 sites correspond to those surveyed in a previous work carried out by Piña-Varas et al. (2014) and 38 were surveyed specifically for this Ph.D. Thesis (Figure 2.3). The model is discretized on a 93x72x133 layer grid and the inversions are undertaken using the off-diagonal components (Z_{xy}, Z_{yx}) of the impedance tensor for 30 periods in the frequency range from 10^{-3} to 10^{2} s.

Regarding volcano monitoring, an extensive survey of 366 soil gas samples was performed in Timanfaya, Lanzarote Island (Figure 2.4), including analysis of ^{222}Rn activity, He, H_2, N_2, CO_2 O_2, and H_2S concentrations, isotopic composition of CO_2 in soil gases and soil temperature measurements.

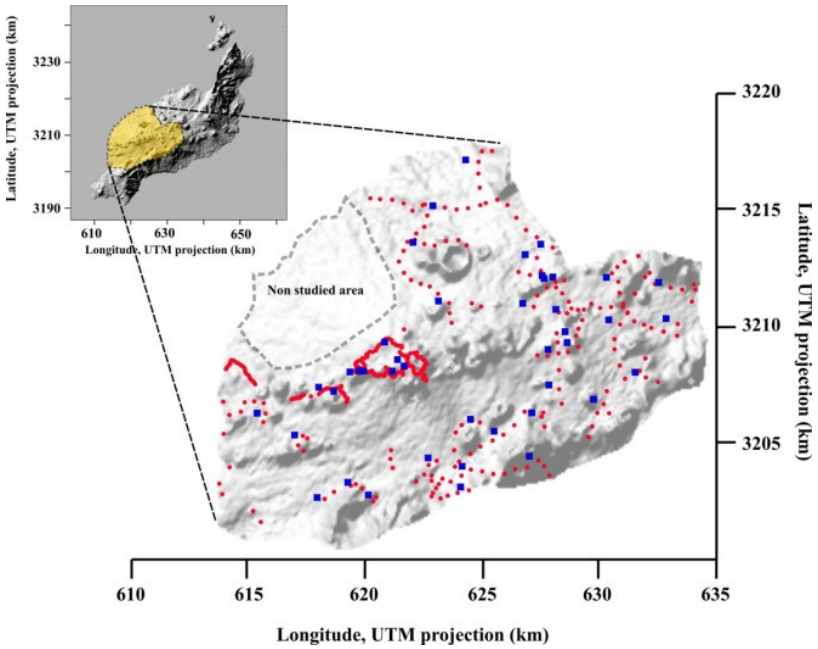

Figure 2.4. *Sampling sites along the surface environment of Timanfaya volcanic area. Red dots indicate the location of the sampling sites to analyze chemical composition of the soil gases collected on May 2011. Blue squares indicate the location of the sampling sites to analyse the soil CO_2 concentration and isotopic composition of CO_2*

At Cumbre Vieja volcano, in La Palma Island, 13 different soil CO_2 efflux surveys were carried out during the 2001-2013 period. Soil CO_2 efflux , soil CO_2 concentration and isotopic composition were measured. Each survey comprises between 505 to 621 samples points depending on the year, but always following a homogeneous pattern along the selected studied area (Figure 2.5). $^{3}He/^{4}He$ ratios were analysed in the gas from the Dos Aguas (DA) CO_2-rich bubbling cold spring (Figure 2.6). The gas of DA was sampled once in 2007, 2008 and 2011 and three times in 2012.

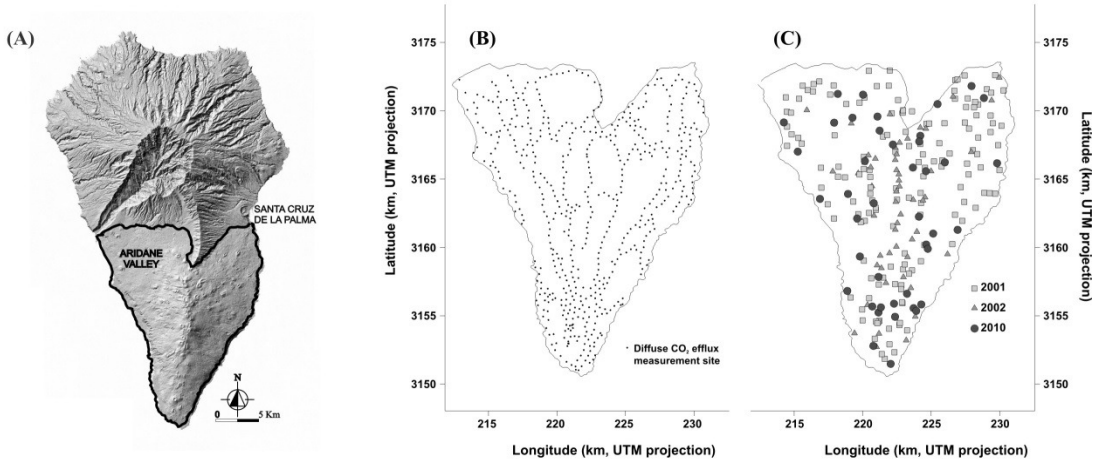

Figure 2.5. *(A) La Palma Island with the location of the Cumbre Vieja volcano study area and location of the sampling sites selected for (B) diffuse CO_2 efflux measurements at 2010 and (C) for chemical and isotopic analysis of the soil CO_2 at Cumbre Vieja*

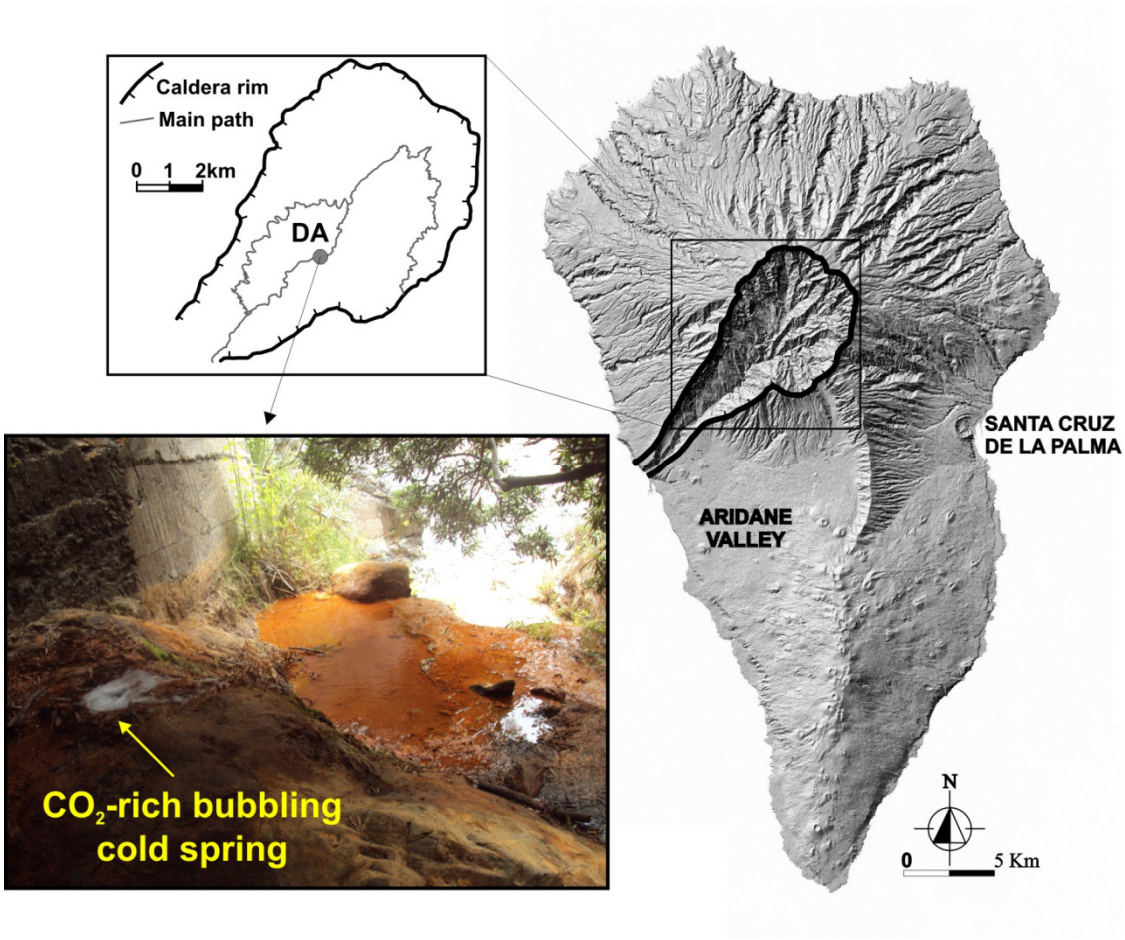

Figure 2.6. *Location and picture of Dos Aguas (DA) CO_2-rich bubbling cold spring*

The studies for volcano monitoring purposes carried out at El Hierro Island were focused in helium emission and thermal imaging surveys. Analyses of thermal images of the sea surface were carried out almost daily during the submarine volcanic eruption period, conducting helicopter flights over the discoloured area (Figure 2.7), using FLIR R&D software, which allowed to correct the IR images for distance, humidity and air temperature recorded during each flight and to estimate apparent temperatures.

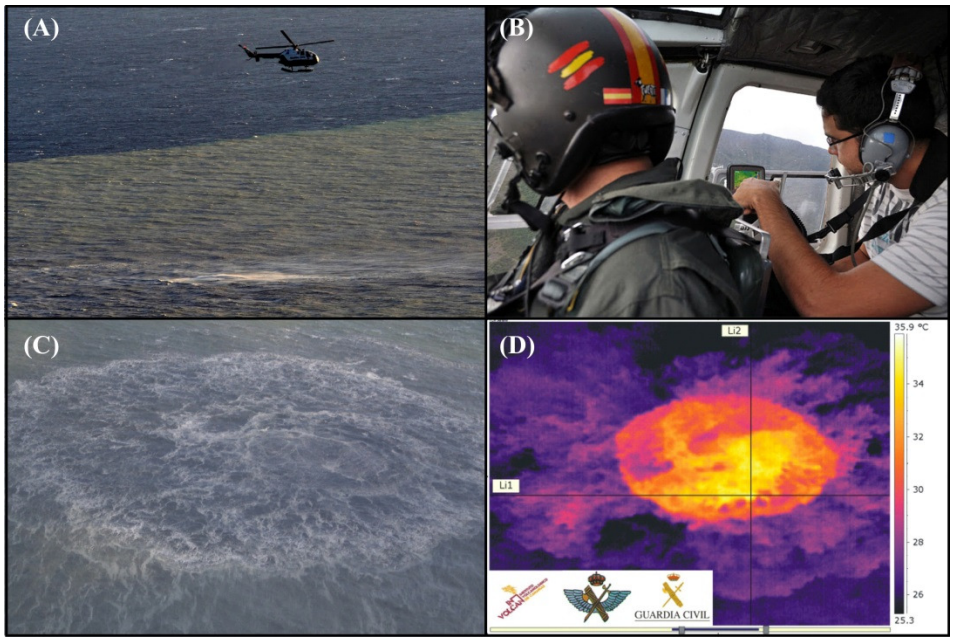

Figure 2.7. *(A) Picture of the helicopter over the discoloured area of the eruption, (B) taking thermal images from the helicopter, (C) visible and (D) thermal infrared image of the discoloured seawater area over the eruption site taken on November 8, 2011*

At El Hierro Island 15 helium emission surveys were performed, 14 of which were performed during the 2011-2012 volcanic unrest period and one in 2003 during a volcanic quiescence period. A total of 601 sampling sites were selected to cover all the surface environment of El Hierro with a site spacing about 400 m (Figure 2.8), always recording the coordinates with a hand size GPS in order to measure at the same sites. The diffusive helium emission was temporarily correlated with the $^{3}He/^{4}He$ ratio measured in 8 groundwaters samples collected in San Simón well (northwest of El Hierro; Figure 2.8), between 28 July 2011 and 11 January 2012.

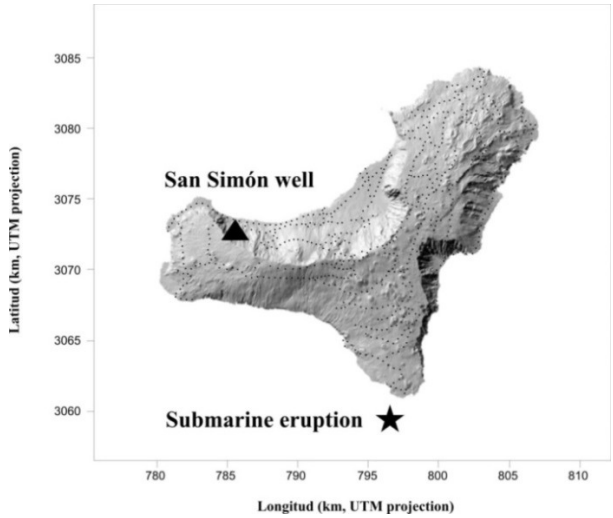

Figure 2.8. *Shaded relief map of El Hierro Island with the location of the measurement points (solid black dots). The triangle indicate the location of San Simón well and the star indicate the location of the submarine eruption of El Hierro 2011-2012*

2.1.1. In situ CO_2 and H_2S efflux measurements at the surface environment

In situ measurements of diffuse CO_2 and H_2S efflux were carried out by means of the accumulation chamber method (Parkinson 1981). This methodology allows to calculate the diffuse CO_2 and H_2S efflux through the slope in the plot between the concentration of the gaseous component and time (Figure 2.9). To perform diffuse CO_2 and H_2S efflux measurements, the open part of the accumulation chamber is placed above the soil surface. A pump allows air to circulate in the chamber through a LICOR CO_2 sensor and an electrochemical Alphasense H_2S-BH sensor, and then return to the chamber. Concentrations of CO_2 and H_2S entering the system increases with time. In the beginning, the increase is almost linear. After a sufficient period of time, the concentration tends to stabilize and the concentration *versus* time plot shows a plate or stable area. When this occurs the concentration in the chamber undergoes a dynamic equilibrium with the gas from the soil surface. The slope of the resulting concentration *versus* time measured at the initial moment is proportional to the gas flux entering the chamber. Under the following considerations (Figure 2.10):

- A is the accumulation chamber area (in m^2), H the height (in m) and V is its volume (in m^3).

- $C(t)$ is the i-gas concentration (in mol L^{-1}) inside the chamber at time t (in s), $C(t+dt)$ is the i-gas concentration (in mol L^{-1}) inside the chamber at time $t+dt$, C_s is the i-gas concentration in the soil-air interface (it is supposed to be constant, in mol L^{-1}) and C_a is the i-gas concentration in the atmospheric air.

- ϕ_{IN} is the volumetric flux of the i-gas from the soil to the chamber (in L s^{-1}) and ϕ_{OUT} is the volumetric flux of the i-gas leaving the chamber (in L s^{-1}), at known P and T conditions.

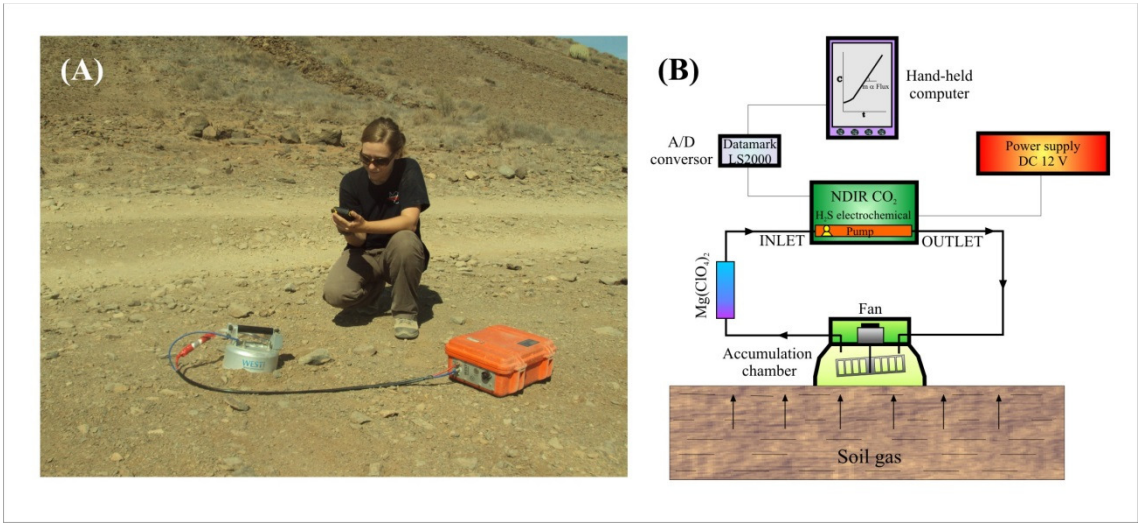

Figure 2.9. *(A) In situ measurement of soil CO_2 and H_2S efflux and (B) scheme of the accumulation chamber method*

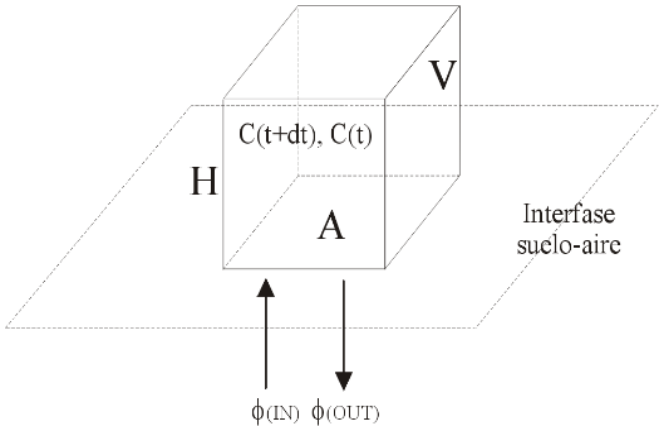

Figure 2.10. *Scheme of an accumulation chamber of known geometry*

The mass balance inside the volumen *V* is as follows:

$$V \cdot C(t+dt) = V \cdot C(t) + \phi_{IN} \cdot A \cdot C_S \cdot dt - \phi_{OUT} \cdot A \cdot C(t) \cdot dt \qquad [2.1]$$

Then, we know that:

$$V = A \cdot H \qquad [2.2]$$

If we divide [2.1] by A, we get:

$$C(t+dt) - C(t) = \frac{1}{H} \cdot \left(\phi_{IN} \cdot C_S - \phi_{OUT} \cdot C(t)\right) \cdot dt = dC(t) \qquad [2.3]$$

We assume not any over-pressure inside the chamber because a small hole has been done to equalize pressure inside and outside. We get:

$$\phi_{IN} = \phi_{OUT} = \phi \qquad [2.4]$$

$$\frac{dC(t)}{dt} + \frac{\phi}{H} \cdot \left(C_S - C(t)\right) = 0 \qquad [2.5]$$

The equation 2.5 is a first order differential equation that can be solved as follows:

$$C(t) = C_S + (C_a - C_S) \cdot \exp\left(-\frac{\phi}{V} \cdot t\right) \qquad [2.6]$$

In the field we only register the *C(t) versus* t plot at the first moments, when the slope is proportional to the i-gas flux from the soil to the chamber.

If we derive equation [2.6]:

$$\frac{dC(t)}{dt} = \frac{\phi}{V_S} \cdot (C_S - C_a) \cdot \exp(-\frac{\phi}{V} \cdot t) \qquad [2.7]$$

In the limit of equation [2.7], when it tends to cero:

$$Lim\left[\frac{dC(t)}{dt}\right]_{t\to 0} = \frac{\phi}{V_S} \cdot (C_S - C_a) Lim\left\{\exp(-\frac{\phi}{V} \cdot t)\right\}_{t\to 0} \qquad [2.8]$$

The exponential term can be replaced by a simple MacLaurin polynomial:,

$$e^{-ax} = 1 - ax + \frac{(ax)^2}{2!} - \frac{(ax)^3}{3!} + \ldots \qquad [2.9]$$

$$Lim\left[\frac{dC(t)}{dt}\right]_{t\to 0} \equiv \frac{\Delta C}{\Delta t} \equiv "slope" \approx \frac{(C_S - C_a)}{V} \cdot \phi \qquad [2.10]$$

We get the general *i-gas* flux equation:

$$\phi \approx \frac{V}{(C_S - C_a)} \cdot [slope]_{t\to 0} \qquad [2.11]$$

Equation [2.11] shows the relationship between the slope of the curve *C(t) versus t* calculated as the time tends to zero, i.e., in the beginning of accumulation inside the camera.

2.1.2. In situ ^{222}Rn activity measurements in the soil atmosphere

Soil ^{222}Rn activity was measured by means of a portable SARAD RTM 2010-2 radon monitor. The instrument pumped gas (with a flow rate of 3 L min^{-1}) through a stainless steel probe inserted at 40 cm depth in the soil and measured the ^{222}Rn activity by electrostatic detection of the positively charged daughter isotopes (^{218}Po$^+$, ^{216}Po$^+$, ^{214}Po$^+$ and ^{212}Po$^+$; Figure 2.11). The precision of the measurements depends on the gas concentration and integration time. The integration time used was 10 minutes.

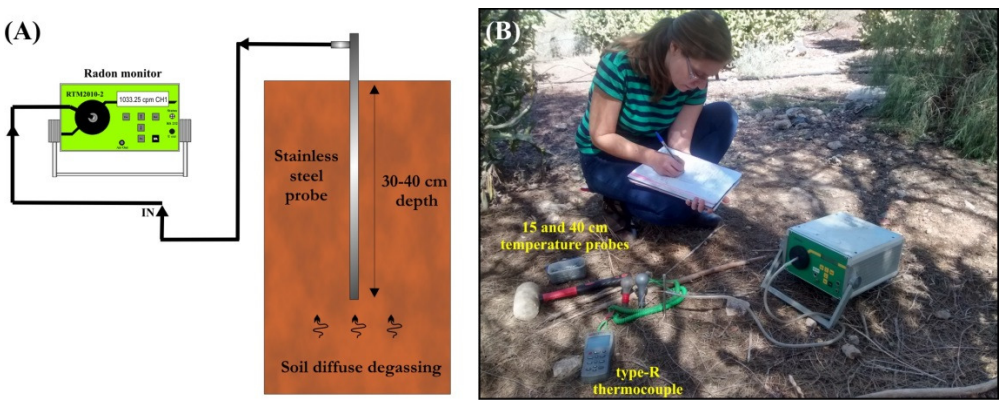

Figure 2.11. *(A) Scheme of the measurement with RTM 2010-2 monitor and (B) in situ measurement*

2.1.3. In situ H_2S concentration measurements in the soil atmosphere

Soil gas H_2S concentration was measured by means of an Arizona Instrument JEROME 631-X. Soil gas was collected at 40 cm depth using a stainless steel probe and a 60 cc syringe. The probe was flushed by drawing 20 mL through it before the gas was pumped into the instrument by an internal pump from the 60 cc syringe (Figure 2.12A). The measurement principle of the instrument is based in a thin gold film that in the presence of H_2S undergoes an increase in electrical resistance proportional to the mass of the compound in the sample (Arizona Instrument 1996). The Jerome's gold film sensing technology displays low-level concentrations in a few seconds with an analysis range of 0.003-50 ppm.

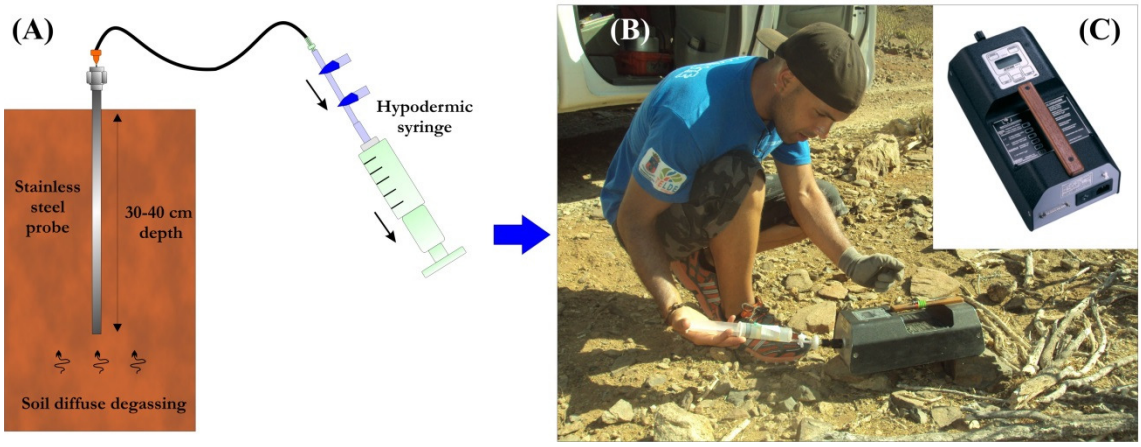

Figure 2.12. *(A) Scheme of soil gas sampling for Jerome instrument, (B) in situ analysis of H_2S concentration by means of a Jerome 631-X analyzer and (C) detail picture of the Jerome 631-X*

2.1.4. Soil temperature measurements

Soil temperature was measured at each sample site at 15 and 40 cm depth by means of a type-K thermocouple (Figure 2.11). Ambient air temperature was also measured with the same device.

2.2. Soil gas sampling and laboratory analysis

Soil gas samples for laboratory analysis were collected in 10 cc glass vials at 40 cm depth using a stainless steel probe and a 60 cc syringe. The probe was flushed by drawing 20 ml through it before the gas sample was inserted into glass vials. Another needle is inserted through the septum in order to allow the internal gas to escape when the gas sample is introduced (Figure 2.13)

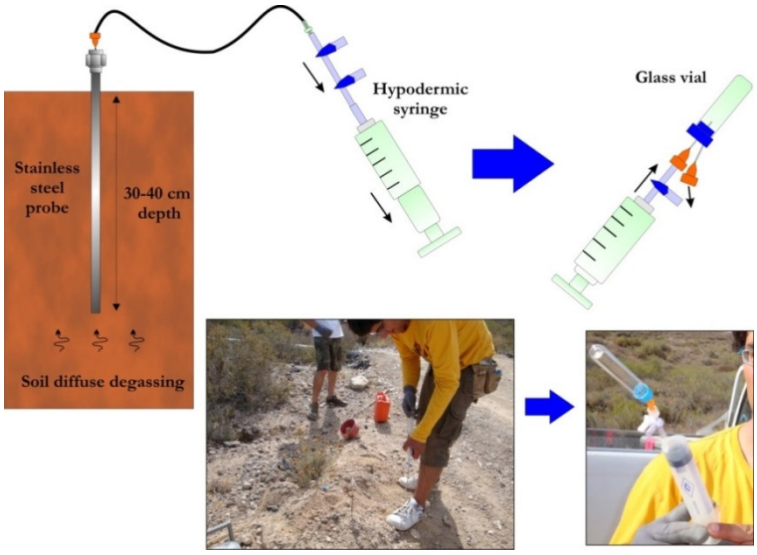

Figure 2.13. *Scheme and pictures of the soil gas sampling*

2.2.1. Soil gas chemical analysis by micro-GC

Soil CO_2, H_2, N_2, Ne and O_2 concentrations were analyzed by means of a double column VARIAN 4900 and CP2002 micro-gas chromatograph (micro-GC). This instrument was previously calibrated with certified standard gases of known composition. The analysis of H_2, O_2, Ne and N_2 was performed with a Thermal Conductivity Detector (TDC), equipped with a 20 m length Molsieve 5Å column and pure Ar as carrier gas. The concentrations of CO_2 were determined using a Poraplot-Q column of 10 m length, a TDC detector and pure Ar as carrier gas (Figure 2.14). The precision and detection limit of the instrument was estimated to be 5% and 0.3 ppm for H_2, 1.5% and 1.5 ppm for Ne, 0.1% and 15 ppm for O_2, 0.1% and 50 ppm for N_2 and 2% and 10 ppm for CO_2.

Figure 2.14. *Analysis of CO_2, H_2, N_2 and O_2 contents with micro-gas chromatograph VARIAN 4900*

2.2.2. Soil gas chemical and isotopic analysis by QMS

To analyze He, N_2, O_2, CO_2, ^{40}Ar and ^{36}Ar contents, a Pfeiffer Omnistar 422 Quadrupole Mass Spectrometer (QMS) was used (Figure 2.15), using atmospheric air as standard for calibration. The quadrupole mass filter consists of four parallel rods arranged in a particular geometry with opposite electrical potential. Ions created through electron bombardment in the ion source are separated by the mass/charge ratio in the rod system and a mass spectrum is obtained by monitoring the ions passing through the quadrupole filter. He is analyzed with high precision with this instrument (±0.3 ppm), reaching a detection limit of 3 ppm.

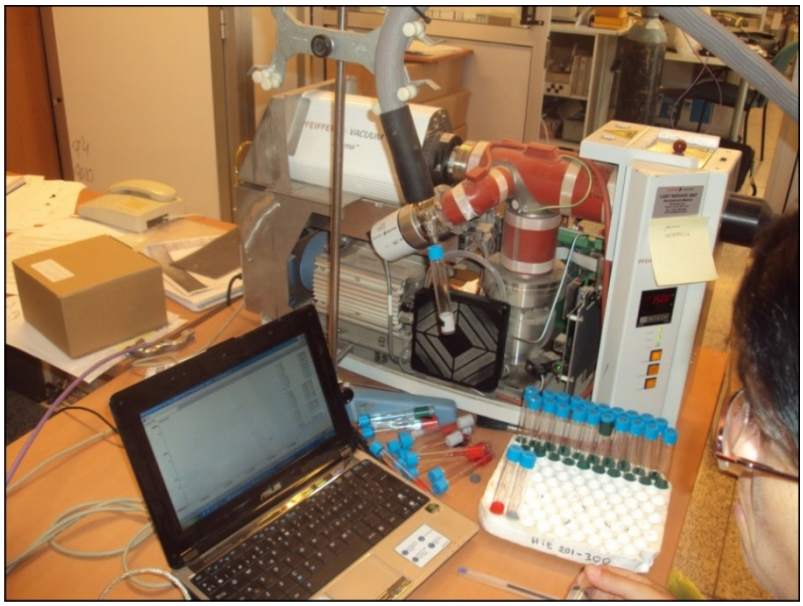

Figure 2.15. *Analysis of He concentration and $^{36}Ar/^{40}Ar$ ratio isotopes with quadrupole mass spectrometer (Balzers-Omnistar model)*

2.2.3. Carbon isotopic analysis of the soil gas CO_2 ($\delta^{13}C$-CO_2) by IRMS

The isotope composition of carbon in soil CO_2 was analyzed in the laboratory by isotopic ratio mass spectrometry (IRMS) with a Finnigan MAT Delta S and a Thermo Finnigan MAT 253 mass spectrometers (Figure 2.16). The $^{13}C/^{12}C$ ratio is given as $\delta^{13}C$-CO_2 values with respect to VPBD standard with an uncertainty of ±0.1‰. GasBench II was used to introduce the soil gas into the Thermo Finnigan MAT 253. The gas injection system uses a two-port needle that adds a gentle flow of helium into the sample vial to displace the sample gas.

Figure 2.16. *Isotope ratio mass spectrometer (IRMS) Thermo Finnigan MAT 253*

2.3. Analysis of helium isotopic composition in groundwaters and CO_2-rich bubbling spring

To collect gas samples in the CO_2-rich bubbling cold spring, the gas was channelled using a funnel and obligated to flow through 50 cc lead-glass bottles fitted with high-vacuum stopcocks at both ends using a syringe connected to the other end of the sample bottle. To study the $^3He/^4He$ ratio in San Simón well groundwater, water samples were collected in the same type of bottles (Figure 2.17). Dissolved gases in the water samples were extracted in vacuum at the Geochemical Research Center of The University of Tokyo using an all metal Toepler pump system (Padrón et al. 2013). Helium isotope ratios and helium and neon concentrations of the extracted gases were determined following the method described by Sumino et al. (2001). Correction factor for helium isotope ratio was determined by measurements of inter-laboratory helium standard named HESJ, with a recommended $^3He/^4He$ value of 20.63 ± 0.10 R_A (Matsuda et al. 2002).The analytical error for R_A determination was <2%. The measured $^3He/^4He$ ratios were corrected for the addition of air based on the $^4He/^{20}Ne$ ratios measured by mass spectrometry, assuming that Ne has an atmospheric origin (Craig and Lupton 1976; Craig et al. 1978; Sano et al. 1985).

Figure 2.17. *(A) Sampling methodology for $^{3}He/^{4}He$ analysis in natural water, (B) San Simón well and (C) sampling methodology for $^{3}He/^{4}He$ analysis in groundwater*

2.4. Magnetotelluric surveys (MT)

Magnetotelluric data were obtained by means of Metronix ADU06 and Metronix ADU07 magnetometers. The x-axis was oriented magnetic north and y-axis was oriented according to magnetic east (Figure 2.18). At each site, the four horizontal components of the electromagnetic field (ex, ey, hx and hy) were recorded at periods of 10^{-3} to 10^{2} s. The 3-D electrical resistivity model has been computed with ModEm code (Egbert and Kelbert 2012).

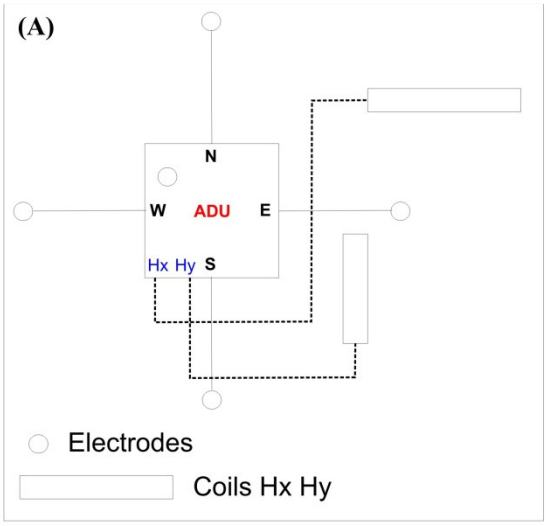

Figure 2.18. *Methodology for MT measurements: (A) scheme showing all parts of the device, (B) coil for magnetic field, (C) ADU07 magnetometer and (D) electrode for electromagnetic field*

2.5. Thermal imaging analysis

Thermal images were collected by means of a hand-held FLIR Thermal Camera P65 (Figure 2.19). The camera consists of an uncooled microbolometer with a thermal sensitivity of 0.05ºC (50/60 Hz 50 mK at 30ºC) sensitive to the 7.5-13 µm spectral range. Internal calibration and atmospheric correction based on user input for reflected ambient temperature, distance, relative humidity, atmospheric transmission and external optics, allow the FLIR built-in software to calculate realistic source temperatures. The accuracy of the instrument (% of reading) is ±2°C or ±2%. During the collection of thermal images at the sea surface, during the El Hierro eruption the lowest temperature range (-40°C to +55°C) for detection of low temperature values was used.

Figure 2.19. *(A) Helicopter flight for taking thermal images and (B) detail of the hand-held FLIR Thermal Camera P65*

The erupted volume of lava and pyroclastic emitted by El Hierro eruption was calculated on the basis of the temperature difference (heat flux exponential reduction) between the seawater contained within the dark patch visible at the sea surface ($T_{surface}$), and the boiling temperature of seawater next to the eruptive vent.

Constraints on the characteristics of this submarine volcano resulted in a heat flux plume that was derived from a model which produced the convective heat flux in a seawater column at each time step and depth of the crater. Thus, upward heat convection was modeled in 2D and time as a heat plume forced by the difference of the boiling temperature of the water surrounding the hot crater vent at each depth (considered for the simulations of 1 m^2), and the anomalous Sea Surface Temperature (T_{camera} - $T_{surrounding\ seawater}$) reported during the event (from 19 October 2011 to 28 February 2012). Results included different temperatures at different depths and horizontal position. Heat flux simulations (Figure 2.20) were computed for each day on "Energy 2D" software (Xie, 2012). The boundary conditions included T at the sea surface, the crater depth, boiling temperature at this depth, density of seawater, heat capacity and

kinematic viscosity for each day. The 2D shape of the plume was idealized as an inverted truncated cone of a fixed radius r of the crater (1 m^2) and a variable radius R_i obtained from the thermal anomaly length at the sea surface. The energy released from the source is propagated

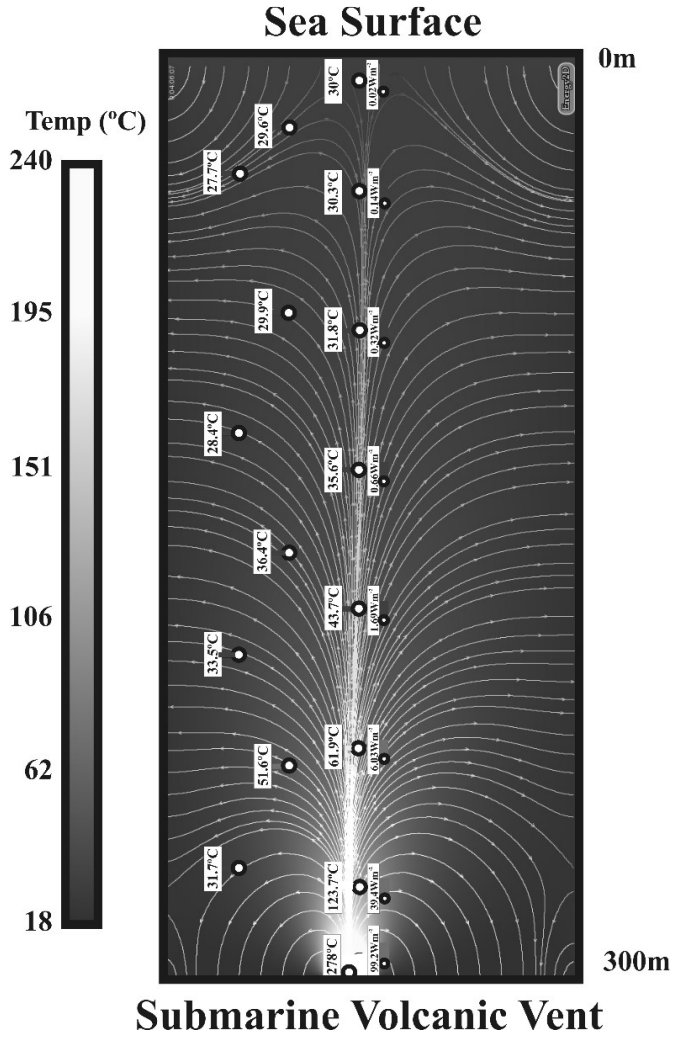

Figure 2.20. *Heat flux simulation computed for 300 m depth crater with "Energy 2D" software*

and stored in the water column in the inverted truncated cone. The total energy released per day is given by the integral of the energy transferred at the different depth within the volume of the cone and it is expressed by the equation 2.12:

$$\sum Qi = \sum \; [W_0 * e - (K * Z_i)] * \left\{ \rho * C_e * [\, 1/3 * \pi * Z_i * (R^2 + r^2 + rR) \,] \right\} * 86400 \qquad [2.12]$$

where Qi (j) is the accumulated energy released during one day and stored in the water column, w_0 (j/s) is the is the instantaneous energy released per s at the source decreasing exponentially with increasing depth, and K the exponential decay constant of the heat flux variation with depth obtained by the Energy 2D simulator and plotted in Figure 2.21 for 100 m, 200 m and 300 m depth; ρ is the density of the seawater (considered constant at 1,020 kg m^3), C_e is the specific heat (considered constant at 4,020 J kg K^{-1}), Z_i the crater depth (m) and 86,400 sec to convert

the heat flux (J s^{-1}) to J d^{-1} to report the heat energy released to the water column daily. Based on calculated Qi values, to compute the lava volume erupted daily for the whole eruptive event, we used a model (Harris et al. 1998; Pinkerton et al. 2002; Calvari et al. 2010) successfully applied to Stromboli for the portion of the lava flow field spreading below sea level, following the equation:

$$V_l(m^3) = \left(\frac{Q_i \times \Delta Tsw}{(d_l \times C_l \times \Delta T_l} \right) \qquad [2.13]$$

where V_l is the calculated erupted volume (m^3), ΔT_{sw} the temperature difference between initial lava temperature (1,373K) and boiling temperature of sea water at the depth of the eruptive vent, d_l the density of lava (2,500 kg m^{-3}), C_l the heat capacity of lava (1,225 J kg^{-1} K), and ΔT_l the decrease in temperature by the lava. We have considered the volume of the discolored area as a closed system having homogeneous temperature, and for simplicity the composition of the lava typical of basalt (Harris et al. 1998; Calvari et al. 2010).

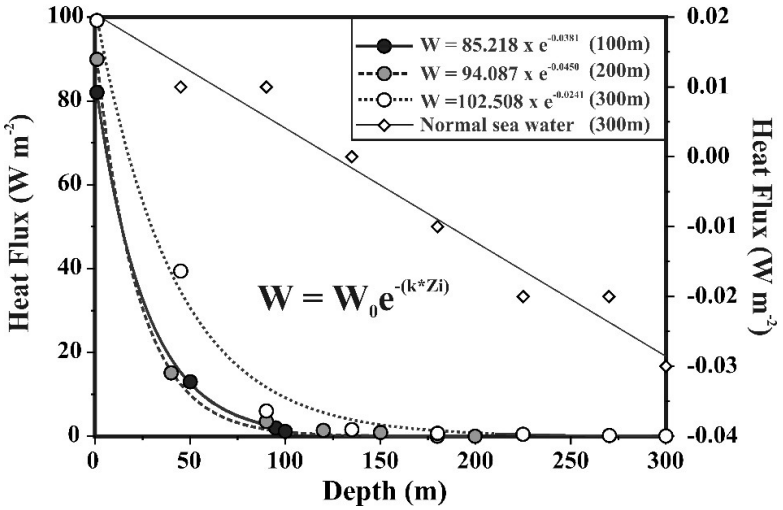

Figure 2.21. *Heat flux variations with depth obtained with the "Energy 2D simulator" for 100 m, 200 m and 300 m depths. Simulation for normal sea water temperature is also shown*

2.6. Data processing

The maps of the spatial distribution of the data were constructed using sequential Gaussian simulation (sGs), provided by the sgsim program (Deutsch and Journel 1998; Cardellini et al. 2003a). In the last decade sGs has been widely applied in the study of soil diffuse degassing at volcanic and non-volcanic systems (Cardellini et al. 2003b; Frondini et al. 2004; Fridriksson et al. 2006; Chiodini et al. 2008; Carapezza et al. 2009; Mazot et al. 2011). The sGs procedure allows to both interpolate the measured variable at not-sampled sites and assess the uncertainty of the total diffuse emission estimated for the entire studied area. The simulation is conditional and sequential, i.e., the variable is simulated at each unsampled location by random sampling of

a Gaussian conditional cumulative distribution function (Cardellini et al. 2003a). The procedure of the sGs program is composed by the following steps: 1) a normal score transformation of the original data to transform the data in a normal population, 2) an experimental variogram computation of the normal score of the transformed data, 3) a variogram model assignation to the experimental variogram, 4) a sequential Gaussian simulation of N equiprobable realizations and 5) a back-transforming of the normal score data into simulated values of the original variable.

The probability plot technique was applied to check whether the log-transformed data comes from mixed polymodal distributions (Sinclair 1974). This technique is based on the recognition of inflection points along a S-type curve produced by plotting cumulative percentile data on a log-normal scale. One inflection point allows distinguishing two modes or populations: normal I and normal II.

In order to estimate the diffusive helium flux, the soil helium concentration data from QMS analysis was used, following Fick's law (Etiope and Martinelli 2002):

$$F_D = -D_e \frac{dC}{dz} \qquad [2.14]$$

where $D_e = n^2 D_m$, is the global diffusion coefficient ($m^2\ s^{-1}$); dC is the variation of gas concentration (kg m^{-3}) along the depth dz (m); n is the effective porosity of the medium (%); and D_m is the diffusion coefficient of helium in air ($0.7\times10^{-4}\ m^2\ s^{-1}$ at 25ºC; Pandey et al. 1974).

Finally in order to compute the 3-D electrical resistivity model of the southern volcanic rift zone of Tenerife the ModEm code (Egbert and Kelbert 2012) was used. ModEm is a modular code in Fortran 95 adapted to the electromagnetic inversion data in general.

Results and Discussion

3. Results and Discussion

In the next lines, the results and discussions included in the different research papers that comprise the present Ph.D. Thesis are summarized.

3.1. Diffuse helium and hydrogen degassing to reveal hidden geothermal resources in oceanic volcanic islands: The Canarian Archipelago case study

In this work, the use of soil gas He and H_2 as a promising technique for geothermal exploration, especially in areas where the resources are either hidden or lie at great depths, has been evaluated. Due to Tenerife and Gran Canaria are promising areas for geothermal resources, five mining licenses were acquired for geothermal exploration studies: *Garehagua, Berolo, Guayafanta, Abeque* (Tenerife) and *Atidama* (Gran Canaria). Four of the study areas are located in the three differentiated volcanic rifts of Tenerife: NE Rift (*Berolo* and *Guayafanta*), NW Rift (*Abeque*) and South Rift (*Garehagua*) (Figure 3.1). The five mining licenses comprise the

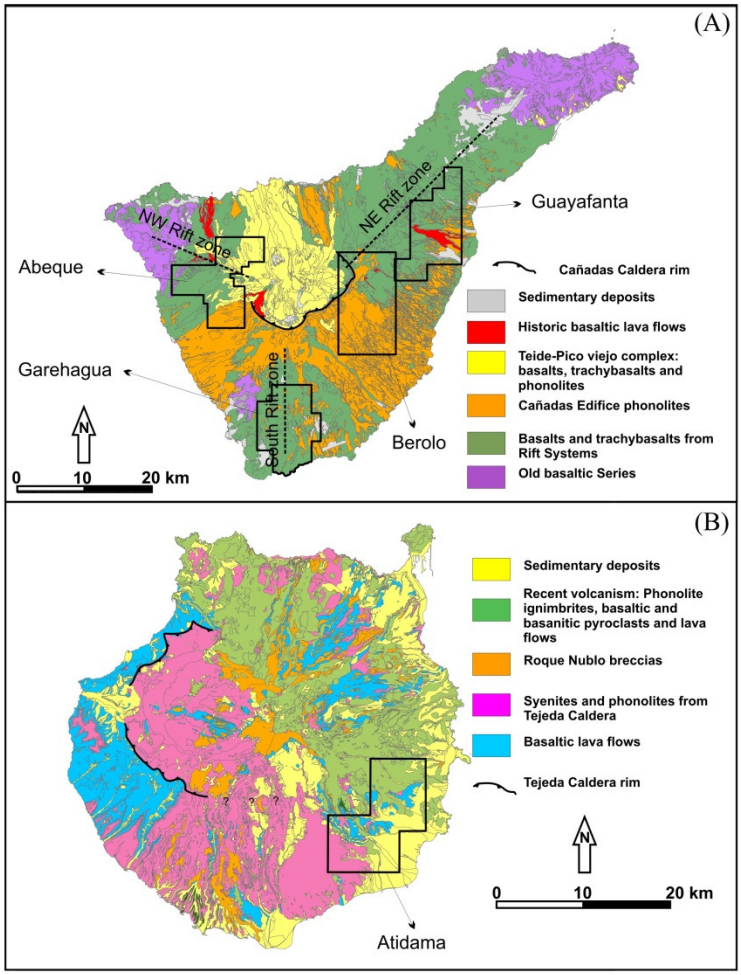

Figure 3.1. *Simplified geological maps (modified from IGME, 2011) of (A) Tenerife, with the location of the four mining licenses (Garehagua, Berolo, Guayafanta and Abeque) studied for geothermal exploration purposes and (B) Gran Canaria with the location of Atidama, the mining license studied for geothermal exploration purposes on that island*

subaerial surface under which groundwater temperature anomalies and high contents of silica (SiO_2) in water were measured during the geothermal exploration studies in the 1980-1990's (IGME, 1977; 1979; 1993a, b, c, d, e, f, g and h; Valentín et al. 1990).

Table 3.1 shows a statistical summary of the soil He and H_2 data measured at *Abeque*, *Berolo, Garehagua, Guayafanta* and *Atidama* mining licenses.

Table 3.1. *Statistical summary of the analytical results of He and H_2 soil gas concentration measured at mining licenses for geothermal exploration in the Canary Islands*

	Average	Minimum	First Quartile (Q1)	Median	Third Quartile (Q3)	Maximum	Interquartile Range (Q3-Q1)
He (ppm)							
Abeque	5.81	4.9	5.28	5.42	5.56	35.1	0.28
Garehagua	5.86	4.3	5.56	5.83	6.14	17.4	0.58
Berolo	5.73	<IDL	5.01	5.67	6.39	11.7	1.38
Guayafanta	5.66	4.6	5.41	5.64	5.90	7.20	0.49
Atidama	5.22	3.8	5.09	5.25	5.39	6.10	0.30
H_2 (ppm)							
Abeque	0.58	<IDL	0.28	0.43	0.66	8.60	0.38
Garehagua	1.35	<IDL	0.50	0.75	1.37	24.4	0.87
Berolo	1.46	<IDL	0.80	1.23	1.98	4.30	1.18
Guayafanta	0.59	<IDL	0.45	0.54	0.66	8.30	0.21
Atidama	1.56	0.7	1.23	1.43	1.70	7.20	0.47

<IDL Below the instrument detection limit

The possible presence of mixed polymodal distributions in the soil He and H_2 data caused by the existence of different geochemical populations was examined by means of the probability-plot technique (Sinclair 1974). Regarding He data, polymodal distributions were distinguished in *Garehagua, Berolo, Abeque* and *Atidama* mining areas, whereas one single log-normal population was identified in *Guayafanta* mining license. The mean of the background population in the five areas was ~5.5 ppm, very similar to atmospheric He value (5.24 ppm, whereas the mean of the peak population was ~8.2 ppm, exceeding 1.70, 1.53, 1.57 and 1.15 times the background values in *Garehagua, Berolo, Abeque* and *Atidama*, respectively (Figure 3.2).

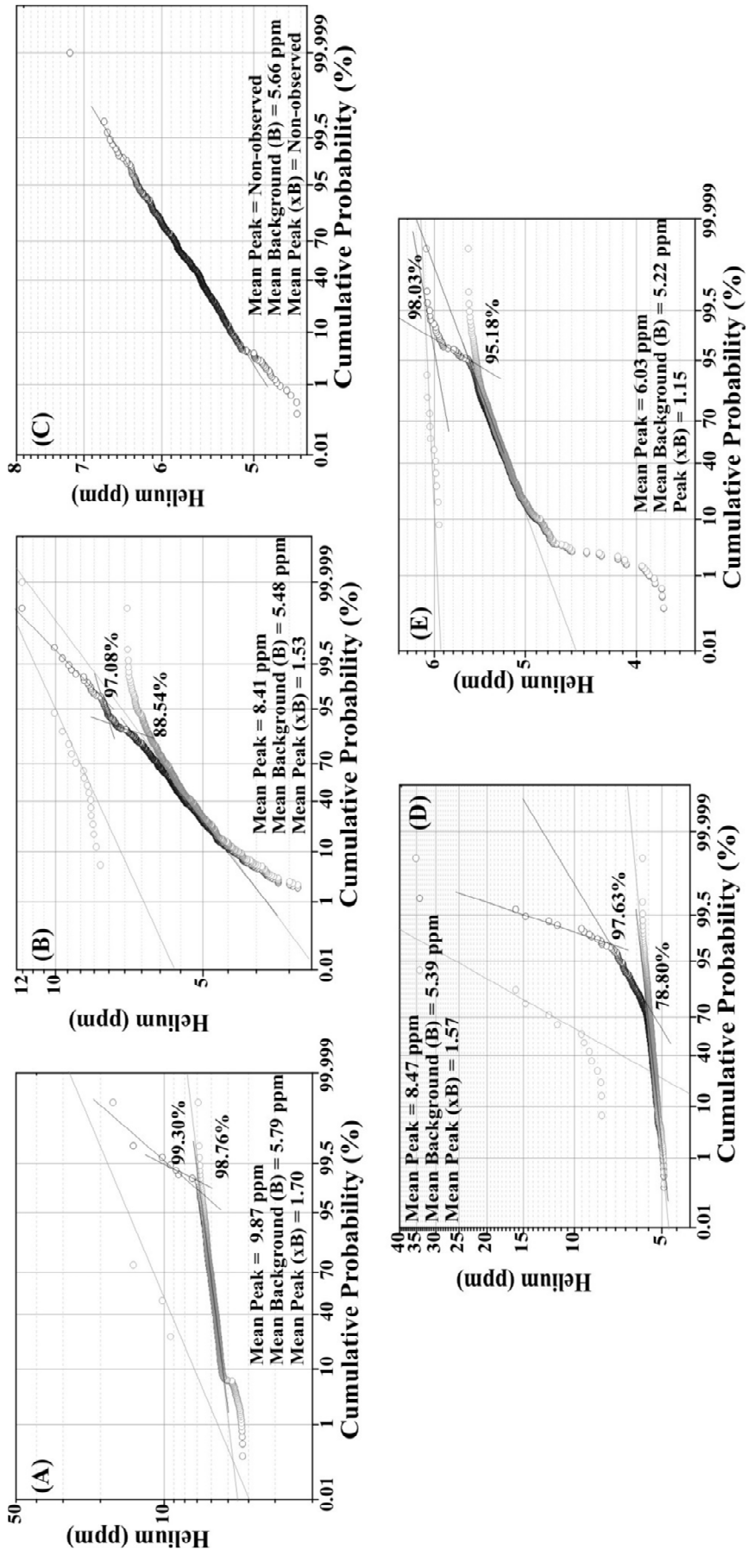

Figure 3.2. *Cumulative probability plots of soil He measured at (A) Garehagua, (B) Berolo, (C) Guayafanta, (D) Abeque and (E) Atidama mining licenses. Solid black lines in the probability plots indicate different log-normal geochemical population in the original data. Solid grey lines indicate the separated background and peak log-normal populations*

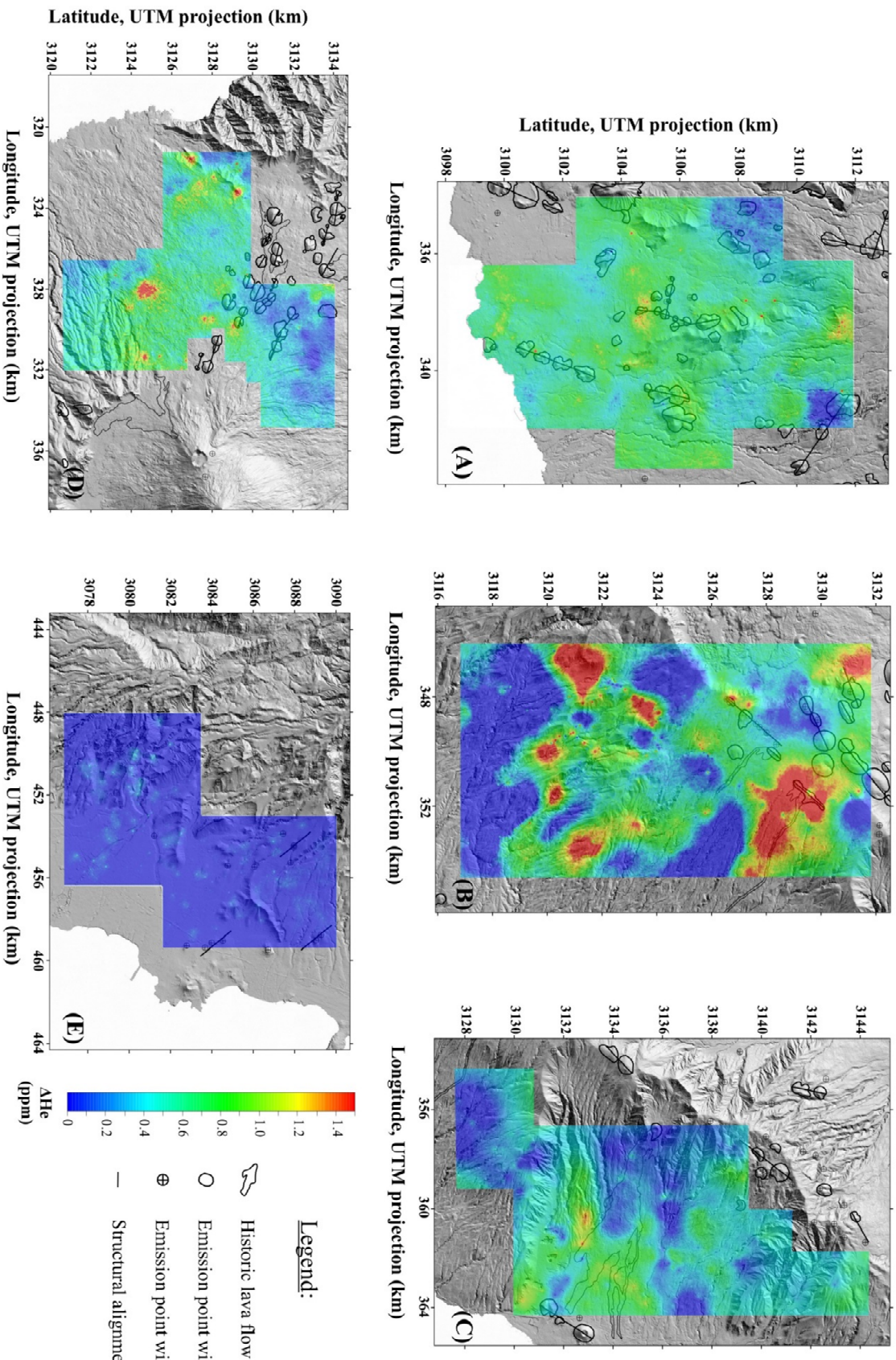

Figure 3.3. Spatial distributions of soil ΔHe at (A) Garehagua, (B) Berolo, (C) Guayafanta, (D) Abeque and (E) Atidama minin g licenses, constructed by sGs algorithm

Figure 3.3 shows the spatial distribution maps of soil ΔHe for each mining license. Soil He enrichments are shown as ΔHe (ΔHe = $[He]_{soil\ atmosphere}$–$[He]_{air}$), being $[He]_{air}$ = 5,240 ppb, (Gluekauf 1946). The highest soil ΔHe value observed in this work was measured in the west part of *Abeque* mining license, whereas *Atidama* showed the lowest soil ΔHe enrichment of the five areas. *Guayafanta* showed just a single soil ΔHe anomaly at southern part of the area. In *Berolo* and *Garehagua*, multiple isolated anomalies were detected at the spatial distribution map of soil ΔHe. It is worth noting that in *Garehagua* relatively high soil ΔHe values were measured in the north of the study area, in good spatial correlation with the vertical surface projection of a bubbling ^3He and CO_2-rich gas spot, located at 2,850 meters of horizontal depth inside Fuente del Valle water gallery (Pérez et al. 1996; Pérez et al. 2007). Chemical and isotopic composition of this bubbling gas exhibits a significant magmatic component with, $^3He/^4He$ ~7.0 R_A (being R_A the atmospheric $^3He/^4He$ ratio; Pérez et al. 1996, 2007). This sampling point is probably related to an upward migration of volcanic-hydrothermal gases through a high permeable pathway.

Regarding soil H_2 data, background (commonly derived from atmospheric H_2) and a peak populations were distinguished in all mining licenses. Data between background and peak values are considered an intermediate population. The mean value of the background population in the five areas was ~0.8 ppm, slightly higher than atmospheric H_2 content, whereas the mean value of the peak population was ~5.1 ppm, exceeding 18.84, 3.25, 3.24, 8.23 and 3.79 times the background values in *Garehagua, Berolo, Abeque, Guayafanta* and *Atidama*, respectively (Figure 3.4).

Figure 3.5 shows the spatial distribution maps of soil H_2 for each mining license. The spatial distribution of soil H_2 in *Guayafanta* and *Abeque* did not show any significant enrichment. However multiple isolated anomalies were located in *Garehagua* and *Berolo*. *Garehagua* showed the main anomaly in the central area, with values higher than 10 ppm. In *Berolo* the highest soil H_2 enrichments were measured at the southwestern part of the study area, showing good spatial coincidence with high values of soil He. Furthermore, *Atidama* showed important values along a NW-SE trend at the northern part of the study area in good spatial correlation with the structural alignment of the Plio-Quaternary volcanic rift (Anguita et al. 1991; Guillou et al. 2004).

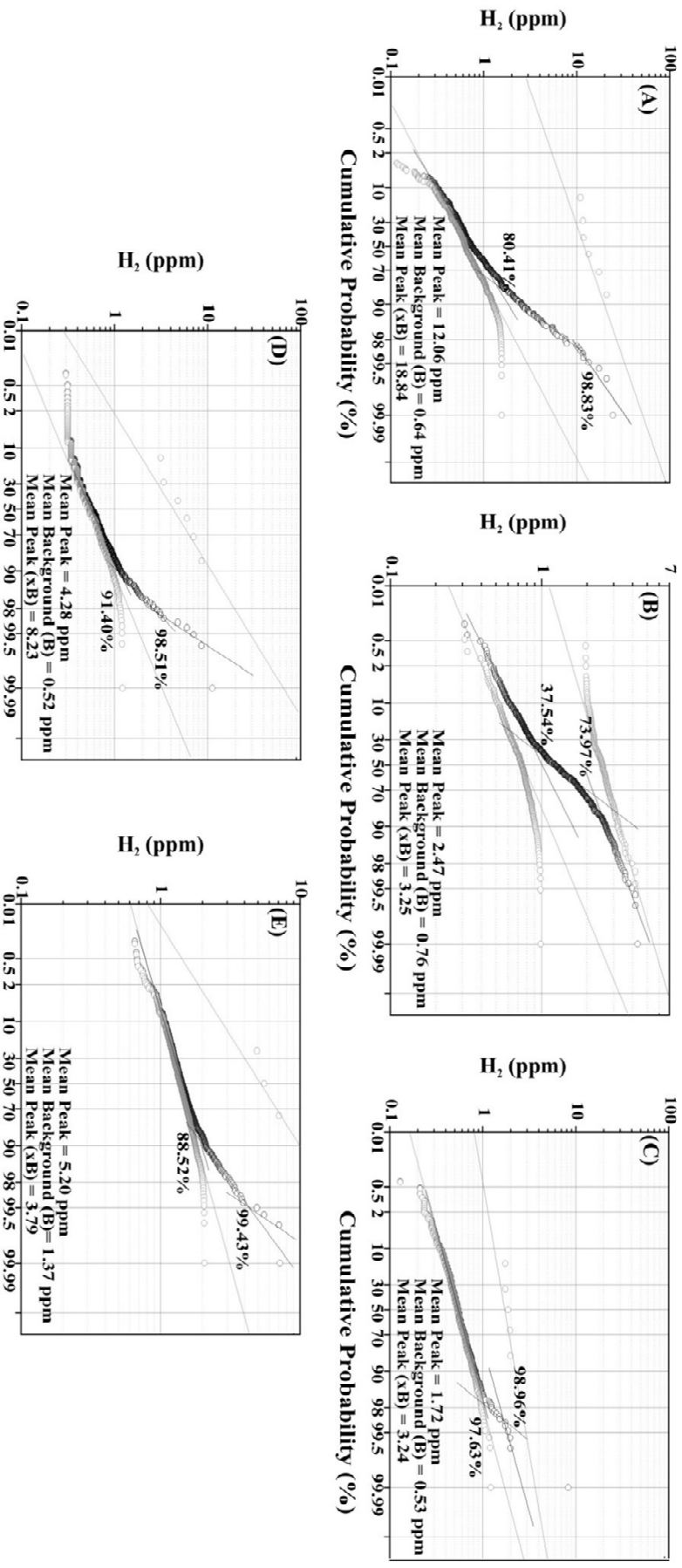

Figure 3.4. *Cumulative probability plots of soil H_2 measured at (A) Garehagua,(B) Berolo,(C) Guayafanta,(D) Abeque and (E) Atidama mining licenses. Solid black lines in the probability plots indicate different log-normal geochemical population in the original data. Solid grey lines indicate the separated background and peak log-normal populations*

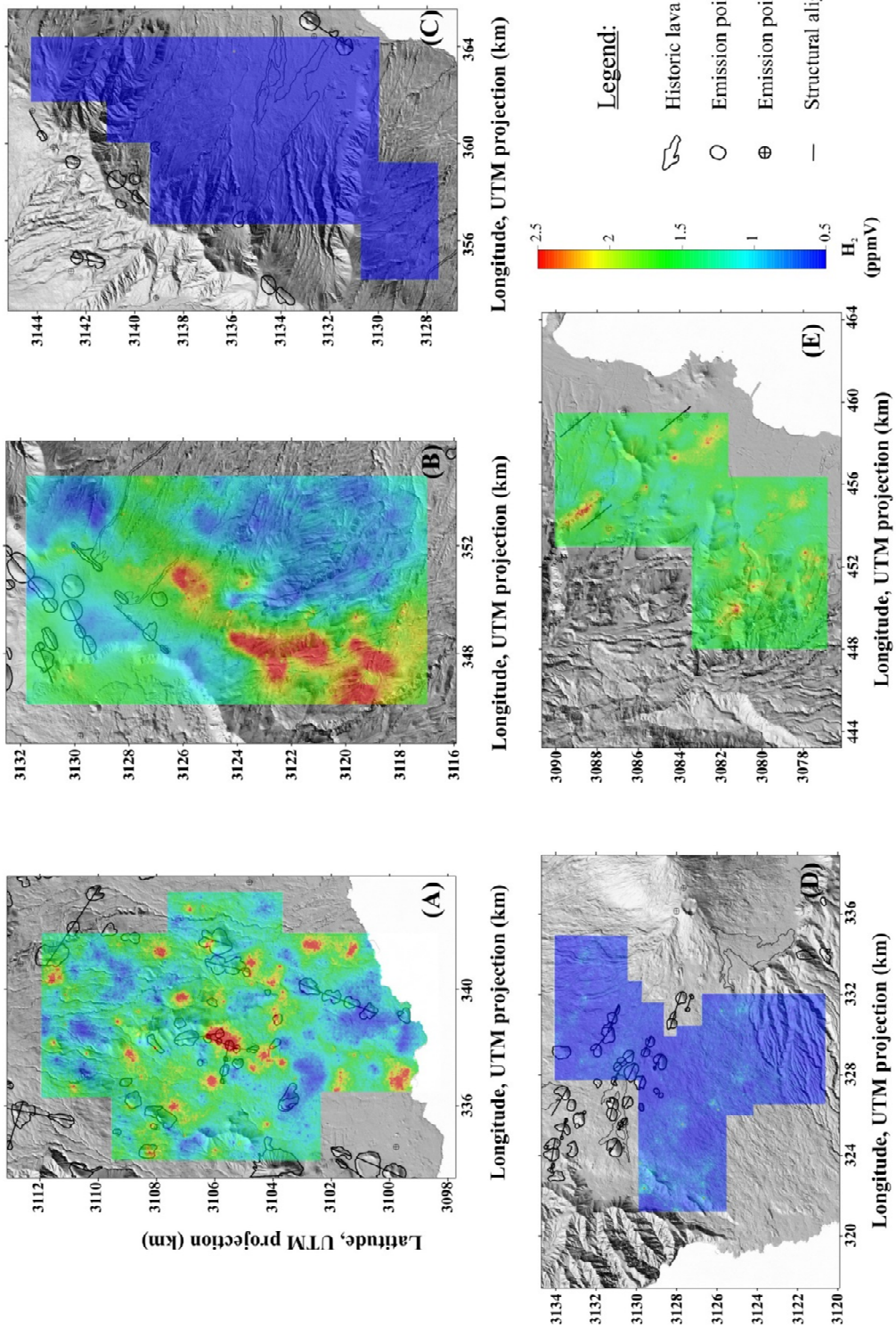

Figure 3.5. *Spatial distributions of soil H_2 at (A) Garehagua, (B) Berolo, (C) Guayafanta , (D) Abeque and (E) Atidama mining licenses, constructed by sGs algorithm*

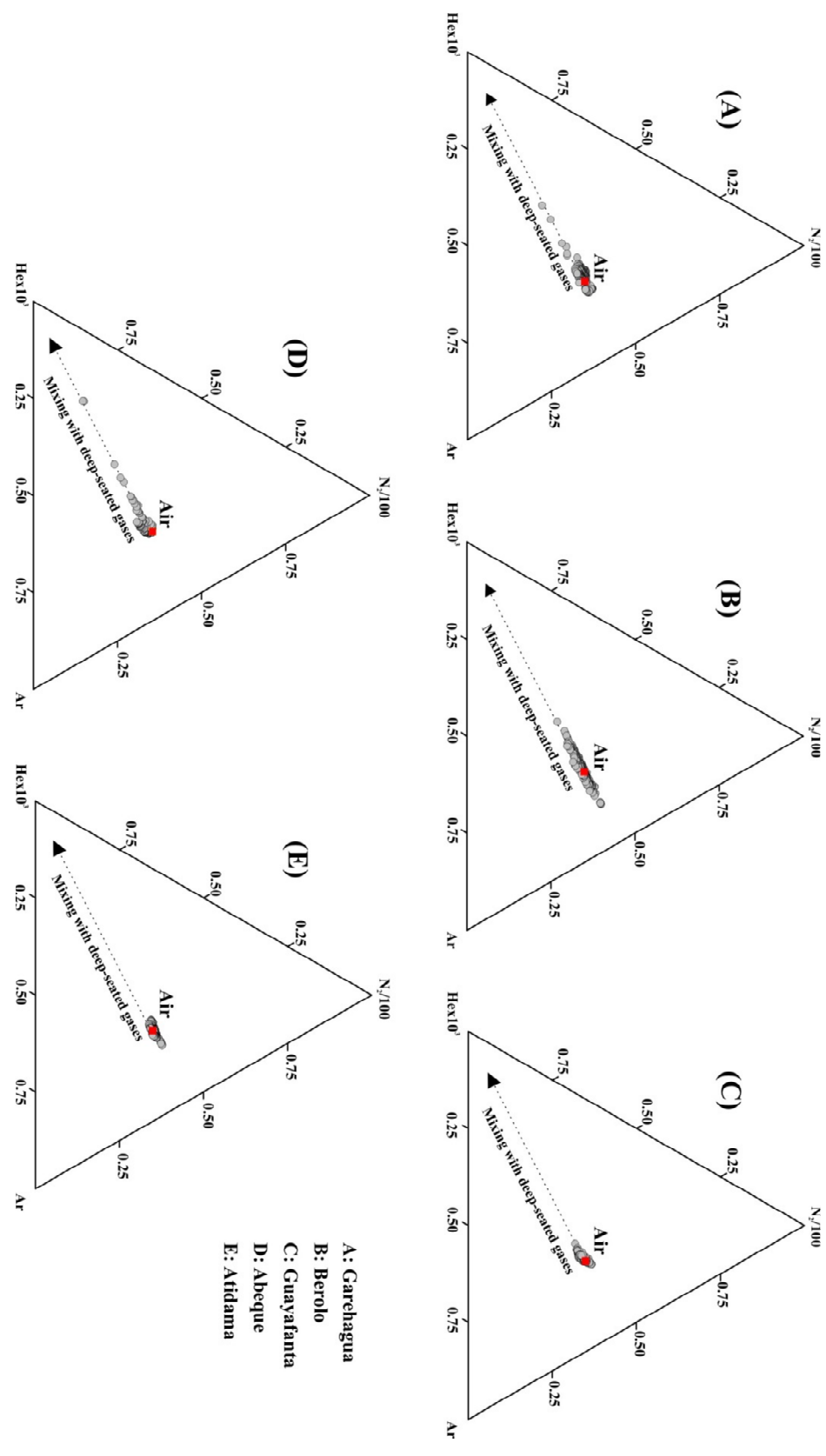

Figure 3.6. *Ternary N_2-Ar-He diagrams of soil gases at (A) Garehagua,(B) Berolo,(C) Guayafanta, (D) Abeque and (E) Atidama mining licenses. Red squares indicates the typical air concentration and dashed line shows the mixing trend with deep-seated gas*

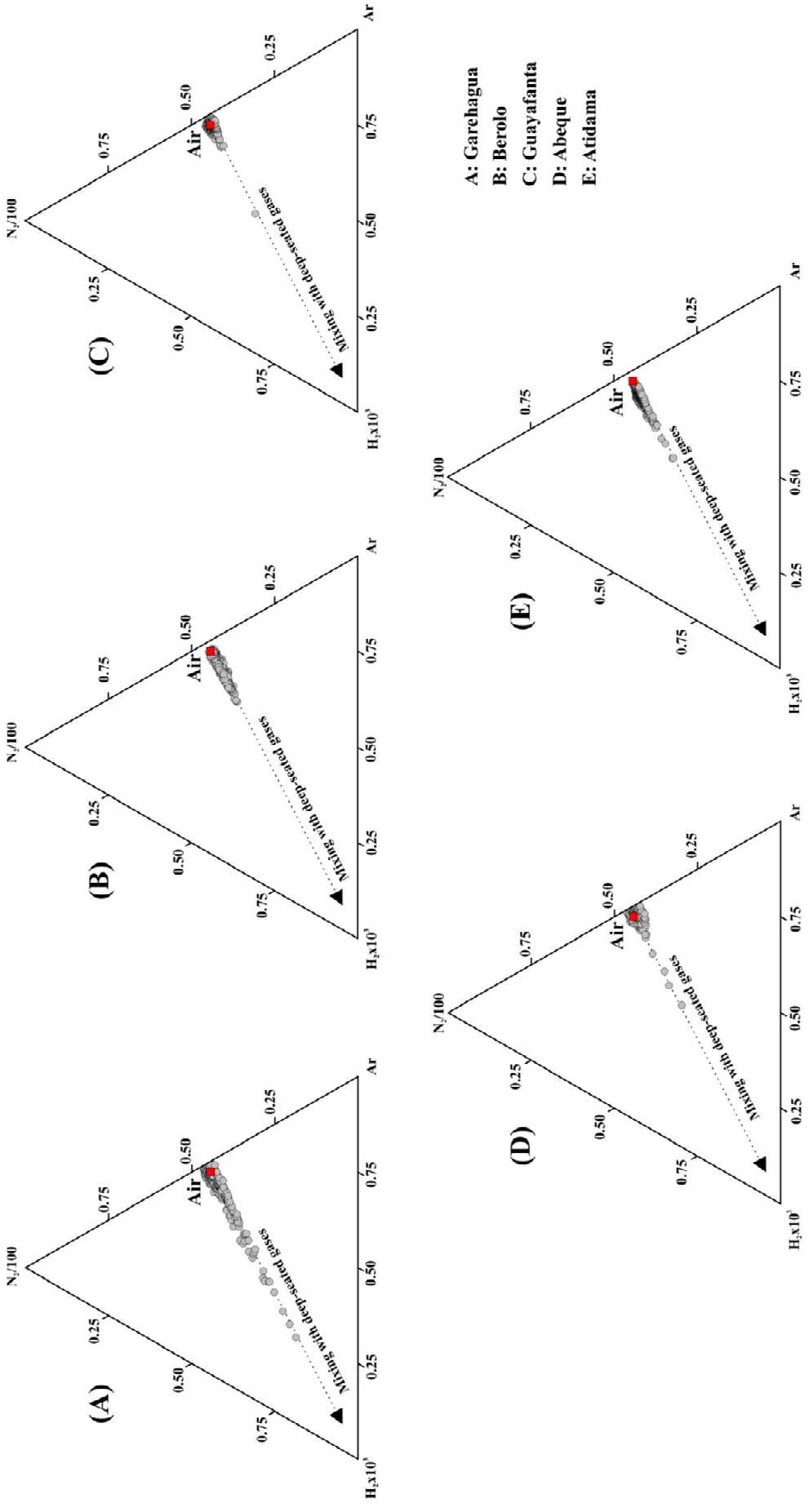

Figure 3.7. *Ternary N_2-Ar-H_2 diagram of soil gases at (A) Garehagua, (B) Berolo, (C) Guayafanta, (D) Abeque and (E) Atidama mining licenses. Red squares indicates the typical air concentration and dashed line shows the mixing trend with deep-seated gas*

The observed enrichments in some chemical ratios in the soil environment may indicate the presence of enhanced vertical permeability areas related to high temperature hydrothermal activity at depth. The relative contributions of the soil gases studied here (He and H_2) with other non-reactive gases present in the soil environment (N_2 and Ar), are displayed as ternary N_2-Ar-He and N_2-Ar-H_2 diagrams (Figures 3.6 and 3.7). The chemical composition of soil gases in the five study areas plots along a typical atmospheric component partially polluted by endogenous He and H_2. As depicted in Figure 3.6, the N_2-Ar-He ternary plot suggests a linear mixing trend of atmospheric air with endogenous gases. This possible endogenous addition of He is evident in *Abeque* and moderate in *Garehagua* and *Berolo*. The results showed by the N_2-Ar-H_2 ternary plot (Figure 3.7) seems to add some slight significance to *Atidama*, but the most obvious endogenous contribution is found in *Garehagua*. In both diagrams the endogenous component in *Abeque*, *Garehagua* and *Berolo* is higher than in *Guayafanta* and *Atidama*.

The molar ratio between an endogenous gas (He or H_2) and a typical atmospheric component can be useful to discriminate the origin of the anomalous emission zones and to weight up the input of the deep-seated gases. Therefore, assuming a pure atmospheric origin for Ne and Ar, we used three specific two-components molar ratios (He/Ar, He/Ne and H_2/Ar) since their values would act as indicators of endogenous gases from volcano-hydrothermal activity, assuming that Ar and Ne are present in the hydrothermal fluids in contents relatively close to those of air saturated groundwater (Giggenbach 1991; Chiodini and Marini 1998; Pedroni et al. 1999). Table 3.2 shows the percentage of He/Ar, He/Ne and H_2/Ar ratios that exceeded 3 times that those observed in the air. This percentage for He/Ar and He/Ne ratios were higher in *Abeque* and *Garehagua*, whereas that corresponding to H_2/Ar ratio was greater for *Atidama* and *Berolo*. With the aim of sorting the endogenous contribution at each study area, a dimensionless parameter (named as Value in Table 3.2) from 1 to 5 was assigned to each chemical ratio, being the lowest assigned to the highest chemical ratio values. The same procedure was also applied to the probability plot parameters of soil ΔHe and H_2 (peak values expressed as times background value, Table 3.2). The sum of the total assigned values gave us a way to geochemically sort the five different mining licenses to weight up the relative potential of finding geothermal resources at each of the study area, thus reducing the uncertainty in the selection of the area with the highest success of future exploratory works.

***Table 3.2**.Geochemical and geographical characteristics of the mining licenses*

Islands	**Tenerife**				**Gran Canaria**
Geothermal mining license	**Abeque**	**Garehagua**	**Berolo**	**Guayafanta**	**Atidama**
Area (km^2)	102	100	130	103	104
# Sampling sites	406	557	577	541	600
He mean peak pop. (x background pop.)	1.57	1.70	1.53	-	1.15
Value for He[a]	2	1	3	5	4
H_2 mean peak pop. (x background pop.)	8.23	18.84	3.25	3.24	3.79
Value for H_2[a]	2	1	4	5	3
He/Ar ratio (>3 x air value) (%)	0.57	0.18	0.00	0.00	0.00
Value for He/Ar[a]	1	2	5	5	5
He/Ne ratio (>3 x air value) (%)	0.80	0.18	0.00	0.00	0.00
Value for He/Ne[a]	1	2	5	5	5
H_2/Ar ratio (>3 x air value) (%)	2.00	19.96	39.64	1.11	41.97
Value for H_2/Ar[a]	4	3	2	5	1
Value for N_2-Ar-He diagram[a]	1	2	2	3	3
Value for N_2-Ar-H_2 diagram[a]	2	1	2	3	3
Total geochemical values	13	12	23	31	24

[a] Geochemical values from 1 (best value) to 5 (worst value)

Through a visual inspection of soil He and H_2 spatial distributions (Figures 3.3 and 3.5) and Figure 3.1, it can be stated that there is not a spatial relation of soil He and H_2 enrichments and the different lithotypes of Tenerife and Gran Canaria. Hernández et al. (2004) investigated the He emission and U and Th contents in shallow rocks and soils of Las Cañadas caldera and surroundings in Tenerife Island. Their data indicate that He was supplied mostly from a deep source, with a minor contribution from U- and Th-rich shallow rocks and soils. These results suggest that peak populations observed in the soil He probability plots showed in the present work are caused mainly by degassing of deep-seated He. Although the two different possible sources for He (shallow degassing by radioactive decay of U- and Th-rich rocks and deep degassing from geothermal systems developed beneath the study areas) cannot be ruled out, those areas with higher value of peak population of soil He (expressed as times the background population) would show higher proportion of the deepest component. In the case of Tenerife island, where 4 mining licences were studied, other evidence to support this assertion is the observed high levels of mantle degassing along the three volcanic-rift zones of Tenerife, as pointed out by the constant levels of $^3He/^4He$ ratio (~7 R_A) in groundwater of the island, even though there is not clear evidence of geothermal activity in the surface environment (Pérez et al. 1996). Additionally, the recent results reported by Padrón et al. (2013) during a volcanic unrest that led a submarine volcanic eruption at the southern coast of El Hierro island also support that, even when there were clear evidences of magmatic degassing, soil He enrichments did not exceed the values shown in this work.

Considering the results obtained by the assigned values to the statistical-graphical parameters of soil ΔHe, the importance of the studied mining licenses can be sorted as

Garehagua>Abeque>Berolo>Atidama>Guayafanta; this result is very similar to that of soil H_2: *Garehagua>Abeque>Atidama>Berolo>Guayafanta*. A visual inspection of the spatial distribution maps (Figures 3.3 and 3.5) seem to suggest a different order: *Berolo>Abeque>Garehagua>Guayafanta>Atidama* for the soil ΔHe data and *Berolo>Garehagua>Atidama>Abeque>Guayafanta* for soil H_2. However, the visual information of the spatial distribution should be taken with caution especially for *Berolo*. Table 3.3 summarizes the parameters used to interpolate the unsampled locations by sGs for soil ΔHe and H_2. The spatial interpolation of data to unsampled locations are strongly influenced by the spatial density of real data, because once a value is simulated in an unsampled location, sGs add it to the data set and uses as an original data to estimate the variable at the next locations of the grid (Cardellini et al. 2003a). Minimum values of spatial densities were used to construct the maps for *Berolo* and *Abeque* mining licenses (Table 3.3). Additionally, those sample locations separated by distances closer than the range value of the semivariogram model used are spatially autocorrelated, whereas locations farther apart than the range are not. Soil H_2 and ΔHe data in *Berolo* and *Garehagua* respectively showed the higher spatial autocorrelation. These results provide a critical view of the spatial distribution obtained by sGs in *Berolo*, because the relative low spatial density together with the high spatial autocorrelation likely yields an oversized anomaly distribution.

***Table 3.3**. Parameters used in the sGs interpolation to construct the spatial distribution maps of soil gas ΔHe and H_2 in the mining licenses*

	Number of samples	Study area (km^2)	Average distance between points (m)	Sampling density (points/km^2)	Semivariogram parameters for soil ΔHe		Semivariogram parameters for soil H_2	
					Nugget effect	Range (m)	Nugget effect	Range (m)
Abeque	406	102	193	4	0.6	3000	0.8	2500
Atidama	600	104	201	6	0.7	700	0.6	1000
Berolo	577	130	220	4	0.4	1600	0.3	3000
Garehagua	557	100	242	6	0.7	5300	0.7	1000
Guayafanta	541	103	244	5	0.3	1500	0.8	300

The number of sampling sites with He/Ar, He/Ne and H_2/Ar ratios higher than 3 times the atmospheric value, suggest a geothermal potential sorted as *Abeque>Garehagua>Atidama>Berolo>Guayafanta* (Table 3.2). Finally, the visual inspection of the ternary N_2-Ar-He and N_2-Ar-H_2 diagrams seems to support the relative order suggested by the statistical-graphical analysis, because the volcano-hydrothermal contribution in the soil He follows the order *Garehagua>Abeque>Berolo>Atidama>Guayafanta* in the case of soil He and *Garehagua>Abeque> Atidama>Berolo>Guayafanta* in the case of soil H_2. Combining the overall information shown in this work, the geothermal potential of the five mining licenses studied here have been sorted by assigning values from 1 to 5 (where 1 means higher

endogenous component; Table 3.2), resulting as *Garehagua>Abeque>Berolo>Atidama>Guayafanta*.

3.2. Surface geochemical and geophysical studies for geothermal exploration at the sourthern volcanic rift zone of Tenerife

In the light of the above results, which demonstrated that the highest geothermal potential of the five study areas belonged to *Garehagua* (from a geochemical point of view), a more detailed study on soil gas geochemistry, complemented by a magnetotelluric study, was performed in this mining license.

A summary of the chemical composition of the 557 soil gas samples taken in *Garehagua* soil gas survey is shown in Table 3.4.

Table 3.4. *Statistical summary of the analytical results of the soil gas concentration and fluxes measured at Garehagua mining license*

	Max.	Min.	Average	SD
Soil temperature (40 cm depth)	40.7	21.6	31	3.2
Diffuse CO_2 efflux ($gm^{-2}d^{-1}$)	37.7	<0.5	2.2	3.0
Diffuse H_2S efflux ($gm^{-2}d^{-1}$)	n.d.	n.d.	-	-
H_2S (ppm)	0.24	0.001	0.03	0.06
^{222}Rn ($pCi\ L^{-1}$)	290	<5	43.9	40.3
CO_2 (mol.%)	1.9	0.04	0.15	0.19
H_2 (ppm)	24.4	<0.5	1.4	2.1
N_2 (mol.%)	81.2	68.5	77.9	0.62
O_2 (mol.%)	21.3	18.8	20.7	0.23
ΔHe (ppb)	20963	-973	925	2506
$\delta^{13}C$-CO_2 (‰ *versus* VPDB)	-10.9	-25	-19.3	1.8

SD (Standard deviation)

No significant soil H_2S emissions were measured; therefore this parameter will not be discussed. As indicated by the N_2-CO_2-O_2 ternary plot (Figure 3.8A), the chemical composition of the gases follows the typical atmospheric component with a significant addition of CO_2. In order to check the origin of CO_2, a binary diagram of $\delta^{13}C$-CO_2 *versus* $1/[CO_2]$ was constructed assuming three geochemical reservoirs (Fig. 3.8B): i) air, characterized by $\delta^{13}C$-CO_2 = -8‰ and $1/[CO_2] = 2.5 \cdot 10^{-3}$ ppm^{-1}; ii) magmatic gas, with $\delta^{13}C$-CO_2 = -6.5‰ and $1/[CO_2] = 10^{-6}$ ppm^{-1}; iii) and biogenic gas, defined by -26‰>$\delta^{13}C$-CO_2>-15‰. The range of the biogenic end-member was selected since the isotopic composition of soil organic matter is in the range -30‰>$\delta^{13}C$-CO_2>-20‰ (Craig 1953), and the biogenic CO_2 in the soil can be +4.4‰ heavier than the soil-respired CO_2 produced by roots, due to CO_2 fractionation by diffusion within the soil (Cerling et al. 1991). CO_2 concentration values in the soil atmosphere ranged from air

values (~0.04 mol.%) to 1.99 mol.%, with an average of 0.15 mol.%. The isotopic composition of carbon in the soil CO_2 ranged from -25.0 to -10.9‰, with an average value of -19.3‰. Figure 3.8B shows that few samples (~6) showed a slight contribution of deep seated CO_2, although most of the samples are plotted in the range defined by the biogenic reservoir. No significant atmospheric contribution was observed.

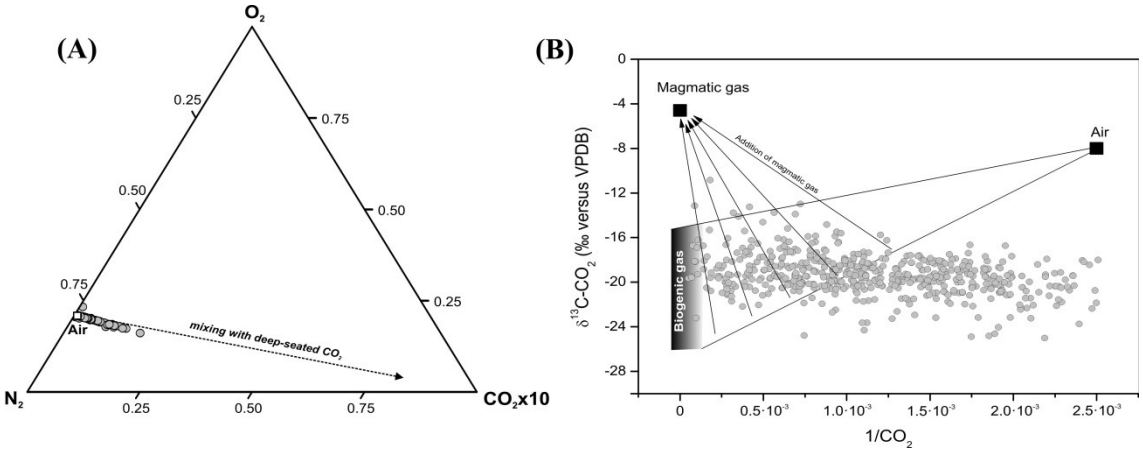

Figure 3.8. *(A) N_2-CO_2-O_2 diagram of soil gases from the study area. The white square shows the typical air end-member and dashed line shows the mixing trend with deep-seated CO_2. (B) Graph of carbon isotopic composition of soil CO_2 versus the reciprocal of CO_2 concentration in the gas samples collected in this study*

The addition of deep-seated CO_2 is suggested also by the existence of different geochemical populations in the soil CO_2 efflux and CO_2 concentration data, as depicted by the cumulative probability plots (Figure 3.9).

In the case of soil CO_2 efflux, the values ranged from non-detectable (<0.5 g m^{-2} d^{-1}) to 37.7 g $m^{-2}d^{-1}$, with an average value of 2.2 g m^{-2} d^{-1}. Two overlapping log-normal geochemical populations were distinguished (Fig. 3.9A): background and peak populations. Background population, indicated as population I, represented a 54.9% of the data and had an average value of 0.6 g $m^{-2}d^{-1}$; population II, or peak population, represented a 1.5% of the data and has an average value of 14.1 g $m^{-2}d^{-1}$. The rest of the data were composed by values between background and peak, and represented a 43.6% of the data. Background population is associated mainly with biogenic CO_2 production, while peak population suggests a slight deep CO_2 contribution.

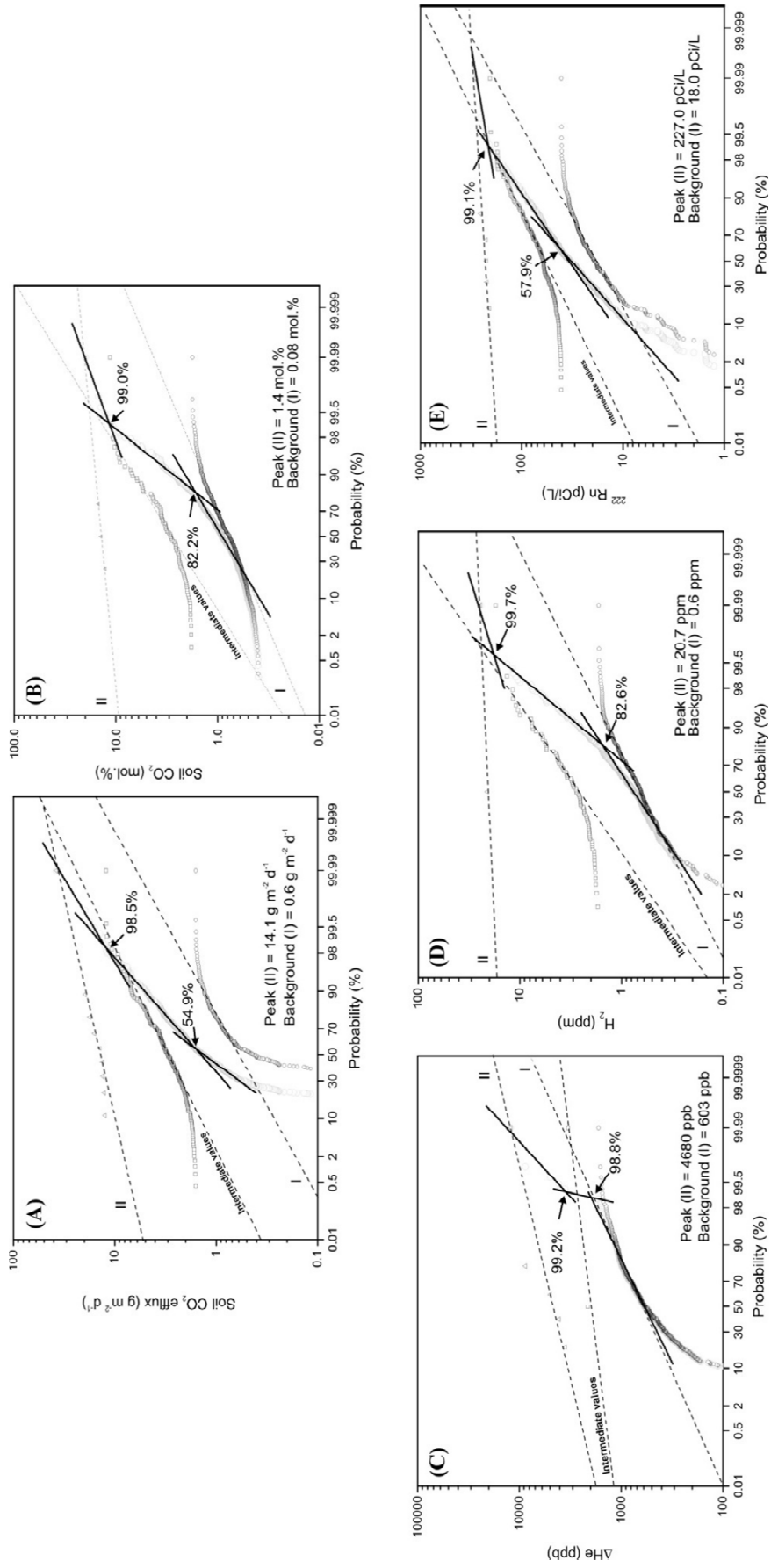

Figure 3.9. *Cumulative probability plots of (A) soil CO_2 efflux, (B) CO_2 concentration values, (C) soil ΔHe, (D) H_2 concentration and (E) ^{222}Rn activity values measured in 557 sampling sites at Garehagua. Solid lines in the probability plots indicate different log-normal geochemical populations in the original data. Dashed lines indicate background, peak and intermediate log-normal populations separated from the original data. Open grey circles represent the original data. I and II represent background (open black circles) and peak population (open triangles), respectively. The rest of the data (intermediate population) represents a mixing between background and peak values (open squares)*

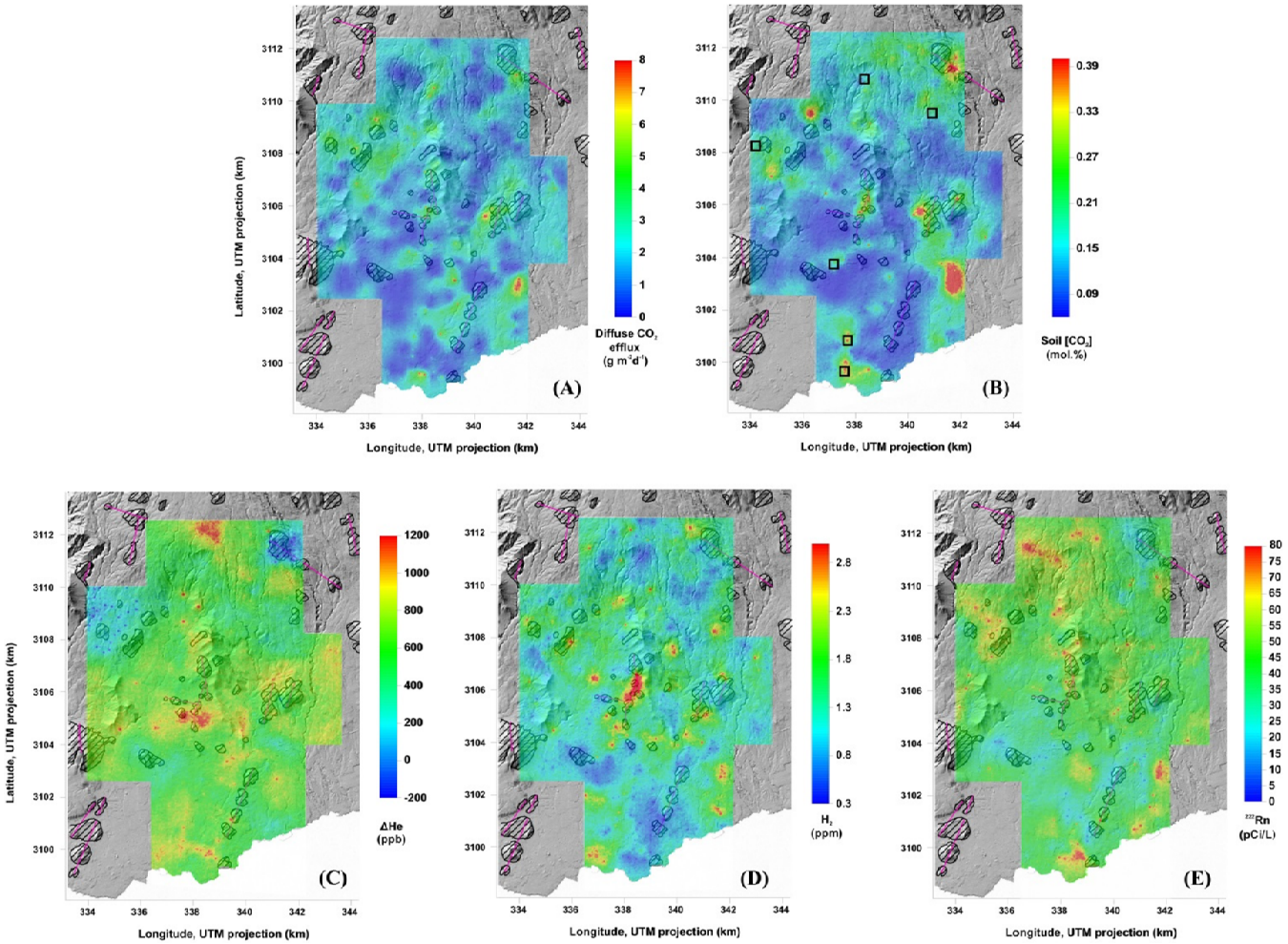

Figure 3.10. *Spatial distributions of (A) diffuse CO_2 efflux, (B) soil CO_2 concentration, (C) ΔHe, (D) H_2 concentration and (E) ^{222}Rn values, based on 100 equiprobable sequential Gaussian simulations. Open squares in (B) indicate the location of samples showing a significant contribution of deep seated CO_2 in Figure 3.8B. The location of eruptive fissures (pink lines) and vents (hatched areas) is also shown*

In the case of soil CO_2 concentration, the probability plot showed again two geochemical populations: background or population I (82.2% of the total data), that showed an average of 0.08 mol.% and the peak or population II (1% of the total data), that showed an average of 1.4 mol.% (Fig. 3.9B). The presence of endogenous gases in the soils of the study area can be also inferred by the existence of different geochemical populations in the soil He (Fig. 3.9C), H_2 concentration (Fig. 3.9D) and ^{222}Rn values (Fig. 3.9E). In the case of soil ^{222}Rn values, they ranged from non-detectable values (<5 pCi L^{-1}) to 290 pCi L^{-1}, with an average of 43.9 pCi L^{-1}. The presence of different log-normal populations in the statistical graphical analysis (Fig. 3.9E) might be explained by a contribution of ^{222}Rn from natural radioactive decay in the soils of the study area and an endogenous contribution of this gas from deeper sources.

Figure 3.10 shows the spatial distribution maps of soil CO_2 efflux, CO_2 concentration, ΔHe, H_2 concentration and ^{222}Rn activity. The highest CO_2 efflux values (Figure 3.10A) were measured as multiple isolated anomalies. Its spatial distribution suggests three main areas with relatively high diffuse CO_2 degassing: the southern half of the area, characterized by a linear distribution of anomalous CO_2 effluxes along NS; the NW part of the area, showing an apparent NE-SW trend; and the SE corner of the area, with no clear direction. The first two areas seem to correspond nicely with the location of old eruptive vents. Similar results were obtained in 2002 by Galindo (2005). The total CO_2 output in the study area was estimated at 187 ± 6.2 t d^{-1}, which correspond to 1.9 t d^{-1} km^{-2}. The spatial distribution of soil CO_2 concentration is shown in Figure 3.10B, where no significant trend in the anomalous values can be observed. Samples that showed a significant contribution of deep seated CO_2 in Figure 3.8B, are depicted as open squares in Figure 3.10B. Finally, ^{222}Rn activity in the soil gases, depicted in Figure 3.10E, shows multiple ‘‘spot’’ anomalies with a non-clear direction. Important soil ^{222}Rn activity values were observed in the N-W and S-E of the study area.

In order to make the volcano-tectonic structures more visible, a map including the anomalous enrichments in each cell of the grid was constructed: each grid cell was normalized by dividing their value by the maximum measured; later a new grid was constructed by summing the value (from 0 to 1) of each normalized grid and normalizing it in turn. The resulting grid includes information of all the studied parameters at each cell and is depicted in Figure 3.11. Due to the high percentage of biogenic CO_2 present, as deduced by Figure 3.8B, an additional spatial distribution map was constructed only with soil He, H_2 concentration and ^{222}Rn activity (Figure 3.11B). In both Figures 3.11A and B, three main vertical permeability structures can be defined: A, B and C. These sub-areas showed important enrichment in the studied parameters (Figure 3.11A) and persist even when soil CO_2 concentration and efflux are not considered (Figure 3.11B).

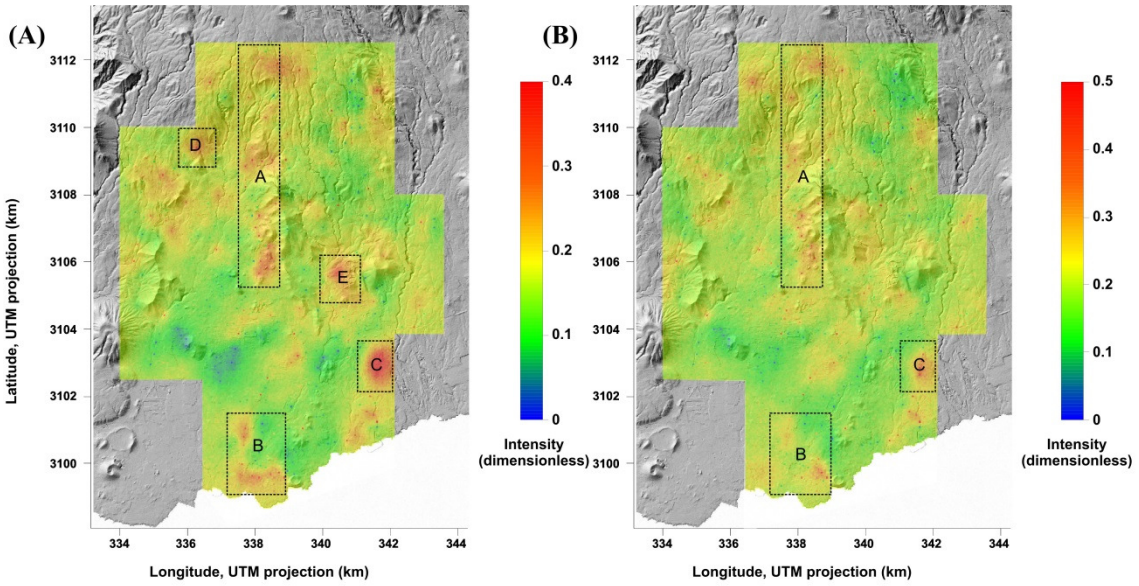

Figure 3.11. *Spatial distribution of the anomaly intensity based on normalized data of soil gases concentrations and diffuse CO_2 emission. (A) Includes diffuse CO_2 efflux, soil CO_2 concentration, ΔHe, H_2 concentration and ^{222}Rn activity. (B) Includes ΔHe, H_2 concentration and ^{222}Rn activity. Dotted squares with A, B, C, D and E represent areas with the highest intensity of the values*

A and B areas extend mainly along a N-S direction, which corresponds to the dominant structural direction in this area. These main degassing structures are not spatially continuous, probably due to the different gas-bearing properties of the main N-S volcanic rift of Tenerife as shown by Ciotoli et al. (2004) and Voltattorni et al. (2010). The N-S-directed volcanic-rift of Tenerife seems to be an area of enhanced permeability for deep gas migration and hence a preferential route for diffuse degassing, similar to what is observed in other volcanic rifts in the Canary Islands (Padrón et al. 2012b). It is worth noting that volcanic rifts are complex structures that include wide fracture zones that can also be cross-cut by other faults, thus resulting in multiple isolated anomalies, as observed at other volcanic systems (Voltattorni et al. 2010). This might be a possible explanation for the presence of spotty anomalies at both sides of the main N-S-directed vertical permeability structure. Another important vertical permeability zone is indicated as C in Figure 3.11. Although this area does not seem to follow the main N-S degassing zone (A and B), the maximum values of several of the studied parameters were measured there.

Regarding to geophysical results (magnetotelluric study), the starting model for the inversion process was that obtained by Piña-Varas et al. (2014) for the whole island. A 5% error baseline in the impedance components was imposed. The starting root mean square (RMS) was 11.56, while the final RMS was 1.99 after 60 iterations. This model includes the topography, obtained from a digital elevation model, and the surrounding ocean, which was fixed during the

inversion process with a resistivity value of 0.33 Ωm. Figure 3.12 shows the model fit by comparison of the apparent resistivity and phases between the model responses and the raw data.

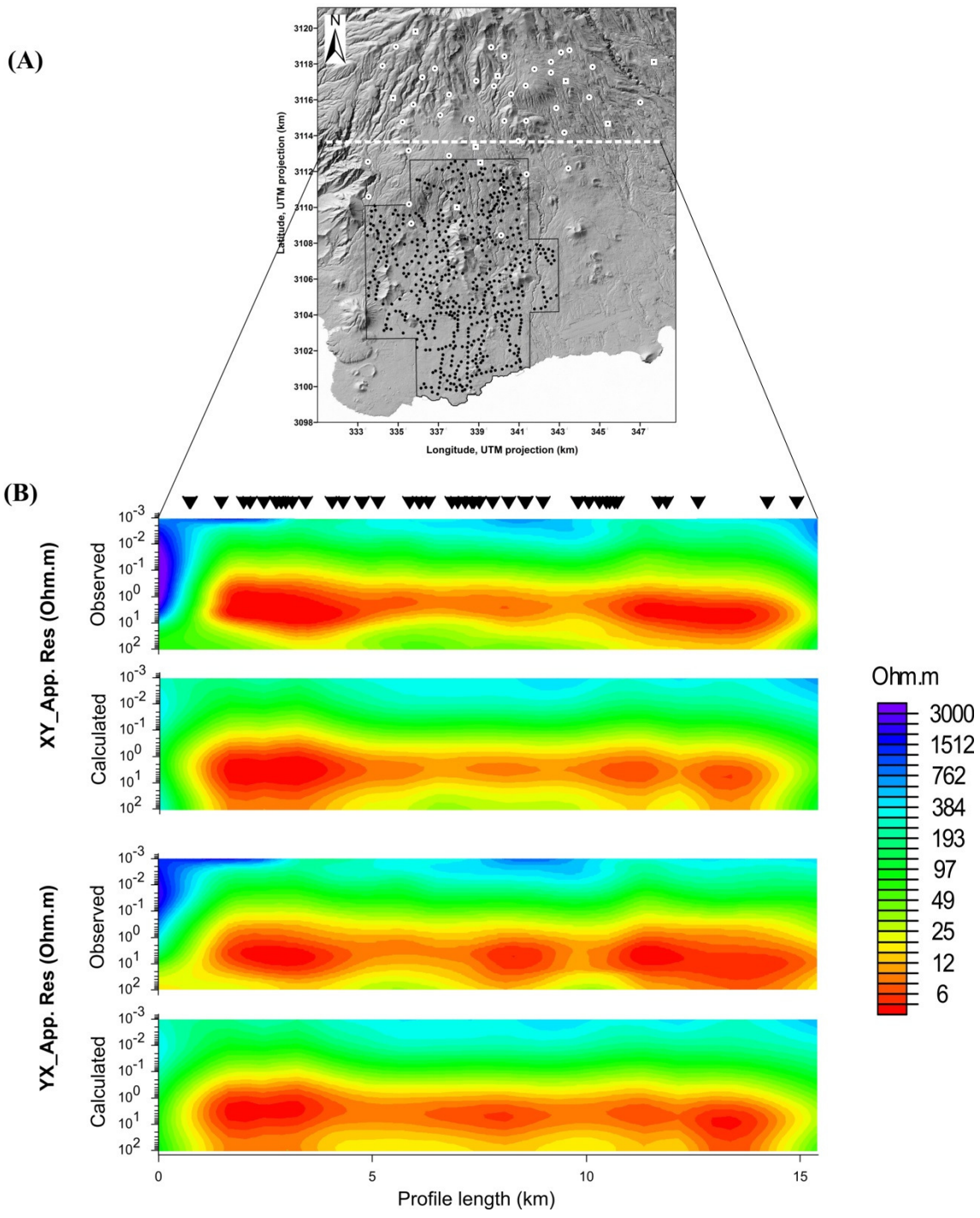

Figure 3.12. *Pseudosection plots of Zxy and Zyx apparent resistivities and phases of impedance tensors for observed and predicted (calculated) data along WE section. Black triangles correspond to the MT sites*

The final 3-D resistivity inversion model is shown in Figures 3.13 and 3.14. Figure 3.13 shows four horizontal slices through the 3-D model at different depths. The most evident feature is a low resistivity body (<10 Ωm) that occupies most of the model area. This anomaly appears in the northern part of the model area at low depths, whereas it is shifting towards the south with increasing depth. It is semi-circular shaped, with the central area occupied by moderate resistivities (20-100 Ωm).

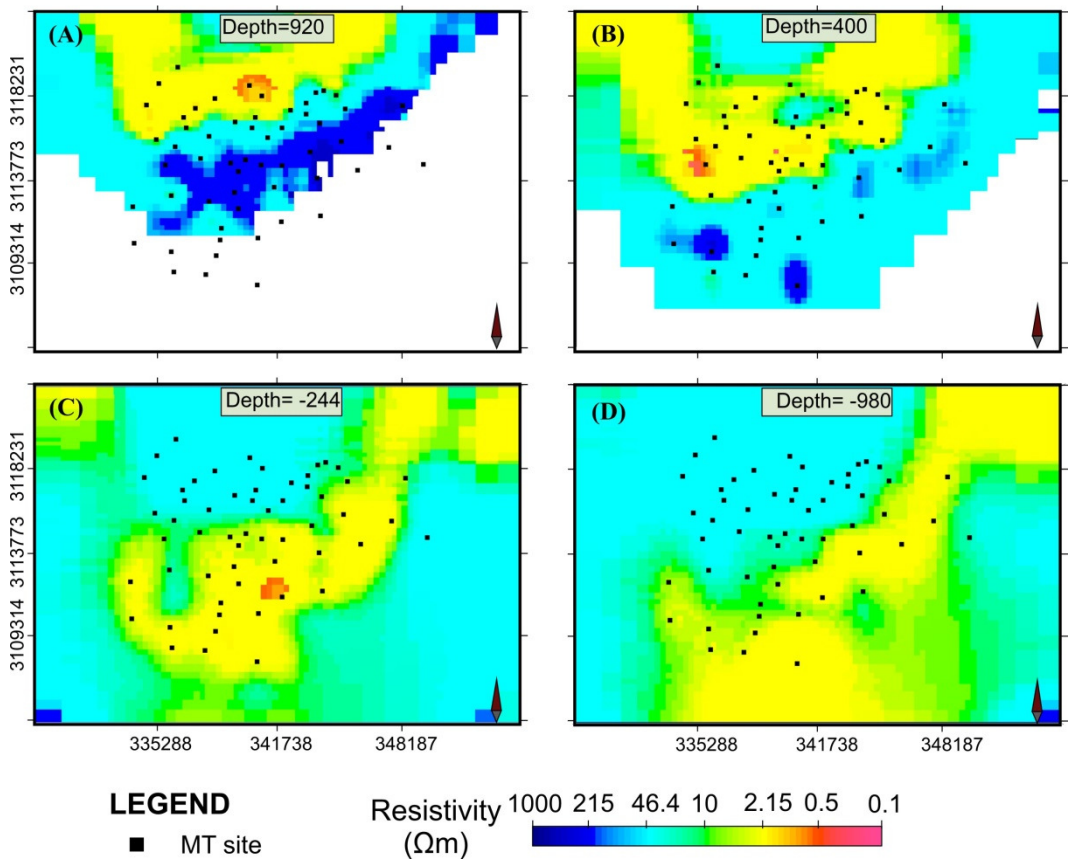

Figure 3.13. *Horizontal slices through the 3-D resistivity model at different depths*

Three different N-S vertical cross-sections of the 3-D model are shown in Figure 3.14. As in the case of the horizontal slices, the most prominent feature is a low resistivity layer that follows the topography of the study area. A similar structure was observed in the whole island. In the 3-D resistivity model presented by Piña-Varas et al. (2014), four geoelectrical structures were distinguished according to the resistivity values: (1) a low resistivity central region (<10Ωm), interpreted as the clay cap derived from hydrothermal alteration from the geothermal system; (2) the area surrounding the low resistivity body occupied by low-medium values of resistivity (20-100 Ωm) and corresponding to rocks at higher temperatures; (3) a shallow part, corresponding to high resistivity values (>500 Ωm), correlated with unaltered basaltic rocks; (4) a deeper structure with medium-high resistivities (100-500 Ωm), associated to a hotter part of

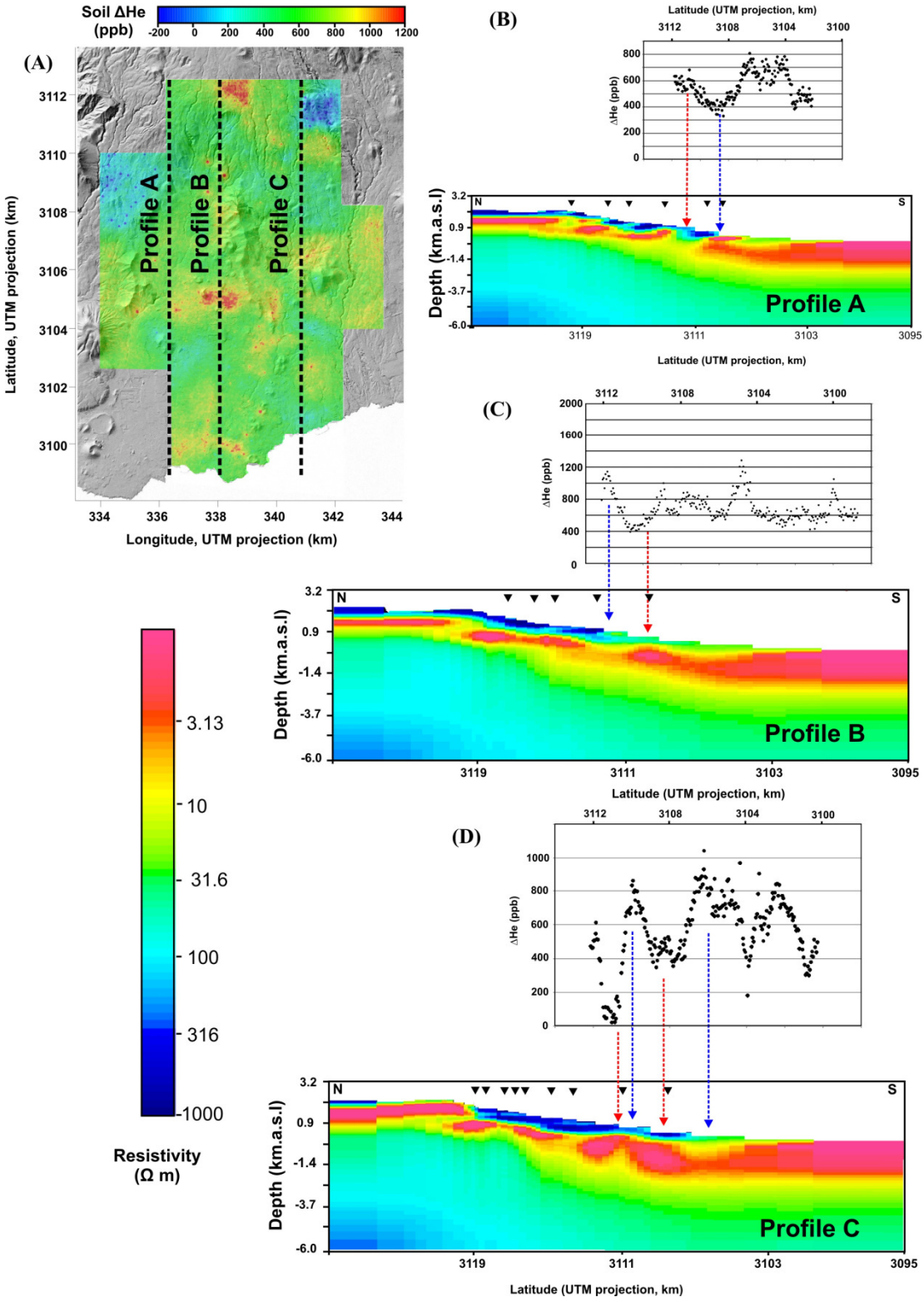

Figure 3.14. *(A) ΔHe map showing the location of the N-S resistivity cross-section corresponding to three N-S profiles. (B), (C) and (D) depict values of soil ΔHe and results of the final 3-D resistivity model along A, B and C vertical N-S cross-sections respectively. Blue and red dashed arrows indicates observed positive and negative correlation between highest values of ΔHe and clay cap discontinuities and lowest values of ΔHe and the thicker clay cap, respectively. Inverse black triangles show the location of MT sites within each profile*

the geothermal system. This interpretation is also suitable for the MT model obtained for *Garehagua*. The clay cap is expected to have a very low permeability, thus acting as a seal and reducing the leakage of deep fluids. Therefore, the continuity and extent of the clay cap should have a strong influence in determining the location of the surface manifestation of gas emissions. Figure 3.14 shows three N-S-directed resistivity cross-sections extracted from the 3-D resistivity model and the spatial distribution of ΔHe data along the corresponding meridian. The distribution of resistivity values shows some gaps that may be associated with a reduced thickness of the clay alteration cap, resulting in enhanced permeability areas. Comparison of the MT section with the ΔHe distribution (Figure 3.14) shows a relatively good correlation between the discontinuities observed in the clay cap and the highest values of ΔHe. This correlation might be useful to infer the thickness of the clay cap towards the south of the studied area, where the MT results lose resolution due to anthropogenic noise.

3.3. Soil gas geochemistry in relation to eruptive fissures on Timanfaya volcano, Lanzarote Island

To investigate the relationship between soil gas concentrations and the volcano-tectonic structures of Timanfaya volcano, a detailed soil gas survey on this volcanic system was focused mainly on CO_2, ^{222}Rn, ^{220}Rn and He concentrations, since the active fractures at Timanfaya volcano are evident from the surface geology, the main aim of this study is to investigate whether these geological structures are actively releasing deep gases.

Lanzarote Island is elongated in the NNE-SSW direction reflecting the trend of the East Canary Ridge (ECR), and most of the emission centers in the central part of the island indicate concentration of vents with an ENE-WSW trend. From 1730 to 1736 Lanzarote suffered the longest eruption in historical times in the Canary Islands, a basaltic-type eruption, with more than 30 volcanic cones (Carracedo et al. 1992). The eruptive vents are aligned along a fracture more than 14 km in lenght (Figure 3.15). One of the most prominent phenomena at Timanfaya volcanic field is the high maintained superficial temperatures occurring in the area since the 1730-1736 volcanic eruption, being the maximum temperature recorded in this zone 605ºC measured at 13 m depth at the Islote de Hilario area.

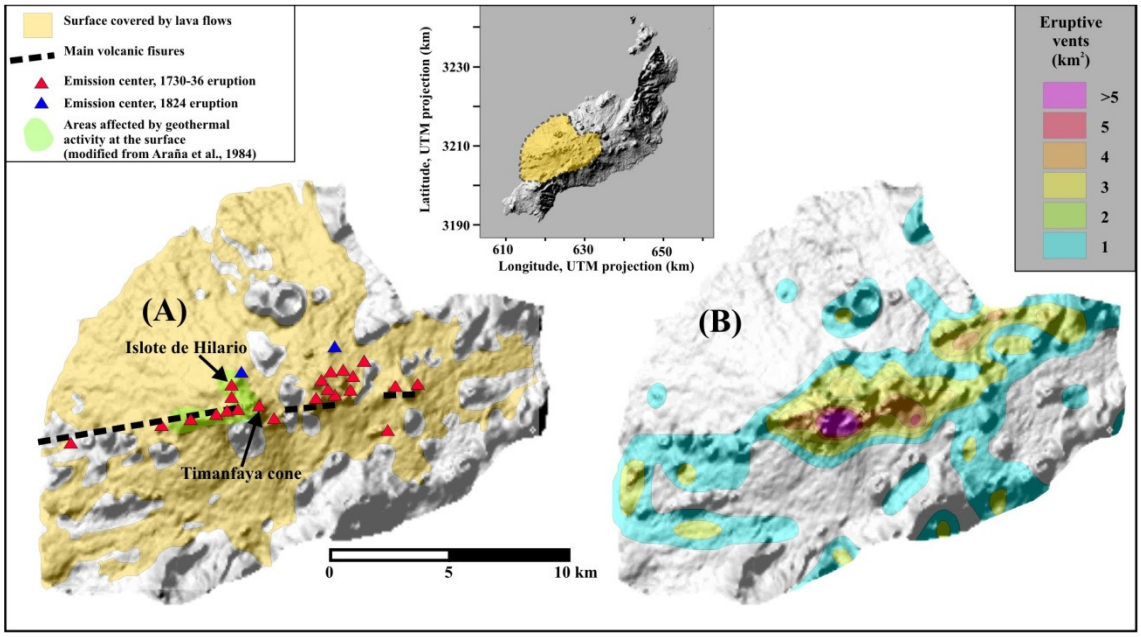

Figure 3.15. *(A) Main eruptive fissures, emission centers and surface covered by lava flows from 1730-1736 eruption of Timanfaya volcano, Lanzarote Island; soil thermalized areas are depicted in green colour. (B) Density distribution of vents of recent eruptive centres along the study area (modified from Carracedo et al. 1992)*

At present there is no surface evidence of gas emissions at Timanfaya volcano, and therefore the study of the spatial distribution of CO_2, ^{222}Rn, ^{220}Rn and He concentrations in soil gases becomes an ideal geochemical tool to identify sites with an anomalous emission of deep-seated gases, which could then be used for volcano monitoring. A descriptive statistic summary of the soil gas composition measured is depicted in Table 3.5.

Table 3.5. *Descriptive statistics of soil gas composition data and the soil temperature measured at 40 cm depth from the surface environment of Timanfaya volcano*

	Range	Mean	SD	No. of samples
ΔHe (ppb)	-1,518 – 18,665	927	2,728	362
N_2 (vol. %)	76.43 – 79.18	77.5	0.54	362
O_2 (vol. %)	19.78 – 22.51	21.48	0.55	362
Ar (vol. %)	0.934 – 1.065	0.972	0.22	362
CO_2 (ppm)	379 – 4,600	772	404	362
$\delta^{13}C$-CO_2 (‰ *versus* VPDB)	-19.9 – -8.1	-10.3	2.4	39
^{222}Rn (Bq m^{-3})	n.d. – 5,670	383	706	366
^{220}Rn (Bq m^{-3})	n.d. – 15,295	445	1424	366
Soil temperature (ºC)	15.7 – 74.4	25.9	6.5	366

In the case of CO_2, the existence of a peak population in the statistical-graphical analysis of the soil gas composition suggests a very slight deep contribution from the Timanfaya volcanic system. The background soil CO_2 concentration values could be mainly characterized as biogenic CO_2 (Figure 3.16A). The analysis of carbon isotopic composition performed in 39 samples, showed an average value of -10.3‰ *versus* VPDB. This value is lighter than the typical biogenic range and closer to atmospheric CO_2 (-8.0‰ *versus* VPDB, Trolier et al. 1996). A binary diagram of the $\delta^{13}C$-CO_2 *versus* CO_2 concentration in the soil gases was constructed to plot all data using three geochemical reservoirs (Figure 3.16B): air, magmatic gas and biogenic reservoir. Air reservoir is characterized by $\delta^{13}C$-CO_2 = -8.0‰ *versus* VPDB and [CO_2] = 380 ppm. Magmatic gas reservoir is characterized by $\delta^{13}C$-CO_2 = -6.5‰ *versus* VPDB (Javoy et al. 1978) and [CO_2] = 100%. As was explained in section 3.2, the biogenic reservoir was defined by -25.6‰>$\delta^{13}C$-CO_2>-15.6‰, *versus* VPDB, with a mean value of -20.6‰. The range of the CO_2 concentration in the biogenic reservoir was 540–740 ppm, equal to the mean value of the background population partitioned by the probability plot (650 ppm) and one standard deviation as uncertainty. Figure 3.16B shows that most of the soil gas samples were plotted close to the atmospheric reservoir and indicate an important biogenic contribution. The binary plot results postulate that there is a very small fraction of magmatic gas in the soil gases of Timanfaya. The lack of further evidence can be attributed to the small number of samples plotted on or close to the mixing line between magmatic and biogenic reservoirs.

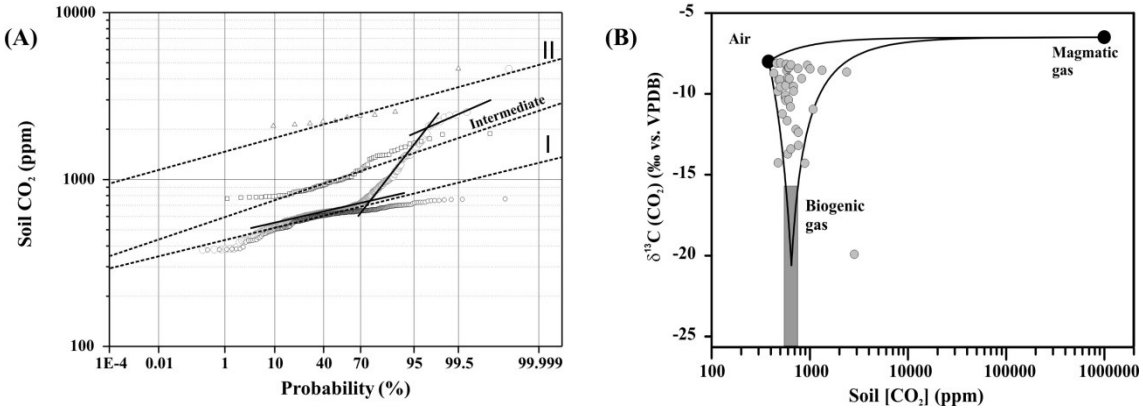

Figure 3.16. *(A) Probability plot of soil CO_2 concentration. Solid lines indicate the partition between the 3 straight transects (populations). Numerals I and II indicate the two different log-normal populations separated: I = background population (open black circles) and II = peak population (open triangles). Total data are presented as open grey circles. The rest of the data were also separated and form the intermediate population, which represents a mixing between background and peak values (open squares). (B) Binary diagram of $\delta^{13}C$-CO_2 versus CO_2 concentration. Mixing lines between biogenic end-member and air and magmatic gas, and between air and magmatic gas end-members are displayed by solid lines. Air and magmatic gas end-members are characterized by $\delta^{13}C$-CO_2 = -8‰ and -6.5‰, and CO_2 = 380 and 10^6 ppm, respectively. Biogenic end-member is characterized by $\delta^{13}C$-CO_2 in the range -25.6‰ − -15.6 ‰ versus VPDB, with a mean value of -20.6 and CO_2 in the range 540 −740 ppm, with a mean value of 650 ppm*

In the case of soil ΔHe, the probability plot showed two distinct modes (Figure 3.17): background and peak, with a mean of 830 ppb for the background population, (which represented 56.5% of the total data), and a peak population (5.1% of the total data), showing a mean of 12,200 ppb. Two possible origins for He enrichments in the Timanfaya soil gases can be postulated on the basis of the existence of two geochemical populations: (I) shallow degassing of crustal He and (II) He released from deeper source (magmatic), which is responsible for the higher ΔHe data and probably emanates from a cooling magma body. A magmatic He contribution cannot be ruled at all the areas where high ΔHe was measured at Timanfaya volcano.

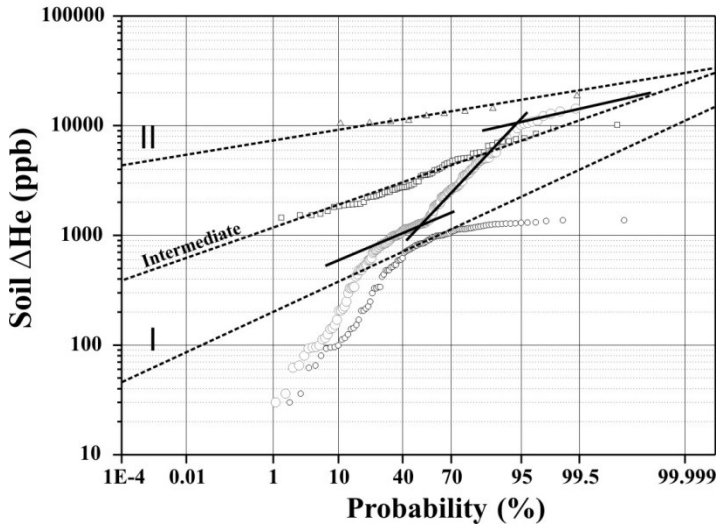

Figure 3.17. *Probability plot of positive ΔHe data. Solid lines indicate the partition between the 3 straight transects (populations). Numerals I and II indicate the two different log-normal populations separated: I = background population (open black circles) and II = peak population (open triangles). Total data are presented as open grey circles. The rest of the data were also separated and form the intermediate population, which represents a mixing between background and peak values (open squares)*

Argon isotopes can provide significant information on the magmatic contribution of endogenous gases, because ^{40}Ar derives from volcanic degassing, the hydrothermal circulation through the crust and the erosion of continental crust, which releases radiogenic Ar (Graham 2002). The $^{40}Ar/^{36}Ar$ ratios in mantle-derived gases are very high compared to the atmospheric value, and ranges from ~8,000 for Ocean Island Basalts (OIB) to 40,000 for Mid-Ocean Ridge Basalts (MORB) (Graham 2002). Because nitrogen concentration correlates with the amount of ^{40}Ar, the $N_2/^{36}Ar$ ratio in MORB-derived gases correlates with $^{40}Ar/^{36}Ar$ (Marty 1995; Graham 2002). Thus it is possible to construct a two-components mixing model composed of a mantle-derived end-member, having $^{40}Ar/^{36}Ar$ = 30,000 and $N_2/^{36}Ar = 2.2\times10^6$ (Graham 2002); and an

atmospheric end-member, with $^{40}Ar/^{36}Ar$ = 295.5 and $N_2/^{36}Ar$ = 2.46×10^4. The $N_2/^{36}Ar$ ratio *versus* $^{40}Ar/^{36}Ar$ ratio in soil gases measured in an area showing active degassing of mantle-derived gases, can be plotted in a mixing trend between both end-members. Figure 3.18 shows the results of $N_2/^{36}Ar$ *versus* $^{40}Ar/^{36}Ar$ plot for the Timnafaya volcano soil gases. Although atmospheric air is the dominant component in the plot, the area around the atmospheric reservoir, as shown in the inset, displays a clear trend on the mixing line with an MORB-type end-member. This observed addition of endogenous argon isotopes in the soils of the Timanfaya volcanic system, suggests a slight magmatic contribution to the soil gas geochemistry. The most plausible explanation for the soil gas composition presented in this work is that biogenic CO_2, deep-seated He, CO_2 and argon, which slightly pollute the atmospheric air, emanate from the degassing of magma bodies, which are probably located at a depth of 4 km under the Timanfaya volcanic system (García 1983).

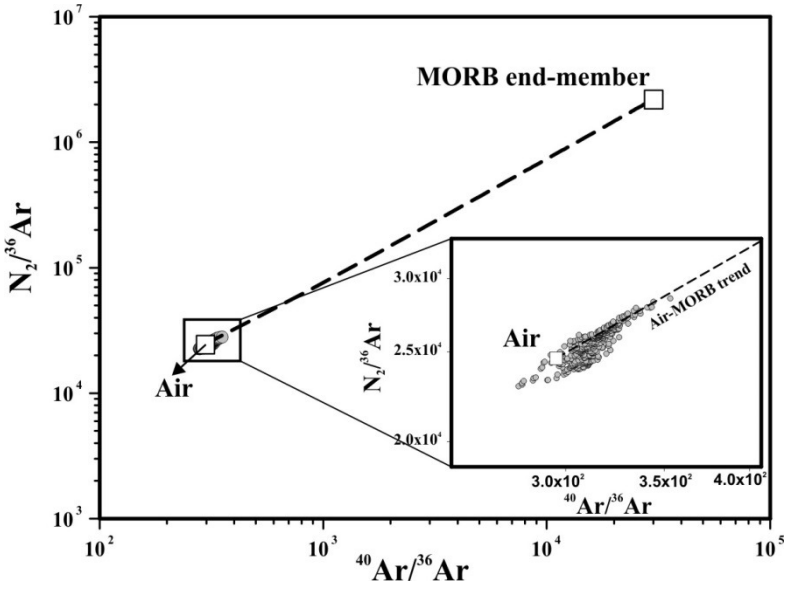

Figure 3.18. *Binary diagram of $N_2/^{36}Ar$ versus $^{40}Ar/^{36}Ar$ measured in the soils of Timanfaya volcanic system. Two different end-members are displayed: mantle-derived (MORB) end-member, with $^{40}Ar/^{36}Ar$ = 30,000 and $N_2/^{36}Ar$ = 2.2×10^6 (Graham 2002), and an atmospheric end-member, with $^{40}Ar/^{36}Ar$ = 295.5 and $N_2/^{36}Ar$ = 2.46×10^4*

The spatial distribution of soil ^{222}Rn activity and $^{222}Rn/^{220}Rn$ ratio indicates that most of the anomalies were measured at areas not covered by lava flows from the 1730–36 eruption (Figure 3.19A and B). The higher average value of soil ^{220}Rn activity relative to ^{222}Rn (Table 3.5), indicate a main shallow main source of radon activity within the Timanfaya volcano soils. No significant spatial correlation between the main eruptive fissures and the location of soil ^{222}Rn and $^{222}Rn/^{220}Rn$ ratio was observed, being the most important anomalies on the eastern part of the study area and at the NW of Caldera Blanca volcano. The only significant anomaly measured in both soil ^{222}Rn activity and $^{222}Rn/^{220}Rn$ ratio was located at Montaña Termesana,

close to the eruptive fissure from the 1730–36 eruption, in an area not covered by lava flows. In the case of the soil CO_2 concentration spatial distribution, nearly all the anomalies were measured in the limits of the study area (Figure 3.19C).

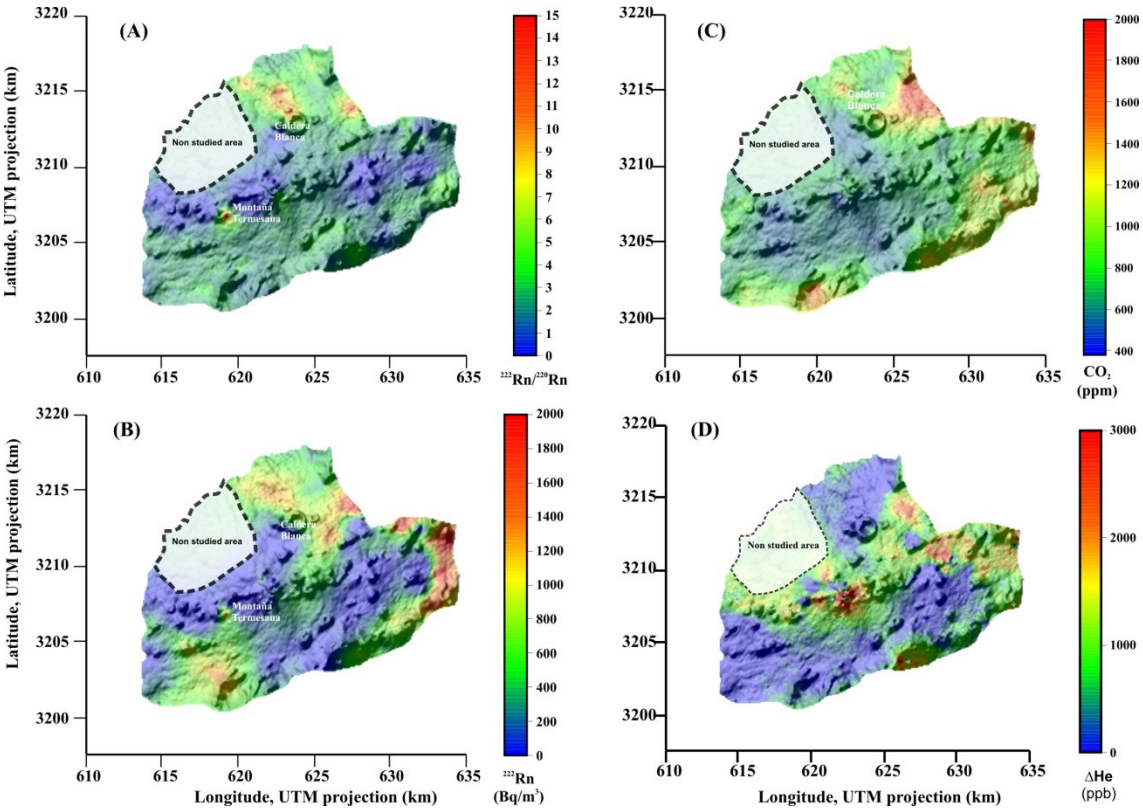

Figure 3.19. *(A) Soil $^{222}Rn/^{220}Rn$ ratio, (B) ^{222}Rn activity, (C) CO_2 concentration and (D) ΔHe average maps of the 100 equiprobable sGs realizations*

In the case of He, the spatial distribution of ΔHe data depicted in Figure 3.19D, indicates an important structural control for the leakage of He at Timanfaya volcano. The main soil ΔHe anomalies were observed in accordance with the main eruptive fissures of the 1730–36 eruption. The highest values were located in an area characterized by a high density of recent eruptive centers. This result confirms, therefore, the efficacy of soil-He surveys as geochemical pathfinders of active permeable structures.

In the case of Timanfaya volcano, a diffusive transport of radiogenic and/or magmatic He is the most likely main transport mechanism for the He leakage. This is because (1) there was no visual correlation between the soil gas composition and soil temperature (Figure 3.20A); (2) according to the data reported by Hernández et al. (2012), CO_2, the most probable carrier gas, does not show advective discharges at Timanfaya volcano, and no significant correlation between soil CO_2 and ΔHe has been observed (Figure 3.20B); and (3) there was not evident correlation between He and any other of the studied soil gases in this work.

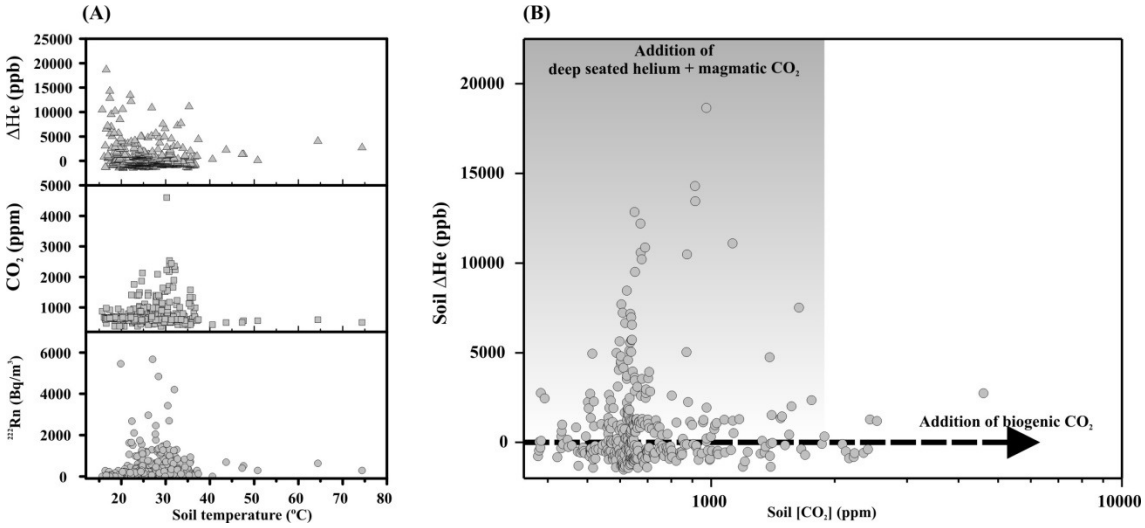

Figure 3.20. *(A) Soil ^{222}Rn, CO_2 and ΔHe versus soil temperature at each sampling site and (B) ΔHe versus soil CO_2 concentration measured in the environmental surface of Timanfaya volcano*

We have, therefore, applied a pure diffusive model following Fick's law in order to estimate the amount of He released by the degassing structure defined by the eruptive fissure. Assuming an average of 25% for the soil porosity, as used for other volcanic systems in the Canaries (Padrón et al. 2008), we estimated a He emission rate of ~15 kg d^{-1} by an area of 80 km^2 which includes the main eruptive fissures of the 1730–36 eruption.

3.4. Dynamics of diffuse carbon dioxide emissions from Cumbre Vieja volcano, La Palma

During its brief geological history (~2 Ma), La Palma is the island with the largest number of historic eruptions (post 1,500 B.C.) of the Canaries, all of them located in the southern part of the island, associated with the Cumbre Vieja volcanic ridge with a main N-S alignment of eruptive vents. The most recent volcanic eruption was that of Teneguía volcano in 1971 (Figure 3.21). In the central part of the island a great depression (Taburiente caldera) formed by a flank collapse of Cumbre Nueva edifice is located. The only known visible gas emanation of La Palma Island is present inside the Taburiente caldera, a CO_2-rich bubbling cold spring called Dos Aguas (DA in Figure 2.6). Gas from this cold spring has the highest $^3He/^4He$ ratio measured in the Canary Islands, ranging from 9.5 to 9.95 R_A (Pérez et al. 1994; Hilton et al. 2000; Padrón et al. 2012b), where R_A is the atmospheric $^3He/^4He$ ratio (1.384×10^{-6}, Clarke et al. 1976).

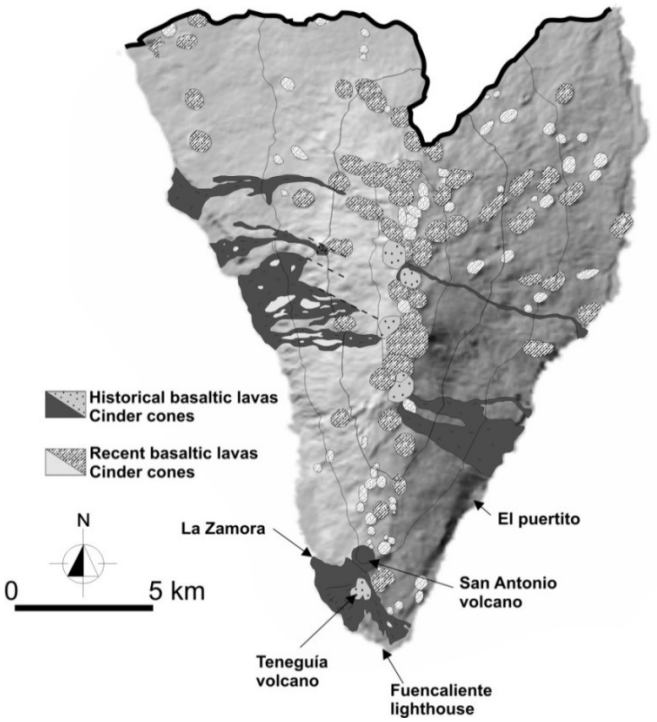

Figure 3.21. *Shaded relief map of Cumbre Vieja volcano*

Several intensive soil CO_2 emission surveys were carried out between 2001 and 2013 at Cumbre Vieja volcano, with the aim of studying the spatial distribution of CO_2 efflux anomalies and estimating the total diffuse CO_2 output to the atmosphere and its relation to the level of volcanic activity. The diffuse CO_2 efflux results for each survey are summarized in Table 3.6.

Soil CO_2 efflux measurements at Cumbre Vieja exhibited high spatial variability (Figure 3.22). In most of the surveys CO_2 efflux values ranging from 15 to 25 g m^{-2} d^{-1} were measured at the north end of Cumbre Vieja, around the surface contact with Cumbre Nueva ridge. This area is characterized by a wet climate and is mainly vegetated by pine forests and heaths. Pine forest can be found also along both sides of the N-S volcanic rift of Cumbre Vieja, where CO_2 efflux values from 5 to 20 g m^{-2} d^{-1} were measured in all the surveys. The maximum flux values (>800 g m^{-2} d^{-1}) were measured in the summit cinder cone of Teneguía, except during the 2007, 2008, 2011 and 2012 surveys. This sampling site showed important soil temperature values, ranging between 90 and 130ºC at 40 cm depth in the studied period. The rest of the soil temperature values seemed to be modulated by ambient temperature values. It is important to point out that the high flux anomaly at Teneguía cinder cone is the result of only one sampling site, and its emission value was strongly disturbed on windy days. This anomalous CO_2 emission might be caused by residual degassing of volatiles from stored magma bodies beneath the southern part of the volcano that were responsible of the volcanic eruption of Teneguía.

Table 3.6. *Statistical results of soil CO_2 efflux measured in the 2001-2013 period surveys and $\delta^{13}C$-CO_2 in the 2001, 2002 and 2010 surveys.*

Year	Soil CO_2 efflux (g m^{-2} day^{-1})				CO_2 output (t day^{-1})[a]	δ ^{13}C-CO_2 (‰ *versus* PDB)				Soil CO_2 concentration (mol.%)		
	Nº samples	Min.	Max.	Median		Nº samples	Min.	Max.	Median	Min.	Max.	Median
2001	621	<0.5	1,461	3.2	1,348 ± 89	143	-35.1	-11.5	-28.8	0.02	1.29	0.21
2002	619	<0.5	1,250	1.4	950 ± 68	57	-33.4	-1.5	-23.7	0.77	10.1	0.24
2003	611	<0.5	1,915	1.8	1,253 ± 111	-	-	-	-	-	-	-
2004	555	<0.5	1,171	1.8	990 ± 79	-	-	-	-	-	-	-
2005	560	<0.5	872	1.6	1,169 ± 110	-	-	-	-	-	-	-
2006	599	<0.5	1,294	1.1	1,060 ± 139	-	-	-	-	-	-	-
2007	531	<0.5	252	2.4	992 ± 44	-	-	-	-	-	-	-
2008	505	<0.5	103	1.8	807 ± 92	-	-	-	-	-	-	-
2009	548	<0.5	1,404	0.9	657 ± 55	-	-	-	-	-	-	-
2010	550	<0.5	878	0.9	748 ± 71	42	-21.2	-8.8	-16.9	0.05	0.62	0.14
2011	572	<0.5	75	3.6	1,544 ± 81	-	-	-	-	-	-	-
2012	565	<0.5	558	0.7	320 ± 31	-	-	-	-	-	-	-
2013	583	<0.5	2,442	1.9	1,538 ± 160	-	-	-	-	-	-	-

[a]The CO_2 output uncertainty is represented as 1 standard deviation (±1σ) of 100 sGs equiprobable realizations

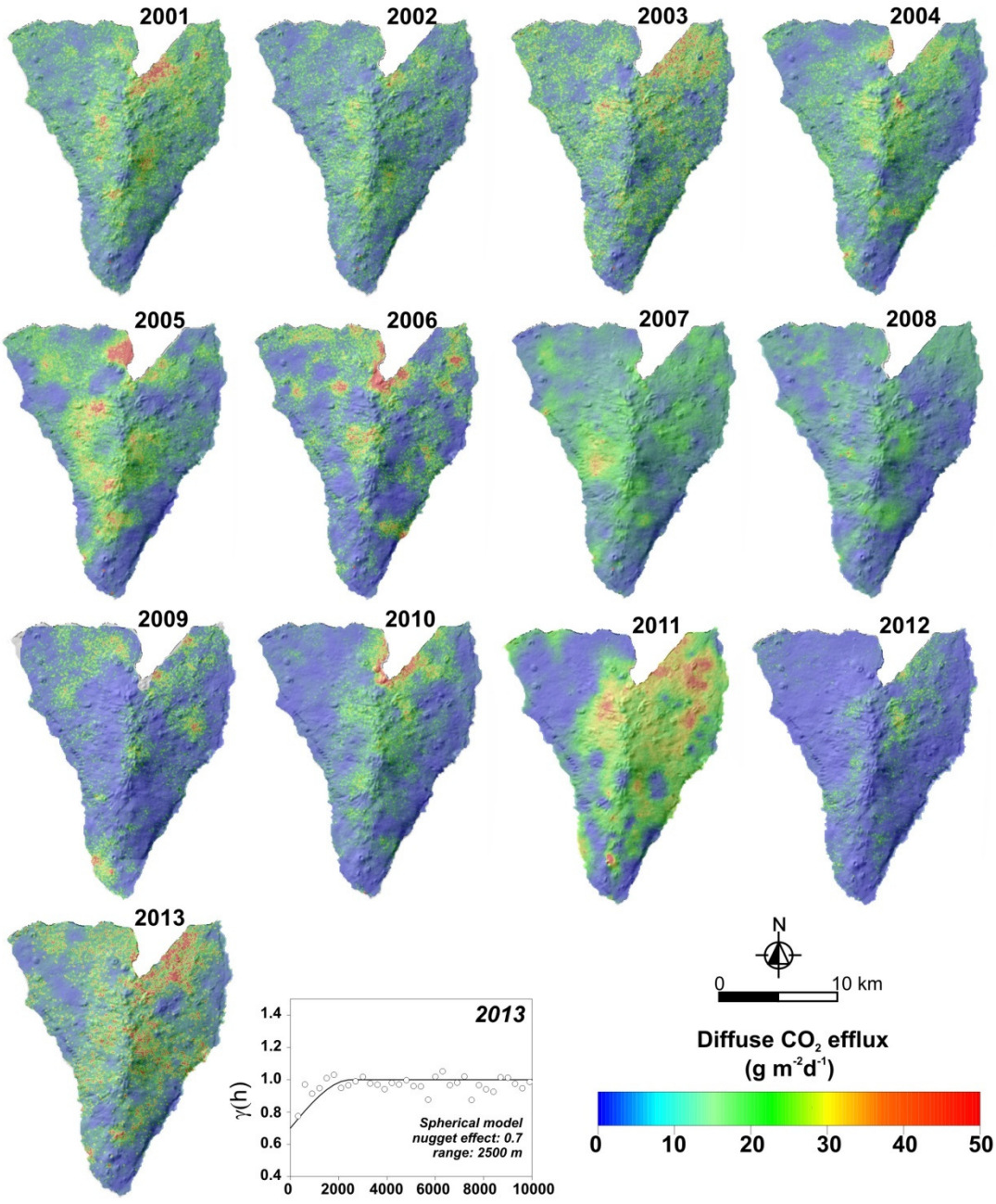

Figure 3.22. *Spatial distribution of diffuse CO_2 efflux on Cumbre Vieja volcano, based on sGs for the 13 surveys. The experimental and the modelled variogram used by sGs to construct the spatial distribution of the 2013 survey are also shown*

The observed strong structural-spatial correlation in the emission of inert gases (He) observed in Cumbre Vieja by Padrón et al. (2012b) and the absence of such correlation in the CO_2 emission, support the interpretation that any reactive gases (such as CO_2, SO_2, H_2S) released from depth by the volcanic system of Cumbre Vieja undergo chemical reactions or are almost completely dissolved in water during their rise. This observation is also supported by the

chemical composition of groundwater extracted in the few existing vertical or horizontal wells at Cumbre Vieja (Veeger 1991; Pérez et al. 1996).

Since most of the highest diffuse CO_2 emission values were measured at the southern part of Cumbre Vieja, Teneguía volcano, and surroundings areas, a more detailed CO_2 diffuse emission survey was carried out during the summer of 2005. A total of 241 sampling points covered 6.2 km^2 and included the sites with the highest CO_2 efflux values. As an approximation, we considered deep seated CO_2 as the main contributor to the total CO_2 efflux at this area. The probability plot of the diffuse CO_2 emission data shows two overlapping populations (Figure 3.23A). The low efflux for the background population (<0.5 g m^{-2} d^{-1}) supports the hypothesis of negligible biogenic contribution to the diffuse CO_2 emission at these sites. Figure 3.23B shows the average flux map from 100 sGs simulations composed of 15,961 cells with size of 20 m x 20 m. The highest diffuse CO_2 emission values were measured at Teneguía cinder cone (870 g m^{-2} d^{-1}) and in the coast area around Fuencaliente lighthouse (up to 674 g m^{-2} d^{-1}).

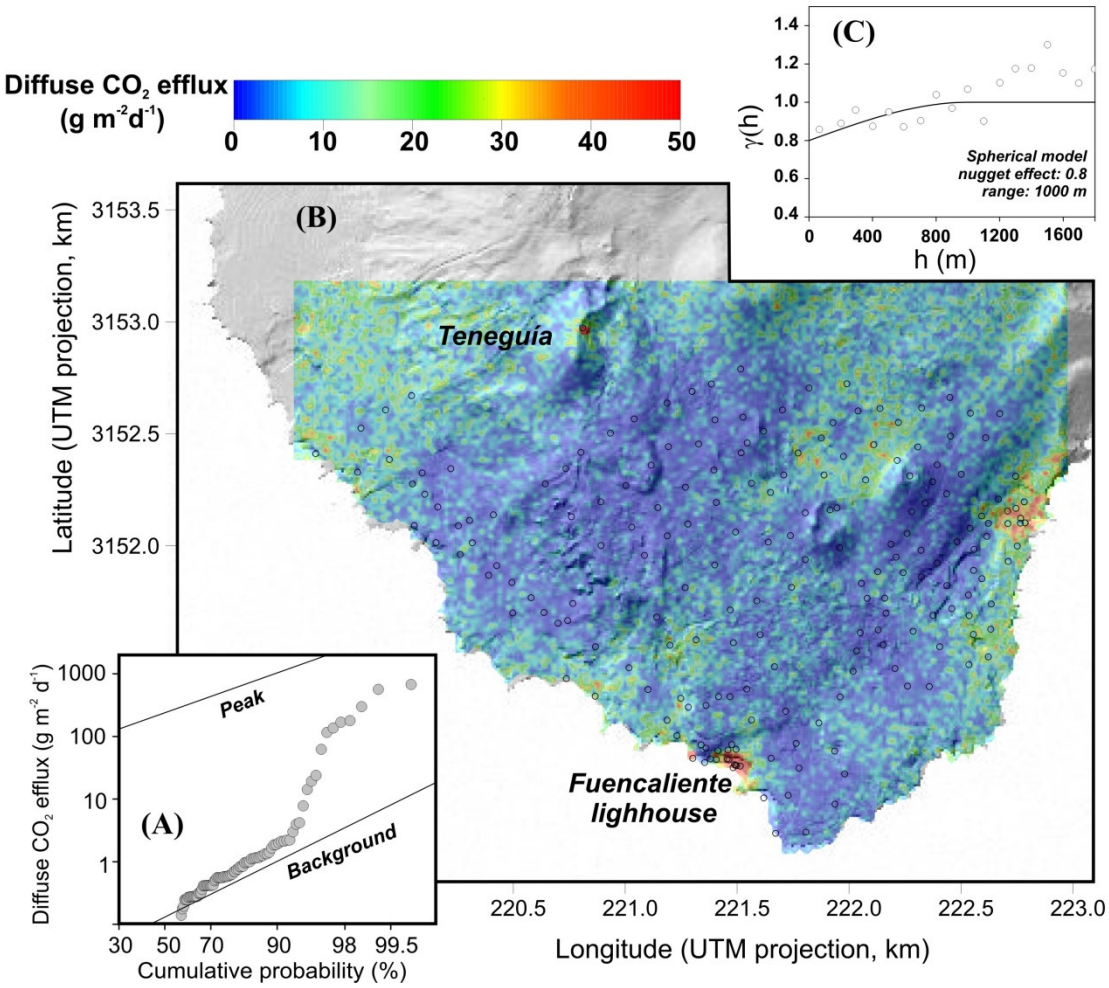

Figure 3.23. *(A) Cumulative frequency plot of diffuse CO_2 efflux data and (B) spatial distribution of diffuse CO_2 efflux from the southern part of Cumbre Vieja volcano. Open circles indicate the location of the measuring sites. (C) Experimental and the modelled variogram used by sGs to construct the spatial distribution*

The total diffuse CO_2 output in metric tons per day released from Cumbre Vieja edifice (220 km^2) for each survey computed by sGs of 24,070 cells (100 m x 100 m) are shown in Table 3.6 and plotted in Figure 3.24. The mean flux of the background populations was assumed to be a representative cut-off value with a confidence level of one standard deviation (±σ). This mean value was calculated as the 50 percentile values of the 13 probability plots, i.e. 1.7 g m^{-2} d^{-1}. Given the studied area of 220 km^2 a total CO_2 output of 374 t d^{-1} is calculated as background emission, with -1σ of 132 t d^{-1} and +1σ of 1,254 t d^{-1} (mean of the 16 and 84 percentile values of the probability plots, respectively, Sinclair 1976). If the confidence limits of the background range are increased up to 95% using ±2σ from the mean, the upper limit of the background emission would be ~1.495 t d^{-1}.

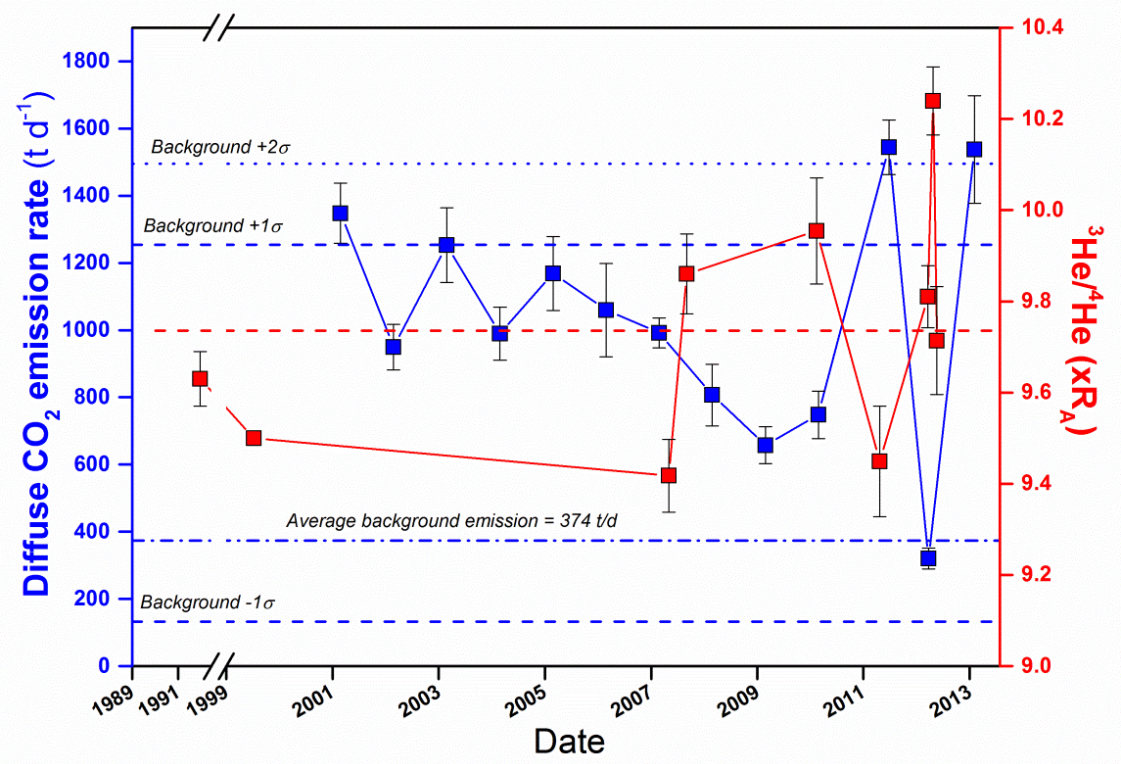

Figure 3.24. *Plot showing annual estimates of the total diffuse CO_2 output released from Cumbre Vieja volcano since 2001 (blue squares) and changes in the $^3He/^4He$ ratio measured in gas from the Dos Aguas cold spring (red squares). Red dashed line indicates the average $^3He/^4He$ ratio during the study period. Uncertainties with reported $^3He/^4He$ ratios are 1 σ, including error of the measured raw $^3He/^4He$ ratio, that of measured raw $^3He/^4He$ ratio of HESJ, and that on the recommended $^3He/^4He$ ratio of HESJ. Data from Pérez et al. (1994), Hilton et al. (2000) and Padrón et al. (2012b) are shown in their respective sampling dates: 1991, 1999 and 2010, respectively*

Compared to other diffuse CO_2 emission rates published worldwide (Burton et al. 2013), the emissions from Cumbre Vieja are some of the lowest per unit area (1.5 – 7.0 t d^{-1} km^{-2}) and support the idea that the volcano is undergoing quiescence. According to the five-stage evolutionary model proposed by Notsu et al. (2006), Cumbre Vieja is exhibiting Stage I behavior, in which plume or diffuse degassing of volcanic gas is very low because magma is present only at significant depth. Results shown in Figure 3.24 depict stable emissions around 1,100 t d^{-1} in the first five surveys, followed by a downward trend that was broken by sudden increases in emissions during 2011 and 2013. Most of the emission estimations in the study period are entirely within the range defined for background emissions. The 2011 and 2013 studies were the only surveys with mean values slightly above the background. It should be noted that in 2011, when the highest total CO_2 emission was estimated, the maximum emission value measured was the lowest and was not measured at Teneguía cinder cone, likely due to atmospheric disturbances (windy weather); however, the median diffuse emission value was the highest of all years (3.6 g m^{-2} d^{-1}, Table 3.6). Recent diffuse degassing studies carried out during a volcanic unrest period on the neighboring island of El Hierro have demonstrated that low CO_2 emission values (in the range 1-20 g m^{-2} d^{-1}) can be slightly increased by endogenous degassing (Pérez et al. 2012; Melián et al. 2014). These observations suggest that we cannot exclude the possibility that an endogenous component is responsible for this increase in the background emission values and, thus in the total emission. In the case of the detailed survey performed at the southern part of the volcano in 2005, the total CO_2 output was 51.1 ± 6 t d^{-1}, compared to the total diffuse CO_2 output from the entire volcano, which was estimated as 1,169 ± 110 t d^{-1} in 2005. We consider this amount as the main deep contribution to the total output, indicating that a maximum of ~4% of the total diffuse CO_2 output is released from a deep source at Cumbre Vieja volcano during volcanic quiescence. Figure 3.24 also shows the temporal evolution of the $^3He/^4He$ ratio measured in Dos Aguas cold spring from 1991 to 2012. Table 3.7 shows all the published $^3He/^4He$ data including the new results reported in this Ph.D. Thesis. The He isotope composition of the bubbling gas emission at Dos Aguas indicates an important mantle contribution with values ranging around an average of 9.73 R_A (red dashed line in Figure 3.24). Diffuse CO_2 increases observed in 2011 and 2013 seem to be preceded by an increase in the $^3He/^4He$ observed in Dos Aguas. Assuming that the measured $CO_2/^3He$ ratio in this cold spring is applicable for the whole island, as was suggested previously by Hilton et al. (2000), the rise in the ^3He emission would suggest corresponding increases in the deep-seated CO_2 release. Enhanced endogenous contributions were likely responsible for the higher CO_2 emission values in 2011 and 2013, with a delayed response of about one year.

***Table 3.7**. Results of the $^{3}He/^{4}He$ and $^{4}He/^{20}Ne$ ratios measured in Dos Aguas cold spring. Atm., MORB and Plume He denote the percentage of He from atmospheric, MORB and mantle plume respectively. Uncertainties with reported $^{3}He/^{4}He$ ratios are 1 sigma, including error of the measured raw $^{3}He/^{4}He$ ratio, that of measured raw $^{3}He/^{4}He$ ratio of HESJ, and that on the recommended $^{3}He/^{4}He$ ratio of HESJ. Errors on concentrations are estimated to be 10% based on reproducibility of noble gas sensitivity of the mass spectrometer during repeated air standard analyses*

Sampling date	$^{3}He/^{4}He$ (xR_A)	$^{4}He/^{20}Ne$	$^{3}He/^{4}He$ corr. (xR_A)	Atm. He (%)	MORB He (%)	Plume He (%)	$\delta\ ^{13}C\text{-}CO_2$ (‰ *versus* VPDB)	$CO_2/^{3}He$ ($x10^{10}$)
15/12/1991*	9.63±0.06	50.0	9.68±0.06	0.6	93.3	6.1	-	-
13/12/1999*	9.5	-	-	-	-	-	-	1.70
07/10/2007	9.40±0.08	119.1	9.42±0.08	0.2	94.6	5.2	-	-
07/02/2008	9.82±0.09	78.3	9.86±0.09	0.4	92.9	6.7	-	-
20/07/2010*	9.95±0.12	181.0	9.96±0.12	0.1	92.7	7.2	-3.58	0.50
28/09/2011	9.43±0.12	169.1	9.45±0.12	0.2	94.5	5.3	-3.19	0.59
24/08/2012	9.80±0.07	212.3	9.81±0.07	0.1	93.3	6.6	-	-
29/09/2012	10.04±0.07	14.9	10.24±0.07	2.1	90.0	8.0	-2.86	0.57
24/10/2012	9.70 ±0.12	215.7	9.71±0.12	0.1	93.6	6.2	-3.71	0.73

Uncertainties with reported $^{3}He/^{4}He$ ratios are 1 sigma, including error of the measured raw $^{3}He/^{4}He$, that of measured raw $^{3}He/^{4}He$ ratio of HESJ, and that on the recommended $^{3}He/^{4}He$ ratio of HESJ. Errors on concentrations are estimated to be 10 % based on reproducibility of noble gas sensitivity of the mass spectrometer during repeated air standars analyses

Atm. percentage of helium from atmospheric, *MORB* percentage of helium from MORB, *plume He* percentage of helium from mantle plume

*Data from Pérez et al. (1994), Hilton et al. (2000), Padrón et al. (2012b)

Assuming that crustal He does not significantly contribute to the observed $^{3}He/^{4}He$ ratios in Dos Aguas and following the model proposed by Sano et al. (1985) and Padrón et al. (2012b), $^{3}He/^{4}He$ ratios in Dos Aguas can be explained by a mixing model of atmospheric-type, MORB-type and plume-type He, and the fraction of He from each reservoir can be calculated following a simple mass balance. Table 3.7 summarizes the estimated amounts of atmospheric-type ($^{3}He/^{4}He = 1R_A$ and $^{4}He/^{20}Ne = 0.318$), MORB-type ($^{3}He/^{4}He = 8\ R_A$ and $^{4}He/^{20}Ne = 1000$) and plume-type ($^{3}He/^{4}He$~35 R_A and $^{4}He/^{20}Ne = 1000$) He released by Dos Aguas cold spring. The calculations reveal a small but persistent component of plume-type He, which suggests a component from the deep mantle, in accordance with the hot-spot model proposed earlier for the Canaries (Pérez et al. 1994; Carracedo et al. 1998).

To investigate the origin of the soil CO_2 at Cumbre Vieja, a binary diagram of the $\delta\ ^{13}C\text{-}CO_2$ *versus* $1/[CO_2]$ was constructed with two geochemical end-members (Figure 3.25): air, characterized by $\delta\ ^{13}C\text{-}CO_2 = -8.0$‰ and $[CO_2] = 400$ ppm and biogenic CO_2. The addition of deep-seated CO_2 (which includes mantle-derived CO_2 and metamorphism of marine carbonate rocks) would produce trends that lie along the arrows shown in Figure 3.25, towards $\delta\ ^{13}C\text{-}CO_2 > -8$ ‰ (Javoy et al. 1978; Barnes et al. 1988) and $[CO_2]$ ~ 100%.

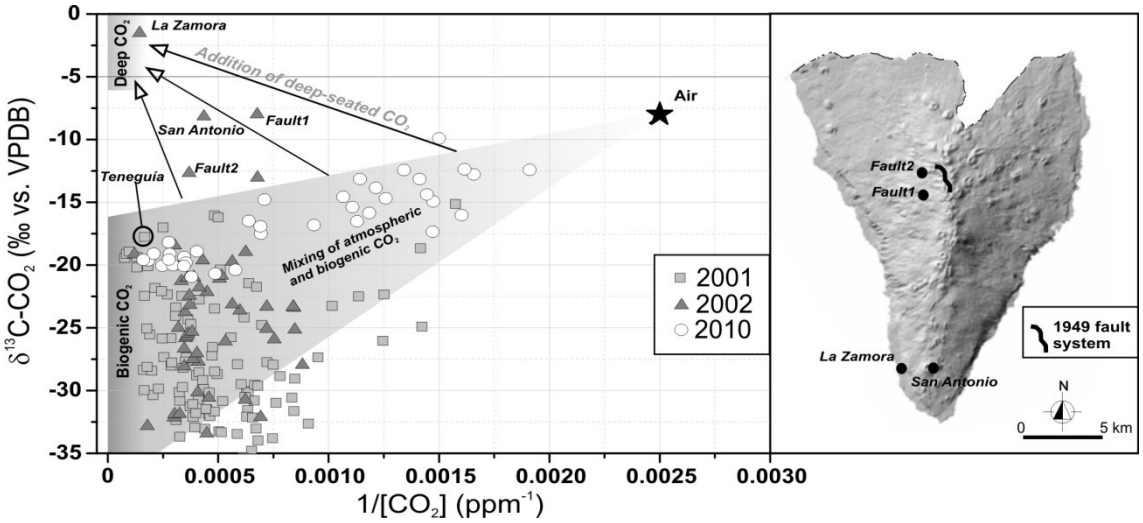

Figure 3.25. *Left: correlation diagrams between $\delta^{13}C\text{-}CO_2$ and $1/[CO_2]$ (ppm^{-1}) from the 2001, 2002 and 2010 surveys. The degraded shaded area from the atmospheric to the biogenic end-member represents samples affected by mixing of atmospheric and biogenic CO_2. The result from the soil CO_2 in Teneguía cinder cone is indicated. Right: location of the samples with the more obvious endogenous CO_2 contribution: La Zamora site, San Antonio volcano, and two sites close to the normal fault system originated in the 1949 eruption (Fault1 and Fault2; Day et al. 1999)*

Figure 3.25 indicates that most of the sampling sites contain CO_2 composed by different degrees of mixing between atmospheric and biogenic CO_2. Soil CO_2 sampled where the high flux anomaly at Teneguía cinder cone was measured (*Teneguía* in Figure 3.25), showed $\delta\ ^{13}C\text{-}CO_2$ = -17.7‰, and $[CO_2]$ = 0.17%. Due to the low $\delta\ ^{13}C\text{-}CO_2$ values the high CO_2 emissions at Teneguía cannot be explained solely on the origin of the gas and indicate an important advective (likely convective), component in the flux, because of the high soil temperature measured. The samples with the more obvious endogenous CO_2 contribution were sampled in 2002 (solid triangles plotted above the area of mixing between atmospheric and biogenic CO_2). Their location is depicted in Figure 3.25: La Zamora site, San Antonio volcano, and two sites close to the normal fault system that was formed during the 1949 eruption (Day et al. 1999), named as Fault1 and Fault2. The $\delta^{13}C\text{-}CO_2$ value of -1.5‰ at La Zamora with $[CO_2]$ = 10.1 mol.% showed the heavier isotopic composition. The isotopic composition of the CO_2 at this site can be explained by diffuse fractionation of magmatic CO_2 with an original non-fractionated value ~-5.9‰ (Cerling et al. 1991). Finally, the presence of significant enrichments in the deep component of the CO_2 in the sites close to the 1949 eruption, (-8.0 and -12.7‰) could be explained by residual emission of volatiles from source magmatic bodies, released preferentially through the fracture zone. A more detailed survey would be necessary to confirm this hypothesis. The other anomalously high CO_2 emission values observed at El Puertito and Fuencaliente lighthouse (Figure 3.21), showed values of -19.0‰ and -8.8‰, respectively, which suggests a slight deep contribution in the CO_2 emission.

In order to investigate the origin of the CO_2 released in Dos Aguas cold spring, the model proposed by Sano and Marty (1995) was used. The four gas samples from Dos Aguas plot close to the mantle end-member in the $\delta^{13}C\text{-}CO_2$ *versus* $CO_2/^3He$ diagram, along the mantle-crust (limestones) mixing trend in Figure 3.26. Using the mass balance proposed by Sano and Marty (1995), an important contribution of mantle carbon, in the range 20 – 29%, have been estimated in Dos Aguas. Similarly, we calculate ~10% mantle CO_2 for gas from La Zamora and Fuencaliente lighthouse sites. To calculate the mantle component at this site we have assumed a similar $^3He/^4He$ ratio for both, measured by Padrón et al. (2012b) in Fuencaliente lighthouse (~1.084 R_A). Under this assumption, it can be conclude that approximately 10% of the anomalous diffuse CO_2 emission observed at several sites along the southern coast of Cumbre Vieja (La Zamora, Fuancaliente lighthouse and El Puertito) are derived by mantle degassing.

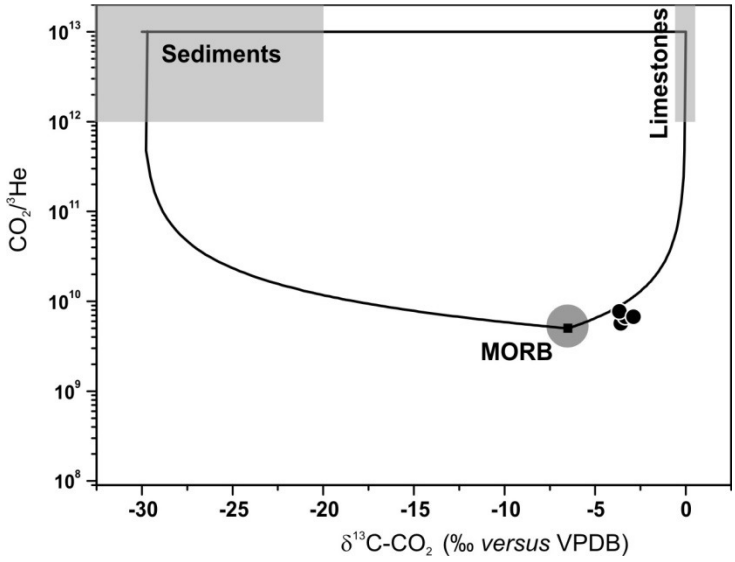

Figure 3.26. *Plot showing $CO_2/^3He$ versus $\delta^{13}C\text{-}CO_2$ for gas from the Dos Aguas spring, following the model of Sano and Marty (1995). The curves indicate sedimentary rock-mantle-marine limestone mixing relationships*

3.5. Diffusive helium emissions as a precursory sign of volcanic unrest

The recent 2011-2012 submarine eruption at El Hierro Island has offered an excellent opportunity to monitor the volcanic activity and apply novel methodologies for the detection and understanding of the eruptive process and to forecast volcanic unrest episodes. One of the most important results has been the first intensive and extensive scientific report on diffuse He degassing on an active volcano which had experienced an unrest followed by an eruption. Through this research work, which forms part of this Ph. D. Thesis, the useful of He in diffuse degassing studies on active volcanoes to forecast volcanic eruptions was tested for the first time.

A seismo-volcanic unrest began on El Hierro Island in July 2011. It was first characterized by the location of a large number of relatively small earthquakes (M<2.5) beneath El Hierro at depths between 8 and 15 km (Figure 3.27B). In mid-to-late September the seismicity migrated toward the south of the island with an increase in the earthquake magnitudes. On 10 October, 2011, a continuous tremor was clearly detected and a submarine eruption was confirmed in the afternoon of 12 October, 2011 by visual observations of a large light-green colored area off the coast of El Hierro, ~2 km south of the small village of La Restinga in the southernmost part of the island (Figure 3.27C). Since then, frequent episodes of turbulent gas emission and foaming, and steamy lava fragments were observed at the sea surface. Ibáñez et al. (2012) grouped the seismic sequence into three well separated spatial clusters and distinct earthquake regimes (Phases 1, 2 and 3 in Figure 3.27A). Phase 1 (between 1 July and 20 September, 2011) was characterized by high earthquake rates and relatively low magnitudes, reflecting the initial intrusion of magma from the upper mantle into the crust. In Phase 2 (21 September-15 October, 2011), seismicity migrated to the south with an apparent ordinary tectonic activity. The eruption occurred in this phase with a substantial lack of shallow seismicity between 8 km depth and the surface. A new burst of seismicity appeared off the northern coast of El Hierro (phase 3 in Figure 3.27A) since 16 October. The significant increase in the number and magnitude recorded during phase 3 culminated in the largest earthquake of the seismic series, a M 4.6 event on 11 November.

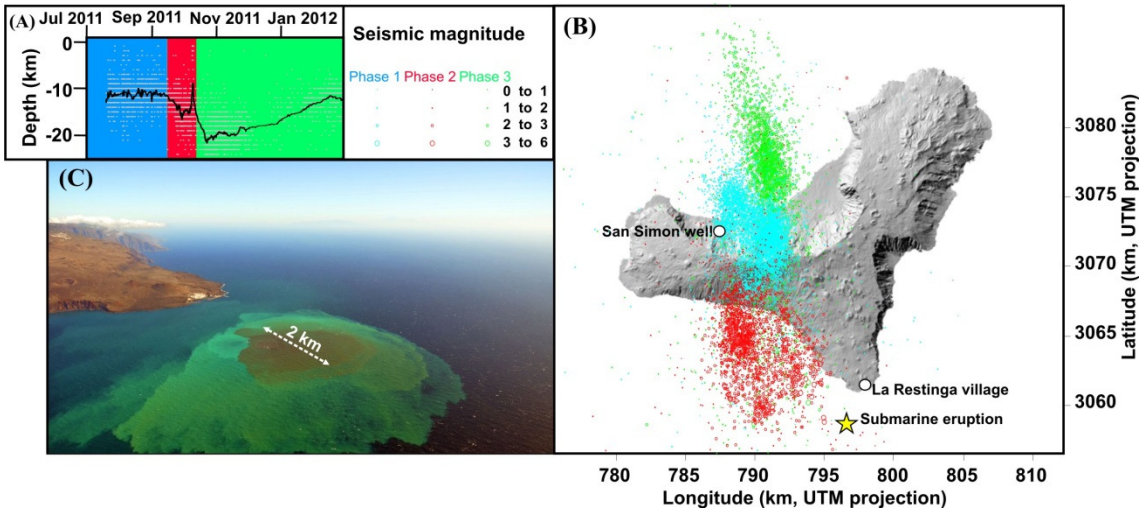

Figure 3.27. *(A) Different phases of seismicity described by Ibañez et al. (2012) are displayed in blue, red and green. Temporal evolution of hypocentral depth of earthquakes is depicted by 100-event moving average (black line). (B) Epicenter locations of 12,178 seismic events recorded until 9 February, 2012. Star indicates location of submarine eruption (UTM-Universal Transverse Mercator). (C) Water discoloration south of La Restinga produced by submarine eruption*

Tables 3.8 show the summary of the diffusive soil He emission results estimated for the entire island. Diffusive He emissions in the 2003 survey are considered as the emission rate

during a volcanic quiescence period. It amounted for 9 ± 1 kg d^{-1} for the entire area of El Hierro Island and it is depicted in Figure 3.28A as a narrow blue band in the lower part of the plot. He isotope ratios and He and Ne concentrations dissolved in San Simón groundwater are shown in Table 3.9.

Table 3.8. *Summary of the diffusive soil He emission results estimated at El Hierro Island between 1 August, 2003 and 15 January, 2012. The amount of He released by the volcanic unrest period was estimated by subtracting the background He emission (~9 kg d^{-1}) and resolving the rest to crustal and magmatic fractions based on $^3He/^4He$ ratio of San Simón water interpolated for the date when each He emission was measured, following the method described by Ballentine et al. 2002*

Survey period	He emission (kg d^{-1})	$^3He/^4He$ (R/R_A)	Crustal ^4He (%)	Magmatic ^4He (%)	Magmatic emission (kg d^{-1})	Crustal emission (kg d^{-1})
Aug 1-30, 2003	9 ± 1	-	-	-	-	-
Jul 25-Aug 4, 2011	11 ± 0.5	2.77	66	34	0.7	1.3
Aug 27- Sep 10, 2011	11 ± 0.5	2.77	66	34	0.7	1.3
Sep 11–22, 2011	24 ± 1	7.25	12	88	13.3	1.7
Sep 22-Oct 1, 2011	26 ± 1	7.43	9	91	15.4	1.6
Oct 2-10, 2011	30 ± 2	7.61	7	93	19.5	1.5
Oct 11-19, 2011	30 ± 2	7.78	5	95	19.9	1.1
Oct 20-26, 2011	13 ± 1	6.64	19	81	3.2	0.8
Oct 28-Nov 1, 2011	20 ± 1	5.64	31	69	7.6	3.4
Nov 2-8, 2011	38 ± 2	4.78	42	58	16.9	12.1
Nov 9-19, 2011	31 ± 1	6.4	22	78	17.2	4.8
Nov 20-29, 2011	19 ± 1	8.2	0	100	10	0
Nov 30-Dec 9, 2011	18 ± 1	8.13	1	99	8.9	0.1
Dec 10-17, 2011	21 ± 1	8.1	1	99	11.8	0.2
Dec 18, 2011-Jan 15, 2012	17 ± 1	8.2	0	100	8	0

Table 3.9. *Helium isotope ratios and helium and neon concentrations dissolved in San Simón groundwater, El Hierro*

Sampling date	$^3He/^4He$ (R/R_A)	$[^4He]$ (10^{-6} cm^3 STP/g)	$[^{20}Ne]$ (10^{-6} cm^3 STP/g)	$^3He/^4He$ corr.* (R/R_A)
July 28, 2011	2.826 ± 0.064	4.32	1.75	3.054 ± 0.081
August 26, 2011	2.242 ± 0.044	2.93	1.7	2.476 ± 0.065
September 16, 2011	6.70 ± 0.15	0.956	0.304	7.25 ± 0.18
October 12, 2011	6.380 ± 0.098	1.12	0.842	7.78 ± 0.28
November 5, 2011	4.225 ± 0.094	1.29	0.696	4.78 ± 0.14
November 23, 2011	7.906 ± 0.085	1.05	0.156	8.199 ± 0.099
December 19, 2011	7.53 ± 0.11	0.603	0.159	8.03 ± 0.14
January 11, 2012	7.878 ± 0.074	1.04	0.168	8.197 ± 0.090

*The air-corrected $^3He/^4He$ ratios are obtained by subtracting atmospheric ^3He and ^4He assuming all ^{20}Ne dissolved in the sample waters are of atmospheric origin and relative solubility of ^4He and ^{20}Ne into groundwater at 25°C is 0.274 (Ozima and Podosek, 2002)

Figure 3.28B shows both diffusive He emissions for the entire island and the corrected $^{3}He/^{4}He$ ratio for the dissolved gases in the San Simón waters together with the seismic energy released up 9 February, 2012. The diffusive He emission estimated in the two first surveys was 11 ± 1 kg d^{-1}, slightly higher than the background emission measured in 2003. By mid September, a drastic increase in the two geochemical parameters had been observed, several days before the beginning of a significant increase in the seismic activity on the island; He emission increased from 11 ± 1 kg d^{-1} to 24 ± 1 kg d^{-1}, and $^{3}He/^{4}He$ increased from 2.48 ± 0.07 R_A to 7.3 ± 0.2 R_A. The increase in diffusive He emissions continued over two more surveys, reaching a relative maximum of 30 ± 2 kg d^{-1} and preceding the onset of the submarine eruption. The survey in which this maximum value was measured started on 2 October and was completed two days before the onset of the submarine eruption. This emission value continued until the following survey, which finished on 19 October. The $^{3}He/^{4}He$ ratio measured in the San Simón waters sampled on 12 October also indicated a relative maximum. After the onset of the eruption, a drastic decrease in diffusive He emissions measured between 20 and 26 October was observed.

Assuming that San Simón water is an indicator of the $^{3}He/^{4}He$ ratio of deep-sourced He during the volcanic unrest period, it is possible to estimate the crustal and mantle fractions of the He released during the studied period. The amount of He released in the volcanic unrest period was estimated by subtracting the background He emission (~9 kg d^{-1}) and resolving the rest to crustal (C) and magmatic (1-C) fractions based on the $^{3}He/^{4}He$ ratio of San Simón water interpolated for the date when each He emission was measured, following the method described by Ballentine et al. 2002 (Table 3.8). Figure 3.28B depicts the evolution of the magmatic and crustal emission rate over the volcanic unrest period. The magmatic He time series began with <1 kg d^{-1} and increased to ~20 kg d^{-1} several days before the eruption onset. However, the crustal He emission remained at around 1 kg d^{-1} throughout the volcanic unrest period, except on November 2011, when it reached 12 kg d^{-1} immediately before the occurrence of the biggest earthquake of the unrest period. A visual inspection of Figure 3.29 reveals that the density of warm colors is higher prior to the eruption than at the beginning of the unrest period, indicating the increase in He emissions from 11 ± 1 to 30 ± 2 kg d^{-1}.

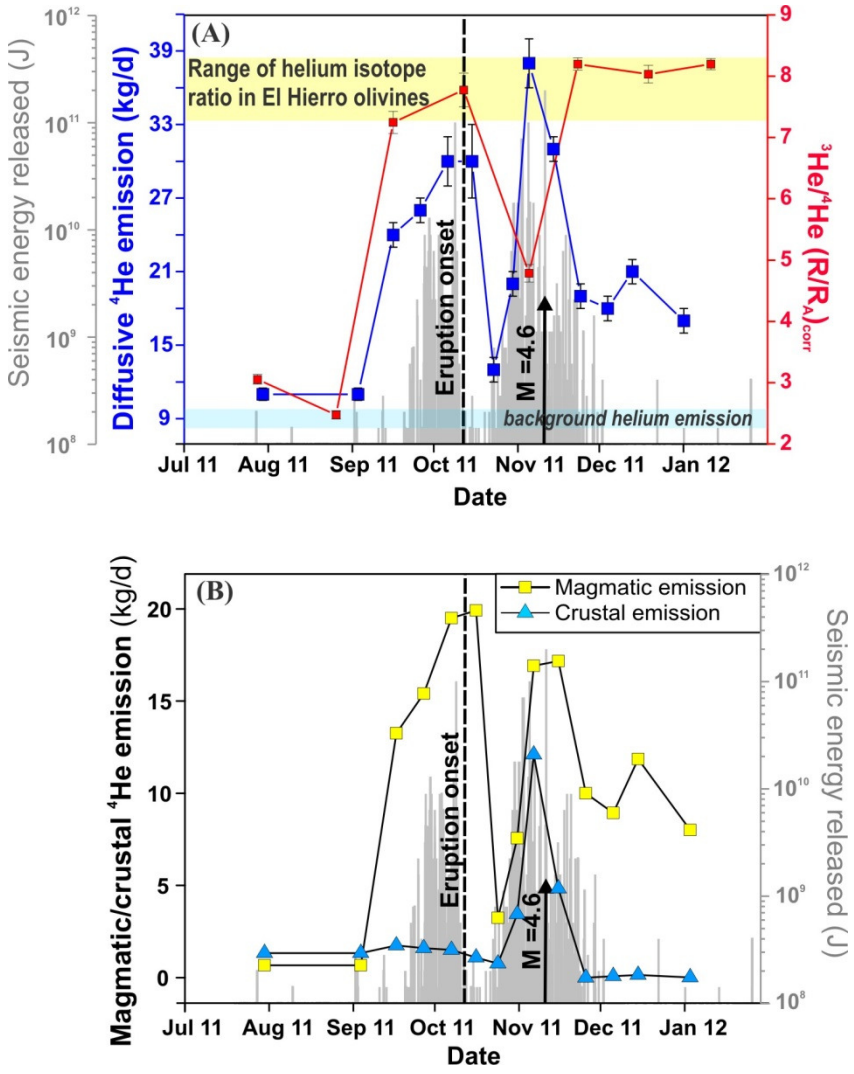

Figure 3.28. *(A) Temporal evolution of the seismic energy released (light gray), diffusive He emission at the entire island (blue squares) and air-corrected $^3He/^4He$ ratio in San Simón groundwater (red squares). R_A denotes the atmospheric $^3He/^4He$ ratio. Errors on diffusive He emission values are 1 sigma of 50 equiprobable realizations by sGs. The yellow band at the upper part represents the range of the $^3He/^4He$ ratios measured on olivine phenocrysts at El Hierro lavas, 7.2–8.2 R_A (Day and Hilton 2011). (B) Temporal evolution of the estimated magmatic (yellow squares) and crustal (blue triangles) He emission during the volcano-seismic unrest and seismic energy released (light gray bars)*

Following the submarine eruption, the third phase of seismicity started (Figure 3.27A). In this stage, both the temporal evolution of He emissions and the $^3He/^4He$ ratio displayed opposite behaviors; an increase in the diffusive He emission, reaching the absolute maximum of the series (38 ± 2 kg d^{-1}) on the survey performed between 2 and 8 November, and the $^3He/^4He$ ratio in the San Simón well groundwaters decreased to 4.8 ± 0.1 R_A in the dissolved gases sampled on 5 November. In Figure 3.29C the density of warm colors is the maximum observed on El Hierro during the survey period between 2 and 8 November. The He emission anomalies in Figure 3.29C are located mainly in the north of the island, in good agreement with the location of the earthquake epicenters during the sampling period. In the following two surveys (performed on 9–19 November and 20–29 November), the He emissions dropped to

19 ± 1 kg d^{-1} and fluctuated around this value until the last survey, showing excellent agreement with the seismic energy released (Figure 3.28A). Conversely, the $^{3}He/^{4}He$ ratio measured in the San Simón groundwaters increased to the maximum values measured in the study period and showed a value similar to the maximum $^{3}He/^{4}He$ ratio measured in phenocrysts from El Hierro lavas, i.e., ~8.2 R_A (Day and Hilton 2011).

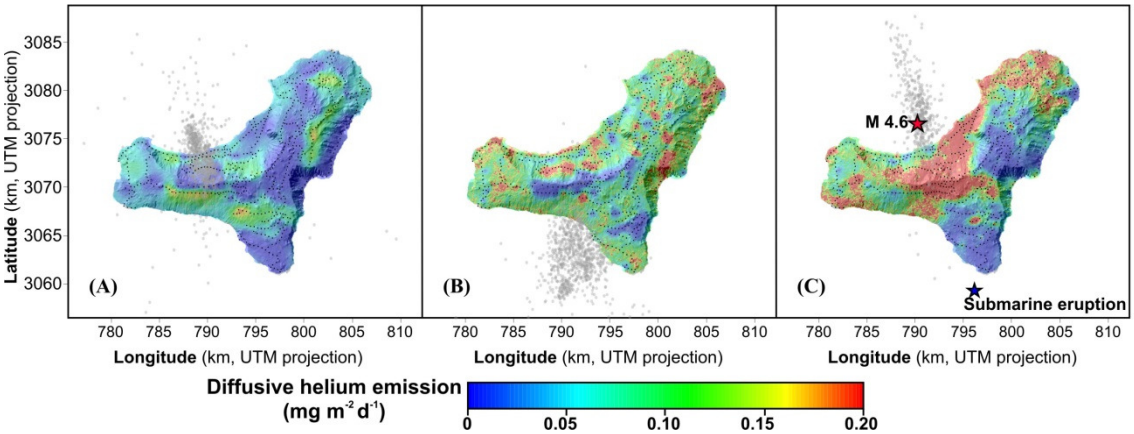

Figure 3.29. *Spatial distribution of the diffusive He emission values measured in the first 2011 survey, 25 July –4 August, 2011 (A), immediately before the occurrence of the submarine eruption, 2–10 October, 2011 (B) and immediately before the occurrence of the biggest earthquake of the seismo-volcanic unrest period (M 4.6, red star), 2–8 November, 2011, (C). The seismicity in the sampling period is indicated by light gray dots and the sampling sites are indicated by black dots. Blue star indicates the location of the submarine eruption. UTM—Universal Transverse Mercator*

At the beginning of the seismo-volcanic unrest period, magma movement beneath El Hierro Island generated new fracture and microfracture systems, allowing volcanic gases to travel to the surface. He could easily ascend from deep areas through structures of high vertical permeability, thereby enhancing the He content of soil gases. This fact was confirmed by an increase in the amount of mantle-derived gases dissolved in the San Simón waters exhibited by the $^{3}He/^{4}He$ ratio. The increases in the diffusive He emission values over the entire island preceded episodes of seismic energy release. Similar results were observed by continuous monitoring of diffuse CO_2 and H_2S emissions by using two different geochemical stations (Pérez et al. 2012). The onset of the submarine eruption produced a sudden release of volcanic gases, and consequently, a decrease in the volcanic gas pressure of the magma bodies moving beneath the island, which was reflected by a drastic decrease in the diffusive He emissions measured between 20 and 26 October, 2011. Seismicity in the third phase was more energetic and was preceded by the highest diffusive He emission value measured in the study period, between 2 and 8 November, 2011. Crustal deformation and fracturing in this phase enhanced the release of radiogenic He produced in the crust and caused a decrease in the $^{3}He/^{4}He$ measured at San Simón well groundwaters (Figure 3.28). The $^{3}He/^{4}He$ ratio seemed to have reached a peak around 8.2 R_A, which indicates a significant mantle-derived contribution to the

dissolved gases in the San Simón groundwaters, and diffusive He emission values, around 17–21 kg d^{-1}, are still over the estimated background.

3.6. Magma emission rates from shallow submarine eruptions using airborne thermal imaging

The second work relative to the submarine eruption of El Hierro during 2011-2012 will described here. This work represents the first estimate of lava volume spread over the sea bottom based on thermal data collected from a helicopter. The thermal data reported in this Ph.D. Thesis, together with seismicity and visual observations, have allowed us to reconstruct the temporal evolution of the eruption and to estimate the total magma volume emitted during the submarine eruption.

Erupted magma volumes were calculated from 18 October 2011 (just a few days after the appearance of the discoloured area on the sea surface on 12 October, 2011) to 28 February 2012, by means of thermal imaging of a brown patch of warm seawater observed in front of La Restinga (Figure 3.30). During this period, a total of 21 thermal surveys were carried out. Maximum sea water temperatures within the discoloured area ranged from 18.6ºC to 30.9ºC, compared with a sea surface temperature of 18-20°C outside the eruption site. Maximum apparent temperatures obtained from thermal images of the sea surface showed interesting changes during the period of observation. Eruptive activity between 5 and 10 November 2011 coincided with the occurrence of (i) large explosive "bubbles" at the sea surface, some potentially as high as 25 m on November 5, and (ii) the largest earthquake (M = 4.6) on November 11 (Ibáñez et al. 2012). This activity caused a sudden increase in the maximum apparent temperature measured at the sea surface, which reached its peak on November 5 (Figure 3.31). Apparent temperature differences between the sea water within and outside the discoloured area ranged from 1.5ºC to 9.1ºC, with a maximum observed on November 7, 2011, indicating a larger discharge of magma and hydrothermal fluids, accompanied by a marked increase in visible explosive activity at the sea surface. Apparent maximum temperatures dropped after November 8, reaching nearly stable values afterwards until mid-January 2012. This increase occurred simultaneously with a change in the seismic activity pattern (Ibáñez et al. 2012), and was marked by stronger explosive activity revealed by a greater amount of floating balloons on the sea surface.

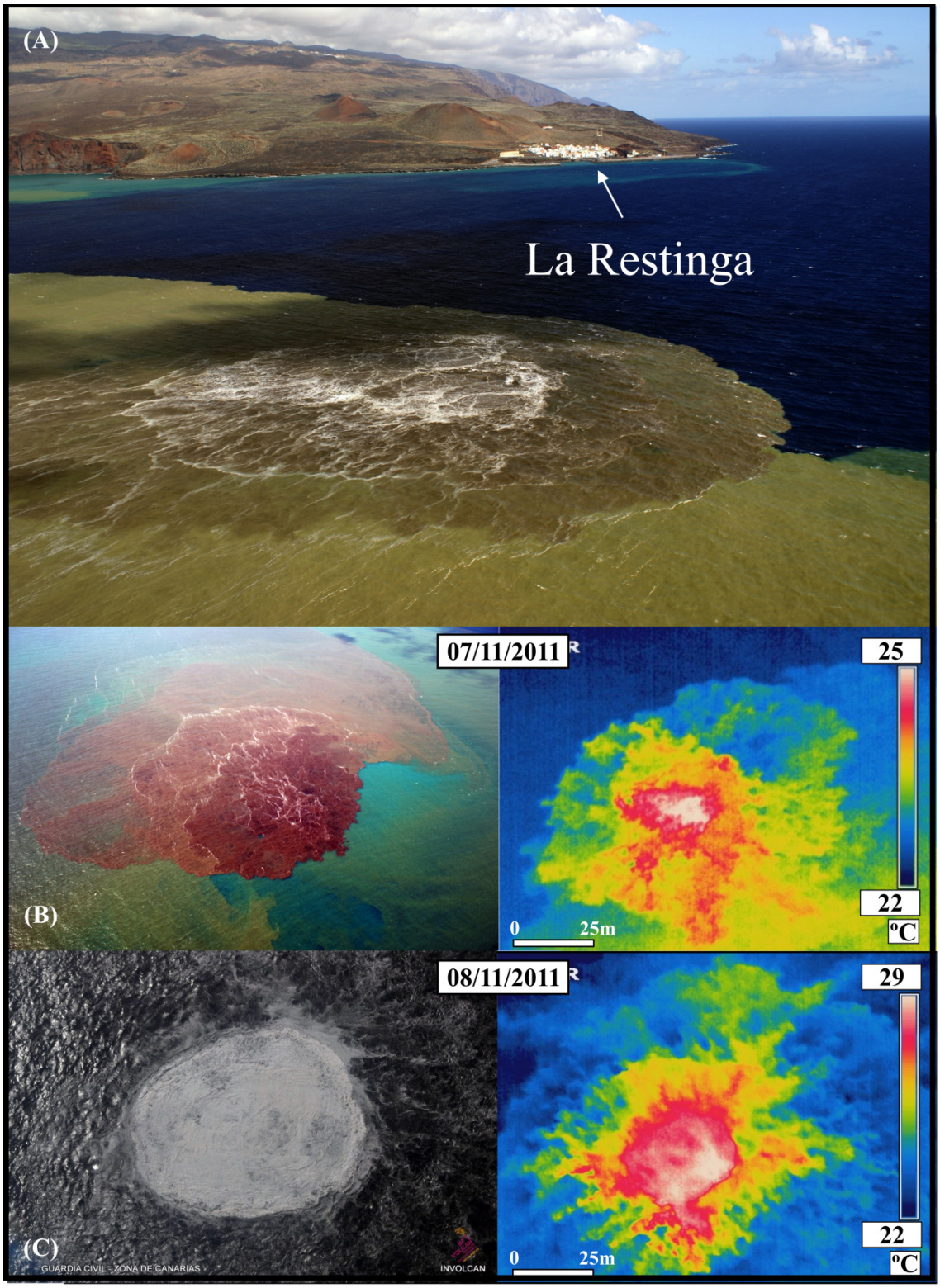

Figure 3.30. *(A) Aerial picture of the discoloured sea water surface where submarine eruption occurred; (B) thermal infrared image of the discoloured seawater area over the eruption site taken on November 7, 2011; (C) thermal infrared image of the discoloured seawater area over the eruption site taken on November 8, 2011*

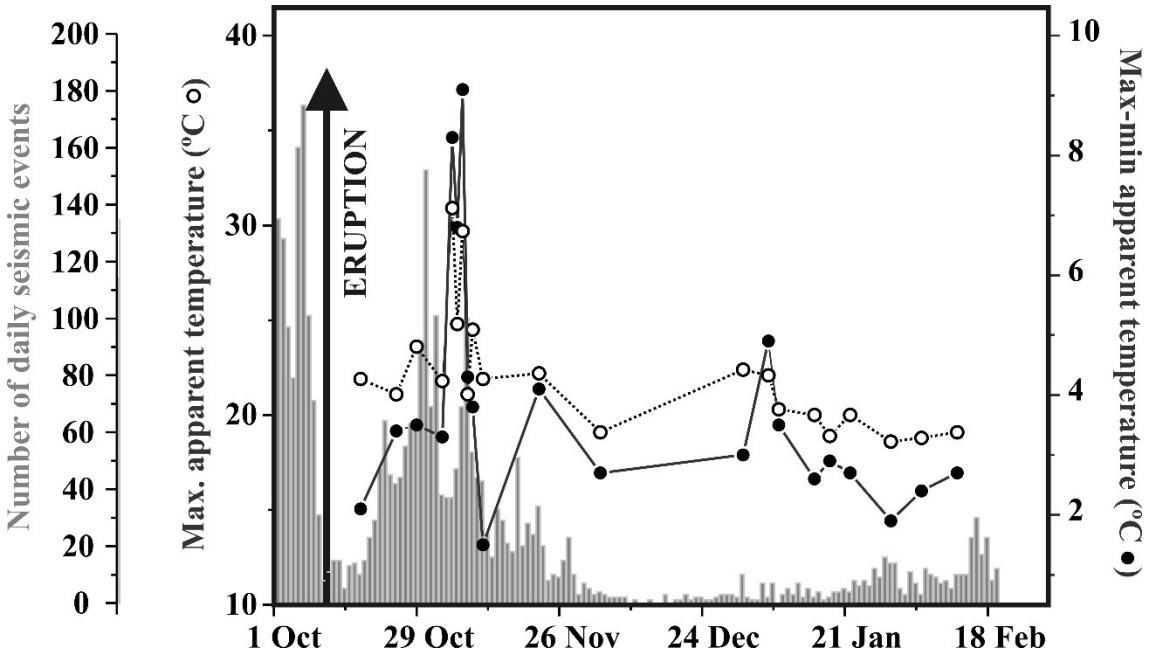

Figure 3.31. *Temporal evolution of maximum apparent temperatures (open circles) and difference between maximum and minimum apparent temperatures (black circles) measured at the seawater surface. Daily seismic events are indicated with light grey bars (source Instituto Geográfico Nacional-IGN)*

To estimate the erupted volume of lava flow and pyroclastic, we measured the surface area of heated seawater, depth of the submarine volcanic cone (lava effusion spot) and temperature of seawater not affected by the eruption. For the 21 thermal infrared surveys, pixels containing temperatures that exceeded normal seawater temperatures were selected, allowing us to calculate the area of anomalous heating. After computing total seawater volumes and depths of the submarine volcanic cone, Equation 2.13 (methodology section 2.5) was used to estimate the daily erupted volumes.

Figure 3.32 shows the estimated erupted volumes for the 21 thermal surveys. The plotted values are just single estimates obtained during each survey, and do not represent the total emitted magma volume. In order to reconstruct the submarine eruptive thermal behavior and estimate the total erupted volume, a graphical interpolation was done between each survey, to obtain the cumulative erupted magma volume (black line in Figure 3.32). On this basis we obtained a total erupted volume of lava flows and pyroclastic of 300×10^6 m^3 during the period of study (18 October, 2011-12 February, 2012), resulting in a Time Averaged Discharge Rate (TADR) of ~25 m^3 s^{-1}. This volume, although roughly estimated, is very close to the total accumulated volume of 329×10^6 non–dense rock equivalent m^3 estimated by the Spanish Oceanographic Institute (IEO) using bathymetric surveys (Rivera et al. 2013). These similar volume estimations suggest that the lava flows erupted during the submarine eruption at El Hierro were very fluids due to their composition and most of the heat released was used to heat the surrounding seawater (Hon et al. 1994; Applegarth et al. 2010). However, this averaged

TADR value is not representative of the effusion rate during the eruption. Effusion rates usually vary during the course of most basaltic eruptions. The eruption rate (when calculated for the entire eruptive episode) will be unrepresentative of the effusion rate at most times during the eruption (Wright et al. 2001). It is well known that the explosivity of magma is largely caused by the exsolution of dissolved volatiles, and hence volatile exsolution is an important means for increasing the rate of magma emission. During the submarine eruption at El Hierro a sharp increase of the magma effusion rate was registered a few days after the onset of the eruption. As magma moves to the surface, it expends energy on opening cracks by forcing intrusions, cooling and increasing viscosity. Assuming that the upper extremities of the cracks are probably filled with exsolved gases rather than cohesive magma, these gases did not have sufficient heat content to raise the temperature of the host rock very much and although the eruption had begun the upward velocity was inhibited by heat loss to the walls (Wadge 1981). For this reason, the effusion rate increases as the initially cold walls of the conduit approach thermal equilibrium with the magma flux (Applegarth et al. 2010). In other words, waning flow is usually the dominant part of a basaltic eruption, and reflects the steady release of stored energy from the volcanic system as a whole.

Figure 3.32 displays two mean peaks in the curve of the erupted volume. The first peak was recorded at the start of the survey on October 18, six days after eruption onset and due to the intense explosive activity during the early stages of the eruption; with a maximum of ~152×10^6 m^3 erupted magma averaged over 24 hours on October 19, 2011. The thermal measurement reached a climax between 5 and 7 November 2011, corresponding to a maximum of ~656×10^6 m^3 erupted magma averaged over 24 hours on November 7, 2011. This output is much smaller than that reported for Mauna Loa (Hawaii, USA) eruptions (Wadge 1981), similar to subaerial basaltic eruptions of Kilauea (Hawaii, USA; Wright et al. 2001), Etna (Italy; Wadge 1981; Calvari et al. 2003), Iceland (Thordarson and Larsen 2007), the East Pacific Rise (Sinton et al. 2002) and the Galapagos Spreading Center (Colman et al. 2012), and Tolbachik (Russia; http://en.ria.ru/russia/20121211/178066660.html) volcanoes, and extremely large if compared to Stromboli and other Etna volcanic eruptions (Italy; Kilburn et al. 1988; Calvari et al. 2005; Calvari et al. 2010; Harris et al. 2011). The maximum erupted magma volume is very close to the peak volcanic tremor, suggesting that it was produced by both strong explosive activity, building up a submarine cinder cone, and vigorous lava output, typically recorded during the initial phases of fissure eruptions (Kilburn et al. 1988; Calvari et al. 2005; Calvari et al. 2010; Harris et al. 2011). A third smaller peak was recorded on January 7, 2012 that corresponds to a volume of 2.6×10^6 m^3 averaged over the 24 hours. Direct observations of the sea surface suggest that significant explosive activity was occurring at the eruption vents. Given that the third peak in erupted magma volume at El Hierro occurred after two months of eruption, we consider feasible the possibility of a small batch of gas-rich magma entering the system as reliable.

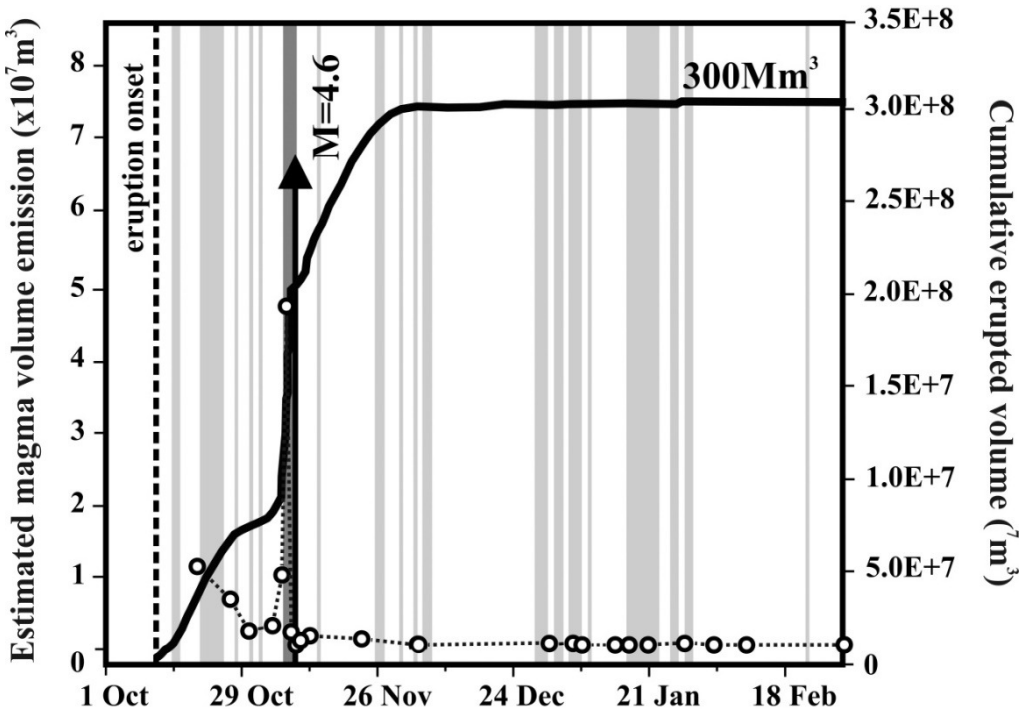

Figure 3.32. *Temporal evolution of estimated magma volume emission (white circles) and cumulative erupted volume (solid black line) during the period of study. Light grey bars indicate formation of a patch with brown color and floating rocks. The dark grey bar indicates the days with stronger eruptive activity (bubbling columns at the sea surface)*

Conclusions

4. Conclusions

The methods presented here have provided extremely useful and relatively economical information for the location of geothermal resources. The results helped to define the most appropriate areas that are susceptible of more detailed research to minimize the uncertainty for the location of a future exploratory drilling. The presence of relative anomalous concentrations of non-reactive and/or highly mobile gases in the soil gas atmosphere such as He and H_2, suggest the current existence of a significant input of deep-seated gases in the five mining licenses studied. The spatial distribution maps of the five study areas confirm in some cases the existence of a good spatial correlation between anomalous concentrations values of soil ΔHe and H_2 and historic and/or recent volcanic alignments, which could act as preferential zones of vertical permeability allowing migration of deep source gases. Combining the overall information shown in this work, based on statistical-graphical analysis of the data, visual inspection of the spatial distribution and analysis of interesting chemical ratios in the soil gas, is possible to obtain weighting tools to sort the five different study areas in terms of their relative potential of finding geothermal resources. In this context, *Garehagua* and *Abeque* mining licenses (corresponding with the southern and western volcanic-rift of Tenerife, respectively) seemed to show the highest geothermal potential of the five mining licenses studied. Additional geochemical and geophysical studies would be necessary to reduce the uncertainty inherent to the selection of the area with the highest success in future exploration works.

Soil gas surveys in *Garehagua* mining license provided useful information about the mechanisms of uprising of deep-seated gases and helped finding vertical permeability structures that favour leakage of endogenous gases from the volcano-geothermal system. Three different spatial clusters in the highest values of soil gas He, H_2 and ^{222}Rn were observed in the study area. Two of them were located along the main volcano-tectonic structural trend of the study area which is mainly N-S-directed. The uneven spatial distribution of the highest values of the soil gas species investigated in *Garehagua* reflects a complex pattern of volcano-tectonic structures, where wide fracture zones are cut by transversal faults. A 3-D resistivity model showed a geoelectrical distribution typical of a high-temperature geothermal system with a low resistivity layer, interpreted as an impermeable clay cap. An inverse correlation between the thickness of this clay alteration cap and enrichments of non-reactive gases as He, suggests the presence of permeability discontinuities in the study area since the uprising of volcano-geothermal gases towards the surface is less hindered where lower thickness of the clay alteration cap is present. The deeper limit of the clay cap was located roughly at 1,500 meters depth, which suggests that an exploratory drilling to reach the upper part of the geothermal system should be about 2,000 m deep, because the clay cap there seems to be the thinnest.

The chemical composition of the soil gases measured in the surface environment of Timanfaya volcano shows a strong atmospheric component, slightly enriched in CO_2 and He. The isotopic composition of the soil CO_2 and the existence of a peak population in soil CO_2 data suggest a very slight, but deep, contribution of the Timanfaya volcanic system in the soil gas composition. No significant spatial correlation between the main eruptive fissures and the location of soil ^{222}Rn, $^{222}Rn/^{220}Rn$ and CO_2 anomalies was observed, with the most important anomalies being located at the eastern part of the study area and at the NW of Caldera Blanca volcano. The most plausible explanation for the absence of anomalies of these gases along the eruptive fissure is the capping nature of the extensive lava flow fields of the 1730–36. He enrichments in Timanfaya soil gases is released from the cooling intrusive magma body located at 4±1 km depth, and a shallow degassing of crustal He cannot be ruled out. The main soil ΔHe anomalies were observed in the area of the main eruptive fissures of the 1730–36 eruption, with the highest values located where the highest density of vents from recent eruptive centers are situated. This indicates an important structural control for the leakage of He at Timanfaya volcano, as the eruptive fissure zones have an enhanced permeability for deep gas migration and preferential routes for degassing. Unlike CO_2 and radon, the geochemical properties of He allow this gas to escape preferentially through the vertical permeability structures of Timanfaya volcano. Atmospheric air slightly polluted by deep-seated He emissions, CO_2 degassed from a cooling magma body, and biogenic CO_2, might be the most plausible explanation for the existence of soil gas, as presented in this work. He is a deep-seated gas, exhibiting important emission rates along the main eruptive fissure of the 1730–36 eruption of Timanfaya volcano. The presence of deep He and CO_2 make the main eruptive fissure of the 1730–36 eruption of Timanfaya volcano an ideal site for volcano monitoring.

In the case of Cumbre Vieja volcano, diffuse CO_2 emissions and the isotopic composition of the soil CO_2 indicate the presence of different CO_2 sources that contribute to the release of this gas. Biological processes such as degradation of organic matter are the main source of CO_2 at Cumbre Vieja with a slight contribution of deep-seated CO_2. The results suggest that this endogenous CO_2 is released diffusively at several sites along the southern coast of the volcano. At these sites, an important component of mantle CO_2 (~10%) is present. The southern part of Cumbre Vieja release the main deep-seated fraction of the CO_2 released through soils. This fraction amounted to around 51 t d^{-1}. This amount indicates that only ~4% of the total diffuse CO_2 output should be considered to be released from a deep source during volcanic quiescence periods. Significant increases in the CO_2 emission rate from Cumbre Vieja were observed in 2011 and 2013, which might be related to inputs of deep-seated CO_2 as observed by important increases in the magmatic component of He measured in Dos Aguas cold spring, one year before the high CO_2 emission rates estimated. The CO_2-rich Dos Aguas cold spring shows

~25% of CO_2 derived directly form mantle degassing, and represents an important site to monitor changes in the volcanic activity of Cumbre Vieja. The spatial distribution of diffuse CO_2 efflux from Cumbre Vieja volcano showed that relatively high values were measured at the northern end of Cumbre Vieja, and at both sides of the N-S volcanic rift, in areas characterized by wet climate and a strong development of vegetation. The maximum diffuse emission values were repeatedly measured in the summit of Teneguía cinder cone, where the last eruption took place at Cumbre Vieja. Enhanced endogenous contributions of deep-seated CO_2 might have been responsible for the higher CO_2 emission values in 2011 and 2013, that likely occurred with a delayed response of about one year. The observed secular variations on the total output of diffuse CO_2 emission observed in the rest of the surveys do not seem to be related with physical-chemical changes on the volcanic system of Cumbre Vieja and might be controlled by meteorological conditions, which can affect strongly to the CO_2 concentrations and, in consequence, its fluxes (Maljanen et al. 2002), as has been observed in other volcanic areas (Viveiros et al. 2008; Hernández et al. 2012).

Diffusive He emission results observed at El Hierro Island demonstrate that higher He emission rates and isotopic composition preceded the recent 2011–2012 El Hierro submarine eruption. The significant changes in the diffuse He flux of the entire island and the simultaneous change in $^3He/^4He$ in groundwater are consistent with pressure build up (and leakage to the surface) of magmatic gas characterized by a high $^3He/^4He$ ratio. The patterns of He release and correlations with seismic energy provide significant insight on the build up and release of subterranean gas pressure, migration of fracture-controlled gas release, and precursory potential of inert gases, such as He, particularly regarding the timing of gas release with respect to the onset of seismic activity. The results clearly show the critical role that He can play in the prediction of major volcanic events and the importance of continuous monitoring of this gas in active volcanic regions, mainly when magma migrates aseismically, i.e., silently, toward the surface. High volcanic-gas pressure in a magma surrounded by a less deformed and fractured crust could be responsible for the high magmatic-He emission rate and eventual submarine eruption during the first two phases of seismic activity, whereas the third phase causing extensive crustal deformation and fracturing resulted in a low gas pressure on the magma and relatively low magmatic-He emission rates. Gases being exsolved from the magmatic melts through fractures and vertical permeability structures generated overpressures sufficient to fracture rocks surrounding the magma reaching the surface prior to trigger the failure of the rock.

Thermal data collected using a hand-held thermal camera during daily helicopter flights, together with seismicity and visual observations, have allowed to reconstruct the temporal evolution of the eruption and to estimate the total magma volume emitted during the submarine

eruption. Aerial thermal images have proven to be an easy method to use, efficient and reliable in producing results during a volcanic crisis, and relatively inexpensive when compared to bathymetric surveys. In addition, the TADR results obtained by thermal imagery allowed us to keep the El Hierro submarine eruption constantly monitored. This technique produced regular estimates of erupted magma that, although interpolated for the days when surveys were missing, gave a total erupted volume within 9% of that obtained by bathymetric surveys.

Bibliography

5. Bibliography

Allard P, Carbonelle J, Dajlevic D, Le Bronec J, Morel, P, Robe MC, Maurenas JM, Faivre-Pierret R, Martins D, Sabroux JC, Zettwoog P (1991) Eruptive and diffuse emissions of CO_2 from Mount Edna. Nature 351:387–391

Allard P (1992) Diffuse degassing of carbon dioxide through volcanic systems: observed facts and implications. In: Hedenquist, J W. (Ed). Magmatic contributions to hydrothermal systems and the behavior of volatiles in magma. Geological Survey of Japan, Report Nº 279

Aizawa K, Ogawa Y, Ishido T (2009) Groundwater flow and hydrothermal systems within volcanic edifices: Delineation by electric selfpotential and magnetotellurics. J Geophys Res 114: B01208, doi:10.1029/2008JB005910

Albert-Beltrán JF, Araña V, Diez JL, Valentín A (1990) Physical-chemical conditions of the Teide volcanic system (Tenerife, Canary Islands). J Volcanol Geotherm Res 43:321–332. doi: 10.1016/0377-0273(90)90059-O

Andronico D, Lodato L (2005) Effusive activity at Mount Etna Volcano (Italy) during the 20th Century: a contribution to volcanic hazard assessment. Nat Hazards 36:407-443

Anguita F, García-Cacho L, Colombo F, González-Camacho A, Vieira R (1991) Roque Nublo caldera: a new stratocone caldera in Gran Canaria, Canary Islands. J Volcanol Geotherm Res 47:45–63. doi: 10.1016/0377-0273(91)90100-E

Arpa MC, Hernández PA, Padrón E, Reniva P, Padilla GD, Bariso E, Melián GV, Barrancos J, Nolasco D, Calvo D, Pérez NM, Solidum RU (2013) Geochemical evidence of magma intrusion inferred from diffuse CO_2 emissions and fumarole plume chemistry: the 2010-2011 volcanic unrest at Taal volcano, Philippines. Bull Volcanol 75:747. doi:10.1007/s00445-013-0747-9

Applegarth LJ, Pinkerton H, James MR, Calvari S (2010) Lava flow superposition: the reactivation of flow units in compound flow fields. J Volcanol Geotherm Res 194:100-106

Ballentine CJ, Burgess R, Marty B (2002) Tracing fluid origin, transport and interaction in the crust: Reviews in Mineralogy and Geochemistry 47:539–614. doi:10.2138/rmg.2002.47.13

Barberi F, Carapezza ML, Cioni R, Lelli M, Menichini M, Ranaldi M, Ricci T, Tarchini L (2013) New geochemical investigations in Platanares and Azacualpa geothermal sites (Honduras). J Volcanol Geotherm Res 257:113–134. doi: 10.1016/j.jvolgeores.2013.03.011

Barnes I, Evans WC, White D (1988) The role of mantle CO_2 in volcanism. Appl Geochem 3:281–285

Baubron JC, Allard P, Toutain, JP (1990) Diffuse volcanic emissions of carbon dioxide from Vulcano Island, (Italy). Nature 344:51–53

Bertrami R, Buonasorte G, Ceccarelli A, Lombardi S, Pieri S, Scandiffio G (1990) Soil gases in geothermal prospecting: Two case histories (Sabatini Volcanoes and Alban Hills, Latium, Central Italy). J Geophys Res 95:21475. doi: 10.1029/JB095iB13p21475

Burton MR, Sawyer GM, Granieri D (2013) Deep carbon emission from volcanoes. Rev Mineral Geochem 75:323–354

Calvari S, Neri M, Pinkerton H (2003) Effusion rate estimations during the 1999 summit eruption on Mt Etna, and growth of two distinct lava flow fields. J Volcanol Geotherm Res 119, 107-123

Calvari S, Spampinato L, Lodato L, Harris AJL, Patrick MR, Dehn, J, Burton MR, Andronico D (2005) Chronology and complex volcanic processes during the 2002–2003 flank eruption at Stromboli volcano (Italy) reconstructed from direct observations and surveys with a handheld thermal camera. J Geophys Res 110:B02201

Calvari S, Lodato L, Steffke A, Cristaldi A, Harris AJL, Spampinato, L, Boschi E (2010) The 2007 Stromboli flank eruption: chronology of the events, and effusion rate measurements from thermal images and satellite data. J Geophys Res 115(B4):B04201

Carapezza ML, Barberi F, Tarchini L, Ranaldi M, Ricci T (2009) Volcanic hazard of Colli Albani. Monograph on "The Colli Albani Volcano", Special Publications of IAVCEI, 3:279–297. Geological Society, London

Cardellini C, Chiodini G, Frondini F (2003a) Application of stochastic simulation to CO_2 flux from soil: mapping and quantification of gas release. J Geophys Res 108:2425. doi:10.1029/2002JB002165

Cardellini C, Chiodini G, Frondini F, Granieri D, Lewicki J, Peruzzi L (2003b) Accumulation chamber measurements of methane fluxes: application to volcanic-geothermal areas and landfills. Appl Geochemistry 18:45–54. doi: 10.1016/S0883-2927(02)00091-4

Carracedo JC, Rodríguez-Badiola E, Soler V (1992) The 1730-1736 eruption of Lanzarote, Canary Islands: a long, high-magnitude basaltic fissure eruption. J Volcanol Geotherm Res 53:239-250

Carracedo JC, Day S, Guillou H, Rodríguez-Badiola E, Canas JA, Pérez-Torrado FJ (1998) Hotspot volcanism close to a passive continental margin: the Canary Islands. Geol Mag 135:591–604

Cerling TE, Solomon DK, Quade J, Bowman JR (1991) On the isotopic composition of carbon in soil carbon dioxide. Geochim Cosmochim Acta 55:3403–3405. doi:10.1016/0016-7037(91)90498-T

Chiodini G, Frondini F, Raco B (1996) Diffuse emission of CO_2 from the Fossa crater, Vulcano Island (Italy). Bull Volcanol 58:41–50

Chiodini G, Marini L (1998) Hydrothermal gas equilibria: the H_2O-H_2-CO_2-CO-CH_4 system. Geochim Cosmochim Acta 62:2673–2687. doi: 10.1016/S0016-7037(98)00181-1

Chiodini G, Frondini F, Cardellini C, Granieri D, Marini L, Ventura G (2001) CO_2 degassing and energy release at Solfatara volcano, Campi Flegrei, Italy. J Geophys Res 106(B8):16213-16221

Chiodini G, Baldini A, Barberi F, Carapezza ML, Cardellini C, Frondini F, Granieri D, Ranaldi M (2007) Carbon dioxide degassing at Latera caldera (Italy): Evidence of geothermal reservoir and evaluation of its potential energy. J Geophys Res 112:B12204. doi: 10.1029/2006JB004896

Chiodini G, Caliro S, Cardellini C, Avino R, Granieri D and Schmidt A (2008) Carbon isotopic composition of soil CO_2 efflux, a poweful method to discriminated different sources feeding soil CO_2 degassing in volcanic-hydrothermal areas. Earth and Planet Sci Lett 274:372-379. doi: 10.1016/j.epsl.2008.07.051

Ciotoli G, Lombardi S, Morandi S, Zarlenga F (2004) A multidisciplinary, statistical approach to study the relationships between helium leakage and neotectonic activity in a gas province: The Vasto basin, Abruzzo-Molise (central Italy). Am Assoc Pet Geol Bull 88:355–372

Clarke WB, Jenkins WJ, Top Z (1976) Determination of tritium by mass spectrometric measurement of ^{3}He. Int J Appl Radiat Isot 27:515–522. doi: 10.1016/0020-708X(76)90082-X

Colman A, Sinton JM, White SM, McClinton JT, Bowles JA, Rubin KH, Behn MD, Cushman B, Eason DE, Gregg TKP, Gronvold K, Hidalgo S, Howell J, Neill O, Russo C (2012) Effects of variable magma supply on mid-ocean ridge eruptions: Constraints from mapped lava flow fields along the Galápagos Spreading Center. Geochem Geophys Geosyst 13:Q08014. doi:10.1029/2012GC004163

Craig H (1953) The geochemistry of the stable carbon isotope. Geochim Cosmohim Acta 3:53–92. doi:10.1016/0016-7037(53)90001-5

Craig H, Lupton JE (1976) Primordial neon, helium and hydrogen in oceanic basalts. Earth Planet Sci Lett 31:369-385

Craig H, Lupton JE, Horibe Y (1978) A mantle helium component in circum Pacific volcanic gases: Hakone, the Marianas, and Mt. Lassen, *in* Alexander EC, Ozima M (Eds) Terrestrial Rare Gases: Tokyo, Japan Scientific Societies Press 3–16

Day SJ, Carracedo JC, Guillou H, Gravestock P (1999) Recent structural evolution of the Cumbre Vieja volcano, Canary Islands: volcanic rift zones reconfiguration as a precursor to volcano flank instability? J Volcanol Geotherm Res 94:135–167

Day JMD, Hilton DR (2011) Origin of $^{3}He/^{4}He$ ratios in HIMU-type basalts constrained from Canary Island lavas. Earth Planet Sci Lett 305:226–234

Deutsch CV, Journel AG (1998) Geostatistical Software Library and User's Guide, 2nd ed. Oxfor Univ Press

Egbert GD, Kelbert A (2012) Computational recipes for electromagnetic inverse problems. Geophys J Int 189:251–267. doi:10.1111/j.1365-246X.2011.05347.x

Etiope G, Martinelli G (2002) Migration of carrier and trace gases in the geosphere: an overview. Phys Earth Planet Int 129:185–204

European Commission (1999) Blue Book on Geothermal Resources: A strategic plan for the development of European Geothermal Sector. Office for Official Publications of the European Communities, Luxembourg. ISBN: 9282858030 9789282858035

Finlayson JB (1992) A soil gas survey over rotorua geothermal field, Rotorua, New Zealand. Geothermics 21:181–195. doi: 10.1016/0375-6505(92)90076-L

Fridriksson T, Kristjánsson BR, Ármannsson H, Margrétardóttir E, Ólafsdóttir S, Chiodini G (2006) CO_2 emissions and heat flow through soil, fumaroles and steam heated mud pools at the Reykjanes geothermal area, SW Iceland. Appl Geochem 21:1551-1569. doi: 10.1016/j.apgeochem.2006.04.006

Frondini F, Chiodini G, Caliro S, Cardelini C, Granieri D, Ventura G (2004) Diffuse CO_2 degassing at Vesuvio, Italy. Bull Volcanol 66:642–651

García A (1983) Modelos corticales a partir de sondeos magnetotelúricos. Aplicación a zonas volcánicas activas. PhD Thesis. Complutense University of Madrid

Galindo I (2005) Estructura volcano-tectónica y emisión difusa de gases de Tenerife (Islas Canarias). PhD Thesis. University of Barcelona

García X, Jones AG (2010) Internal structure of the western flank of the Cumbre Vieja volcano, La Palma, Canary Islands, from land magnetotelluric imaging. J Geophys Res Solid Earth 115: B07104. doi:10.1029/2009JB006445

Gerlach TM, Doukas MP, McGee KA, Kessler R (2001) Soil efflux and total emission rates of magmatic CO_2 at the Horseshoe Lake tree kill, Mammoth Mountain, California, 1995–1999. Chem Geol 177:101–116

Giggenbach WF (1991) Chemical techniques in geothermal exploration. In: D'Amore F (coordinator) Application of geochemistry in geothermal reservoir development. UNITAR/UNDP publication, Rome, 119-142

Gluekauf (1946) A microanalysis of helium and neon contents of air. Proc R Soc London Ser A 185:98–119. doi: 10.1098/rspa.1946.0007

Graham DW (2002) Noble gas isotope geochemistry of Mid-Ocean Ridge and Ocean Island Basalts: Characterization of mantle source reservoirs. Reviews in Mineralogy and Geochemistry 47:247–317. doi:10.2138/rmg.2002.47.8

Granieri D, Carapezza ML, Chiodini G, Avino R, Caliro S, Ranaldi M, Ricci T, Tarchini L (2006) Correlated increase in CO_2 fumarolic content and diffuse emission from La Fossa crater (Vulcano, Italy): Evidence of volcanic unrest or increasing gas release from a stationary deep magma body? Geophys Res Lett 33:L13316

Guillou H, Pérez-Torrado FJ, Hansen A, Carracedo JC, Gimeno D (2004) The Plio-Quaternary volcanic evolution of Gran Canaria based on new K-Ar ages and magnetostratigraphy. J Volcanol Geotherm Res 135:221-246. doi: 10.1016/j.jvolgeores.2004.03.003

Hanson MC, Oze C, Horton TW (2014) Identifying blind geothermal systems with soil CO_2 surveys. Appl Geochem 50:106–114

Harris AJL, Flynn LP, Keszthelyi L, Mouginis-Mark PJ, Rowland SK, Resing JA (1998) Calculation of lava effusion rates from Landsat TM data. Bull Volcanol 60:52– 71

Harris AJL, Steffke A, Calvari, S, Spampinato L (2011) Thirty years of satellite-derived lava discharge rates at Etna: Implications for steady volumetric output. J Geophys Res 116:B08204

Hernández PA, Notsu K, Salazar JM, Mori T, Natale G, Okada H, Virgili G, Shimoike Y, Sato M, Pérez NM (2001a) Carbon dioxide degassing by advective flow from Usu volcano, Japan. Science 292:83–86

Hernández PA, Salazar JM, Shimoike Y, Mori T, Notsu K, Pérez NM (2001b). Diffuse emission of CO_2 from Miyakejima volcano, Japan. Chem Geol 177:175–185

Hernández PA, Notsu K, Tsurumi M, Mori T, Ohno M, Shimoike Y, Salazar J, Pérez N (2003) Carbon dioxide emissions from soils at Hakkoda, north Japan. J Geophys Res 108(B4):2210

Hernández PA, Pérez NM, Salazar J, Reimer M, Wakita H (2004) Radon and helium in soil gases at Cañadas Caldera, Tenerife, Canary Islands, Spain. J Volcanol Geotherm Res 131:59–76. doi: 10.1016/S0377-0273(03)00316-0

Hernández PA, Notsu K, Okada H, Mori T, Sato M, Barahona F, Pérez NM (2006) Diffuse Emission of CO_2 from Showa-Shinzan, Hokkaido, Japan: A Sign of Volcanic Dome Degassing. Pure Appl Geophys 163:869–881

Hernández PA, Pérez NM, Varekamp JC, Henríquez B, Barrancos J, Padrón E, Calvo D, Melián G (2007) Crater lake temperature changes of the 2005 eruption of Santa Ana volcano, El Salvador, Central America. Pure Appl Geophys 164:2507-2522

Hernández PA, Pérez NM, Fridriksson T, Egbert J, Ilyinskaya E, Thárhallsson A, Ívarsson G, Gíslason G, Gunnarsson I, Jónsson B, Padrón E, Melián G, Mori T, Notsu K (2012) Diffuse volcanic degassing and thermal energy release from Hengill volcanic system, Iceland. Bull Volcanol 74:2435–2448. doi: 10.1007/s00445-012-0673-2

Hilton DR, MacPherson CG, Elliot TR (2000) Helium isotope ratios in mafic phenocrysts and geothermal fluids from La Palma, the Canary Islands (Spain): Implications for HIMU mantle sources. Geochim Cosmochim Acta 64(12):2119–2132

Hon K, Kauahikaua J, Denlinger R, Mackay K (1994) Emplacement and inflation of pahoehoe sheet flows: Observations and measurements of active lava flows on Kilauea Volcano, Hawaii. Geol Soc Am Bull 106, 351–370

Ibáñez JM, De Angelis S, Díaz-Moreno A, Hernández PA, Alguacil G, Posadas A, Pérez NM (2012) Insights into the 2011–2012 submarine eruption off the coast of El Hierro (Canary Islands, Spain) from statistical analyses of earthquake activity: Geophysical Journal International 191:659–670. doi:10.1111/j.1365-246X.2012.05629.x

Instituto Geológico y Minero de España (IGME) (1977) Evaluación del potencial geotérmico de la isla de Lanzarote y selección de anomalías en las Islas Canarias. Informe final I. 137 pp

Instituto Geológico y Minero de España (IGME) (1979) Convenio con empresa nacional Adaro para prospección geotérmica en las Islas Canarias. Informe final. 105 pp

Instituto Geológico y Minero de España (IGME) (1993a) Prospección geotérmica de la Caldera de Las Cañadas del Teide (Tenerife). Estudio Geovolcanológico. Informe Final. 110 pp

Instituto Geológico y Minero de España (IGME) (1993b) Prospección geotérmica de la Caldera de Las Cañadas del Teide (Tenerife). Estudio Geoquímico e Isotópico de las fumarolas del Teide. Informe Final. 64 pp

Instituto Geológico y Minero de España (IGME) (1993c) Prospección geotérmica de la Caldera de Las Cañadas del Teide (Tenerife) mediante el empleo de scanners aerotransportados sensibles al infrarrojo térmico. 162 pp

Instituto Geológico y Minero de España (IGME) (1993d) Prospección geotérmica de la Caldera de Las Cañadas del Teide (Tenerife). Termologia Aérea Teide (Nota complementaria). 15 pp

Instituto Geológico y Minero de España (IGME) (1993e) Prospección geotérmica de la Caldera de Las Cañadas del Teide (Tenerife). Estudio Hidrogeoquímico. Informe Final. 80 pp

Instituto Geológico y Minero de España (IGME) (1993f) Prospección geotérmica de la Caldera de Las Cañadas del Teide (Tenerife). Estudio geoquimico general de las aguas subterráneas en la isla de Tenerife. 59 pp. + Anexos

Instituto Geológico y Minero de España (IGME) (1993g) Investigación geotérmica en las islas Canarias y evaluación de recursos y reservas geotérmicas en España. 201 pp

Instituto Geológico y Minero de España (IGME) (1993h) Investigación geotérmica en el área central de la isla de Tenerife. Informe Final. 104 pp

Instituto Geológico y Minero de España (IGME) (2011) Mapa Geológico de Canarias. GRAFCAN Ediciones, Santa Cruz de Tenerife

Javoy M, Pineau F, Ilyama I (1978) Experimental determination of the isotopic fractionation between gaseous CO_2 and carbon dissolved in tholeitic magma. Contrib Mineral Petrol 67:35-39

Johnston JM, Pellerin L, Hohmann GW (1992) Evaluation of Electromagnetic Methods for Geothermal Reservoir Detection. Geothermal Resources Council Transactions. 16:241-245

Jolie E, Klinkmueller M, Moeck I (2015) Diffuse surface emanations as indicator of structural permeability in fault-controlled geothermal systems. J Volcanol Geotherm Res 290:97-113. doi: 10.1016/j.jvolgeores.2014.11.003

Kilburn CRJ, Lopes RMC (1988) The growth of aa lava flow fields on Mount Etna, Sicily. J Geophys Res 93(B12), 14759-14772

Maljanen M, Martikainen PJ, Aaltonen H, Silvola J (2002) Short-term variation in fluxes of carbon dioxide, nitrous oxide and methane in cultivated and forested organic boreal soils. Soil Biol Biochem 34:577-584

Manzella A, Zaja A (2006) Volcanic structure of the southern sector of Mt. Etna after the 2001 and 2002 eruptions defined by magnetotelluric measurements. Bull Volcanol 69: 41–50

Marty B (1995) Nitrogen content of the mantle inferred from N_2-Ar correlation in oceanic basalts. Nature 377:326-329

Matsuda J, Matsumoto T, Sumino H, Nagao K, Yamamoto J, Miura Y, Kaneoka I, Takahata N, Sano Y (2002) The $^{3}He/^{4}He$ ratio of the new internal He Standard of Japan (HESJ). Geochem J 36:191–195

Mazot AD, Rouwet Y, Taran Y, Inguaggiato S and Varley N (2011) CO_2 and He degassing at El Chichón volcano (Chiapas, Mexico): gas flux, origin and relationship with local and regional tectonics. Bull Volcanol 73(4): 423-441. doi:10.1007/s00445-010-0443-y

Melián G, Hernández PA, Padrón E, Pérez NM, Barrancos J, Padilla G, Dionis S, Rodríguez F, Calvo D (2014) Spatial and temporal variations of diffuse CO_2 degassing at El Hierro volcanic system: relation to the 2011-2012 submarine eruption. J Geophys Res 119(9): 6976–6991

Mori T, Hernández PA, Salazar JML, Pérez NM, Notsu K (2001) An in situ method for measuring CO_2 flux from volcanic-hydrothermal fumaroles. Chem Geol 177:85-99

Notsu K, Mori T, Chanchah Do Vale S, Kagi H, Ito T (2006) Monitoring quiescent volcanoes by diffuse CO_2 degassing: case study of Mt. Fuji, Japan. Pure Appl Geophys 163:825–835

Ogawa Y, Bibby HM, Caldwell TG, Takakura S, Uchida T, Matsushima N, Bennie SL, Tosha T, Nishi Y (1999) Wide-band magnetotelluric measurements across the Taupo Volcanic Zone, New Zealand. Geophys Res Lett 26:3673-3676. doi: 10.1029/1999GL010914

Oppenheimer C (1998) Volcanological applications of meteorological satellites. Int J Remote Sens 19:2829-2864

Ozima M, Podosek FA (2002) Noble Gas Geochemistry, 2nd ed. 286. Cambridge University Press

Padrón E (2008) Emisión difusa de dióxido de carbono y otros volátiles en el volcán Cumbre Vieja, La Palma, Islas Canarias. PhD Thesis. University of La Laguna

Padrón E, Melián G, Marrero R, Nolasco D, Barrancos J, Padilla G, Hernández PA and Pérez NM (2008) Changes in the diffuse CO_2 emission and relation to seismic activity in and around El Hierro, Canary Islands. Pure Appl Geophys 165:95-114. doi: 10.1007/s00024-007-0281-9

Padrón E, Hernández PA, Pérez NM, Toulkeridis T, Melián G, Barrancos J, Virgili G, Sumino H, Notsu K (2012a) Fumarole/plume and diffuse CO_2 emission from Sierra Negra caldera, Galapagos archipelago. Bull Volcanol 74:1509–1519. doi:10.1007/s00445-012-0610-4

Padrón E, Pérez NM, Hernández PA, Sumino H, Melián G, Barrancos J, Nolasco D, Padilla G (2012b) Helium emission at Cumbre Vieja volcano, La Palma, Canary Islands. Chem Geol 312-313:138–147. doi:10.1016/j.chemgeo.2012.04.018

Padrón E, Pérez NM, Hernández PA, Sumino H, Melián GV, Barrancos J, Nolasco D, Padilla G, Dionis S, Rodríguez F, Hernández I, Calvo D, Peraza MD, Nagao K (2013) Diffusive helium emissions as a precursory sign of volcanic unrest. Geology 41:539–542. doi: 10.1130/G34027.1

Pandey GN, Rasintek M, Katz DL (1974) Diffusion of fluids through porous media with implication in petroleum geology. Am. Assoc Petrol Geol Bull 58(2):291–303

Parkinson KJ (1981) An improved method for measuring soil respiration in the field. J Appl Ecol 18:221–228. doi:0021-8901/81/0400-0221.

Patrick MR, Orr T, Antolik L, Lee L, Kamibayashi K (2014) Continuous monitoring of Hawaiian volcanoes with thermal cameras. J Appl Volcanology 3:1

Pedroni A, Hammerschmidt K, Friedrichsen H (1999) He, Ne, Ar and C isotope systematics of geothermal emanations in the Lesser Antilles Islands Arc. Geochim Cosmochim Acta 63(3-4):515-532. doi: 10.1016/S0016-7037(99)00018-6

Pérez NM, Wakita H, Nakai S, Sano Y, Williams SN (1994) $^{3}He/^{4}He$ isotopic ratios in volcanic hydrothermal discharges from the Canary Islands, Spain: implications on the origin of the volcanic activity. Mineral Mag 58ª:709-710

Pérez NM, Nakai S, Wakita H, Hernández PA, Salazar JM (1996) Helium-3 emission in and around Teide Volcano, Tenerife, Canary Islands, Spain. Geophys Res Lett 23:3531–3534. doi:10.1029/96GL03470

Pérez NM, Hernández PA, Padrón E, Melián G, Marrero R, Padilla G, Barrancos J, Nolasco D (2007) Precursory subsurface ^{222}Rn and ^{220}Rn degassing signatures of the 2004 seismic crisis at Tenerife, Canary Islands. Pure Appl Geophys 164:2431-2448. doi: 10.1007/s00024-007-0280-x

Pérez NM, Hernández PA (2008) La vigilancia volcánica en España: una apuesta crucial para la reducción del riesgo volcánico. In: Galindo Jiménez I, Lain Huerta L, Llorente Isidro M (Eds) El estudio y la gestión de los riesgos geológicos. Publicaciones del Instituto Geológico y Minero de España. Serie Medio Ambiente. Riesgos Geológicos 12:159-174

Pérez NM, Hernández PA, Padilla G, Nolasco D, Barrancos J, Melián G, Padrón E, Dionis S, Calvo D, Rodríguez F, Notsu K, Mori T, Kusakabe M, Arpa MC, Reniva P and Ibarra M (2011) Global CO2 emission from volcanic lakes. Geological Society of America 39,3:235-238. doi: 10.1130/G31586.1

Pérez NM, Padilla GD, Padrón E, Hernández PA, Melián G, Barrancos J, Dionis S, Nolasco D, Rodríguez F, Calvo D, Hernández I (2012) Precursory diffuse CO_2 and H_2S emission signatures of the 2011-2012 El Hierro submarine eruption, Canary Islands. Geophys Res Lett 39. doi:10.1029/2012GL052410

Pérez NM, Hernández PA, Padrón E, Melián G, Nolasco D, Barrancos J, Padilla G, Calvo D, Rodríguez F, Dionis S, Chiodini G (2013) An increasing trend of diffuse CO_2 emission from Teide volcano (Tenerife, Canary Islands): geochemical evidence of magma degassing episodes. J Geol Soc London 170(4):585–592. doi: 10.1144/jgs2012-125

Pinkerton H, James M, Jones A (2002) Surface temperature measurements of active lava flows on Kilauea Volcano, Hawaii. J Volcanol Geotherm Res 113:159–176

Piña-Varas P, Ledo J, Queralt P, Marcuello A, Bellmunt F, Hidalgo R, Messeiller M (2014) 3-D Magnetotelluric Exploration of Tenerife Geothermal System (Canary Islands, Spain). Surv Geophys 35:1045-1064. doi: 10.1007/s10712-014-9280-4

Piña-Varas P, Ledo J, Queralt P, Marcuello A, Bellmunt F, Ogaya X, Pérez NM and Rodríguez-Losada JA (2015) Vertical collapse origin of Las Cañadas caldera (Tenerife, Canary Islands) revealed by 3-D magnetotelluric inversion. Geophys Res Lett 42. doi: 10.1002/2015GL063042

Rivera J Lastras G, Canals M, Acosta J, Arrese B, Hermida N, Micallef A, Tello O, Amblas D (2013) Construction of an oceanic island: Insights from the El Hierro (Canary Islands) 2011-2012 submarine volcanic eruption. Geology 41:355-358

Salazar JM, Hernández PA, Pérez NM, Melián G, Álvarez J, Segura F, Notsu K (2001) Diffuse emissions of carbon dioxide from Cerro Negro volcano, Nicaragua, Central America. Geophys Res Lett 28:4275–4278

Sano Y, Urabe A, Wakita H (1985) Chemical and Isotopic composition of gases in geothermal fluids in Iceland. Geochem J 19:135–148

Sano Y, Marty B (1995) Origin of carbon in fumarolic gas from island arcs. Chem Geol 119:265-274

Schmincke H, Sumita M (2010) Geological Evolution of the Canary Islands: A Young Volcanic Archipelago Adjacent to the Old African Continent. Görres-Verlag, Koblenz. ISBN: 978-3-86972-005-0

Sinclair AJ (1974) Selection of threshold values in geochemical data using probability graphs. J Geochemical Explor 3:129–149. doi: http://dx.doi.org/10.1016/0375-6742(74)90030-2

Spampinato L, Calvari S, Oppenheimer C, Boschi E (2011) Volcano surveillance using infrared cameras. Earth Sci Rev 106:63-91

Spichak VV, Zakharova OK, Goidina AG (2013) A new conceptual model of the Icelandic crust in the Hengill geothermal area based on the indirect electromagnetic geothermometry. J Volcanol Geotherm Res 257: 99–112. doi:10.1016/j.jvolgeores.2013.03.013

Sumino H, Nagao K, Notsu K (2001) Highly sensitive and precise measurement of helium isotopes using a mass spectrometer with double collector system. J Mass Spectrom Soc Jpn 492:61–68

Thordarson T, Larsen G (2007) Volcanism in Iceland in historical time: Volcano types, eruption styles and eruptive history. Journal of Geodynamics 43:118–152. doi:10.1126/science.204.4398.1195

Trolier M, White JWC, Tans PP, Masarie KA, Gemery PA (1996) Monitoring the isotopic composition of atmospheric CO_2: Measurements from the NOAA Global Air Sampling Network. J Geophys Res 101 No. D20, 25897-25916. doi:10.1029/96JD02363

Valentín A, Albert-Beltrán JF, Diez JL (1990) Geochemical and geothermal constraints on magma bodies associated with historic activity, Tenerife (Canary Islands). J Volcanol Geotherm Res 44:251–264. doi: 10.1016/0377-0273(90)90020-G

Veeger AI (1991) Geochemical methods for evaluating the origin and evolution of ground water in volcanic rocks at La Palma Canary Islands, Spain. PhD Thesis, The University of Arizona.

Viveiros F, Ferreira T, Cabral Vieira J, Silva C, Gaspar JL (2008) Environmental influences on soil CO_2 degassing at Furnas and Fogo volcanoes (São Miguel Island, Azores archipelago). J Volcanol Geotherm Res 177:883-893

Voltattorni N, Sciarra A, Quattrocchi F (2010) The application of soil-gas technique to geothermal exploration: study of hidden potential geothermal systems. Proc World Geotherm Congr Bali, Indonesia

Wadge G (1981) The variation of magma discharge during basaltic eruption. J Volcanol Geotherm Res 11:139-168

Wright R, Blake S, Harris AJL, Rothery DA (2001) A simple explanation for the space-based calculation of lava eruption rates. Earth Plan Sci Lett 192:223-233

Appendix

6. Appendix (Research papers published)

I. Rodríguez F., Pérez N.M., Padrón E., Melián G., Hernández P., Asensio-Ramos M., Dionis S., López G., Marrero R., Padilla G., Barrancos J. and Hidalgo R. (2015). Diffuse helium and hydrogen degassing to reveal hidden geothermal resources in oceanic volcanic islands: The Canarian archipelago case study. *Surveys in Geophysics*, DOI: 10.1007/s10712-015-9320-8 (2014 Impact Factor: 3.447)

II. Rodríguez F., Pérez N. M., Padrón E., Melián G., Piña-Varas P., Dionis S., Barrancos J., Padilla G., Hernández P., Marrero R., Ledo J., Bellmunt F., Queralt P., Marcuello A. and Hidalgo R. (2015). Surface geochemical and geophysical studies for geothermal exploration at the Southern Volcanic Rift Zone of Tenerife, Canary Islands, Spain. *Geothermics*, 55, 195–206, DOI: 10.1016/j.geothermics.2015.02.007 (2014 Impact Factor: 2.949)

III. Padrón E., Padilla G., Hernández P. A., Pérez N. M., Calvo D., Nolasco D., Barrancos J., Melián G., Dionis S. and Rodríguez F. (2013). Soil gas geochemistry in relation to eruptive fissures on Timanfaya volcano, Lanzarote Island (Canary Islands, Spain) Timanfaya. *Journal of Volcanology & Geothermal Research*, 250, 91–99, DOI: 10.1016/j.volgeores.2012.10.013 (2013 Impact Factor: 2.515)

IV. Padrón E., Pérez N. M., Rodríguez F., Melián G., Hernández P. A., Sumino H., Padilla G., Barrancos J., Dionis S., Notsu K., and Calvo D. (2015). Dynamics of diffuse carbon dioxide emission from Cumbre Vieja volcano, La Palma, Canary Islands. *Bulletin of Volcanology*, 77, 1-15, DOI 10.1007/s00445-015-0914-2 (2014 Impact Factor: 2.519)

V. Padrón E., Pérez N. M., Hernández P. A., Sumino H., Melián G. V., Barrancos J., Nolasco D., Padilla G., Dionis S., Rodríguez F., Hernández I., Calvo D., Peraza M. D. and Nagao K. (2013). Diffusive helium emissions as a precursory sign of volcanic unrest. *Geology*, DOI:10.1130/G34027.1 (2013 Impact Factor: 4.638)

VI. Hernández P. A., Calvari S., Ramos A., Pérez N. M., Márquez A., Quevedo R., Barrancos J., Padrón E., Padilla G. López D., Rodríguez-Santana, A., Melían G., Dionis S., Rodríguez F., Calvo D. and Spampinato L. (2014). Magma emission rates from shallow submarine eruptions using thermal airbone imaging. *Remote Sensing of Environment*, DOI: 10.1016/j.rse.2014.08.027 (2014 Impact Factor: 6.393)

Surv Geophys
DOI 10.1007/s10712-015-9320-8

Diffuse Helium and Hydrogen Degassing to Reveal Hidden Geothermal Resources in Oceanic Volcanic Islands: The Canarian Archipelago Case Study

Fátima Rodríguez · Nemesio M. Pérez · Eleazar Padrón · Gladys Melián · Pedro A. Hernández · María Asensio-Ramos · Samara Dionis · Gabriel López · Rayco Marrero · Germán D. Padilla · José Barrancos · Raúl Hidalgo

Received: 22 July 2014 / Accepted: 6 February 2015

Abstract We report herein the results of soil gas geochemistry studies, focused mainly on nonreactive and/or highly mobile gases such as He and H_2, in five mining licenses at Tenerife and Gran Canaria, Canary Islands, Spain, during 2011–2014. The primary objective was to sort the possible geothermal potential of these five mining licenses, thus reducing the uncertainty inherent to the selection of the areas with highest geothermal potential for future exploration works. By combining the overall information obtained by the statistical–graphical analysis of the soil He and H_2 data, the spatial distribution of soil gas concentrations and the analysis of selected chemical ratios of the soil gas to evaluate the influence of deep-seating degassing, two of the five mining licenses (*Garehagua* and *Abeque*, both located in Tenerife Island) seemed to show the highest geothermal potential. These results will be useful for future implementation and development of geothermal energy in the Canaries, the only Spanish territory with potential high-enthalpy geothermal resources, thus the most promising area for high-enthalpy geothermal installations.

F. Rodríguez (✉) · N. M. Pérez · E. Padrón · G. Melián · P. A. Hernández · M. Asensio-Ramos · S. Dionis · G. López · R. Marrero · G. D. Padilla · J. Barrancos
Instituto Volcanológico de Canarias (INVOLCAN), 38400 Puerto de la Cruz, Tenerife, Canary Islands, Spain
e-mail: fatima@iter.es

N. M. Pérez · E. Padrón · G. Melián · P. A. Hernández · R. Marrero · G. D. Padilla · J. Barrancos
Environmental Research Division, Instituto Tecnológico y de Energías Renovables (ITER), 38600 Granadilla de Abona, Tenerife, Canary Islands, Spain

N. M. Pérez · E. Padrón · G. Melián · P. A. Hernández
Agencia Insular de Energía de Tenerife (AIET), 38600 Granadilla de Abona, Tenerife, Canary Islands, Spain

Present Address:
R. Marrero
Laboratorio Nacional de Energia e Geologia (LNEG), Alfragide, 2610-999 Lisbon, Portugal

R. Hidalgo
EurGeol, La Esperanza 2, pta 9, 21200 Aracena, Huelva, Spain

Published online: 13 March 2015

Keywords Geothermal exploration · Helium · Hydrogen · Soil gas · Canary Islands

1 Introduction

During geothermal exploration, the geochemical methods are extensively used and play a major role in both exploration and exploitation phases (Nicholson 1993). Geochemical methods are particularly useful to assess the subsurface temperatures in the reservoir, the origin of the fluid and flow directions within the reservoir (Ármannsson and Fridriksson 2009). The geochemical exploration is based on the assumption that fluids on the surface reflect physico-chemical and thermal conditions in the geothermal reservoir at depth. However, on some occasions, there is not any evidence of endogenous fluids manifestations at surface that traditionally provides evidence of the presence of an active geothermal system, in the form of aqueous solutions (hot springs, mud pools, geysers), hydrothermal alteration deposits (travertine, phreatic craters, explosion breccias) or gas mixtures (fumaroles). Discovery of new geothermal systems will therefore require exploration of areas where the resources are either hidden or lie at great depths (i.e., Dixie Valley, Nevada, U.S.A., Lewicki and Oldenburg 2004). Geochemical methods for geothermal exploration of these areas must include soil gas surveys, based on the detection of anomalously high concentrations of some hydrothermal gases in the soil atmosphere, generally between 40 cm and 1 m depth from the surface (Bertrami et al. 1990; Finlayson 1992; Voltattorni et al. 2010). The observed enrichments of some chemical species or chemical ratios in the soil environment may indicate the presence of enhanced vertical permeability areas related to high-temperature hydrothermal activity at depth. Mapping these soil gas enrichments relative to background concentrations and/or their fluxes can be useful in delineating main upflow regions and areas of increased subsurface permeability related to high-temperature hydrothermal activity at depth (Werner and Cardellini 2006; Chiodini et al. 2007; Hernández et al. 2012; Barberi et al. 2013).

One of the most studied gases in the soil atmosphere for geothermal exploration purposes has been CO_2, because its emission rate in active hydrothermal regions can be as high as those from active volcanoes (Mörner and Etiope 2002; Werner and Cardellini 2006). However, the occurrence of interfering processes affecting the reactive gases such as CO_2 during its ascent from magmatic bodies or hydrothermal systems toward the surface environment hinders the interpretation of their enrichments in the soil atmosphere and fluxes for geothermal exploration purposes (Marini and Gambardella 2005; Agusto et al. 2013). These processes include gas scrubbing by groundwaters and interaction with rocks, decarbonatation processes, biogenic production, etc. Within the rest of the soil gases, particular interest has been addressed to nonreactive (noble) gases. They offer important advantages for the detection of vertical permeability structures, because their interaction with the surrounding rocks or fluids during the ascent toward the surface is minimum (Hernández et al. 2004; Padrón et al. 2012, 2013a). This is the case for helium (He). He has unique characteristics as a geochemical tracer: it is chemically inert and radioactively stable, non-biogenic, highly mobile and relatively insoluble in water (Reimer 1980; Ozima and Podosek 2002; Fu et al. 2005). There are two naturally occurring isotopes of helium: ^{4}He and ^{3}He, with an atmospheric ^{3}He/^{4}He ratio (R_A) of 1.384×10^{-6} (Clarke et al. 1976). Radioactive decay of ^{238}U, ^{235}U and ^{232}Th is the main source of ^{4}He, while ^{3}He is considered a primordial gas that is being released to the atmosphere by mantle degassing (Graham 2002). Soil helium surveys have been used extensively for many objectives: (1) as an indicator of tritium groundwater contamination (Olsen et al. 2006); (2) as an indicator of crustal leaks along faults (Fu et al. 2005; Lombardi and Voltattorni 2010); (3) to study seismicity along active faults (Reimer

1980; 1985); (4) to detect structures of enhanced permeability for deep gas migration and preferential routes for degassing in a volcanic system (Hernández et al. 2004; Padrón et al. 2012, 2013a); (5) to select areas for exploratory drilling for uranium deposits (Reimer and Bowles 1979; Reimer 1986); and (6) for volcano monitoring (Padrón et al. 2013b). With regard to geothermal exploration, although few works have been reported to date on its application, soil He surveys have been revealed as a quick, inexpensive and promising tool for this purpose (McCarthy 1982, 1983; Di Filippo et al. 1999).

Hydrogen (H_2) is the second most abundant reduced gas in the atmosphere (after methane), with a concentration $\sim$530 ppb (Novelli et al. 1999). It is one of the most abundant trace species in volcano-hydrothermal systems and is a key participant in many redox reactions occurring in the hydrothermal reservoir gas (Giggenbach 1987; Chiodini and Marini 1998). Although H_2 can be produced in soils by N_2-fixing and fertilizing bacteria (Conrad 1996), soils are considered nowadays as sinks of molecular hydrogen (Smith-Downey et al. 2006). Oxidation by soil hydrogenases and methanogens, sulfate-reducing and ferric iron-reducing bacteria are the main causes for this uptake of molecular H_2 by soils (Trevors 1985; Conrad 1996; Gödde et al. 2000). Because of its chemical and physical characteristics, H_2 generated within the crust moves rapidly and escapes to the atmosphere. These characteristics make H_2 one of the best geochemical indicators of magmatic and geothermal activity at depth.

The Canary Islands, owing to its recent volcanism, are the only Spanish territory with potential high-enthalpy geothermal resources (European Commission 1999). From the 1970s to the 1990s, the Spanish Geological Survey (IGME, http://www.igme.es) performed intensive research on geothermal resources in the country, including studies at Lanzarote, Gran Canaria, Tenerife and La Palma islands in the Canaries: geochemical and isotopic analysis of hydrothermal discharges (fumaroles) of Teide volcano, volcano-structural and magnetotelluric studies at Las Cañadas caldera, and groundwater hydrochemistry studies (Instituto Geológico y Minero de España (IGME) 1977, 1979, 1993a, b, c, d, e, f, g, h; Albert-Beltrán et al. 1990; Valentín et al. 1990). As a result of these exploratory studies, one exploratory drilling in Tenerife and two in Gran Canaria were performed with unsatisfactory results (Instituto Geológico y Minero de España (IGME) 1993h). Recently, interest in the development of geothermal energy in Canaries has increased again (García-Yeguas et al. 2012; Rodríguez et al. 2015; Piña-Varas et al. 2014). In this paper, we present the results of five detailed soil He and H_2 surveys carried out with geothermal exploration purposes in several areas of interest (mining licenses) on the islands of Tenerife and Gran Canaria.

The main limitation of geothermal energy with respect to other renewable energies is the investment required in the initial exploration phase. The primary objective is to sort geochemically the five different mining licenses based on its geothermal potential to reduce the uncertainty inherent to the selection of the area with the highest potential success in the selection of exploratory wells. The location of such exploratory drillings within the areas in order to detect the hydrothermal system that might support economically the development of a geothermal plant for energy generation is beyond the objective of this paper. Future additional geophysical and geological studies would be necessary within the studied area to reduce the uncertainty in their location.

2 Local Geology and Volcano-structural Features of the Selected Mining Licenses

The Canary Islands archipelago comprises a group of seven major volcanic islands forming a roughly east–west chain with the ages progressively younger to the west. It is located

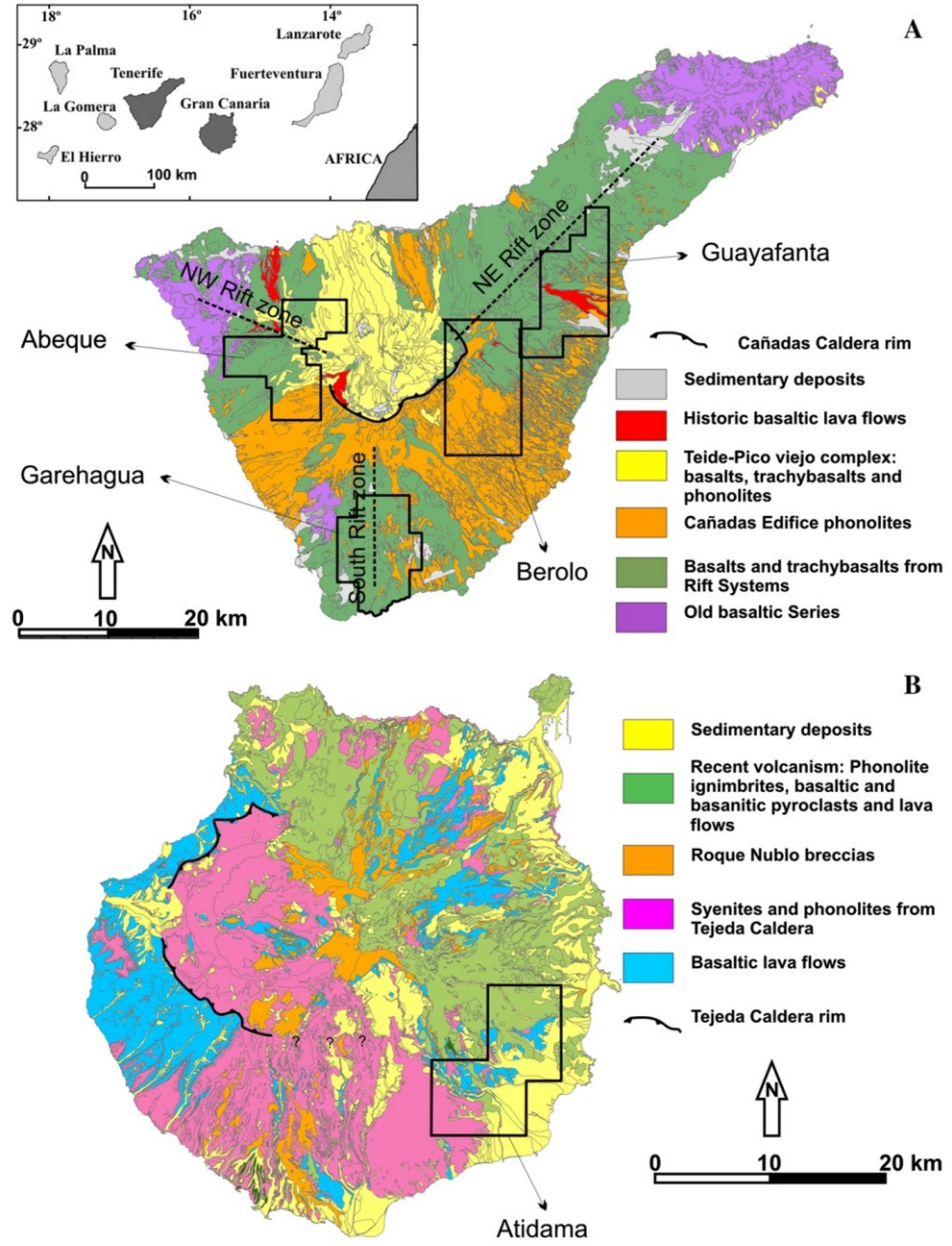

Fig. 1 Geographic location of the Canary Islands and simplified geological maps (modified from IGME, 2011) of **a** Tenerife, with the location of the four mining licenses (*Garehagua*, *Berolo*, *Guayanta* and *Abeque*) studied for geothermal exploration purposes and **b** Gran Canaria with the location of *Atidama*, the mining license studied for geothermal exploration purposes on that island

over ocean crust of 185–190 million years old off the passive continental margin of NW Africa (Schmincke and Sumita 2010). Gran Canaria and Tenerife are the central islands of this group (Fig. 1). The oldest subaerial rocks dated in both are 14.5 and 11.5 Ma, respectively (Ancochea et al. 1990; Schmincke and Sumita 1998). These two islands are

unique with a central volcanic complex that started to grow at about 5 Ma in the case of Gran Canaria (Schmincke and Sumita 1998) and 3.5 Ma in the case of Tenerife (Ancochea et al. 1990). A sector of the central volcanic edifice in Gran Canaria suffered a great gravitational collapse 3.5 Ma ago, resulting in debris avalanches episodes: Roque Nublo Breccias (García-Cacho et al. 1994). Previously, Tejeda Caldera produced several differentiated magmas: syenites, trachytes and phonolites. The central volcanic complex in Tenerife is characterized by mafic, intermediate and differentiated phonolitic magmas (Martí and Gudmundsson 2000). Multiple vertical collapses of the central volcanic complex formed Las Cañadas caldera (16 × 9 km, Fig. 1a) partially filled by post-caldera volcanic activity. The last activity inside Cañadas Caldera constructed Pico Viejo and Teide stratovolcanoes. The central volcanic complex and old basaltic edifices are connected by a "Mercedes star" volcano-rift system (Carracedo 1994).

Since Tenerife and Gran Canaria are promising areas for geothermal resources, five mining licenses were acquired for geothermal exploration studies: four in Tenerife Island and one in Gran Canaria (see locations in Fig. 1). Four of the study areas are located in the three differentiated volcanic rifts of Tenerife: NE Rift, NW Rift and south Rift (Fig. 1a). The five mining licenses comprise the subaerial surface under which groundwater temperature anomalies and high contents of silica (SiO_2) in water were measured during the geothermal exploration studies in the 1970–1990s (IGME 1977, 1979, 1993a, b, c, d, e, f, g, h; Valentín et al. 1990).

Garehagua investigation license (Fig. 2a) comprises a large part of the southern volcanic rift of Tenerife. Its main structural characteristic is an apparent absence of a distinct ridge and a fan-shaped distribution of monogenetic cones (Kröchert and Buchner 2008). Basaltic and trachybasaltic rocks predominate in this study area (Fig. 1a). It is important to note that, inside this study area, a bubbling ^{3}He- and CO_2-rich gas spot, located at 2,850 m of horizontal depth inside *Fuente del Valle* water gallery, has been identified and characterized by previous studies (Pérez et al. 1996, 2007). Chemical and isotopic composition of this bubbling gas exhibits a significant magmatic component with: $CO_2 \sim 85$ %, He $\sim$ 10 ppm; $^{3}He/^{4}He \sim 7.0\ R_A$; $^{222}Rn \sim 100$ KBq/m^3 (Pérez et al. 1996, 2007). This sampling point is probably related to an upward migration of volcano-hydrothermal gases through a highly permeable pathway (Pérez et al. 2007; Marrero 2010).

Berolo (Fig. 2b) and *Guayafanta* (Fig. 2c) mining licenses comprise a large part of the northeast volcanic rift of Tenerife. The northeast rift is more complex than NW or NS rifts due the existence of Pedro Gil stratovolcano that broke the main NE–SW structure. Pedro Gil caldera was formed $\sim$0.8 Ma ago by a vertical collapse of this stratovolcano (Ancochea et al. 1990) (Fig. 2c). A fissural eruption (*Arafo–Fasnia–Siete Fuentes*) along $\sim$13 km took place and affected both mining licenses in 1704–1705 AD (Romero 1991), following a similar direction of the main volcanic rift alignment (N45E). The northern part of *Berolo* includes the location of two of the three surface thermal anomalies reported by IGME (1993b). Several different lithotypes can be distinguished in *Berolo*: inside Cañadas caldera, basaltic, trachybasaltic and phonolite rocks; in the rest of the study area, basaltic rocks predominate in the northern part and phonolites at the southern (Fig. 1a). In the case of *Guayafanta*, most of the area is covered by basaltic lava flows (Fig. 1a).

Abeque (Fig. 2d) investigation license is located inside of the northwest volcanic rift of Tenerife. The rift is formed by alignment of cones along a main NW–SE direction, including the last volcanic eruption that has taken place in Tenerife (Chinyero eruption, 1909 AD). This mining license includes one exploratory drilling carried out in Tenerife by IGME (1993h). This area shows mainly three different lithotypes: basalts, trachybasalts and phonolites (Fig. 1a).

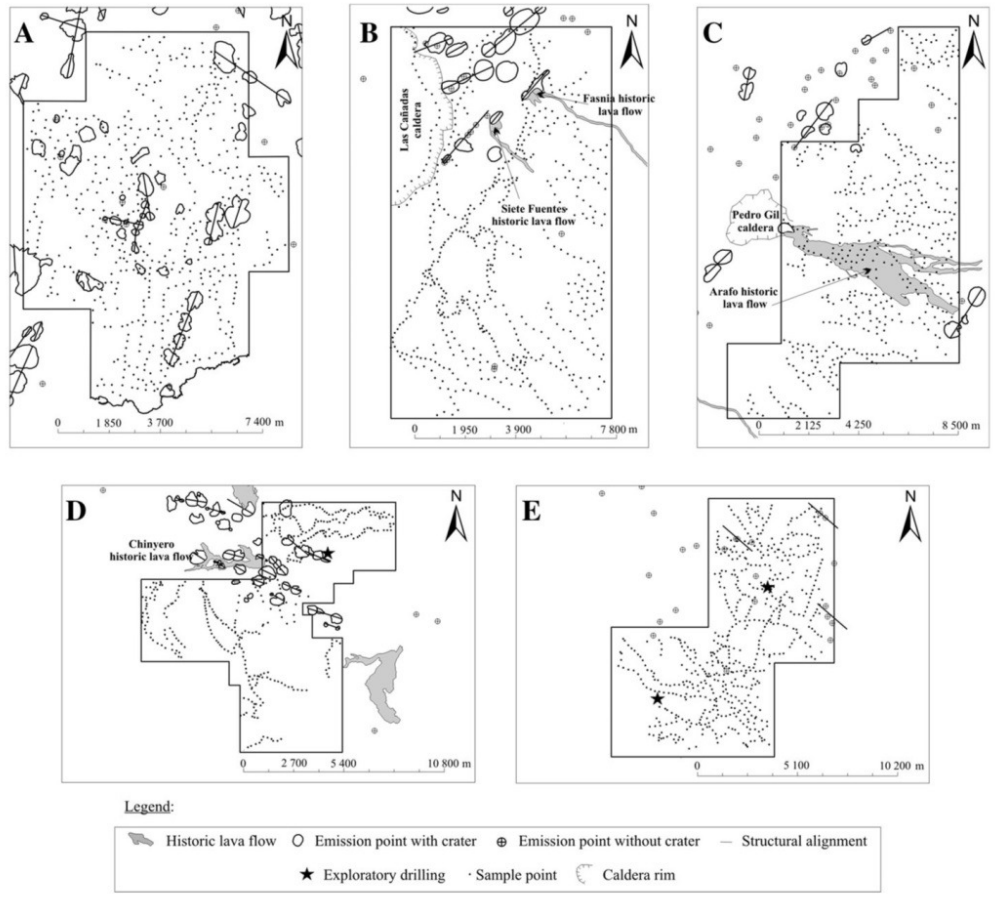

Fig. 2 Volcano-structural map and sample sites location of *Garehagua* (**a**), *Berolo* (**b**), *Guayafanta* (**c**), *Abeque* (**d**) and *Atidama* (**e**) mining licenses. Surfaces covered by historic lava flows are also displayed. *Stars* indicate the locations of the exploratory drillings carried out in Tenerife and Gran Canaria by IGME (1993h)

Atidama mining license (Fig. 2e), the only license located in Gran Canaria, was selected owing to the presence of several groundwater temperature anomalies (up to 42 °C) and the results of hydrogeological studies carried out (Gasparini et al. 1987, 1990). For these reasons, two drilling exploratory wells were carried out in this area. Alignments of volcanic cones along NW–SE can be observed in the northern part of the grid, as occurred in other parts of Gran Canaria. Atidama comprises three predominant lithotypes: phonolites at southern part, mostly basanites at northern part and a great area of sedimentary deposits at southeast (Fig. 1b).

3 Methods

Soil gas samples were collected at 557, 577, 600, 406 and 541 sites selected in July–August, 2011, July–September, 2012 and March–April, 2014, in *Garehagua* and *Berolo*, *Atidama* and *Abeque* and *Guayafanta,* respectively (Fig. 2). The sampling sites were selected based on their accessibility and geological criteria. Soil gases were sampled at ∼40 cm depth using a metallic probe with a 60 cc hypodermic syringes and stored in 10 cc glass vials for later

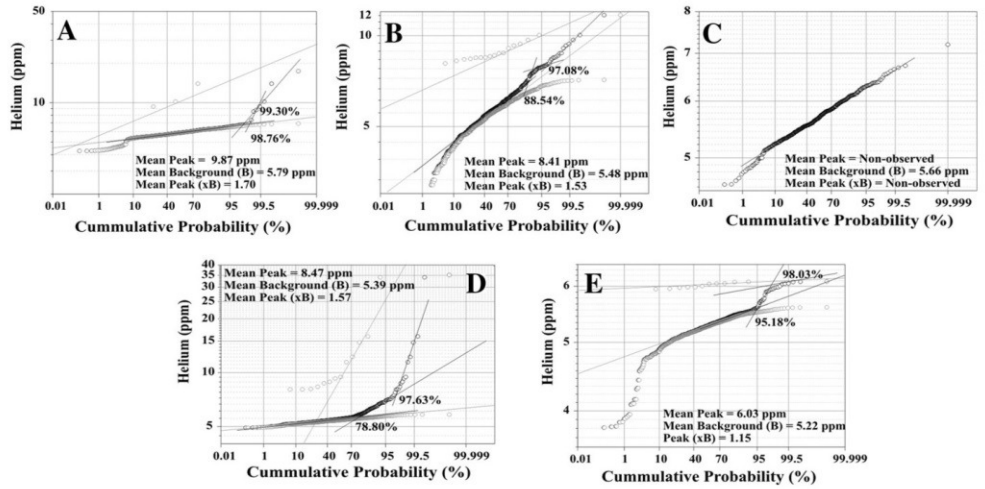

Fig. 3 Cumulative probability plots of soil He measured at *Garehagua* (**a**), *Berolo* (**b**), *Guayafanta* (**c**), *Abeque* (**d**) and *Atidama* (**e**) mining licenses. *Solid black lines* in the probability plots indicate different log-normal geochemical population in the original data. *Solid gray lines* indicate the separated background and peak log-normal populations

laboratory analysis. Helium and Argon contents were analyzed at each sample by means of a Quadropole Mass Spectrometer (QMS; Pfeiffer Omnistar 422) and hydrogen, nitrogen and neon concentrations by a VARIAN CP4900 micro-gas chromatograph. The accuracy and detection limit of the instruments were estimated to be 0.3 and 3 and 0.05 and 0.45 ppm, respectively, for helium and hydrogen. Spatial distribution maps of soil He and H_2 were constructed by using sequential Gaussian simulation (sGs) algorithm, provided by the *sgsim* program (Deutsch and Journel 1998; Cardellini et al. 2003). Soil helium enrichments were depicted as ΔHe (ΔHe = $[He]_{soil\ atmosphere}$–$[He]_{air}$). The atmospheric He concentration ($[He]_{air}$) used was 5.24 ppm (Gluekauf 1946). The sGs procedure allows us to interpolate the measured variable at not-sampled sites. The simulation is conditional and sequential, i.e., the variable is simulated at each unsampled location by random sampling of a Gaussian conditional cumulative distribution function (Cardellini et al. 2003). To check whether the soil He and H_2 data came from mixed polymodal distributions (Figs. 3, 5), the probability-plot technique (Tennant and White 1959; Sinclair 1974) was applied to the entire data sets. This technique is based on the recognition of inflection points along a curve defined by plotting cumulative percentile of the data on a log-normal scale. A bimodal distribution consisting of two log-normal populations plots as an S-type curve, where the inflection point shows the presence of two different modes: normal I and normal II. The two distinct populations are known as background (commonly derived from atmospheric He and H_2) and peak (soil degassing), respectively.

4 Results

Table 1 shows a statistical summary of the soil He and H_2 data measured in the five areas. Soil He values ranged from typical atmospheric values up to 35.1 ppm (measured in *Abeque*). The other mining areas showed values up to 17.4 ppm in *Garehagua*, 11.7 ppm in *Berolo*, 7.2 ppm in *Guayafanta* and 6.1 ppm in *Atidama*. The median values were

Table 1 Statistical summary of the analytical results of He and H_2 soil gas concentration measured at mining licenses for geothermal exploration in the Canary Islands

	Average	Minimum	First quartile (Q1)	Median	Third quartile (Q3)	Maximum	Interquartile range (Q3–Q1)
He (ppm)							
Abeque	5.81	4.9	5.28	5.42	5.56	35.1	0.28
Garehagua	5.86	4.3	5.56	5.83	6.14	17.4	0.58
Berolo	5.73	<IDL	5.01	5.67	6.39	11.7	1.38
Guayafanta	5.66	4.6	5.41	5.64	5.90	7.2	0.49
Atidama	5.22	3.8	5.09	5.25	5.39	6.1	0.30
H_2 (ppm)							
Abeque	0.58	<IDL	0.28	0.43	0.66	8.6	0.38
Garehagua	1.35	<IDL	0.50	0.75	1.37	24.4	0.87
Berolo	1.46	<IDL	0.80	1.23	1.98	4.3	1.18
Guayafanta	0.59	<IDL	0.45	0.54	0.66	8.3	0.21
Atidama	1.56	0.7	1.23	1.43	1.70	7.2	0.47

<IDL Below the instrument detection limit

similar or slightly higher than the atmospheric one: 5.42, 5.83, 5.67, 5.64 and 5.25 ppm for *Abeque*, *Garehagua*, *Berolo*, *Guayafanta* and *Atidama,* respectively (Table 1). Soil H_2 concentrations measured in the five mining licenses ranged from typical atmospheric values (~0.5 ppm) up to 24.4 ppm in *Garehagua*, 8.6 ppm in *Abeque*, 8.3 ppm in *Guayafanta*, 7.2 ppm in *Atidama* and 4.3 ppm in *Berolo*. The median values measured for H_2 were 0.43, 0.75, 1.23, 0.54 and 1.43 for *Abeque*, *Garehagua*, *Berolo*, *Guayafanta* and *Atidama,* respectively (Table 1).

4.1 Data Analysis and Spatial Distribution

4.1.1 Garehagua

The possible presence of mixed polymodal distributions in the soil helium data caused by the existence of different geochemical populations was examined by means of the probability-plot technique (Fig. 3a). Soil helium data showed two log-normal geochemical populations with a mean value of 5.79 ppm, for the background population (98.76 % of the total data) and a 9.87 ppm, for the peak population (0.7 % of the total data). The rest of the data is considered as intermediate values between background and peak populations. Peak values exceeded 1.70 times the background ones. The spatial distribution ΔHe (Fig. 4a) showed that highest values roughly defined a N–S trend (>1.6 ppm). The highest relative enrichment (>5.0 ppm) was measured in the central part of the study area. Other important values were measured in the north of the study area in good spatial correlation with the vertical surface projection of the bubbling gas spot already mentioned above (Pérez et al. 1996; Marrero 2010).

The possible presence of mixed polymodal distributions in the soil H_2 data was also examined by means of the probability-plot technique (Fig. 5a). Two geochemical

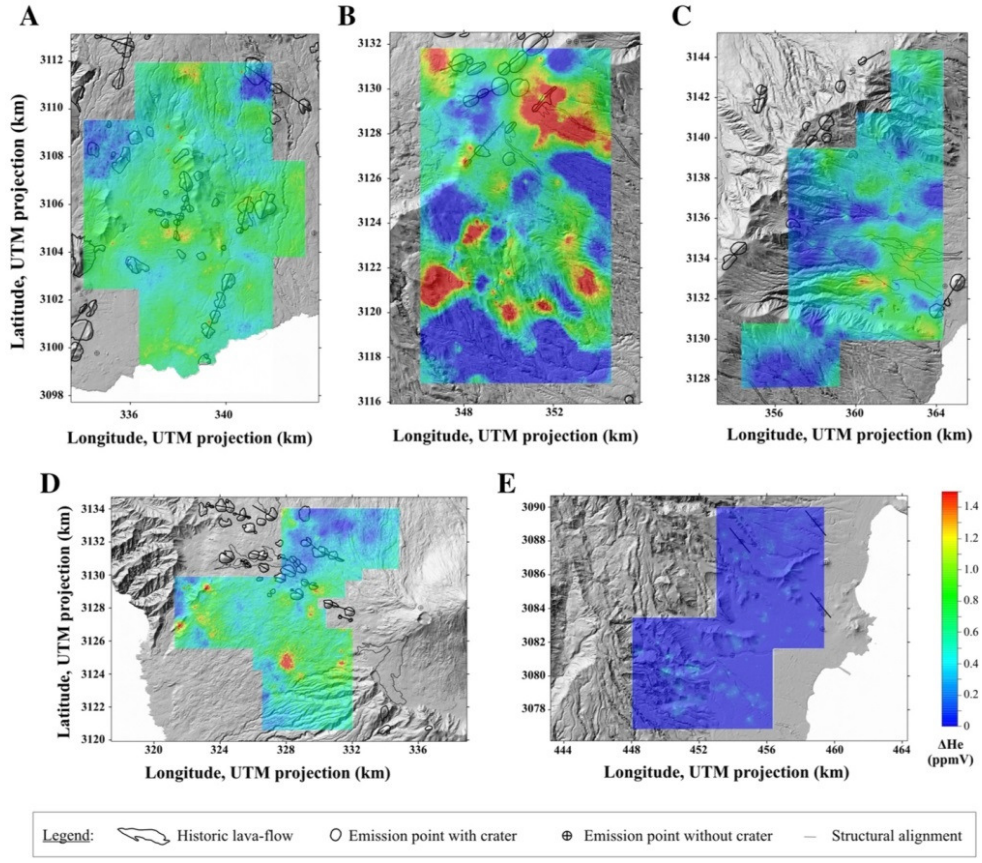

Fig. 4 Spatial distributions of soil ΔHe at *Garehagua* (**a**), *Berolo* (**b**), *Guayafanta* (**c**), *Abeque* (**d**) and *Atidama* (**e**) mining licenses, constructed by the sGs algorithm

populations were distinguished whose mean and percentage were 0.64 ppm (80.41 %) and 12.06 ppm (1.17 %) for the background and peak populations, respectively. The peak value was 18.84 times the background population value. The spatial distribution maps of soil H_2 depicted in Fig. 6a showed multiple isolated anomalies, with a main one located in the central area, following a volcanic alignment of eruption centers, with highest values higher than 10 ppm.

4.1.2 Berolo

Background and peak populations of soil He showed mean values of 5.48 ppm (88.54 % of the total data) and 8.41 ppm (2.92 % of the total data), respectively (Fig. 3b). The rest of the data formed intermediate values. Peak values exceeded by 1.53 times the background population in *Berolo*. Multiple isolated anomalies were detected at the spatial distribution map of soil ΔHe (Fig. 4b). The most important ones were measured in the northern part of the area (>5.0 ppm) and are composed by ∼35 sampling sites that correspond spatially with one of the eruptive centers of the 1704–1705 volcanic eruption (Fasnia eruptive center).

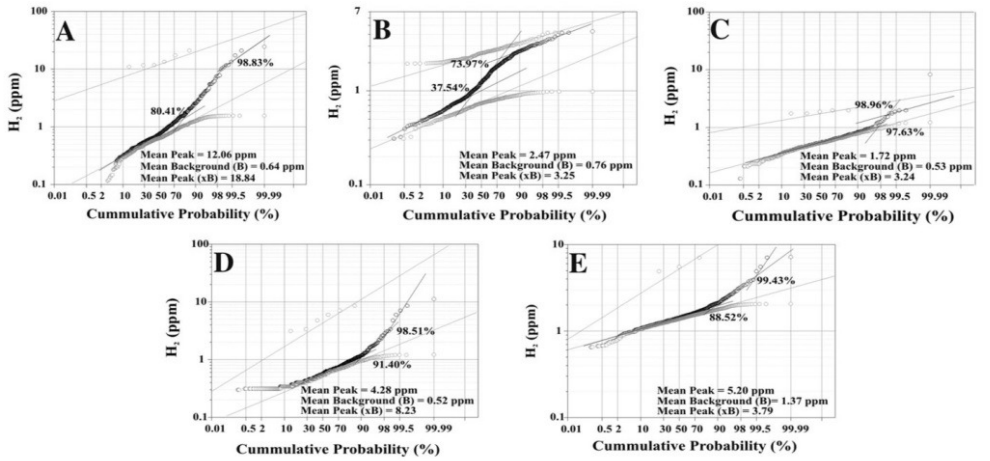

Fig. 5 Cumulative probability plots of soil H_2 measured at *Garehagua* (**a**), *Berolo* (**b**), *Guayafanta* (**c**), *Abeque* (**d**) and *Atidama* (**e**) mining licenses. *Solid black lines* in the probability plots indicate different log-normal geochemical population in the original data. *Solid gray lines* indicate the separated background and peak log-normal populations

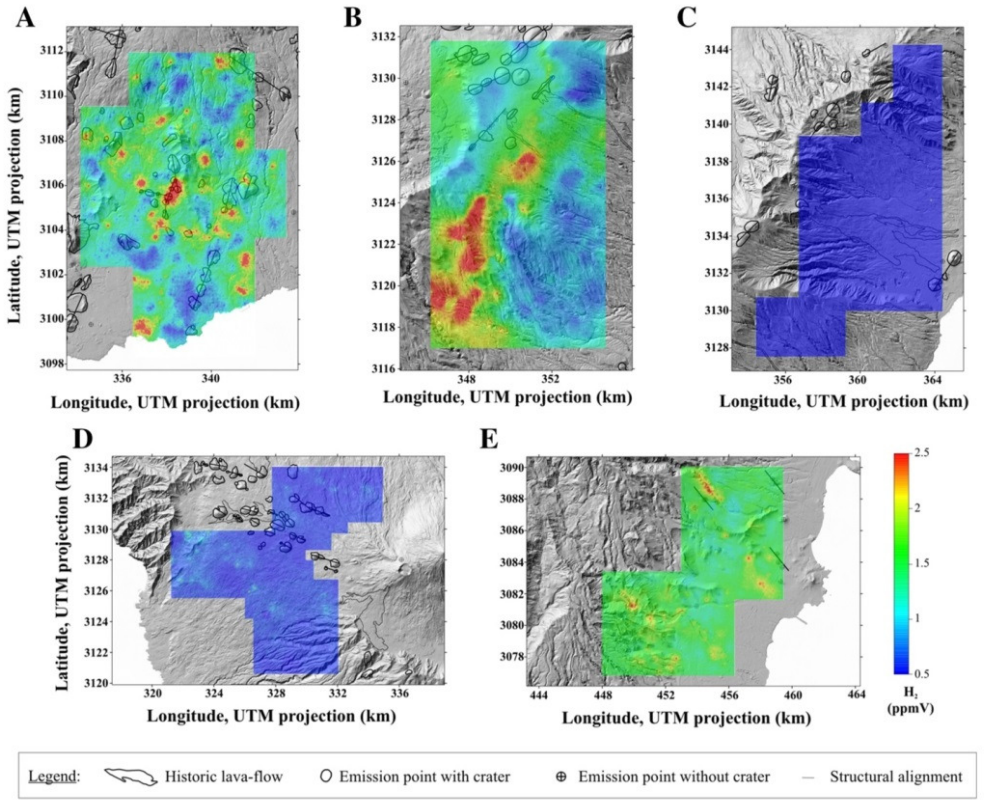

Fig. 6 Spatial distributions of soil H_2 at *Garehagua* (**a**), *Berolo* (**b**), *Guayafanta* (**c**), *Abeque* (**d**) and *Atidama* (**e**) mining licenses, constructed by the sGs algorithm

The probability-plot technique (Fig. 5b) depicted two populations in the soil H_2 data, characterized by a mean and percentage of 0.76 ppm (37.54 %) and 2.47 ppm (26.03 %). In this case, peak values exceeded by 3.25 times the background population. The highest soil H_2 enrichments were measured at the southwestern part of the study area (>4 ppm) and partially overlap with a soil helium enrichment (Fig. 6b).

4.1.3 Guayafanta

One single log-normal was identified in the probability-plot analysis of the soil He data analyzed (Fig. 3c), with a mean value of 5.66 ppm. *Guayafanta* area (Fig. 4c) showed just a single main soil ΔHe anomaly (>1.5 ppm) at southern part, in the border limit of Arafo lava flow emitted during the 1704–1705 volcanic eruption.

The mean and percentage of the background and peak population of soil H_2 were 0.53 ppm (97.63 %) and 1.72 ppm (1.04 %) (Fig. 5c). Peak values of soil H_2 exceeded by 3.24 times the background population. The spatial distribution of soil H_2 (Fig. 6c) did not show any area with a significant enrichment.

4.1.4 Abeque

The probability-plot analysis for soil He data measured in Abeque showed two log-normal geochemical populations (Fig. 3d): background, with a mean of 5.39 ppm (78.80 % of the total data) and peak, with a mean of 8.47 ppm (2.37 % of the total data), exceeding 1.57 times the background value. *Abeque* area showed the highest soil ΔHe value observed in this work and was measured in the west part of the area (>5.0 ppm), but other multiple relatives enrichments were detected as isolated anomalies (Fig. 4d).

In the case of soil H_2 data, *Abeque* showed two overlapping log-normal geochemical populations, with mean and percentage of 0.52 ppm (91.40 %) and 4.28 ppm (1.49 %) (Fig. 5d). In this case, peak values of soil H_2 exceeded by 8.23 times the background population. The only slight enrichments at *Abeque* were measured at the western area (Fig. 6d).

4.1.5 Atidama

In the case of soil helium data, two overlapping log-normal geochemical populations were also observed (Fig. 3e): background (95.18 % of the data) with a mean value of 5.22 ppm and a peak (1.97 % of the data) with a mean value of 6.03 ppm, and intermediate values between both populations. In this case, peak values exceeded 1.15 times the background population. *Atidama* area had the lower soil ΔHe values of the five areas studied in this work (Fig. 4e). Some slights enrichments were observed at southern part of the study area, with a highest value up to 0.8 ppm, close to the location of the exploratory drilling (Fig. 4e).

Soil H_2 measured at *Atidama* showed two overlapping log-normal geochemical populations with mean and percentage of 1.37 ppm (88.52 %) and 5.20 ppm (0.57 %) (Fig. 5e). In this case, peak values of soil H_2 exceeded by 3.79 times the background population. *Atidama* showed important values ($\sim$7 ppm) along a NW–SE trend at the northern part of the study area (Fig. 6e) in good spatial correlation with the structural alignment of the Plio-Quaternary volcanic rift (Anguita et al. 1991; Guillou et al. 2004).

4.2 Chemical Ratios of the Soil Gases

The relative contributions of the soil gases studied here (He and H_2) with other nonreactive gases present in the soil environment (N_2 and Ar) are displayed as ternary N_2–Ar–He and N_2–Ar–H_2 diagrams (Figs. 7, 8). The chemical composition of soil gases in the five study areas plots along a typical atmospheric component partially polluted by endogenous He and H_2. As depicted in Fig. 7, the N_2–Ar–He ternary plot suggests a linear mixing trend of atmospheric air with endogenous gases. This possible endogenous addition of helium is evident in *Abeque* and moderate in *Garehagua* and *Berolo*. The results shown by the N_2–Ar–H_2 ternary plot (Fig. 8) seem to add some slight significance to *Atidama*, but the most obvious endogenous contribution is found in *Garehagua*. In both diagrams, the endogenous component in *Abeque*, *Garehagua* and *Berolo* is higher than in *Guayafanta* and *Atidama*.

The molar ratio between an endogenous gas (helium or hydrogen) and a typical atmospheric component can be useful to discriminate the origin of the anomalous emission zones and to weigh up the input of the deep-seated gases. Therefore, assuming a pure atmospheric origin for Ne and Ar, we used three specific two-components molar ratios (He/Ar, He/Ne and H_2/Ar) since their values would act as indicators of endogenous gases from volcano-hydrothermal activity, assuming that Ar and Ne are present in the hydrothermal fluids in relative contents close to those of air-saturated groundwater (Giggenbach 1991; Chiodini and Marini, 1998; Pedroni et al. 1999). Table 2 shows the percentage of He/Ar, He/Ne and H_2/Ar ratios that exceed by three times that observed in the air. This percentage of He/Ar and He/Ne ratios was higher for *Abeque* and *Garehagua*, whereas that corresponding to H_2/Ar ratio was greater for *Atidama* and *Berolo*. With the aim of sorting the endogenous contribution at each study area, a dimensionless parameter (value in Table 2) from 1 to 5 was assigned to each chemical ratio, being the lowest assigned to the highest chemical ratio values. The same procedure was also applied to the probability-plot parameters of soil ΔHe and H_2 (peak values expressed as times background value, Table 2).

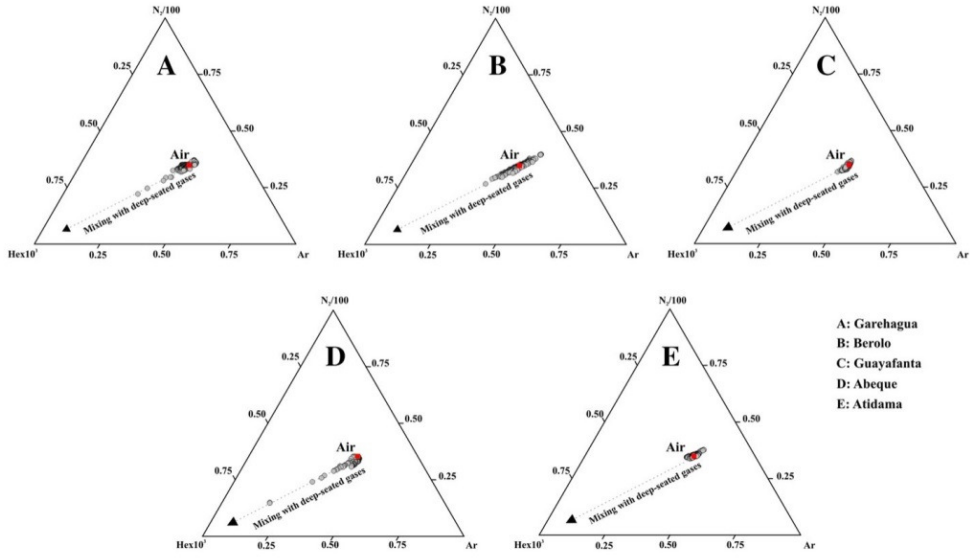

Fig. 7 Ternary N_2–Ar–He diagrams of soil gases at *Garehagua* (**a**), *Berolo* (**b**), *Guayafanta* (**c**), *Abeque* (**d**) and *Atidama* (**e**) mining licenses. *Red squares* indicate the typical air concentration, and *dashed line* shows the mixing trend with deep-seated gas

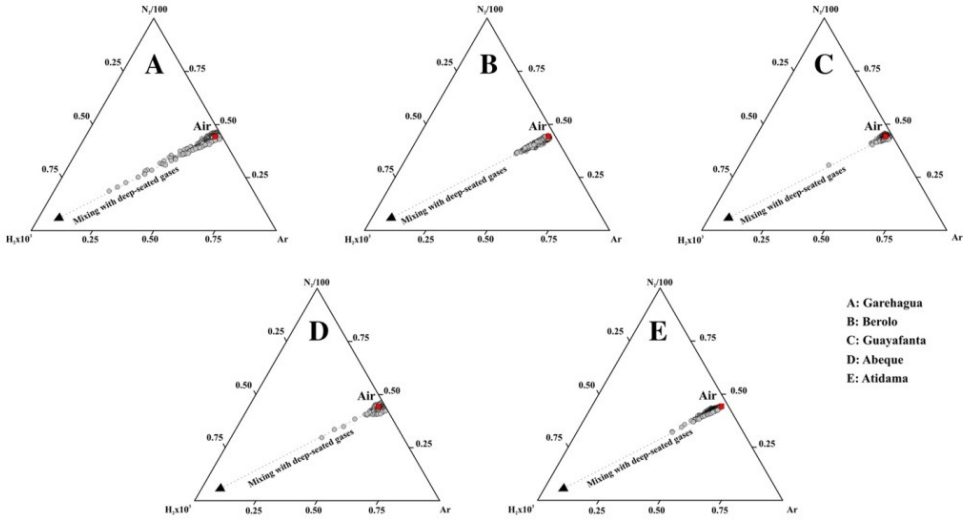

Fig. 8 Ternary N_2–Ar–H_2 diagram of soil gases at *Garehagua* (**a**), *Berolo* (**b**), *Guayafanta* (**c**), *Abeque* (**d**) and *Atidama* (**e**) mining licenses. *Red squares* indicate the typical air concentration, and *dashed line* shows the mixing trend with deep-seated gas

Table 2 Geochemical and geographical characteristics of the mining licenses

Islands	Tenerife				Gran Canaria
Geothermal mining grid	Abeque	Garehagua	Berolo	Guayafanta	Atidama
Area (km^2)	102	100	130	103	104
# Sampling sites	406	557	577	541	600
He mean peak pop. (×background pop.)	1.57	1.70	1.53	–	1.15
Value for He[a]	2	1	3	5	4
H_2 mean peak pop. (×background pop.)	8.23	18.84	3.25	3.24	3.79
Value for H_2[a]	2	1	4	5	3
He/Ar ratio (>3 × air value) (%)	0.57	0.18	0.00	0.00	0.00
Value for He/Ar[a]	1	2	5	5	5
He/Ne ratio (>3 × air value) (%)	0.80	0.18	0.00	0.00	0.00
Value for He/Ne[a]	1	2	5	5	5
H_2/Ar ratio (>3 × air value) (%)	2.00	19.96	39.64	1.11	41.97
Value for H_2/Ar[a]	4	3	2	5	1
Value for N_2–Ar–He diagram[a]	1	2	2	3	3
Value for N_2–Ar–H_2 diagram[a]	2	1	2	3	3
Total geochemical values	13	12	23	31	24

[a] Geochemical values from 1 (best value) to 5 (worst value)

The sum of the total assigned values gave us a way to sort geochemically the five different mining licenses to weigh up the relative potential of finding geothermal resources at each of the study area, thus reducing the uncertainty in the selection of the area with the highest success of future exploratory works.

5 Discussion

Through a visual inspection of soil He and H_2 spatial distributions (Figs. 4, 6) and Fig. 1, it can be stated that there are no spatial relations of soil He and H_2 enrichments and the different lithotypes of Tenerife and Gran Canaria. Hernández et al. (2004) investigated the helium emission and U and Th contents in shallow rocks and soils of Las Cañadas caldera and surroundings, Tenerife Island. Their data indicate that helium was supplied mostly from a deep source, with a minor contribution from U- and Th-rich shallow rocks and soils. These results suggest that peak populations observed in the soil helium probability plots shown in the present work are caused mainly by degassing of deep-seated helium. Although the two different possible sources for helium (shallow degassing by radioactive decay of U- and Th-rich rocks and deep degassing from geothermal systems developed beneath the study areas) cannot be ruled out, those areas with higher values of peak population of soil helium (expressed as times the background population) would show a higher proportion of the deepest component. In the case of Tenerife island, where 4 mining licenses were studied, other evidence to support this assertion is the observed high levels of mantle degassing along the three volcanic rift zones of Tenerife, as pointed out by the constant levels of $^3He/^4He$ ratio ($\sim 7\ R_A$) in groundwater of the island, even though there is no clear evidence of geothermal activity in the surface environment (Pérez et al. 1996). Additionally, the recent results reported by Padrón et al. (2013a, b) during the volcanic unrest that led a submarine volcanic eruption at the southern coast of El Hierro island (see location of El Hierro in Fig. 1) also support that, even when there were clear evidences of magmatic degassing, soil helium enrichments did not exceed the enrichment values shown in this work.

Through the results obtained by the assigned values to the statistical–graphical parameters of soil ΔHe, the importance of the studied mining licenses is sorted as *Garehagua* > *Abeque* > *Berolo* > *Atidama* > *Guayafanta*; this result is very similar to that of soil H_2: *Garehagua* > *Abeque* > *Atidama* > *Berolo* > *Guayafanta*. A visual inspection of the spatial distribution maps (Figs. 4, 6) seems to suggest a different order: *Berolo* > *Abeque* > *Garehagua* > *Guayafanta* > *Atidama* for the soil ΔHe data and *Berolo* > *Garehagua* > *Atidama* > *Abeque* > *Guayafanta* for soil H_2. However, the visual information of the spatial distribution should be treated with caution, especially in *Berolo*.

Table 3 summarizes the parameters used to interpolate the unsampled locations by sGs for soil ΔHe and H_2. The spatial interpolation of data to unsampled locations is strongly influenced by the spatial density of real data, because once a value is simulated in an unsampled location, sGs adds it to the data set and uses as an original data to estimate the variable at the next locations of the grid (Cardellini et al. 2003). Minimum values of spatial densities were used to construct the maps for *Berolo* and *Abeque* mining licenses (Table 3). Additionally, those sample locations separated by distances closer than the range value of the semi-variogram model used are spatially autocorrelated, whereas locations farther apart than the range are not. Soil H_2 and ΔHe data in *Berolo* and *Garehagua,* respectively, showed the higher spatial autocorrelation. These results provide a critical view of the spatial distribution obtained by sGs in *Berolo*, because the relative low spatial density together with the high spatial autocorrelation likely yields an oversized anomaly distribution.

The number of sampling sites with He/Ar, He/Ne and H_2/Ar ratios higher than 3 times the atmospheric value suggests a geothermal potential sorted as *Abeque* > *Garehagua* > *Atidama* > *Berolo* > *Guayafanta* (Table 2). Finally, the visual inspection of the ternary N_2–Ar–He and N_2–Ar–H_2 diagrams (Figs. 7, 8) seems to support the relative order suggested by the

Table 3 Parameters used in the sGs interpolation to construct the spatial distribution maps of soil gas ΔHe and H_2 in the mining licenses

	Number of samples	Study area (km^2)	Average distance between points (m)	Sampling density (points/km^2)	Semi-variogram parameters for soil ΔHe		Semi-variogram parameters for soil H_2	
					Nugget effect	Range (m)	Nugget effect	Range (m)
Abeque	406	102	193	4	0.6	3000	0.8	2500
Atidama	600	104	201	6	0.7	700	0.6	1000
Berolo	577	130	220	4	0.4	1600	0.3	3000
Garehagua	557	100	242	6	0.7	5300	0.7	1000
Guayafanta	541	103	244	5	0.3	1500	0.8	300

statistical–graphical analysis, because the volcano-hydrothermal contribution in the soil helium follows the order *Garehagua* > *Abeque* > *Berolo* > *Atidama* > *Guayafanta* in the case of soil He and *Garehagua* > *Abeque* > *Atidama* > *Berolo* > *Guayafanta* in the case of soil H_2. Combining the overall information shown in this work, we sorted the geothermal potential of the five mining licenses studied here by assigning values from 1 to 5 (where 1 means higher endogenous component; Table 2), resulting as *Garehagua* > *Abeque* > *Berolo* > *Atidama* > *Guayafanta*.

6 Conclusions

There is no current evidence of endogenous fluids manifestations (active or fossil) at the surface environment of the mining licenses studied here that might evidence the presence of active geothermal systems at depth, except the magmatic bubbling gas spot located inside a water gallery at *Garehagua*. However, the presence of relative anomalous concentrations of nonreactive and/or highly mobile gases in the soil gas atmosphere such as helium and hydrogen suggests the current existence of a significant input of deep-seated gases. The spatial distribution maps of the five study areas confirm in some cases the existence of a good spatial correlation between anomalous concentrations values of soil ΔHe and H_2 and historic and/or recent volcanic alignments, which could act as preferential zones of vertical permeability allowing the migration of deep source gases.

Combining the overall information shown in this work, based on statistical–graphical analysis of the data, visual inspection of the spatial distribution and analysis of interesting chemical ratios in the soil gas, it is possible to obtain weighting tools to sort the five different study areas in terms of their relative potential of finding geothermal resources. In this context, *Garehagua* and *Abeque* (corresponding to the southern and western volcanic rifts of Tenerife, respectively) seemed to show the highest geothermal potential of the five mining licenses studied. Additional geochemical and geophysical studies would be necessary to reduce the uncertainty inherent to the selection of the area with the highest success in future exploration works.

Acknowledgments This work has been partially funded by the Projects GEOTHERCAN (IPT-2011-1186-920000) and GEOHELIO (PTQ-12-05661) of the Spanish National R + D + I Plan 2008–2011, the Instituto Tecnológico y de Energías Renovables (ITER), the Instituto Volcanológico de Canarias (INVOLCAN), Petratherm España, the Cabildo de Tenerife and the D.G. Industry and Energy of the Canary Islands

Government. We are especially grateful to D. Nolasco, M. Díaz, R. Antón, D. Aragón, C. Báncora, M. Cordero, P. González, A. González-Santana, D. Mani, A. Nannoni, D. Nieto, R. Pérez, M. Refoyo, P. Rodríguez, A. Toscano and R. Vega for their assistance in the field works and laboratory analysis. We also want to thank Cañadas del Teide National Park and the Municipality of Guía de Isora for the logistic support during the survey periods, as well as to Michael Rycroft and two anonymous reviewers whose useful comments and constructive suggestions greatly improved the manuscript.

References

Agusto M, Tassi F, Caselli AT, Vaselli O, Rouwet D, Capaccioni B, Caliro S, Chiodini G, Darrah T (2013) Gas geochemistry of the magmatic-hydrothermal fluid reservoir in the Copahue–Caviahue volcanic complex (Argentina). J Volcanol Geotherm Res 257:44–56. doi:10.1016/j.jvolgeores.2013.03.003

Albert-Beltrán JF, Araña V, Diez JL, Valentín A (1990) Physical–chemical conditions of the Teide volcanic system (Tenerife, Canary Islands). J Volcanol Geotherm Res 43:321–332. doi:10.1016/0377-0273(90)90059-O

Ancochea E, Fuster JM, Ibarrola E, Cendrero A, Coello J, Hernán F, Cantagrel JM, Jamond C (1990) Volcanic evolution of the island of Tenerife (Canary Islands) in the light of new K–Ar data. J Volcanol Geotherm Res 44:231–249. doi:10.1016/0377-0273(90)90019-C

Anguita F, García-Cacho L, Colombo F, González-Camacho A, Vieira R (1991) Roque Nublo caldera: a new stratocone caldera in Gran Canaria, Canary Islands. J Volcanol Geotherm Res 47:45–63. doi:10.1016/0377-0273(91)90100-E

Ármannsson H, Fridriksson T (2009) Application of geochemical methods in geothermal exploration. In: Presented at "Short course on surface exploration for geothermal resources". UNU-GTP and LaGeo. Ahuachapan and Santa Tecla, El Salvador

Barberi F, Carapezza ML, Cioni R, Lelli M, Menichini M, Ranaldi M, Ricci T, Tarchini L (2013) New geochemical investigations in Platanares and Azacualpa geothermal sites (Honduras). J Volcanol Geotherm Res 257:113–134. doi:10.1016/j.jvolgeores.2013.03.011

Bertrami R, Buonasorte G, Ceccarelli A, Lombardi S, Pieri S, Scandiffio G (1990) Soil gases in geothermal prospecting: two case histories (Sabatini Volcanoes and Alban Hills, Latium, Central Italy). J Geophys Res 95:21475. doi:10.1029/JB095iB13p21475

Cardellini C, Chiodini G, Frondini F, Granieri D, Lewicki J, Peruzzi L (2003) Accumulation chamber measurements of methane fluxes: application to volcanic-geothermal areas and landfills. Appl Geochem 18:45–54. doi:10.1016/S0883-2927(02)00091-4

Carracedo JC (1994) The Canary Islands: an example of structural control on the growth of large oceanic-island volcanoes. J. Volcanol Geotherm Res 60:225–241. doi:10.1016/0377-0273(94)90053-1

Chiodini G, Marini L (1998) Hydrothermal gas equilibria: the H_2O–H_2–CO_2–CO–CH_4 system. Geochim Cosmochim Acta 62:2673–2687. doi:10.1016/S0016-7037(98)00181-1

Chiodini G, Baldini A, Barberi F, Carapezza ML, Cardellini C, Frondini F, Granieri D, Ranaldi M (2007) Carbon dioxide degassing at Latera caldera (Italy): evidence of geothermal reservoir and evaluation of its potential energy. J Geophys Res 112:B12204. doi:10.1029/2006JB004896

Clarke WB, Jenkins WJ, Top Z (1976) Determination of tritium by mass spectrometric measurement of 3 He. Int J Appl Radiat Isot 27:515–522. doi:10.1016/0020-708X(76)90082-X

Conrad R (1996) Soil microorganisms as controllers of atmospheric trace gases (H_2, CO, CH_4, OCS, N_2O, and NO). Microbiol Rev 60:609–640. http://mmbr.asm.org/content/60/4/609.abstract

Deutsch CV, Journel AG (1998) Geostatistical software library and user's guide, 2nd edn. Oxford University Press, Oxford

Di Filippo M, Lombardi S, Nappi G, Reimer GM, Renzulli A, Toro B (1999) Volcano–tectonic structures, gravity and helium in geothermal areas of Tuscany and Latium (Vulsini volcanic district), Italy. Geothermics 28:377–393. doi:10.1016/S0375-6505(99)00014-0

European Commission (1999) Blue book on geothermal resources: a strategic plan for the development of European geothermal sector. Office for Official Publications of the European Communities, Luxembourg. ISBN:9282858030, 9789282858035

Finlayson JB (1992) A soil gas survey over rotorua geothermal field, Rotorua, New Zealand. Geothermics 21:181–195. doi:10.1016/0375-6505(92)90076-L

Fu CC, Yang TF, Walia V, Chen CH (2005) Reconnaissance of soil gas composition over the buried fault and fracture zone in southern Taiwan. Geochem J 39:427–439. doi:10.2343/geochemj

García-Cacho L, Díez-Gil JL, Araña V (1994) A large volcanic debris avalanche in the Pliocene Roque Nublo Stratovolcano, Gran Canaria, Canary Islands. J Volcanol Geotherm Res 63:217–229. doi:10.1016/0377-0273(94)90075-2

García-Yeguas A, Koulakov I, Ibáñez JM, Rietbrock A (2012) High resolution 3D P wave velocity structure beneath Tenerife Island (Canary Islands, Spain) based on tomographic inversion of active-source data. J Geophys Res 117:B09309. doi:10.1029/2011JB008970

Gasparini A, Fontes JC, Custiodio E, Jiménez J, Nuñez JA (1987) Primeros datos sobre las características químicas e isotópicas del agua subterránea del Macizo monolítico de Amurga, Gran Canaria. Simposio Canarias 2000. IV Simposio de hidrogeología (in Spanish)

Gasparini A, Custodio E, Fontes JC, Jiménez J, Nuñez JA (1990) Exemple d'etude geochimiche et isotopique de circulations aquifers en terrain volcanique sous climat semi-aride (Amurga, Gran Canaria, Iles Canaries). J Hydrol 114:61–91. doi:10.1016/0022-1694(90)90075-9

Giggenbach WF (1987) Redox processes governing the chemistry of fumarolic gas discharges from White Island, New Zealand. Appl Geochem 2:143–161. doi:10.1016/0883-2927(87)90030-8

Giggenbach WF (1991) Chemical techniques in geothermal exploration. In: D'Amore F (coordinator) Application of geochemistry in geothermal reservoir development. UNITAR/UNDP publication, Rome, pp 119–142

Gluekauf E (1946) A microanalysis of helium and neon contents of air. Proc R Soc Lond Ser A 185:98–119. doi:10.1098/rspa.1946.0007

Gödde M, Meuser K, Conrad R (2000) Hydrogen consumption and carbon monoxide production in soils with different properties. Biol Fertil Soils 32:129–134

Graham DW (2002) Noble gas isotope geochemistry of mid-ocean ridge and ocean island basalts: characterization of mantle source reservoirs. Rev Mineral Geochem 47:247–317. doi:10.2138/rmg.2002.47.8

Guillou H, Pérez-Torrado FJ, Hansen A, Carracedo JC, Gimeno D (2004) The Plio-Quaternary volcanic evolution of Gran Canaria based on new K–Ar ages and magnetostratigraphy. J Volcanol Geotherm Res 135:221–246. doi:10.1016/j.jvolgeores.2004.03.003

Hernández PA, Pérez NM, Salazar J, Reimer M, Wakita H (2004) Radon and helium in soil gases at Cañadas caldera, Tenerife, Canary Islands, Spain. J Volcanol Geotherm Res 131:59–76. doi:10.1016/S0377-0273(03)00316-0

Hernández PA, Pérez NM, Fridriksson T, Egbert J, Ilyinskaya E, Thárhallsson A, Ívarsson G, Gíslason G, Gunnarsson I, Jónsson B, Padrón E, Melián G, Mori T, Notsu K (2012) Diffuse volcanic degassing and thermal energy release from Hengill volcanic system, Iceland. Bull Volcanol 74:2435–2448. doi:10.1007/s00445-012-0673-2

Instituto Geológico y Minero de España (IGME) (1977) Evaluación del potencial geotérmico de la isla de Lanzarote y selección de anomalías en las Islas Canarias. Informe final I (in Spanish)

Instituto Geológico y Minero de España (IGME) (1979) Convenio con empresa nacional Adaro para prospección geotérmica en las Islas Canarias. Informe final (in Spanish)

Instituto Geológico y Minero de España (IGME) (1993a) Prospección geotérmica de la Caldera de Las Cañadas del Teide (Tenerife). Estudio Geovolcanológico. Informe Final (in Spanish)

Instituto Geológico y Minero de España (IGME) (1993b) Prospección geotérmica de la Caldera de Las Cañadas del Teide (Tenerife). Estudio Geoquímico e Isotópico de las fumarolas del Teide. Informe Final (in Spanish)

Instituto Geológico y Minero de España (IGME) (1993c) Prospección geotérmica de la Caldera de Las Cañadas del Teide (Tenerife) mediante el empleo de scanners aerotransportados sensibles al infrarrojo térmico (in Spanish)

Instituto Geológico y Minero de España (IGME) (1993d) Prospección geotérmica de la Caldera de Las Cañadas del Teide (Tenerife). Termologia Aérea Teide (Nota complementaria) (in Spanish)

Instituto Geológico y Minero de España (IGME) (1993e) Prospección geotérmica de la Caldera de Las Cañadas del Teide (Tenerife). Estudio Hidrogeoquímico. Informe Final (in Spanish)

Instituto Geológico y Minero de España (IGME) (1993f) Prospección geotérmica de la Caldera de Las Cañadas del Teide (Tenerife). Estudio geoquimico general de las aguas subterráneas en la isla de Tenerife. 59 pp. + Anexos (in Spanish)

Instituto Geológico y Minero de España (IGME) (1993g) Investigación geotérmica en las islas Canarias y evaluación de recursos y reservas geotérmicas en España (in Spanish)

Instituto Geológico y Minero de España (IGME) (1993h) Investigación geotérmica en el área central de la isla de Tenerife. Informe Final (in Spanish)

Instituto Geológico y Minero de España (IGME) (2011) Mapa Geológico de Canarias. GRAFCAN Ediciones, Santa Cruz de Tenerife

Kröchert J, Buchner E (2008) Age distribution of cinder cones within the Bandas del Sur Formation, southern Tenerife, Canary Islands. Geol Mag 146:161. doi:10.1017/S001675680800544X

Lewicki J, Oldenburg C (2004) Strategies for detecting hidden geothermal systems by near-surface gas monitoring. Lawrence Berkeley National Laboratory. Retrieved from https://escholarship.org/uc/item/32t1m8wm

Lombardi S, Voltattorni N (2010) Rn, He and CO_2 soil gas geochemistry for the study of active and inactive faults. Appl Geochem 25:1206–1220. doi:10.1016/j.apgeochem.2010.05.006

Marini L, Gambardella B (2005) Geochemical modeling of magmatic gas scrubbing. Ann Geophys 48:739–753. http://hdl.handle.net/2122/935

Marrero R (2010) Modelo Hidrogeoquímico del acuífero de las Cañadas del Teide, Tenerife, Islas Canarias. University of Barcelona, Barcelona (in Spanish)

Martí J, Gudmundsson A (2000) The Las Cañadas caldera (Tenerife, Canary Islands): an overlapping collapse caldera generated by magma-chamber migration. J Volcanol Geotherm Res 103:161–173. doi:10.1016/S0377-0273(00)00221-3

McCarthy KP (1982) Helium and ground temperature surveys at steamboat springs, Colorado. Colorado Geological Survey, United States

McCarthy KP (1983) Helium exploration survey for the Animas Valley, Colorado. Geotherm Resour Counc Bull 12:9–14. ISSN:0160-7782

Mörner NA, Etiope G (2002) Carbon degassing from the lithosphere. Glob Planet Change 33:185–203. doi:10.1016/S0921-8181(02)00070-X

Nicholson K (1993) Geothermal fluids: chemistry and exploration techniques. Springer. ISBN:978-3-642-77844-5

Novelli PC, Lang PM, Masarie KA, Hurst DF, Myers R, Elkins JW (1999) Molecular hydrogen in the troposphere: global distribution and budget. J Geophys Res 104:30427–30444. doi:10.1029/1999JD900788

Olsen KB, Dresel PE, Evans JC, McMahon WL, Poreda R (2006) Measurement of helium isotopes in soil gas as an indicator of tritium groundwater contamination. Environ Sci Technol 40:2895–2902. doi:10.1021/es0518575

Ozima M, Podosek FA (2002) Noble gas geochemistry, 2nd edn. Cambridge University Press, Cambridge

Padrón E, Pérez NM, Hernández PA, Sumino H, Melián GV, Barrancos J, Nolasco D, Padilla G (2012) Helium emission at Cumbre Vieja volcano, La Palma, Canary Islands. Chem Geol 312–313:138–147. doi:10.1016/j.chemgeo.2012.04.018

Padrón E, Padilla G, Hernández PA, Pérez NM, Calvo D, Nolasco D, Barrancos J, Melián GV, Dionis S, Rodríguez F (2013a) Soil gas geochemistry in relation to eruptive fissures on Timanfaya volcano, Lanzarote Island (Canary Islands, Spain). J Volcanol Geotherm Res 250:91–99. doi:10.1016/j.jvolgeores.2012.10.013

Padrón E, Pérez NM, Hernández PA, Sumino H, Melián GV, Barrancos J, Nolasco D, Padilla G, Dionis S, Rodríguez F, Hernández I, Calvo D, Peraza MD, Nagao K (2013b) Diffusive helium emissions as a precursory sign of volcanic unrest. Geology 41:539–542. doi:10.1130/G34027.1

Pedroni A, Hammerschmidt K, Friedrichsen H (1999) He, Ne, Ar and C isotope systematics of geothermal emanations in the Lesser Antilles Islands Arc. Geochim Cosmochim Acta 63(3–4):515–532. doi:10.1016/S0016-7037(99)00018-6

Pérez NM, Nakai S, Wakita H, Hernández PA, Salazar JM (1996) Helium-3 emission in and around Teide volcano, Tenerife, Canary Islands, Spain. Geophys Res Lett 23:3531–3534. doi:10.1029/96GL03470

Pérez NM, Hernández PA, Padrón E, Melián G, Marrero R, Padilla G, Barrancos J, Nolasco D (2007) Precursory subsurface ^{222}Rn and ^{220}Rn degassing signatures of the 2004 seismic crisis at Tenerife, Canary Islands. Pure appl Geophys 164:2431–2448. doi:10.1007/s00024-007-0280-x

Piña-Varas P, Ledo J, Queralt P, Marcuello A, Bellmunt F, Hidalgo R, Messeiller M (2014) 3-D magnetotelluric exploration of tenerife geothermal system (Canary Islands, Spain). Surv Geophys 35:1045–1064. doi:10.1007/s10712-014-9280-4

Reimer GM (1980) Use of soil-gas helium concentrations for earthquake prediction: limitations imposed by diurnal variation. J Geophys Res 85:3107–3114. doi:10.1029/JB085iB06p03107

Reimer GM (1985) Prediction of central California earthquakes from soil-gas helium fluctuations. Pure appl Geophys 122:369–375. doi:10.1007/BF00874605

Reimer GM (1986) Helium soil-gas survey of the aurora uranium deposit, McDermitt Caldera Complex, Oregon. J Geophys Res 91:12355–12358. doi:10.1029/JB091iB12p12355

Reimer GM, Bowles CG (1979) Soil-gas helium concentrations in the vicinity of a uranium deposit, Red Desert, Wyoming. United States Geological Survey, Reston

Rodríguez F, Pérez NM, Padrón E, Melián GV, Piña-Varas P, Dionis S, Barrancos J, Padilla G, Hernández PA, Marrero R, Ledo J, Bellmunt F, Queralt P, Marcuello A, Hidalgo R (2015) Surface geochemical and geophysical studies for geothermal exploration at the Southern Volcanic Rift Zone of Tenerife, Canary Islands, Spain. Geothermics. doi: 10.1016/j.geothermics.2015.02.007

Romero C (1991) Las manifestaciones volcánicas históricas del archipiélago Canario. University of La Laguna (in Spanish)

Schmincke H, Sumita M (1998) Volcanic evolution of Gran Canaria reconstructed from apron sediments: synthesis of Vicap project drilling. In: Weaver PPE, Schmincke H, Firth JV, Duffield W (eds) Proceedings of the ocean drilling program, Scientific Results

Schmincke H, Sumita M (2010) Geological evolution of the Canary Islands: a young volcanic archipelago adjacent to the old African continent. Görres, Koblenz. ISBN 978-3-86972-005-0

Sinclair AJ (1974) Selection of threshold values in geochemical data using probability graphs. J Geochem Explor 3:129–149. doi:10.1016/0375-6742(74)90030-2

Smith-Downey NV, Randerson JT, Eiler JM (2006) Temperature and moisture dependence of soil H_2 uptake measured in the laboratory. Geophys Res Lett 33:L14813. doi:10.1029/2006GL026749

Tennant CB, White ML (1959) Study of the distribution of some geochemical data. Econ Geol 54:1281–1290. doi:10.2113/gsecongeo.54.7.1281

Trevors J (1985) Hydrogen consumption in soil. Plant Soil 2:417–422

Valentín A, Albert-Beltrán JF, Diez JL (1990) Geochemical and geothermal constraints on magma bodies associated with historic activity, Tenerife (Canary Islands). J Volcanol Geotherm Res 44:251–264. doi:10.1016/0377-0273(90)90020-G

Voltattorni N, Sciarra A, Quattrocchi F (2010) The application of soil-gas technique to geothermal exploration: study of hidden potential geothermal systems. In: Proceedings of world geothermal congress, Bali, Indonesia

Werner C, Cardellini C (2006) Comparison of carbon dioxide emissions with fluid upflow, chemistry, and geologic structures at the Rotorua geothermal system, New Zealand. Geothermics 35:221–238. doi:10.1016/j.geothermics.2006.02.006

Geothermics 55 (2015) 195–206

Contents lists available at ScienceDirect

Geothermics

journal homepage: www.elsevier.com/locate/geothermics

Surface geochemical and geophysical studies for geothermal exploration at the southern volcanic rift zone of Tenerife, Canary Islands, Spain

Fátima Rodríguez[a,*], Nemesio M. Pérez[a,b,c], Eleazar Padrón[a,b,c], Gladys Melián[a,b,c], Perla Piña-Varas[d,1], Samara Dionis[a], José Barrancos[a,b], Germán D. Padilla[a,b], Pedro A. Hernández[a,b,c], Rayco Marrero[a,b,2], Juan José Ledo[a,d], Fabián Bellmunt[d], Pilar Queralt[d], Alejandro Marcuello[d], Raúl Hidalgo[e]

[a] Instituto Volcanológico de Canarias (INVOLCAN), 38400 Puerto de la Cruz, Tenerife, Canary Islands, Spain
[b] Environmental Research Division, ITER, 38600 Granadilla de Abona, Tenerife, Canary Islands, Spain
[c] Agencia Insular de Energía de Tenerife (AIET), 38600 Granadilla de Abona, Tenerife, Canary Islands, Spain
[d] Departament de Geodinàmica i Geofísica, Facultad de Geología, GEOMODELS Research Institute, Universitat de Barcelona, C/ Martí Franquès s/n, 08028 Barcelona, Spain
[e] EuroGeol, La Esperanza 2, pta 9, 21200 Aracena, Huelva, Spain

ARTICLE INFO

Article history:
Received 21 October 2014
Accepted 25 February 2015

Keywords:
Geothermal exploration
Soil gas survey
Diffuse degassing
3D Magnetotelluric
Tenerife
Canary Islands

ABSTRACT

A joint geochemistry and magnetotellurics survey was carried out in the southern volcanic rift zone of Tenerife (Canary Islands, Spain) covering an area ~100 km^2 for geothermal exploration purposes. Soil CO_2 and H_2S diffuse effluxes, ^{222}Rn and ^{220}Rn activities, soil He, H_2, N_2, CO_2, O_2 and H_2S concentrations and isotopic composition of CO_2 were measured in 557 selected sampling sites. Magnetotelluric survey (MT) was carried out in the northern part of the study area. A total of 47 MT sites were surveyed and a new 3-D resistivity model was obtained. The observed geochemical anomalies at the soil surface have allowed the detection of areas of deep-seated gas emanations as well as the identification of high vertical permeability volcano-tectonic features in the study area. The resistivity distribution model shows a prominent low-resistivity structure interpreted as a clay alteration cap of variable thickness that might play a role on the mechanism of upward motion of deep-seated gases from the volcano-geothermal system. This is supported by positive correlation between thickness of clay alteration cap and helium emission.

1. Introduction

The Canary Islands, owing to their recent volcanism, are the only Spanish territory with potential high enthalpy geothermal resources (European Commission, 1999). Tenerife (2034 km^2) is the largest island of the archipelago and shows evident geothermal surface manifestations (Teide volcano fumaroles, the only visible discharge of geothermal fluids existing nowadays in the Canary Islands), where gas composition indicates that steam derives from a mature liquid dominated geothermal reservoir with temperatures in the range of 250–300 °C (Hernández et al., 2000). However, very few efforts have been made to develop the potential geothermal energy resources in the archipelago. From the 1970s to the 1990s, the Spanish Geological Survey (IGME) performed intensive research on geothermal resources in the country, due mainly to the oil crisis of the 1970s (Sánchez-Guzmán and García de la Noceda, 2010). Later geothermal research declined sharply and only a few projects on geothermal resources were active in Spain from 1994 to 2006, compared with the many projects carried out during the previous two decades (Sánchez-Guzmán and García de la Noceda, 2010).

The final goal of geothermal exploration in a specific area is to locate and define the size, shape, structure of hidden geothermal resources, and determine their characteristics (fluid type, temperature, chemical composition and ability to produce energy). Exploration methods include a broad range of disciplines such as geochemistry, geophysics, geology and engineering. We report

* Corresponding author at: Instituto Volcanológico de Canarias (INVOLCAN), 38400, Puerto de la Cruz, Tenerife, Canary Islands, Spain. Tel.: +34 922 747770; fax: +34 922747701.
E-mail address: fatima@iter.es (F. Rodríguez).
[1] Present address: Centre for Exploration Targeting, The University of Western Australia, 35 Stirling Highway, Crawley, WA 6009, Australia.
[2] Present address: Laboratorio Nacional de Energia e Geologia (LNEG), Alfragide, 2610-999 Lisboa, Portugal.

http://dx.doi.org/10.1016/j.geothermics.2015.02.007
0375-6505/

herein the results of detailed soil gas and magnetotelluric surveys performed in the southern part of Tenerife Island with the aim of evaluating the application of these techniques for geothermal exploration. The combination of two techniques (geochemical and geophysical) is used to better characterize the existence of geothermal reservoirs in the subsurface of the southern volcanic rift zone of Tenerife. The study area comprises a large part of the southern volcanic rift zone of Tenerife, with an area of ~100 km^2. During the study period, visible geothermal manifestations in the surface environment (i.e. fumaroles, hot springs) were absent in the study area.

1.1. Soil gas geochemistry

Geochemical studies for geothermal exploration are carried out performing a wide chemical and isotopic characterization of evident geothermal manifestations (i.e. fumaroles, hot springs) existing in an area under investigation. However, at those areas where there is a lack of visible geothermal manifestations in the surface environment, geochemical prospecting of soil gases and volatiles in the soil matrix itself can provide useful information on the location of areas where deep-seated fluids can reach the surface along active tectonic structures (Alparone et al., 2004; Giammanco et al., 2006; Hernández et al., 2000; Padrón et al., 2012; Voltattorni et al., 2010; Hanson et al., 2014). Gases released from active geothermal systems, might freely rise through the overlying cover to be detected in the soil surface. Owing to their high mobility, some gases are good pathfinders for concealed geothermal systems. They can escape towards the surface by diffusion, through convective transportation by rising hot fluids and by advective migration along fractures and faults. Therefore, studies on soil gases and volcanic/hydrothermal volatiles have become an important tool to identify vertical permeability areas for the rise of hydrothermal gases in geothermal exploration at those areas where no obvious surface geothermal manifestations are present. These surveys can also help to delineate the boundaries of a geothermal system, particularly where the interpretation and application of geophysical data is difficult.

Among soil gases, a special attention has been addressed to CO_2, Rn, He and H_2. CO_2 is the most abundant gas, after water, in the volatile phase exsolved from magma and hydrothermal systems due to its low solubility in silicate melts (Giggenbach, 1992; Stolper and Holloway, 1988). Different sources can explain the presence of CO_2 in the surface environment: biogenic CO_2, deep seated CO_2 of magmatic and/or hydrothermal origin, crustal carbon including marine limestone and organic carbon from sedimentary rocks and atmospheric CO_2 (Irwin and Barnes, 1980). Helium is considered as an almost ideal geochemical indicator due to its geochemical characteristics (Ciotoli et al., 2004): it is chemically inert, physically stable, sparingly soluble in water under ambient conditions and almost non-adsorbable. Due to its characteristics and its deep origin, helium appears as a powerful pathfinder for crustal discontinuities, faults and fractures (Padrón et al., 2012). Helium enrichment in soil gases is related to migration of fluids from deep sources, controlled by the tectonic characteristics of the studied area (Padrón et al., 2012; Walia et al., 2005). ^{222}Rn is a short-lived decay product derived from the ^{238}U decay series, with a half-life of 3.8 days. Due to its noble characteristics, the spatial pattern of radon contents in the soil gas is useful to unveil active fault zones and vertical permeability structures (Padilla et al., 2013). In volcanic-geothermal systems, the interpretation of soil ^{222}Rn data is often complicated because of the wide variety of factors influencing the source and transport of this gas. In this context, variations in soil ^{222}Rn concentration can be produced by fluid release from new magma injection, crustal micro-fracturing, changes in the temperature and depth of the hydrothermal system and variations in rock permeability because of the opening or sealing of gas conduits, cracks and fissures (Del Pezzo et al., 1981; Hernández et al., 2004; Semprini and Kruger, 1984; Whitehead, 1984). Finally, the low solubility of H_2 in groundwater, coupled with its low atmospheric concentration (~530 ppb, Novelli et al., 1999), make H_2 an excellent tracer for processes operating deep in the crust. High concentrations of H_2 have been often detected in soil and dissolved gases in faulted zones (Sugisaki et al., 1980; Wakita et al., 1980). H_2 can be generated abundantly by several chemical reactions induced by a water–rock interaction.

1.2. Geophysical exploration (magnetotelluric method, MT)

The MT method uses naturally occurring electromagnetic (EM) field variations as a source for imaging the electrical resistivity structure of the earth (Vozoff, 1991). Electrical resistivity is a physical property dominated by the presence of minor phases in the host rock matrix and is complementary to bulk properties determined by seismic and potential field methods. Magnetotelluric data involve simultaneous measurements of temporal variations in the electric and magnetic fields at the Earth's surface (Chave and Jones, 2012). The penetration of the electromagnetic field is a function of the electrical resistivity of the subsurface (ρ; Ωm) and the frequency (f; Hz) of the incident field, referred to as the skin depth: $\delta \approx 500(\rho/f)^{1/2}$ (m). Electric and magnetic fields decay exponentially within the earth over this characteristic distance δ. High-frequency waves penetrate a relatively short distance and low-frequency waves penetrate deeper, averaging over a larger volume. The measured fields are transformed into the frequency domain, and the transfer functions, which relate the electric (E) and magnetic (H) fields, can be estimated:

$$[E] = [Z][H],$$

where Z is the impedance, a frequency-dependent 2×2 complex tensor containing information on the electrical conductivity of the subsurface. The magnetotelluric response functions can be obtained from each impedance tensor element: apparent resistivity (ρ_a) and phase (φ). The appearance of the impedance tensor is related to the dimensionality of the electromagnetic field, which reflects the complexity of the distribution of subsurface conductivity. Structural dimensionality of the dataset requires appropriate multi-dimensional inversion algorithm, since if the MT responses have an intrinsically higher dimension than is being used in the interpretation, the final model will be incorrect (Chave and Jones, 2012).

In volcanic areas with hydrothermal circulation, a clay cap (smectite, smectite–illite) is commonly developed by the alteration of the volcanic rocks (Cumming, 2009; Pellerin et al., 1996). This alteration layer is expected to have a very low permeability, so any gap in this layer could be related with surface manifestations of gases. Magnetotelluric surveys have been used in volcanic areas for structural investigation, geothermal evaluation and hydrothermal circulation (García and Jones, 2010; Heise et al., 2008; Ingham et al., 2009; Uchida and Sasaki, 2006). Five MT surveys have been performed in Tenerife (Coppo et al., 2008, 2010; Ortiz et al., 1986; Piña-Varas et al., 2014; Pous et al., 2002). In this island, the existence of a clay cap was pointed out by Piña-Varas et al. (2014), and its morphology follows the topography at relatively shallow depths (about 1500 m).

In this work, the resistivity structure of the southern volcanic rift zone of Tenerife was determined by a 3-D MT data inversion at 47 sites. This new electrical resistivity model will be correlated with the soil gases distribution presented in this work, since the bulk resistivity is sensitive to factors as fluids content and/or temperature at the surface.

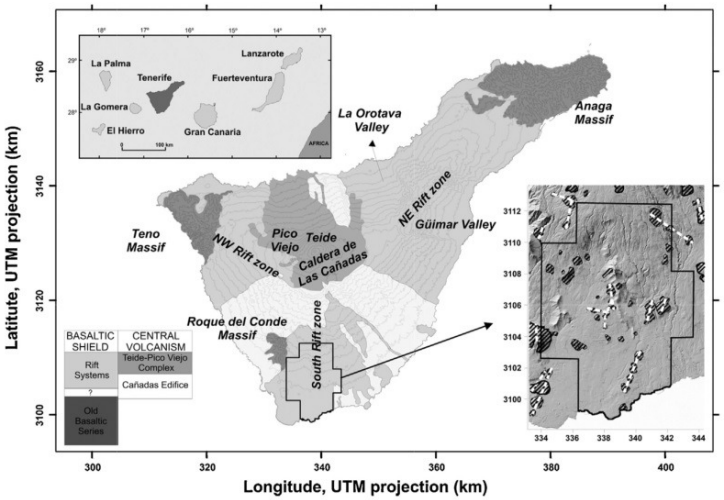

Fig. 1. Geographic location and simplified geologic map of Tenerife Island (modified from (Ablay and Martıí, 2000). Solid black line inside Tenerife bounds the study area (Garehagua mining license). A zoom in of the study area shows a volcano-structural map of the southern volcanic rift of Tenerife Island (modified from Galindo, 2005). Dashed white lines indicate alignments of eruptive centres, highlighted with black line pattern.

2. Geological and structural settings

Tenerife is the largest of the Canary Islands and, together with Gran Canaria island, is the only island with a central volcanic complex, that started to grow at about 3.5 Ma (Ancochea et al., 1990). Nowadays the central complex is formed by Las Cañadas caldera, a volcanic depression measuring 16 km × 9 km that resulted from multiple vertical collapses and was partially filled by post-caldera volcanic products (Ablay and Martıí, 2000) (Fig. 1).

This last activity concentrated mainly on the northern part of the caldera, where the Pico Viejo and Teide stratovolcanoes have been constructed (Ablay and Martıí, 2000). Up to 297 mafic monogenetic cones have been recognized on Tenerife, and they represent the most common eruptive activity occurring on the island during the last 1 Ma (Dóniz et al., 2008). Most of the monogenetic cones are aligned following a triple junction-shaped rift system, as result of inflation produced by the concentration of emission vents and dykes in bands at 120° to one another as a result of minimum stress fracturing of the crust by mantle upwelling (Carracedo, 1994). The study area comprises a large part of the southern volcanic rift zone of Tenerife. Its main structural characteristic is an apparent absence of a distinct ridge and a fan shaped distribution of monogenetic cones (Fig. 1). Kröchert and Buchner (2008), identified four main volcanic successions in the southern volcanic rift zone of Tenerife, temporally separated by long periods (~70–250 ka) without volcanic activity. The authors interpreted the occurrence of syenitic rocks as evidence for shallow magma pockets, located in the distal part of the southern volcanic rift.

3. Methodology

3.1. Soil gases survey

During July and August, 2011, a soil gas survey was undertaken in Garehagua mining license (Fig. 2).

In order to obtain a representative distribution of the whole study area, 557 sampling sites were selected with a homogeneous spatial distribution. The sampling distribution was subject to accessibility constraints, with an average distance between sites of ~250 m. Radon (^{222}Rn) and thoron (^{220}Rn) activities, soil H_2S gas concentration and CO_2 and H_2S diffuse effluxes were measured in situ at each sampling site. ^{222}Rn and ^{220}Rn activities were measured by means of a SARAD RTM 2010-2 radon monitor; the instrument pumped gas through a stainless steel probe inserted at 40 cm depth and measured the ^{222}Rn and ^{220}Rn activities by electrostatic detection of the positively charged daughter isotopes ($^{218}Po^+$, $^{216}Po^+$, $^{214}Po^+$ and $^{212}Po^+$). Soil H_2S gas concentration was measured in a 60 cc soil gas aliquot collected at 40 cm depth with a hypodermic syringe through a stainless steel probe by means of a Arizona Instruments JEROME 631-X. The accumulation chamber method (Parkinson, 1981) was used to perform in situ soil CO_2 and H_2S efflux measurements by means of a portable non-dispersive (NDIR) CO_2 sensor, model LICOR-Li-820 and a αLPHASENSE H2S-A1 sensor, for CO_2 and H_2S respectively. The portable flux-metre was interfaced to a hand-sized computer that runs customized data acquisition software. At each sampling site, both soil temperatures at 15 and at 40 cm depth were also measured by means of a type-R thermocouple.

Additionally, soil gas samples were collected at a depth of 40 cm depth using a stainless steel probe and stored in glass vials for a later analysis in the laboratory. This depth is considered below the major influence of meteorological variables (Hinkle, 1994). CO_2, H_2, N_2 and O_2 contents were analyzed by means of a VARIAN CP4900 micro-gas chromatography. Helium was analyzed by means of a Pfeiffer Omnistar 422 quadrupole mass spectrometer and the isotopic composition of CO_2 (expressed as $\delta^{13}C_{CO_2}$, defined as ‰ deviation vs. VPDB) by a Thermo Finnigan MAT 253 isotope ratio mass spectrometer.

Spatial distribution maps of the studied variables were constructed using sequential Gaussian simulation (sGs) provided by the *sgsim* program (Cardellini et al., 2003; Deutsch and Journel, 1998). The final maps were constructed as an average of the 100 equiprobable realizations displayed over a grid of 159,615 squared cells (25 m × 25 m). A statistical-graphical analysis (Sinclair, 1974)

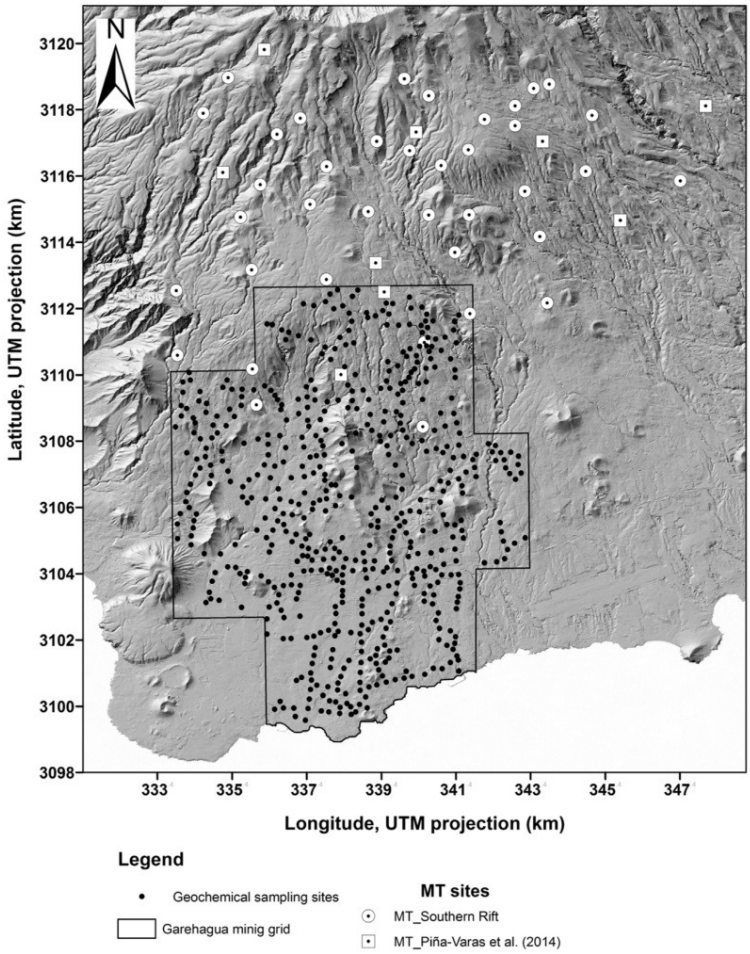

Fig. 2. Location of sampling points selected for geochemical analysis (solid black circles) and MT stations (white circles). The location of the MT stations reported by Piña-Varas et al. (2014) is shown as white squares.

was applied to the data in order to check the presence of a single or multiple statistical populations. This technique consists on plotting the logarithm of the data vs. the cumulative frequency percent on a probability scale. In such scale a log-normal (Gaussian) cumulative distribution plots as a straight line. The bimodal distribution consisting on two log-normal populations plots as an S-type curve. The inflection point of the curve allows us to distinguish the threshold value between both populations.

3.2. MT survey and data

In this work, a dataset consisting of 47 broadband (10^{-3}–10^{2} s) magnetotelluric soundings was used. The MT data were acquired in different surveys, 9 sites correspond to those surveyed in a previous work carried out by Piña-Varas et al. (2014) and 38 were surveyed specifically for this study (Fig. 2). Only six MT sites are located inside the Garehagua mining license due to the anthropogenic electromagnetic noise present in the southern area of the island. Some tests were undertaken in this area, but the low quality of the MT data led us to discard the possibility of acquiring more data further south. For the acquisition of the new MT data the instrumentation consisted of Metronix ADU06 and Metronix ADU07 magnetometers. The *x*-axis was oriented magnetic *N* and *y*-axis was oriented according to magnetic *E*. At each site, the four horizontal components of the electromagnetic field (*ex*, *ey*, *hx* and *hy*) were recorded at periods of 10^{-3}–10^{2} s.

4. Results

4.1. Soil gas survey

A summary of the chemical composition of the 557 soil gas samples is shown in Table 1.

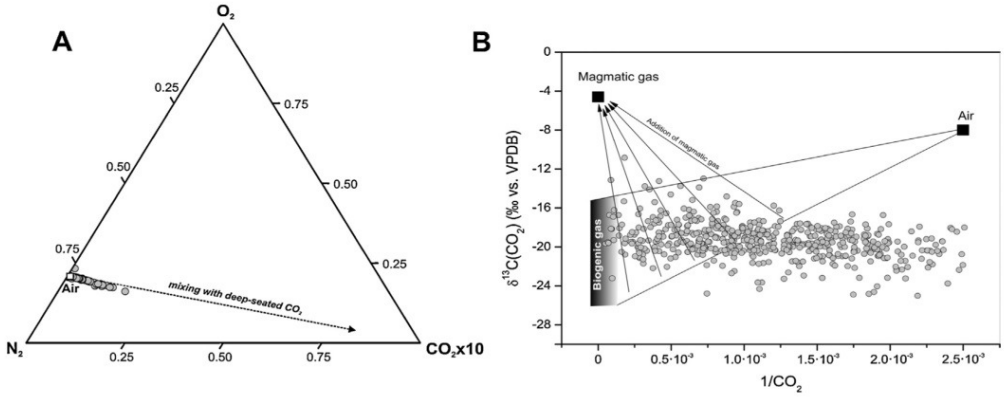

Fig. 3. (A) N_2–CO_2–O_2 diagram of soil gases from the study area. White square shows the typical air end-member and dashed line shows the mixing trend with deep-seated CO_2. (B) Graph of carbon isotopic composition of soil CO_2 vs. the reciprocal of CO_2 concentration in the gas samples collected in this study.

Table 1
Statistical summary of the analytical results of the soil gas concentration and fluxes measured at Garehagua mining license.

	Max.	Min.	Average	SD
Soil temperature (40 cm depth)	40.7	21.6	31.0	3.2
Diffuse CO_2 efflux (g m^{-2} d^{-1})	37.7	<0.5	2.2	3.0
Diffuse H_2S efflux (g m^{-2} d^{-1})	n.d.	n.d.	–	–
H_2S (ppm)	0.24	0.001	0.03	0.06
^{222}Rn (pCi L^{-1})	290.0	<5	43.9	40.3
CO_2 (mol.%)	1.9	0.04	0.15	0.19
H_2 (ppm)	24.4	<0.5	1.4	2.1
N_2 (mol.%)	81.2	68.5	77.9	0.62
O_2 (mol.%)	21.3	18.8	20.7	0.23
ΔHe (ppb)	20,963	−973	925	2506
$\delta^{13}C$ (CO_2) (‰ vs. VPDB)	−10.9	−25.0	−19.3	1.8

SD – standard deviation.

No significant soil H_2S emissions were measured, therefore this parameter will not be discussed. As indicated by the N_2–CO_2–O_2 ternary plot (Fig. 3A), the chemical composition of the gases follows the typical atmospheric component with a significant addition of CO_2. In order to check the origin of CO_2, a binary diagram of $\delta^{13}C(CO_2)$ vs. $1/[CO_2]$ was constructed assuming three geochemical reservoirs (Fig. 3B): (i) air, characterized by $\delta^{13}C(CO_2) = -8‰$ and $1/[CO_2] = 2.5 \times 10^{-3}$ ppm V^{-1}; (ii) magmatic gas, with $\delta^{13}C(CO_2) = -6.5‰$ and $1/[CO_2] = 10^{-6}$ ppm V^{-1}; (iii) and Biogenic gas, defined by $-26‰ > \delta^{13}C(CO_2) > -15‰$. The range of the biogenic end-member was selected since the isotopic composition of soil organic matter is in the range $-30‰ > \delta^{13}C(CO_2) > -20‰$ (Craig, 1953), and the biogenic CO_2 in the soil can be +4.4‰ heavier than the soil-respired CO_2 produced by roots, due to CO_2 fractionation by diffusion within the soil (Cerling et al., 1991). CO_2

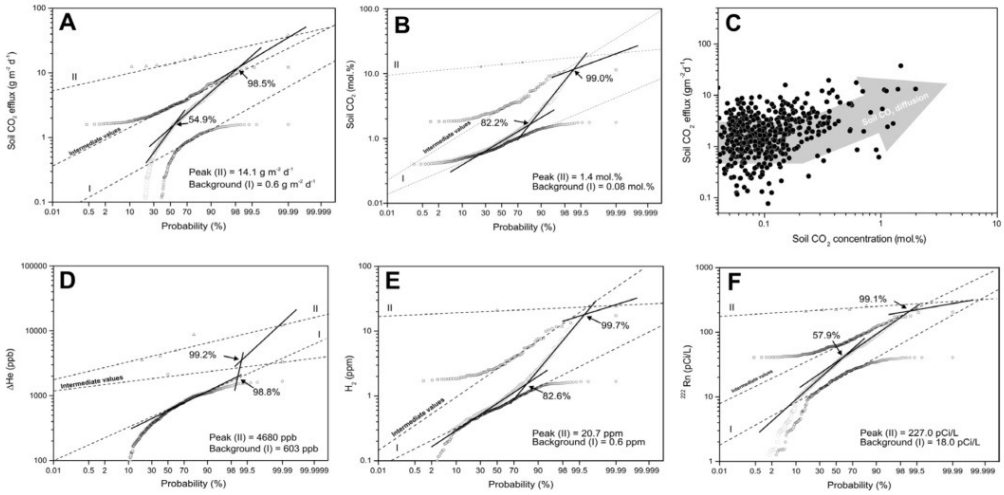

Fig. 4. Cumulative probability plots of soil CO_2 efflux (A), and CO_2 concentration values (B). Binary diagram between the diffuse CO_2 emission vs. CO_2 concentration values (C). Cumulative probability plots of soil ΔHe (D), H_2 concentration (E) and ^{222}Rn activity values (F) measured in 557 sampling sites at Garehagua. Solid lines in the probability plots indicate different log-normal geochemical populations in the original data. Dashed lines indicate background, peak and intermediate log-normal populations separated from the original data. Open grey circles represent the original data. I and II represent background (open black circles) and peak population (open triangles), respectively. The rest of the data (intermediate population) represents a mixing between background and peak values (open squares).

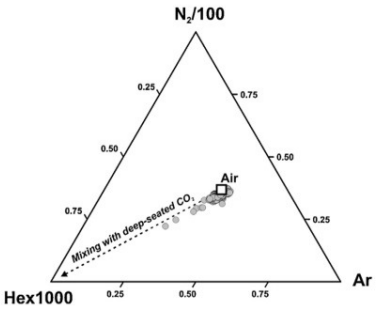

Fig. 5. He–Ar–N_2 diagram of soil gases from the study area. The white square shows the typical air concentration and the dashed line shows the mixing trend with deep-seated gas.

concentration values in the soil atmosphere ranged from air values (~0.04 mol.%) to 1.99 mol.%, with an average of 0.15 mol.%. The isotopic composition of carbon in the soil CO_2 ranged from −25.0 to −10.9‰, with an average value of −19.3‰. Fig. 3B shows that most of the samples plotted in the range defined by the biogenic reservoir, with different soil CO_2 concentrations. No significant atmospheric contribution was observed. However, few samples (~6) showed a significant contribution of deep seated CO_2.

The addition of deep-seated CO_2 is suggested also by the existence of different geochemical populations in the soil CO_2 efflux and CO_2 concentration data, as depicted by the cumulative probability plots (Fig. 4A and B).

In the case of soil CO_2 efflux, the values ranged from non-detectable (<0.5 g m^{-2} d^{-1}) to 37.7 g m^{-2} d^{-1}, with an average value of 2.2 g m^{-2} d^{-1}. Two overlapping log-normal geochemical populations were distinguished (Fig. 4A): background and peak populations. Background population, indicated as population I, represented 54.9% of the data and had an average value of 0.6 g m^{-2} d^{-1}; population II, or peak population, represents 1.5% of the data and has an average value of 14.1 g m^{-2} d^{-1}. The rest of the data were composed by values between background and peak, and represented 43.6% of the data. Background population is associated mainly with biogenic CO_2 production, while peak population suggests a slight deep CO_2 contribution. Recently, Pérez et al. (2012) demonstrated that even low CO_2 emissions values measured at El Hierro (Canary Islands) can be related to an endogenous (magmatic) origin.

In the case of soil CO_2 concentration, the probability plot showed again two geochemical populations: background or population I (82.2% of the total data), that showed an average of 0.08 mol.% and the peak or population II (1% of the total data), that showed an average of 1.4 mol.% (Fig. 4B). The binary diagram between diffuse CO_2 efflux and CO_2 concentration at 40 cm depth (Fig. 4C) indicates the absence of any significant correlation at low values between the two variables. This suggests a complex gas transport mechanism at

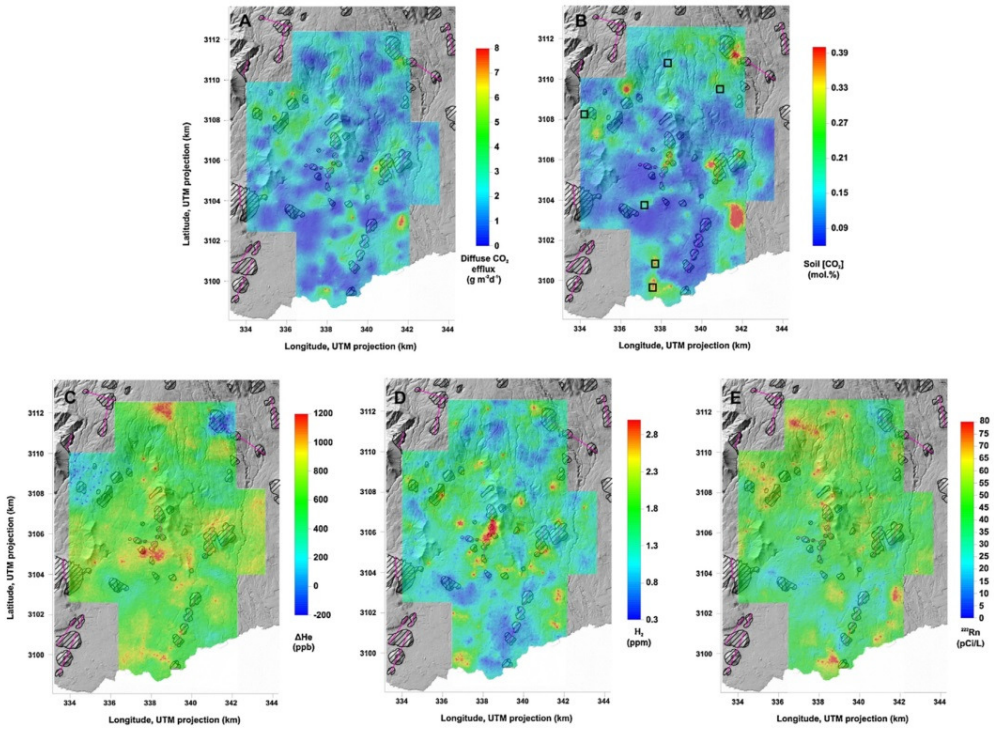

Fig. 6. Spatial distributions of diffuse CO_2 efflux (A), soil CO_2 concentration (B), ΔHe (C), H_2 concentration (D) and ^{222}Rn values (E), based on 100 equiprobable sequential Gaussian simulations. Open squares in (B) indicate the location of samples showing a significant contribution of deep seated CO_2 in Fig. 3B. The location of eruptive fissures (pink lines) and vents (hatched areas) is also shown. (For interpretation of the references to colour in this figure legend, the reader is referred to the web version of the article.)

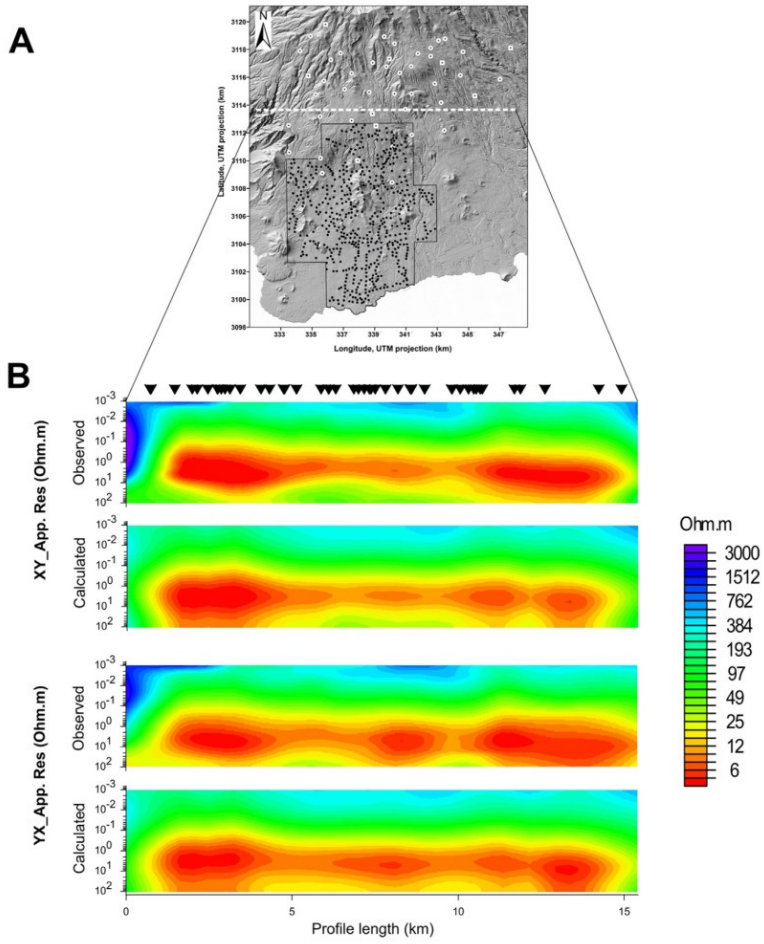

Fig. 7. Pseudosection plots of Z_{xy} and Z_{yx} apparent resistivities and phases of impedance tensors for observed and predicted (calculated) data along WE section. Black triangles correspond to the MT sites.

low values that includes diffusion and advection, the latter probably caused by meteorological conditions (i.e. daily variations in the pressure gradient between barometric pressure and gas pressure in the soil environment). At higher CO_2 concentrations, diffusion seems to be the main gas transport mechanism, due to the apparent correlation observed between the two parameters at CO_2 concentrations above 0.1 mol.%. Different diffusion coefficients for CO_2 are probably responsible for this apparent correlation, depending, among other factors, on the presence of CO_2-emitting roots in the soils, root channels, moisture variability and presence of organic matter (Billings et al., 2000).

The presence of endogenous gases in the soils of the study area can be also inferred by the existence of different geochemical populations in the soil He (Fig. 4D), H_2 concentration (Fig. 4E) and ^{222}Rn values (Fig. 4F). Soil helium enrichments are shown as ΔHe [$\Delta He = [He]_{soil\ atmosphere} - [He]_{air}$], being $[He]_{air} = 5240$ ppb (Gluekauf, 1946). ΔHe values measured on the soil atmosphere ranged from −972 to 12,188 ppb, with an average of 621 ppb. The probability plot technique depicted two geochemical populations (Fig. 4D): background and peak, with an average of 603 ppb for the background population (which represented 98.8% of the total data) and an average of 4680 ppb for the peak population (0.8% of the total data). Background ΔHe values are mainly due to radiogenic (crustal) helium emission and peak values may correspond to an additional volcano-hydrothermal contribution, with an important magmatic component. The latter was previously detected in the groundwater of the study area as having high $^3He/^4He$ ratio values (Marrero, 2010; Pérez et al., 1996). Soil H_2 values ranged from typical atmospheric values (~0.5 ppm) up to 24.4 ppm, with an average value of 1.4 ppm. Two log-normal geochemical populations were distinguished in the H_2 probability plot analysis (Fig. 4E): background population (82.6% of the total data), with an average value of 0.6 ppm; and peak population (0.3% of the total data), with an average value of 20.7 ppm. Different biological processes as those produced by microorganisms and soil enzymes might participate in decomposing H_2 and hence they could mask the original endogenous H_2 supply into the soil (Conrad and Seiler, 1981). Very few soil H_2 data are available to be compared with the data reported here.

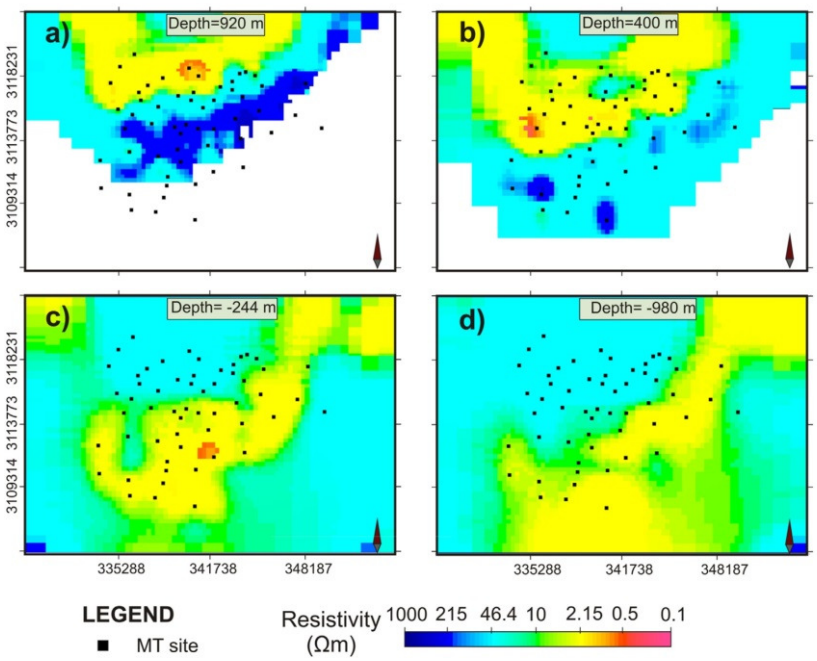

Fig. 8. Horizontal slices through the 3-D resistivity model at different depths.

The background value is similar to that measured at Poás volcano (Costa Rica) in a quiescence period (~0.6 ppm, Melián et al., 2007).

In the case of soil ^{222}Rn values, they ranged from non-detectable values (<5 pCi L^{-1}) to 290 pCi L^{-1}, with an average of 43.9 pCi L^{-1}. The statistical graphical analysis (Fig. 4F) showed again two overlapping geochemical populations: background (57.9% of the data) with an average value of 18 pCi L^{-1} and a peak population (0.9% of the data) with an average value of 227 pCi L^{-1}. The presence of different log-normal populations might be explained by a contribution of ^{222}Rn from natural radioactive decay in the soils of the study area and an endogenous contribution of this gas from deeper sources. The background values are similar to those found at other volcanic systems in the Canaries: i.e. the island of El Hierro (~16 pCi L^{-1}, Padilla et al., 2013) and Timanfaya volcano (~10.3 pCi L^{-1}, Padrón et al., 2013), although lower than those measured in the Cañadas Caldera (~50 pCi L^{-1}, Hernández et al., 2004). The ternary plot constructed with the relative concentrations of the non-reactive gases He–Ar–N_2 (Fig. 5) also suggests the presence of endogenous gases in the soils of the study area. The He-enriched soil gases plotted on a mixing line between air and a He-rich magmatic-hydrothermal end-member (deep-seated gas) (Fig. 5).

Fig. 6 shows the spatial distribution maps of soil CO_2 efflux, [CO_2], ΔHe, [H_2] and ^{222}Rn activity. The highest CO_2 efflux values (Fig. 6A) were measured as multiple isolated anomalies. Its spatial distribution suggests three main areas with relatively high diffuse CO_2 degassing: the southern half of the area, characterized by a linear distribution of anomalous CO_2 effluxes along NS; the NW part of the area, showing an apparent NE–SW trend; and the SE corner of the area, with no clear direction. The first two areas seem to correspond nicely with the location of old eruptive vents. Similar results were obtained in 2002 by Galindo (2005). The total CO_2 output in the study area was estimated at 187 6.2 t d^{-1}, which correspond to 1.9 t d^{-1} km^{-2}. The spatial distribution of soil CO_2 concentration is shown in Fig. 6B. No significant trend in the anomalous values can be observed. Samples that showed a significant contribution of deep seated CO_2 in Fig. 3B, are depicted as open squares in Fig. 6B. In the spatial distribution of ΔHe (Fig. 6C), the highest values were measured in the centre of the study area, and minor anomalies were detected both in its southern and northern parts. It is noteworthy that the highest values in the north of the study area were measured in the vertical surface of a visible gas emission (bubbling gas) that occurs at 2.3 km from the entrance of a horizontal well for groundwater caption (gallery). This gas shows a significant magmatic helium component, with relatively high ^{3}He/^{4}He ratio [6.95 R/Ra and 6.28 R/Ra, measured in 1993 and 2006 by Marrero (2010) and Pérez et al. (1996)]. Fig. 6D depicts the spatial distribution of soil H_2. As observed for the distribution of soil ΔHe, the central part of the area showed significant soil H_2 values. Finally, ^{222}Rn activity in the soil gases, depicted in Fig. 6E, shows multiple "spot" anomalies with a non-clear direction. Important soil ^{222}Rn activity values were observed in the N-W and S-E of the study area.

4.2. Geophysical results

4.2.1. 3-D inversion

A 3-D electrical resistivity model of the southern volcanic rift zone of Tenerife has been computed with ModEm code (Egbert and Kelbert, 2012). In total, 47 MT sites were chosen from the different field surveys. The model is discretized on a 93 × 72 × 133 layer grid and the inversions are undertaken using the off-diagonal components (Z_{xy}, Z_{yx}) of the impedance tensor for 30 periods in the frequency range from 10^{-3} to 10^2 s. Maps of the apparent resistivity from determinant of impedance tensors in four periods are shown as supplementary material (Fig. S-1).

In the inversion process, a 5% error baseline in the impedance components was imposed. The starting model was that obtained

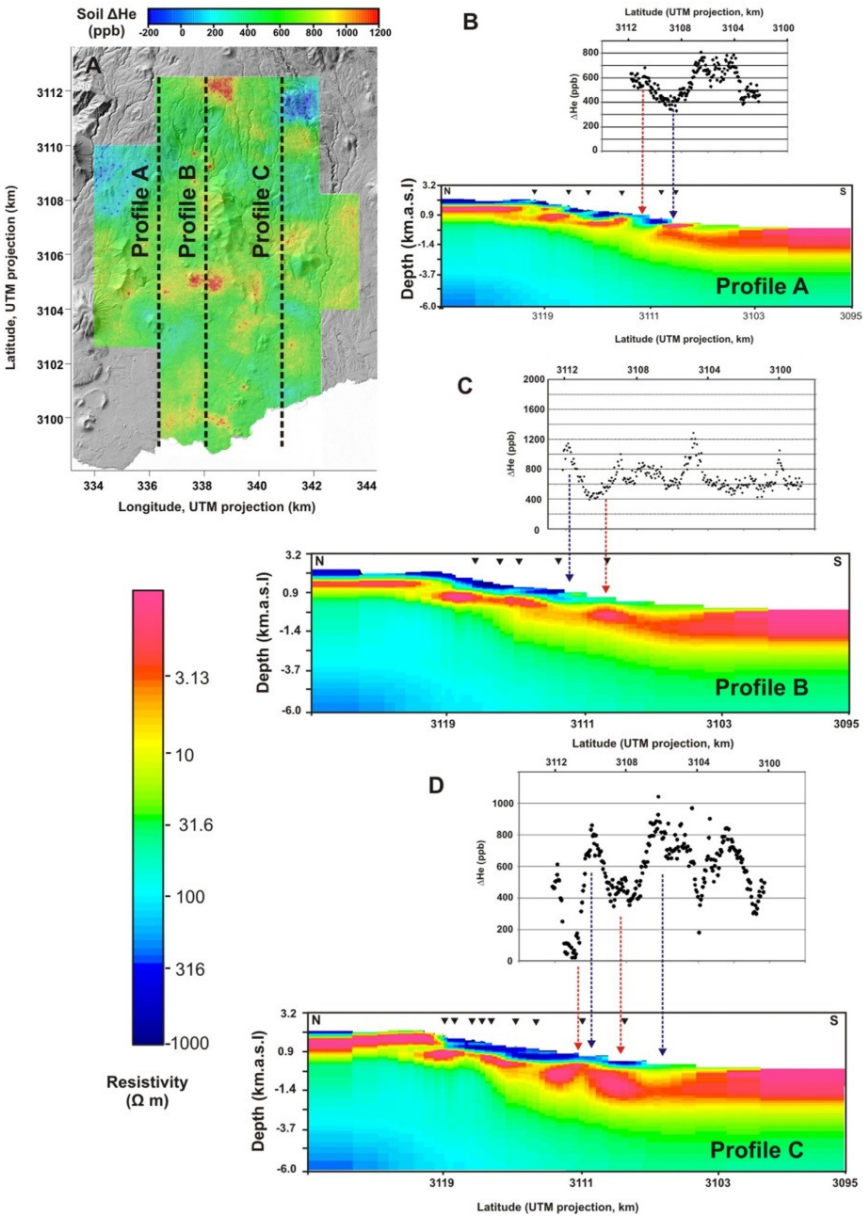

Fig. 9. (A) ΔHe map showing the location of the N–S resistivity cross-section corresponding to three N–S profiles. (B), (C) and (D) depict values of soil ΔHe and results of the final 3-D resistivity model along A, B and C vertical N–S cross-sections respectively. Blue and red dashed arrows indicate observed positive and negative correlation between highest values of ΔHe and clay cap discontinuities and lowest values of ΔHe and the thicker clay cap, respectively. Inverse black triangles show the location of MT sites within each profile. (For interpretation of the references to colour in this figure legend, the reader is referred to the web version of the article.)

by Piña-Varas et al. (2014) for the whole island. The starting RMS was 11.56, while the final RMS was 1.99 after 60 iterations. This model includes the topography, obtained from a digital elevation model, and the surrounding ocean, which was fixed during the inversion process with a resistivity value of 0.33 Ωm. Fig. 7 shows the model fit by comparison of the apparent resistivity and phases between the model responses and the raw data.

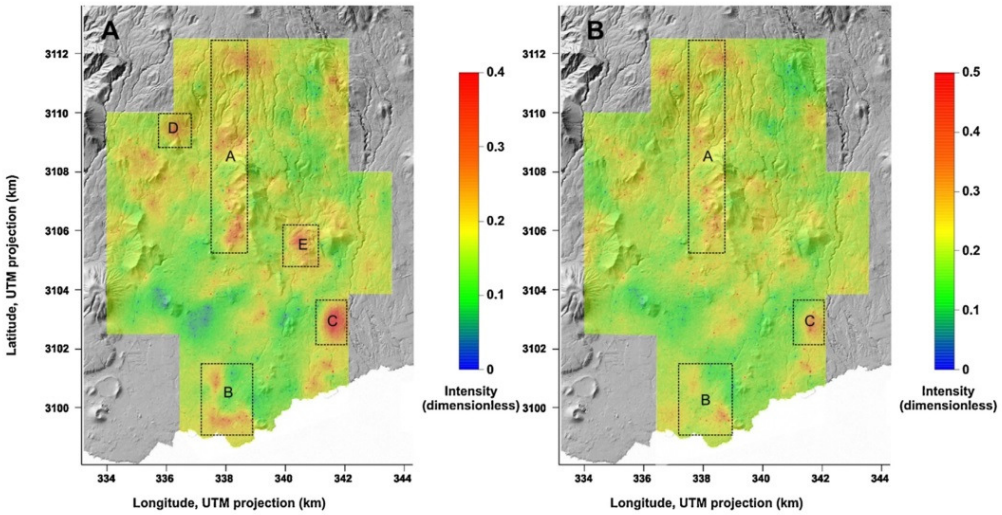

Fig. 10. Spatial distribution of the anomaly intensity based on normalized data of soil gases concentrations and diffuse CO_2 emission. (A) Includes diffuse CO_2 efflux, soil CO_2 concentration, ΔHe, H_2 concentration and ^{222}Rn activity. (B) Includes ΔHe, H_2 concentration and ^{222}Rn activity. Dotted squares with A, B, C, D and E represent areas with the highest intensity of the values.

4.2.2. 3-D resistivity model

The final 3-D resistivity inversion model is shown in Figs. 8 and 9. Fig. 8 shows four horizontal slices through the 3-D model at different depths. The most evident feature is a low resistivity body (<10 Ωm) that occupies most of the model area. This anomaly appears in the northern part of the model area at low depths, whereas it is shifting towards the south with increasing depth. It is semi-circular shaped, with the central area occupied by moderate resistivities (20–100 Ωm).

Three different N–S vertical cross-sections of the 3-D model are shown in Fig. 9. As in the case of the horizontal slices (Fig. 8), the most prominent feature is a low resistivity layer that follows the topography of the study area. A similar structure was observed in the whole island. In the 3-D resistivity model presented by Piña-Varas et al. (2014), four geoelectrical structures were distinguished according to the resistivity values: (1) a low resistivity central region (<10 Ωm), interpreted as the clay cap of the geothermal system; (2) the area surrounding the low resistivity body occupied by low-medium values of resistivity (20–100 Ωm) and corresponding to rocks at higher temperatures; (3) A shallow part, corresponding to high resistivity values (>500 Ωm), correlated with unaltered basaltic rocks; (4) a deeper structure with medium-high resistivities (100–500 Ωm), associated to a hotter part of the geothermal system. This interpretation is also suitable for the MT model presented in this work.

5. Discussion

Multiple isolated anomalies in the studied parameters (soil CO_2 concentration and efflux, soil He, H_2 concentration, and ^{222}Rn activity), were observed in the studied area. The locations of these anomalous enrichments in soil gases and in their fluxes, however, were located along well-defined volcano-tectonic structures. In order to make these vertical permeability structures more visible, a map including the anomalous enrichments in each cell of the grid was constructed: each grid cell was normalized by dividing their value by the maximum measured; later a new grid was constructed by summing the value (from 0 to 1) of each normalized grid and normalizing it in turn. The resulting grid includes information of all the studied parameters at each cell and is depicted in Fig. 10. Fig. 10A includes all the parameters described above. Due to the high percentage of biogenic CO_2 present, as deduced by Fig. 3B, an additional spatial distribution map was constructed only with soil He, H_2 concentration and ^{222}Rn activity (Fig. 10B). In both Fig. 10A and B, three main vertical permeability structures can be defined: A, B and C. These sub-areas showed important enrichment in the studied parameters (Fig. 10A) and persist even when soil CO_2 concentration and efflux are not considered (Fig. 10B).

Areas A and B extend mainly along an N–S direction, which corresponds to the dominant structural direction in this area. These main degassing structures are not spatially continuous, probably due to the different gas-bearing properties of the main N–S volcanic rift of Tenerife as shown by Ciotoli et al. (2004) and Voltattorni et al. (2010). The N−−S-directed volcanic-rift of Tenerife seems to be an area of enhanced permeability for deep gas migration and hence a preferential route for diffuse degassing, similar to what observed in other volcanic rifts in the Canary Islands (Padrón et al., 2012). It is worth noting that volcanic rifts are complex structures that include wide fracture zones that can also be cross-cut by other faults, thus resulting in multiple isolated anomalies, as observed at other volcanic systems (Voltattorni et al., 2010). This might be a possible explanation for the presence of spotty anomalies at both sides of the main N–S-directed vertical permeability structure. Another important vertical permeability zone is indicated as C in Fig. 10. Although this area does not seem to follow the main N–S degassing zone (A and B), the maximum values of several of the studied parameters were measured there.

The 3-D resistivity model obtained in this study shows a very low-resistivity structure interpreted as a clay layer derived from hydrothermal alteration. This clay cap is expected to have a very low permeability, thus acting as a seal and reducing the leakage of deep fluids. Therefore, the continuity and extent of the clay cap should have a strong influence in determining the location of the surface manifestation of gas emissions. Fig. 9 shows three

N–S-directed resistivity cross-sections extracted from the 3-D resistivity model and the spatial distribution of ΔHe data along the corresponding meridian. The distribution of resistivity values shows some gaps that may be associated with a reduced thickness of the clay alteration cap, resulting in enhanced permeability areas. Comparison of the MT section with the ΔHe distribution (Fig. 9C) shows a relatively good correlation between the discontinuities observed in the clay cap and the highest values of ΔHe. This correlation might be useful to infer the thickness of the clay cap towards the south of the studied area, where the MT results lose resolution due to anthropogenic noise (Fig. 9C). Regarding the values of CO_2, H_2 and ^{222}Rn, no relationship with the resistivity distribution was observed along this profile.

6. Conclusions

Soil gas surveys in the study area provided useful information about the mechanisms of uprising of deep-seated gases and they helped finding vertical permeability structures that favour leakage of endogenous gases from the volcano-geothermal system. Three different spatial clusters in the highest values of soil gas He, H_2 and ^{222}Rn were observed in the study area. Two of them were located along the main volcano-tectonic structural trend of the study area which is mainly N–S-directed. The uneven spatial distribution of the highest values of the soil gas species investigated here reflects a complex pattern of volcano-tectonic structures in the study area, where wide fracture zones are cut by transversal faults.

A 3-D resistivity model of the study area was produced through a magnetotelluric survey, showing a geoelectrical distribution typical of a high-temperature geothermal system with a low resistivity layer, interpreted as an impermeable clay cap. An inverse correlation between the thickness of this clay alteration cap and enrichments of non-reactive gases as He, suggests the presence of permeability discontinuities in the study area since the uprising of volcano-geothermal gases towards the surface is less hindered where lower thickness of the clay alteration cap is present.

The deeper limit of the clay cap was located roughly at 1500 m depth, which suggests that an exploratory drilling to reach the upper part of the geothermal system should be about 2000 m deep, because the clay cap there seems to be the thinnest. These methods provided extremely useful and relatively economical information for the location of geothermal resources. The results can help to define the most appropriate areas that are susceptible of more detailed research to minimize the uncertainty for the location of a future exploratory drilling.

Acknowledgements

This research was financially supported by project “GEOTHERCAN” (Ref. IPT-2011-1186-920000), co-financed by the Spanish National Research Plan 2008–2011 of Ministerio de Economía y Competitividad, European Union ERDF funds, Instituto Tecnológico y de Energías Renovables (ITER, S.A.), Instituto Volcanológico de Canarias (INVOLCAN) and Petratherm España S.L. The authors are grateful to C. Báncora, R. Antón, D. Aragón, P. González, D. Nieto, M. Refoyo, P. Rodríguez, A. Toscano and R. Vega, for their help during the field and laboratory work and especially to M. Díaz, D. Nolasco and C. Guillén for their support with the data analysis.

Appendix A. Supplementary data

Supplementary material related to this article can be found, in the online version, at http://dx.doi.org/10.1016/j.geothermics.2015.02.007.

References

Ablay, G., Martí, J., 2000. Stratigraphy, structure, and volcanic evolution of the Pico Teide–Pico Viejo formation, Tenerife, Canary Islands. J. Volcanol. Geotherm. Res. 103, 175–208, http://dx.doi.org/10.1016/S0377-0273(00)00224-9.

Alparone, S., Andronico, D., Giammanco, S., Lodato, L., 2004. A multidisciplinary approach to detect active pathways for magma migration and eruption at Mt. Etna (Sicily, Italy) before the 2001 and 2002–2003 eruptions. J. Volcanol. Geotherm. Res. 136, 121–140, http://dx.doi.org/10.1016/j.jvolgeores.2004.05.014.

Ancochea, E., Fuster, J.M., Ibarrola, E., Cendrero, A., Coello, J., 1990. Volcanic evolution of the island of Tenerife (Canary Islands) in the light of new K–Ar data. J. Volcanol. Geotherm. Res. 44, 231–249.

Billings, S.A., Richter, D.D., Yarie, J., 2000. Sensitivity of soil methane fluxes to reduced precipitation in boreal forest soils. Soil Biol. Biochem. 32, 1431–1441, http://dx.doi.org/10.1016/S0038-0717(00)00061-4.

Cardellini, C., Chiodini, G., Frondini, F., 2003. Application of stochastic simulation to CO_2 flux from soil: mapping and quantification of gas release. J. Geophys. Res. 108, 2425, http://dx.doi.org/10.1029/2002JB002165.

Carracedo, J.C., 1994. The Canary Islands: an example of structural control on the growth of large oceanic-island volcanoes. J. Volcanol. Geotherm. Res. 60, 225–241, http://dx.doi.org/10.1016/0377-0273(94)90053-1.

Cerling, T.E., Solomon, D.K., Quade, J., Bowman, J.R., 1991. On the isotopic composition of carbon in soil carbon dioxide. Geochim. Cosmochim. Acta 55, 3403–3405, http://dx.doi.org/10.1016/0016-7037(91)90498-T.

Chave, A.D., Jones, A.G., 2012. Introduction to magnetotellurics. In: Chave, A.D., Jones, A.G. (Eds.), The Magnetotelluric Method: Theory and Practice. Cambridge University Press, pp. 1–18.

Ciotoli, G., Lombardi, S., Morandi, S., Zarlenga, F., 2004. A multidisciplinary, statistical approach to study the relationships between helium leakage and neotectonic activity in a gas province: the Vasto basin, Abruzzo-Molise (central Italy). Am. Assoc. Pet. Geol. Bull. 88, 355–372.

Conrad, R., Seiler, W., 1981. Decomposition of atmospheric hydrogen by soil microorganisms and soil enzymes. Soil Biol. Biochem. 13, 43–49, http://dx.doi.org/10.1016/0038-0717(81)90101-2.

Coppo, N., Schnegg, P., Heise, W., Falco, P., Costa, R., 2008. Multiple caldera collapses inferred from the shallow electrical resistivity signature of the las Cañadas Caldera, Tenerife Canary Islands. J. Volcanol. Geotherm. Res. 170, 153–166.

Coppo, N., Schnegg, P.A., Falco, P., Costa, R., 2010. Conductive structures around Las Cañadas caldera, Tenerife (Canary Islands, Spain): a structural control. Geol. Acta 8, 67–82, http://dx.doi.org/10.1344/105.000001516.

Craig, H., 1953. The geochemistry of the stable carbon isotope. Geochim. Cosmohim. Acta 3, 53–92, http://dx.doi.org/10.1016/0016-7037(53)90001-5.

Cumming, W., 2009. Geothermal resource conceptual models using surface exploration data. In: Proceedings of Thirty-Fourth Workshop on Geothermal Reservoir Engineering, Stanford University, Stanford, California.

Del Pezzo, E., Gasparini, P., Mantovani, M.S.M., Martini, M., Capaldi, G., Gomes, Y.T., Pece, R., 1981. A case of correlation between Rn anomalies and seismic activity on a volcano (Vulcano Island, Southern Tyrrhenian Sea). Geophys. Res. Lett. 8, 962–965, http://dx.doi.org/10.1029/GL008i009p00962.

Deutsch, C., Journel, A., 1998. GSLIB: Geostatistical Software Library and Users Guide, 2nd ed. Oxford University Press, New York.

Dóniz, J., Romero, C., Coello, E., Guillén, C., Sánchez, N., García-Cacho, L., García, A., 2008. Morphological and statistical characterisation of recent mafic volcanism on Tenerife (Canary Islands, Spain). J. Volcanol. Geotherm. Res. 173, 185–195, http://dx.doi.org/10.1016/j.jvolgeores.2007.12.046.

Egbert, G.D., Kelbert, A., 2012. Computational recipes for electromagnetic inverse problems. Geophys. J. Int. 189, 251–267, http://dx.doi.org/10.1111/j.1365-246X.2011.05347.x.

European Commission, 1999. Blue Book on Geothermal Resources: A Strategic Plan for the Development of European Geothermal Sector, Belgium.

Galindo I., (Ph.D. thesis) 2005. Estructura volcano-tectónica y emisión difusa de gases de Tenerife (Islas Canarias). University of Barcelona (in Spanish).

García, X., Jones, A.G., 2010. Internal structure of the western flank of the Cumbre Vieja volcano, La Palma, Canary Islands, from land magnetotelluric imaging. J. Geophys. Res. Solid Earth 115, B07104, http://dx.doi.org/10.1029/2009JB006445.

Giammanco, S., Gurrieri, S., Valenza, M., 2006. Fault-controlled soil CO_2 degassing and shallow magma bodies: summit and lower east rift of Kilauea volcano (Hawaii), 1997. Pure Appl. Geophys. 163, 853–867, http://dx.doi.org/10.1007/s00024-006-0039-9.

Giggenbach, W., 1992. The composition of gases in geothermal and volcanic systems as a function of tectonic setting. In: Kharaka, Y.K., Maest, A.S. (Eds.), Proceedings of the 7th International Symposium on Water Rock Interaction, Volume 2, Moderate and High Temperature Environments. Rotterdam, Balkema, pp. 873–878.

Gluekauf, 1946. A microanalysis of helium and neon contents of air. Proc. R. Soc. Lond. A 185, 98–119.

Hanson, M.C., Oze, C., Horton, T.W., 2014. Identifying blind geothermal systems with soil CO_2 surveys. Appl. Geochem. 50, 106–114.

Heise, W., Caldwell, T.G., Bibby, H.M., Bannister, S.C., 2008. Three-dimensional modelling of magnetotelluric data from the Rotokawa geothermal field, Taupo Volcanic Zone, New Zealand. Geophys. J. Int. 173, 740–750, http://dx.doi.org/10.1111/j.1365-246X.2008.03737.x.

Hernández, P.A., Pérez, N.M., Salazar, J., Sato, M., Notsu, K., Wakita, H., 2000. Soil gas CO_2, CH_4, and H_2 distribution in and around Las Cañadas caldera, Tenerife,

Canary Islands, Spain. J. Volcanol. Geotherm. Res. 103, 425–438, http://dx.doi.org/10.1016/S0377-0273(00)00235-3.
Hernández, P.A., Pérez, N.M., Salazar, J., Reimer, M., Notsu, K., Wakita, H., 2004. Radon and helium in soil gases at Cañadas caldera, Tenerife, Canary Islands, Spain. J. Volcanol. Geotherm. Res. 131, 59–76, http://dx.doi.org/10.1016/S0377-0273(03)00316-0.
Hinkle, M.E., 1994. Environmental conditions affecting concentrations of He, CO_2, O_2 and N_2 in soil gases. Appl. Geochem. 9, 53–63, http://dx.doi.org/10.1016/0883-2927(94)90052-3.
Ingham, M.R., Bibby, H.M., Heise, W., Jones, K.A., Cairns, P., Dravitzki, S., Bennie, S.L., Caldwell, T.G., Ogawa, Y., 2009. A magnetotelluric study of Mount Ruapehu volcano, New Zealand. Geophys. J. Int. 179, 887–904, http://dx.doi.org/10.1111/j.1365-246X.2009.04317.x.
Irwin, W.P., Barnes, I., 1980. Tectonic relations of carbon dioxide discharges and earthquakes. J. Geophys. Res. Solid Earth 85, 3115–3121, http://dx.doi.org/10.1029/JB085iB06p03115.
Kröchert, J., Buchner, E., 2008. Age distribution of cinder cones within the Bandas del Sur Formation, southern Tenerife, Canary Islands. Geol. Mag. 146, 161, http://dx.doi.org/10.1017/S001675680800544X.
Marrero, R., (Ph.D. thesis) 2010. Modelo Hidrogeoquímico del acuífero de las Cañadas del Teide, Tenerife, Islas Canarias. University of Barcelona (in Spanish).
Melián, G., Galindo, I., Pérez, N.M., Hernández, P.A., Fernández, M., Ramírez, C., Mora, R., Alvarado, G.E., 2007. Diffuse emission of hydrogen from Poás volcano, Costa Rica, Central America. Pure Appl. Geophys. 164, 2465–2487, http://dx.doi.org/10.1007/s00024-007-0282-8.
Novelli, P.C., Lang, P.M., Masarie, K.A., Hurst, D.F., Myers, R., Elkins, J.W., 1999. Molecular hydrogen in the troposphere: global distribution and budget. J. Geophys. Res. Atmos. 104, 30427–30444, http://dx.doi.org/10.1029/1999JD900788.
Ortiz, R., Araña, V., Astiz, M., Garcia, A., 1986. Magnetotelluric study of the Teide (Tenerife) and Timanfaya (Tanzarote) volcanic areas. J. Volcanol. Geotherm. Res. 30, 357–377, http://dx.doi.org/10.1016/0377-0273(86)90061-2.
Padilla, G.D., Hernández, P.A., Padrón, E., Barrancos, J., Pérez, N.M., Melián, G., Nolasco, D., Dionis, S., Rodríguez, F., Calvo, D., Hernández, I., 2013. Soil gas radon emissions and volcanic activity at El Hierro (Canary Islands): the 2011–2012 submarine eruption. Geochem. Geophys. Geosyst. 14, 432–447, http://dx.doi.org/10.1029/2012GC004375.
Padrón, E., Pérez, N.M., Hernández, P.A., Sumino, H., Melián, G., Barrancos, J., Nolasco, D., Padilla, G., 2012. Helium emission at Cumbre Vieja volcano, La Palma, Canary Islands. Chem. Geol. 312–313, 138–147, http://dx.doi.org/10.1016/j.chemgeo.2012.04.018.
Padrón, E., Padilla, G., Hernández, P.A., Pérez, N.M., Calvo, D., Nolasco, D., Barrancos, J., Melián, G.V., Dionis, S., Rodríguez, F., 2013. Soil gas geochemistry in relation to eruptive fissures on Timanfaya volcano, Lanzarote Island (Canary Islands, Spain). J. Volcanol. Geotherm. Res. 250, 91–99, http://dx.doi.org/10.1016/j.jvolgeores.2012.10.013.
Parkinson, K.J., 1981. An improved method for measuring soil respiration in the field. J. Appl. Ecol. 18, 221–228, doi: 0021-8901/81/0400-0221.
Pellerin, L., Johnston, J., Hohmann, G., 1996. A numerical evaluation of electromagnetic methods in geothermal exploration. Geophysics 61, 121–130, http://dx.doi.org/10.1190/1.1443931.
Pérez, N.M., Nakai, S., Wakita, H., Hernández, P.A., Salazar, J.M., 1996. Helium-3 emission in and around Teide Volcano, Tenerife, Canary Islands, Spain. Geophys. Res. Lett. 23, 3531–3534, http://dx.doi.org/10.1029/96GL03470.
Pérez, N.M., Padilla, G.D., Padrón, E., Hernández, P.A., Melián, G., Barrancos, J., Dionis, S., Nolasco, D., Rodríguez, F., Calvo, D., Hernández, Í., 2012. Precursory diffuse CO_2 and H_2S emission signatures of the 2011–2012 El Hierro submarine eruption, Canary Islands. Geophys. Res. Lett. 39, http://dx.doi.org/10.1029/2012GL052410.
Piña-Varas, P., Ledo, J., Queralt, P., Marcuello, A., Bellmunt, F., Hidalgo, R., Messeiller, M., 2014. 3-D magnetotelluric exploration of Tenerife geothermal system (Canary Islands, Spain). Surv. Geophys., http://dx.doi.org/10.1007/s10712-014-9280-4.
Pous, J., Heise, W., Schnegg, P.-A., Muñoz, G., Martí, J., Soriano, C., 2002. Magnetotelluric study of the Las Cañadas caldera (Tenerife, Canary Islands): structural and hydrogeological implications. Earth Planet. Sci. Lett. 204, 249–263, http://dx.doi.org/10.1016/S0012-821X(02)00956-1.
Sánchez-Guzmán, J., García de la Noceda, C., 2010. The evolution of geothermal energy in Spain – country update (2005–2009). In: Proceedings World Geothermal Congress, Bali, Indonesia.
Semprini, L., Kruger, P., 1984. Relationship of radon concentration to spatial and temporal variations of reservoir thermodynamic conditions in the Cerro Prieto geothermal field. Geothermics 13, 103–115, http://dx.doi.org/10.1016/0375-6505(84)90010-5.
Sinclair, A.J., 1974. Selection of threshold values in geochemical data using probability graphs. J. Geochem. Explor. 3, 129–149, http://dx.doi.org/10.1016/0375-6742(74)90030-2.
Stolper, E., Holloway, J.R., 1988. Experimental determination of the solubility of carbon dioxide in molten basalt at low pressure. Earth Planet. Sci. Lett. 87, 397–408, http://dx.doi.org/10.1016/0012-821X(88)90004-0.
Sugisaki, R., Anno, H., Adachi, M., Ui, H., 1980. Geochemical features of gases and rocks along active faults. Geochem. J. 14, 101–112, http://dx.doi.org/10.2343/geochemj.14.101.
Uchida, T., Sasaki, Y., 2006. Stable 3D inversion of MT data and its application to geothermal exploration. Soc. Explor. Geophys. 37, 223–230, http://dx.doi.org/10.1071/EG06223.
Voltattorni, N., Sciarra, A., Quattrocchi, F., Nazionale, I., Murata, V., 2010. The application of soil-gas technique to geothermal exploration: study of hidden potential geothermal systems. In: Proceedings World Geothermal Congress, Bali, Indonesia.
Vozoff, K., 1991. The magnetotelluric method. Soc. Explor. Geophys., 641–711.
Wakita, H., Nakamura, Y., Kita, I., Fujii, N., Notsu, K., 1980. Hydrogen release: new indicator of fault activity. Science 210, 188–190, http://dx.doi.org/10.1126/science.210.4466.188.
Walia, V., Su, T.C., Fu, C.C., Yang, T.F., 2005. Spatial variations of radon and helium concentrations in soil-gas across the Shan-Chiao fault, Northern Taiwan. Radiat. Meas. 40, 513–516, http://dx.doi.org/10.1016/j.radmeas.2005.04.011.
Whitehead, N.E., 1984. Geothermal prospecting by ground radon measurements. J. Volcanol. Geotherm. Res. 20, 213–229, http://dx.doi.org/10.1016/0377-0273(84)90040-4.

Journal of Volcanology and Geothermal Research 250 (2013) 91–99

Contents lists available at SciVerse ScienceDirect

Journal of Volcanology and Geothermal Research

journal homepage: www.elsevier.com/locate/jvolgeores

Soil gas geochemistry in relation to eruptive fissures on Timanfaya volcano, Lanzarote Island (Canary Islands, Spain)

Eleazar Padrón *, Germán Padilla, Pedro A. Hernández, Nemesio M. Pérez, David Calvo, Dácil Nolasco, José Barrancos, Gladys V. Melián, Samara Dionis, Fátima Rodríguez

Environmental Research Division, ITER, 38611 Granadilla de Abona, Tenerife, Canary Islands, Spain
Instituto Volcanológico de Canarias (INVOLCAN), 38400 Puerto de la Cruz, Tenerife, Canary Islands, Spain

ARTICLE INFO

Article history:
Received 31 March 2012
Accepted 21 October 2012
Available online 2 November 2012

Keywords:
Timanfaya volcano
Soil gas
Radon
Carbon dioxide
Helium

ABSTRACT

We report herein the first results of an extensive soil gas survey performed on Timanfaya volcano on May 2011. Soil gas composition at Timanfaya volcano indicates a main atmospheric source, slightly enriched in CO_2 and He. Soil CO_2 concentration showed a very slight deep contribution of the Timanfaya volcanic system, with no clear relation to the main eruptive fissures of the studied area. The existence of soil helium enrichments in Timanfaya indicates a shallow degassing of crustal helium and other possible deeper sources probably form cooling magma bodies at depth. The main soil helium enrichments were observed in good agreement with the main eruptive fissures of the 1730–36 eruption, with the highest values located at those areas with a higher density of recent eruptive centers, indicating an important structural control for the leakage of helium at Timanfaya volcano. Atmospheric air slightly polluted by deep-seated helium emissions, CO_2 degassed from a cooling magma body, and biogenic CO_2, might be the most plausible explanation for the existence of soil gas. Helium is a deep-seated gas, exhibiting important emission rates along the main eruptive fissure of the 1730–36 eruption of Timanfaya volcano.

1. Introduction

The presence of soil gas anomalies are related to the preferential release of deep-seated gases along active tectonic structures, and as a consequence, the use of soil gas surveys in earth science studies has become increasingly common in recent years. Such studies have been widely applied to locate active faults and have been used in earthquake and volcanic eruption precursory studies (King et al., 1996; Baubron et al., 2002; Hernández et al., 2004; Walia et al., 2005; Giammanco et al., 2006; Lan et al., 2007). Soil gas surveys are mainly based on the analysis of gases in the soil atmosphere at a usual depth of between 40 cm and 1 m depth from the surface. Studies carried out over active faults and fractures have shown that these geological structures act as preferential pathways for the ascent of gases from different origins toward the surface (King et al., 1996; Padrón et al., 2003; Yang et al., 2003; Walia et al., 2005, 2010; Giammanco et al., 2006; Neri et al., 2011). Studies of soil gas compositions and diffuse degassing surveys in volcanic environments have focused mainly on CO_2. This is because of the fact that, after water vapor, CO_2 is the most abundant gas species dissolved in magma (Stolper and Holloway, 1988). On active or quiescent volcanoes, CO_2 is the main species in soil gas, and is released through tectonic structures (Giammanco et al., 1995, 2006, 2007; Hernández et al., 2000; Dogan et al., 2007; Lombardi and Voltattorni, 2010).

Radon is probably one of the most investigated soil gases emanating from faults (Banwell and Parizek, 1988; Hernández et al., 2004; Walia et al., 2005, 2010; Reddy et al., 2006), and has been also used to monitor volcanic and seismic activity (Zimmer and Erzinger, 2003; Immè et al., 2006; Pérez et al., 2007, 2008). It has three isotopes: ^{222}Rn (radon), ^{220}Rn (thoron), and ^{219}Rn (actinon). ^{222}Rn is generated from the radioactive decay of ^{238}U and has a half-life of 3.82 days. Soil gas ^{222}Rn measured at the ground level originates from a shallow source unless driving mechanisms such as underground water movements or carrier gas, facilitate the transport from deeper sources to the surface (Etiope and Martinelli, 2002; Yang et al., 2003). Several factors control its concentration in soil gases: the distribution of ^{238}U in the bedrock, soil porosity and humidity, surface wind speed, and granulation. Thoron is a decay product derived from the ^{232}Th decay series and has a relatively half-life of 55 s. Owing to their different half-lives. a ^{222}Rn/^{220}Rn ratio is used to distinguish between gases released from shallower or deeper zones. However, a low ^{222}Rn/^{220}Rn reading can also be found in zones with a very fast soil–gas transport mechanism (Giammanco et al., 2007).

Helium, owing to its special geochemical properties, is considered by geochemists to be an almost ideal indicator of geochemical processes (Pogorski and Quirt, 1981). It is highly mobile, chemically

* Corresponding author at: Environmental Research Division, ITER, Polígono Industrial de Granadilla, 38611 Granadilla de Abona, S/C de Tenerife, Canary Islands, Spain. Tel.: +34 922747700; fax: +34 922747701.
E-mail address: eleazar@iter.es (E. Padrón).

0377-0273/$ – see front matter © 2012 Elsevier B.V. All rights reserved.
http://dx.doi.org/10.1016/j.jvolgeores.2012.10.013

inert, physically stable, nonbiogenic, sparingly soluble in water under ambient conditions, almost non-adsorbable, and highly diffusive with a diffusion coefficient about 10 times that of CO_2. These properties minimize the interactions of this noble gas during its movement toward the earth's surface and its concentration is not modified by subsequent chemical reactions. An excess of ^{4}He (hereafter simply referred to as helium) in soil gases compared to atmospheric values has been reported by several authors, and is found mainly near fractures (Lombardi et al., 1984; D'Alessandro and Parello, 1997; Padrón et al., 2003; Padrón et al., 2012; Hong et al., 2010; Lombardi and Voltattorni, 2010).

In May 2011, we performed a soil gas survey on Timanfaya volcanis system (Lanzarote, Canary Islands, Spain), which focused mainly on CO_2, ^{222}Rn, ^{220}Rn and He concentrations, to investigate the relationship between soil gas concentrations and the volcano-tectonic structures of Timanfaya volcano. Since the active fractures at Timanfaya volcano are evident from the surface geology, the main aim of this study is to investigate whether these geological structures are actively releasing deep gases. At present there is no surface evidence of gas emissions at Timanfaya volcano, and therefore the study of the spatial distribution of CO_2, ^{222}Rn, ^{220}Rn and He concentrations in soil gases becomes an ideal geochemical tool to identify sites with an anomalous emission of deep-seated gases, which could then be used for volcano monitoring.

2. Geological settings

The Canary Archipelago is located in the eastern Central Atlantic off the Moroccan coast, and consists of seven major islands and several islets extending about 450 km from east to west (Fig. 1). There is a recognized east-to-west age progression of the oldest subaerial volcanism, from about 20 Ma for the eastern islands of Lanzarote and Fuerteventura (Dañobeitia and Canales, 2000) to 2 Ma for the westernmost islands of La Palma and El Hierro (Ancochea et al., 1994; Guillou et al., 1996). This apparent east to west progression of the oldest subaerial volcanism and its agreement with the increase of ^{3}He/^{4}He ratio measured in terrestrial fluids from Lanzarote to La Palma and El Hierro Islands (Pérez et al., 1994), seem to be compatible with the hotspot trace proposed for the Canaries by Morgan (1971) and Pérez et al. (1994). Lanzarote Island (795 km^2, Fig. 1) is an emerged part of the East Canary Ridge (ECR), which is a ca. 70-km-long, 65-km-wide, NNE–SSW linear volcanic structure offshore Morocco (Marinoni and Pasquaré, 1994). It is the easternmost island in the Canary Islands and it is situated approximately 100 km from the NW coast of Morocco, Africa. The ECR consists of a number of uplifted blocks of oceanic basement covered by a thick sedimentary sequence (10 km) mantled by 5 km of volcanic rocks, with an intrusive complex between the two layers (Banda et al., 1981). The emergent part of the island is essentially formed of volcanic rocks, mainly basaltic in composition (Marinoni and Pasquaré, 1994). The island is elongated in NNE–SSW direction reflecting the trend of the ECR, and most of the emission centers in the central part of the island indicate concentration of vents with a ENE–WSW trend (Fig. 2). From 1730 to 1736 Lanzarote suffered the longest eruption in historical times in the Canary Islands, a basaltic-type eruption with tholeiitic composition, with more than 30 volcanic cones formed in different eruptive phases which covered 23% of the island (Carracedo et al., 1992). The eruptive vents are aligned along a fracture more than 14 km in length (Fig. 2). The main fissure that fed the 1730 eruption is related to the general trend (N70°E) of alignment of recent emission centers that shows the path of the central structural rift-type zone (Carracedo et al., 1992). The last eruption at Lanzarote Island occurred during 1824 at Tinguaton volcano, and produced a small lava flow that reached the SW coast.

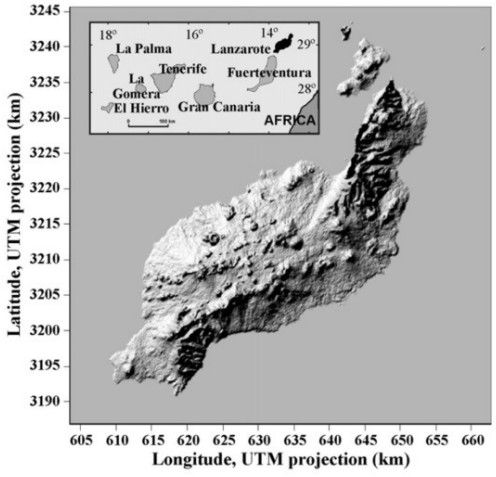

Fig. 1. Geographic location of Lanzarote Island, Canarian archipelago.

One of the most prominent phenomena at Timanfaya volcanic field is the high maintained superficial temperatures occurring in the area since the 1730–1736 volcanic eruption. Thermal anomalies are confined either in fracture-related alignments or along the rims of craters (Araña et al., 1984). The maximum temperature recorded in this zone is 605 °C, measured inside a slightly inclined 13 m deep well. The main thermal anomalies are located in the area known as Islote de Hilario, 0.6 km to the north-west of the Timanfaya cinder cone. Other areas with superficial temperatures of 125–200 °C occur along one of the main crater rim (Araña et al., 1984). Ortiz et al. (1986) inferred a shallow magma chamber that fed the 1730–1736 eruptions located at approximately 4 km depth with temperatures in the range 900–1100 °C. Araña et al. (1984) suggested that thermal energy would be transported through fractures by magmatic volatiles and/or by water vapor coming from a deep-seated 3–4 km water table.

3. Sampling and analytical methods — May 2011

In order to study the relationship between soil gas composition and volcano-tectonic structures at Timanfaya volcano, we collected 366 soil gas samples following a homogeneous pattern in a distribution of sampling sites along the surface environment of Timanfaya volcano (Fig. 3). We took into consideration the local geology, the location of the volcano-tectonic structures and their accessibility. Owing to the low degree of soil development, soil gas sampling was not possible on large surfaces of the Timanfaya volcanic system that has been covered by very recent lava flows (non studied area in Fig. 3). A higher sampling density was used at those areas where surface temperature anomalies were present. At each sampling site, soil gas samples were collected at a depth of 40 cm depth using a stainless steel probe. Samples were then stored in glass vials. He, N_2, O_2, ^{40}Ar, ^{36}Ar and CO_2 concentrations were analyzed within 24 h by means of a Quadrupole Mass Spectrometer (QMS; Pfeiffer Omnistar 422). Atmospheric gas was used to calibrate the instrument for the He, N_2, O_2, ^{40}Ar and ^{36}Ar, while specific gas-standards were used for CO_2. The accuracy of the gas contents determined by the instrument was estimated to be 300 ppb, for helium, 1%, for N_2 and O_2, 50 ppm for ^{40}Ar and 5 ppm for ^{36}Ar. ^{222}Rn and ^{220}Rn concentrations in soil gases were measured in-situ at each sampling site by means of a SARAD Rn monitor, model RTM-2010-2. The instrument was connected to the metallic probe and inserted into the soil at a depth of 40 cm. Soil gas was pumped through the measurement

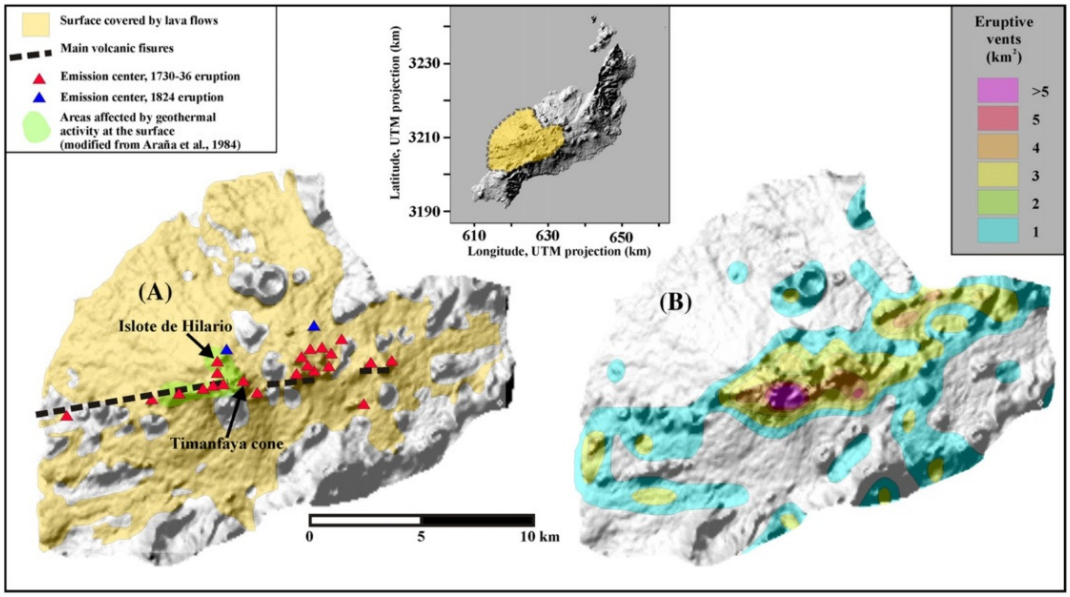

Fig. 2. (A) Main eruptive fissures, emission centers and surface covered by lava flows from 1730–1736 eruption of Timanfaya volcano, Lanzarote Islands; soil thermalized areas are depicted in green colour. (B) Density distribution of vents of recent eruptive centres along the study area (modified from Carracedo et al., 1992).

chamber at 0.5 mL/min for 10 min at each site. Soil temperature was also measured at each sampling site at a depth of 40 cm, by using a type K thermocouple.

Soil gas concentration data was used to construct spatial distribution maps using sequential Gaussian simulation (sGs) provided by the *sgsim* program (Deutsch and Journel, 1998; Cardellini et al., 2003). The simulation procedure involves the following steps: (1) a normal score transformation of the original data to transform the data in a normal population; (2) an experimental variogram computation of the normal score of the transformed data; (3) a variogram model

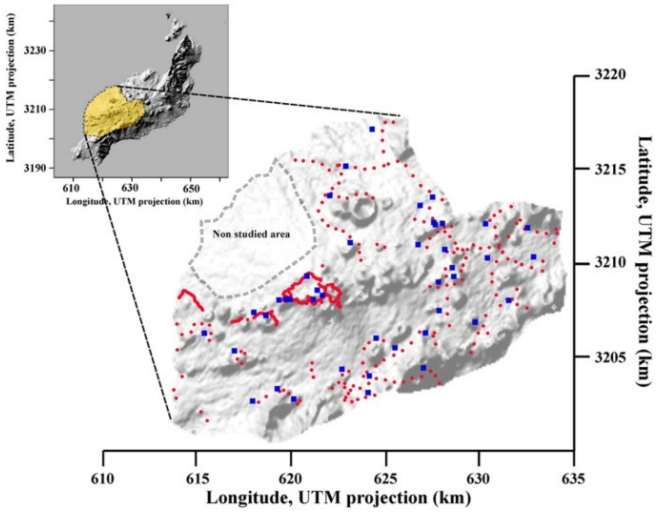

Fig. 3. Sampling sites along the surface environment of Timanfaya volcano. Red dots indicate the location of the sampling sites to analyze chemical composition of the soil gases collected on May 2011. Blue squares indicate the location of the sampling sites to analyze the soil CO_2 concentration and isotopic composition of CO_2.

Table 1
Descriptive statistics of soil gas composition data and the soil temperature measured at 40 cm depth from the surface environment of Timanfaya volcano.

	Range	Mean	S. D.	No. of samples
ΔHe (ppb)	−1518 to 18,665	927	2728	362
N_2 (vol.%)	76.43–79.18	77.50	0.54	362
O_2 (vol.%)	19.78–22.51	21.48	0.55	362
Ar (vol.%)	0.934–1.065	0.972	0.22	362
CO_2 (ppm)	379–4,600	772	404	362
$\delta^{13}C(CO_2)$ (‰ vs. VPDB)	−19.9 to −8.1	−10.3	2.4	39
^{222}Rn (Bq/m^3)	n.d. to 5,670	383	706	366
^{220}Rn (Bq/m^3)	n.d. to 15,295	445	1424	366
Soil temperature (°C)	15.7–74.4	25.9	6.5	366

assignation to the experimental variogram; (4) a sequential Gaussian simulation of N equiprobable realizations; and (5) a back-transformation of the normal score data into simulated values of the original variable. The final map was constructed as an average of the 100 equiprobable realizations displayed over a grid of 24,190 squared cells (100 m × 100 m).

To study the isotopic composition of the soil CO_2, 39 sampling sites were selected along the study area following the same methodology used for the soil gas samples. The isotopic composition of CO_2 was analyzed by means of a Thermo Finnigan MAT 253 Isotope Ratio Mass Spectrometer (IRMS), with a continuous flow injection from a Finnigan GasBench II. The gas injection system uses a two-port needle that adds a gentle flow of He into the sample vial to displace the sample gas. Water was removed from the sample gas through diffusion traps to avoid possible interferences on the spectrometer. The uncertainty in the results was estimated in 0.1‰ vs. VPDB.

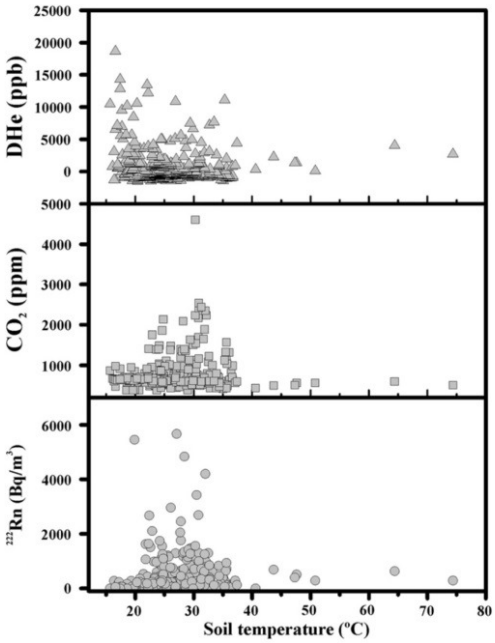

Fig. 5. Soil ^{222}Rn, CO_2 and ΔHe versus soil temperature at each sampling site.

4. Results and discussion

A descriptive statistic summary of the soil gas composition is depicted in Table 1. In the case of helium, values are given using the ΔHe notation: $\Delta He = [He]_{soil\ atmosphere} - [He]_{air}$, being $[He]_{air} = 5240$ ppb (Gluekauf, 1946). The observed correlation in Fig. 4 indicates that an ambient temperature modulates the soil temperature in most of the sampling sites. Only 7 measuring sites (1.9% of the total data) showed a soil temperature which was clearly out of the observed correlation, and these are highlighted as the grey area in Fig. 4. All these soil thermal anomalies measurements were taken in the area known as Islote de Hilario. The presence of soil CO_2, He, and ^{222}Rn enrichments does not seem to be driven by a convective movement of gases, because, as depicted in Fig. 5, there was no visual correlation between the soil gas composition and soil temperature. The chemical composition of the soil gases shows a main atmospheric component slightly enriched in CO_2 and helium. A similar atmospheric composition was observed by Pérez et al. (1992, 1994) in a noble soil gas study carried out on Timanfaya volcano.

In order to distinguish the possible different contributions for the CO_2 and helium enrichments, a statistical-graphical analysis (Sinclair, 1974) was applied to the CO_2 and the positive ΔHe data (48.9% of the 362 valid soil gas analyses) in order to check the presence of a single or multiple statistical populations (Fig. 6A). This method is based on the recognition of infection points along a curve and is defined by plotting data on a Log-normal probability scale. The statistical-graphical analysis of total soil CO_2 data showed a polymodal shape with two overlapping Log-normal geochemical populations. These two distinct populations are known as the background population (74.0% of the total data), with a mean of 650 ppm, and a peak population (2.8%) with a mean of 2,230 ppm. An intermediate "threshold"

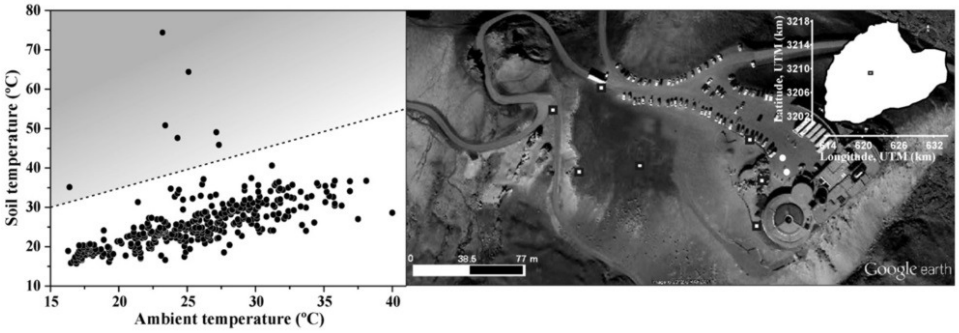

Fig. 4. Observed correlation between soil and ambient temperatures. Those sampling sites out of this correlation, depicted in the gray area, were located around Islote de Hilario area (white squares in the picture).

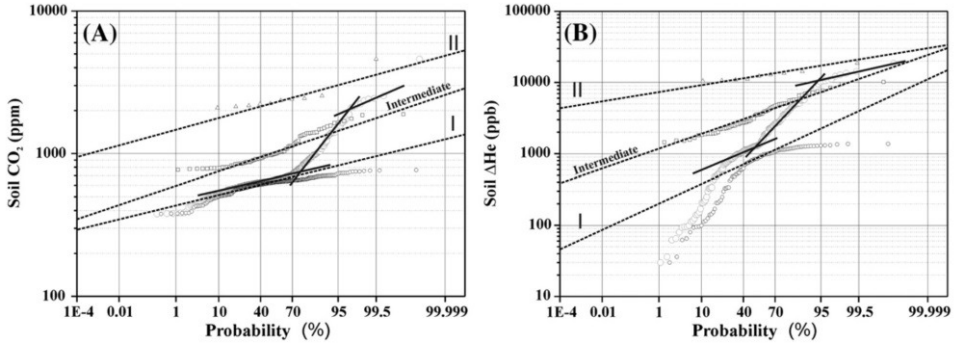

Fig. 6. Probability plots of soil CO_2 concentration (A) and positive ΔHe data (B). Solid lines indicate the partition between the 3 straight transects (populations). Numerals I and II indicate the two different Log-normal populations separated: I = background population (open black circles) and II = peak population (open triangles). Total data are presented as open grey circles. The rest of the data were also separated and form the intermediate population, which represents a mixing between background and peak values (open squares).

population (population III), which represents a mixing between background and peak values, had a mean of 1,000 ppm of CO_2 with 23.2% of the total data. In the case of CO_2, the existence of a peak population in the soil gas composition suggests a very slight deep contribution from the Timanfaya volcanic system. The background soil CO_2 concentration values could be mainly characterized as biogenic CO_2.

The results of carbon (CO_2) isotopic composition showed an average value of −10.3‰ vs. VPDB. This value is lighter than the typical biogenic range and closer to atmospheric CO_2 (−8.0‰ vs. VPDB, Trolier et al., 1996). To investigate the origin of the soil CO_2 at Timanfaya, a binary diagram of the $\delta^{13}C(CO_2)$ versus CO_2 concentration in the soil gases was constructed using three geochemical reservoirs: air, characterized by $\delta^{13}C(CO_2) = -8.0$‰ vs. VPDB and $[CO_2] = 380$ ppm; magmatic gas, characterized by $\delta^{13}C(CO_2) = -6.5$‰ vs. VPDB (Javoy et al., 1978) and $[CO_2] = 100$%. To construct the biogenic reservoir, it was necessary to determine the isotopic composition of soil CO_2 (the gas occupying pore spaces in the soil layer) and the soil-respired CO_2 (representing the flux of CO_2 through a soil), eventually identical to the isotopic composition of soil organic matter. Cerling et al. (1991) indicated that biogenic CO_2 in the soil can be +4.4‰ heavier than the soil-respired CO_2 produced by roots, owing to the fractionation of diffusion within the soil. Since the isotopic composition of soil organic matter is in the range $-30‰ > \delta\ ^{13}C(CO_2) > -20‰$ for plants using the C3 photosynthetic pathway, the isotopic composition for the soil CO_2 was defined by $-25.6‰ > \delta\ ^{13}C(CO_2) > -15.6‰$, vs. VPDB, with a mean value of −20.6. The range of the CO_2 concentration in the biogenic reservoir was 540–740 ppm, equal to the mean value of the background population partitioned by the probability plot (650 ppm) and one standard deviation as uncertainty. Fig. 7 shows that most of the soil gas samples were plotted close to the atmospheric reservoir, and indicate an important biogenic contribution. The contribution of atmospheric air could be because of the high permeability of the volcanic ash layers in most of the soils studied at Timanfaya volcano. The probability plot results postulate that there is a very small fraction of magmatic gas (which can be seen in the $\delta^{13}C(CO_2)$ versus CO_2 concentration diagram). The lack of further evidence can be attributed to the small number of samples plotted on or close to the mixing line between magmatic and biogenic reservoirs.

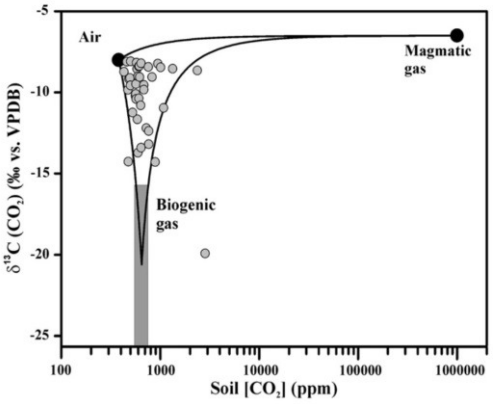

Fig. 7. Binary diagram of $\delta^{13}C(CO_2)$ versus CO_2 concentration. Mixing lines between biogenic end-member and air and magmatic gas, and between air and magmatic gas end-members are displayed by solid lines. Air and magmatic gas end-members are characterized by $\delta^{13}C(CO_2) = -8$ and −6.5, and $CO_2 = 380$ and 10^6 ppm, respectively. Biogenic end-member is characterized by $\delta^{13}C(CO_2)$ in the range −25.6 to −15.6‰ vs. VPDB, with a mean value of −20.6 and CO_2 in the range 540–740 ppm, with a mean value of 650 ppm.

In the case of soil ΔHe, the probability plot showed two distinct modes (Fig. 6B): background and peak, with a mean of 830 ppb for the background population (which represented 56.5% of the total data), and a peak population (5.1% of the total data), showing a mean of 12,200 ppb. The intermediate "threshold" population (population III), which represents a mixing between background and peak values, had a mean of 3,400 ppb with 38.4% of the total data. Two possible origins for helium enrichments in the Timanfaya soil gases can be postulated on the basis of the existence of two geochemical populations: (I) shallow degassing of crustal helium and (II) helium released from deeper source (magmatic), which is responsible for the higher ΔHe data, and probably emanates from a cooling magma body. The isotopic composition of helium measured by Pérez et al. (1994) and Hernández et al. (2012), rules out the possibility of a contribution of magmatic gases to the volcanic gas emission process at Timanfaya volcano. However, the $^3He/^4He$ ratio data presented in both papers was measured solely in a 10-m-deep vertical well in Islote de Hilario. $^4He/^{20}Ne$ data presented by Pérez et al. (1994), indicates a dominant atmospheric contribution, causing the low $^3He/^4He$ ratio (~1.0 R/R_A). Thus, a magmatic helium contribution can not be ruled at all the areas where high ΔHe was measured at Timanfaya volcano. There was no correlation evident between ΔHe vs. soil CO_2 concentration, as indicated in Fig. 8. Two different tendencies are depicted in this Figure: the addition of a biogenic CO_2 tendency (which was observed in most of the samples), and the addition of deep-seated helium (Fig. 8).

Argon isotopes can provide significant information on the magmatic contribution of endogenous gases, because ^{40}Ar derives from

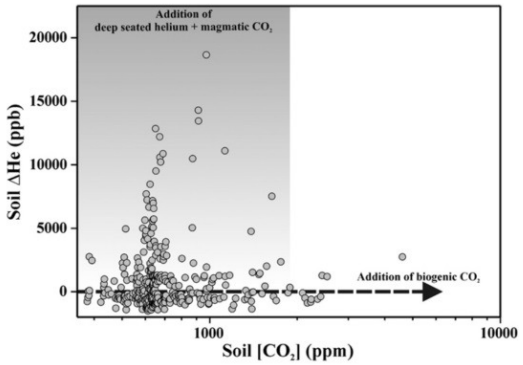

Fig. 8. ΔHe versus soil CO_2 concentration measured in the environmental surface of Timanfaya volcano.

volcanic degassing, the hydrothermal circulation through the crust, and the erosion of continental crust, which releases radiogenic Ar (Graham, 2002). $^{40}Ar/^{36}Ar$ ratios in mantle-derived gases is very high compared to the atmospheric value, and ranges from between ~8000 for Ocean Island Basalts (OIB) and 40,000 for Mid-Ocean Ridge Basalts (MORB) (Graham, 2002). Because nitrogen concentration correlates with the amount of ^{40}Ar, the $N_2/^{36}Ar$ ratio in MORB-derived gases correlates with $^{40}Ar/^{36}Ar$ (Marty, 1995; Graham, 2002). Thus it is possible to construct a two-components mixing model composed of a mantle-derived end-member (having $^{40}Ar/^{36}Ar = 30{,}000$ and $N_2/^{36}Ar = 2.2 \cdot 10^6$ (Graham, 2002); and an atmospheric end-member (with $^{40}Ar/^{36}Ar = 295.5$ and $N_2/^{36}Ar = 2.46 \cdot 10^4$). $N_2/^{36}Ar$ versus $^{40}Ar/^{36}Ar$ ratios in soil gases measured in an area showing active degassing of mantle-derived gases, can be plotted in a mixing trend between both end-members. Fig. 9 shows the results of $N_2/^{36}Ar$ versus $^{40}Ar/^{36}Ar$ plot for the Timnafaya volcano soil gases. Although atmospheric air is the dominant component in the plot, the area around the atmospheric reservoir, as shown in the inset, displays a clear trend on the mixing line with an MORB-type end-member. This observed addition of endogenous argon isotopes in the soils of the Timanfaya volcanic system, suggests a slight magmatic contribution to the soil gas geochemistry of Timanfaya. The most plausible explanation for the soil gas composition presented in this work is that biogenic CO_2, deep-seated helium, CO_2 and argon, which slightly pollute the atmospheric air, emanate from the degassing of magma bodies, (which are probably located at a depth of 4 km under the Timanfaya volcanic system (García, 1983)).

The higher average value of soil ^{220}Rn activity relative to ^{222}Rn (Table 1) indicates a main shallow main source of radon activity within the Timanfaya volcano soils, unlike that observed in other volcanic systems in the Canaries (Martín et al., 2003; Hernández et al., 2004; Padrón, 2008; Padilla et al., 2012). The spatial distribution of soil ^{222}Rn and $^{222}Rn/^{220}Rn$ ratio indicates that most of the anomalies were measured at areas not covered by lava flows from the 1730–36 eruption (Fig. 10). No significant spatial correlation between the main eruptive fissures and the location of soil ^{222}Rn and $^{222}Rn/^{220}Rn$ ratio was observed, being the most important anomalies on the eastern part of the study area and at the NW of Caldera Blanca volcano. The only significant anomaly measured in both soil ^{222}Rn and $^{222}Rn/^{220}Rn$ ratio was located at Montaña Termesana, close to the eruptive fissure from the 1730–36 eruption, in an area not covered by lava flows. In the case of the soil CO_2 concentration spatial distribution, nearly all the anomalies were measured in the limits of the study area (Fig. 11). The areas where higher soil CO_2 concentration values were expected to be measured are those ones where a higher density of volcanic vents occurs. However, the relatively low soil CO_2 measured along the main fractures related to the 1730–36 volcanic eruption are correlated with the existence of poorly evolved soils, where, consequently, biogenic CO_2 production is expected to be low.

In the case of helium, the spatial distribution of ΔHe data depicted in Fig. 12A indicates an important structural control for the leakage of helium at Timanfaya volcano. The main soil ΔHe anomalies were

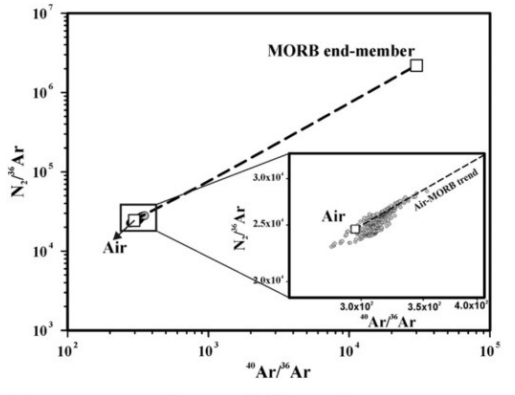

Fig. 9. Binary diagram of $N_2/^{36}Ar$ versus $^{40}Ar/^{36}Ar$ measured in the soils of Timanfaya volcanic system. Two different end-members are displayed: mantle-derived (MORB) end-member, with $^{40}Ar/^{36}Ar = 30{,}000$ and $N_2/^{36}Ar = 2.2 \times 10^6$ (Graham, 2002), and an atmospheric end-member, with $^{40}Ar/^{36}Ar = 295.5$ and $N_2/^{36}Ar = 2.46 \times 10^4$.

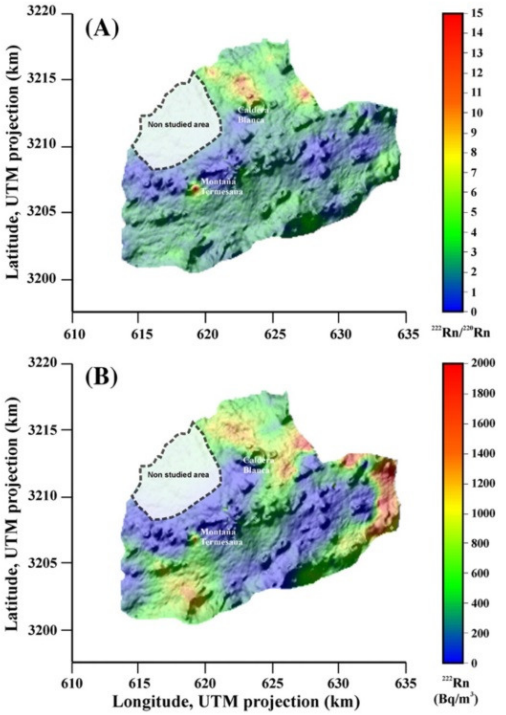

Fig. 10. Soil $^{222}Rn/^{220}Rn$ ratio (A) and ^{222}Rn (B) average maps of the 100 equiprobable *sgsim* realizations.

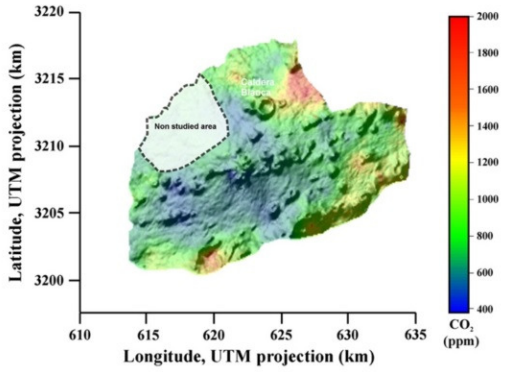

Fig. 11. Soil CO_2 concentration average map of the 100 equiprobable *sgsim* realizations.

observed in accordance with the main eruptive fissures of the 1730–36 eruption. The highest values were located in an area characterized by a high density of recent eruptive centers. This result confirms, therefore, the efficacy of soil–helium surveys as geochemical pathfinders of active permeable structures. The geochemical properties of helium minimize its interaction with hydrothermal fluids, its chemical reaction with minerals and the condensation and dissolution into shallow meteoric waters that soak the volcanic edifice, and are not trapped by the water table which is located at a supposed depth of 3–4 km (Araña et al., 1984).

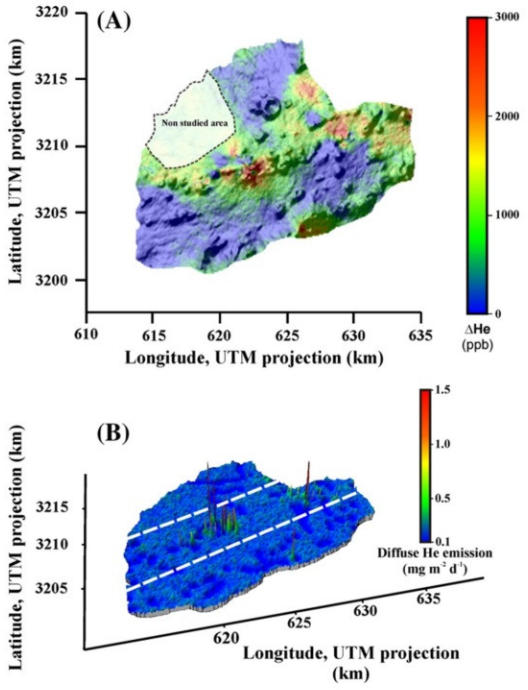

Fig. 12. (A) Soil ΔHe average map of the 100 equiprobable *sgsim* realizations. (B) 3D image of the diffusive He efflux spatial distribution. White dashed lines indicate the limits of the area used to estimate the helium emission through the main eruptive fissures of the 1730–36 eruption.

Because of the presence of significant temperature anomalies within the soils at Timanfaya, it is possible that convection is a mechanism for helium leakage in those areas where the highest helium concentrations were found. As described by Etiope and Martinelli (2002), the amount of helium in the subsurface is too small to flow autonomously by advection and needs a "carrier gas" (e.g. CO_2, N_2, …), which is able to form large domains to carry the noble gas. The carrier gas moves upward with a velocity much higher than the diffusion rate. However, in the case of Timanfaya volcano, a diffusive transport of radiogenic and/or magmatic helium is the most likely main transport mechanism for the helium leakage. This is because (1) there was no visual correlation between the soil gas composition and soil temperature (Fig. 5); (2) according to the data reported by Hernández et al. (2012), CO_2, the most probable carrier gas, does not show advective discharges at Timanfaya volcano, and no significant correlation between soil CO_2 and ΔHe has been observed (Fig. 8); and (3) there was not evident correlation between helium and any other of the studied soil gases in this work. We have, therefore, applied a pure diffusive model following Fick's law in order to estimate the amount of helium released by the degassing structure defined by the eruptive fissure:

$$F_D = -D_m \frac{\Delta C}{\Delta z}$$

where D_m is the molecular diffusion coefficient (m^2/s), ΔC is the variation of gas concentration (kg/m^3) along Δz (m). In this case, the considered concentration gradient is ΔHe divided by the sampling depth, 0.4 m. D_m is a constant for the specific gas and depends on temperature, pressure and the physical nature of the substance through which the molecular motion takes place. In the soil, this substance is generally air, or a gas mixture. In the case of helium, D_m in air is 0.7×10^{-4} m^2/s at 25 °C (Pandey et al., 1974). The assignation of a proper diffusion coefficient is a key factor for a correct estimation of the flux. To describe the diffusion in relation to the gas molecule motion through the soil, the global diffusion coefficient (D) must be used: $D_e = n^2 D_m$, where n is the effective porosity of the medium (%) (Etiope and Martinelli, 2002). Assuming an average of 25% for the soil porosity, as used for other volcanic systems in the Canaries (Padrón et al., 2012), we estimated a helium emission rate of ~15 kg/d by an area of 80 km^2 which includes the main eruptive fissures of the 1730–36 eruption. Fig. 12B shows a 3D image of the helium emission.

Araña et al. (1984) reported the convective rise of steam mixed probably with magmatic gases as being the responsible mechanism for the observed thermal anomalies at Timanfaya. Even though the highest thermal anomalies in the Canaries occur in this area, the absence of any surface hydrothermal features indicates that the fluid volume involved in the convection process must be very small. This possibility is not supported, however, by the presence of the low soil CO_2 concentration values measured at the thermalized surface areas, and the strong air contamination found in the gas samples collected. González and Fernández (2011) reported a ground deformation where the surface temperature anomalies occur at Timanfaya volcano. Two possible mechanisms were suggested to explain the observed inflation: (1) the cooling and crystallization of a molten remnant in the 1730–1736 magmatic reservoir, and/or (2) a shallow hydrothermal fluid circulation. However, the soil gas composition presented in this work characterized by low CO_2 concentration values, and the CO_2 emission data presented by Hernández et al. (2012) do not support the existence of a shallow hydrothermal fluid circulation. The cooling intrusive magma body that is located at 4 1 km depth and may still remain partially molten, may also be almost completely trapped by the water table (Araña et al., 1984). Magmatic gases released from this body would explain the low soil CO_2 in this

area, and the relatively high soil helium concentration values measured in the Timanfaya soils.

5. Conclusions

The chemical composition of the soil gases measured in the surface environment of Timanfaya volcano shows a strong atmospheric component, slightly enriched in CO_2 and helium. The isotopic composition of the soil CO_2 and the existence of a peak population in soil CO_2 data suggest a very slight, but deep, contribution of the Timanfaya volcanic system in the soil gas composition. No significant spatial correlation between the main eruptive fissures and the location of soil ^{222}Rn, $^{222}Rn/^{220}Rn$ and CO_2 anomalies was observed, with the most important anomalies being located at the eastern part of the study area and at the NW of Caldera Blanca volcano. The most plausible explanation for the absence of anomalies of these gases along the eruptive fissure, is the capping nature of the extensive lava flow fields of the 1730–36. Helium enrichments in Timanfaya soil gases is released from the cooling intrusive magma body located at 4 1 km depth, and a shallow degassing of crustal helium cannot be ruled out. The main soil ΔHe anomalies were observed in the area of the main eruptive fissures of the 1730–36 eruption, with the highest values located where the highest density of vents from recent eruptive centers are situated. This indicates an important structural control for the leakage of helium at Timanfaya volcano as the eruptive fissure zones have an enhanced permeability for deep gas migration and preferential routes for degassing. Unlike CO_2 and radon, the geochemical properties of helium allow this gas to escape preferentially through the vertical permeability structures of Timanfaya volcano. Atmospheric air slightly polluted by deep-seated helium emissions, CO_2 degassed from a cooling magma body, and biogenic CO_2, might be the most plausible explanation for the existence of soil gas as presented in this work. Helium is a deep-seated gas, exhibiting important emission rates along the main eruptive fissure of the 1730–36 eruption of Timanfaya volcano. The presence of deep helium and CO_2 makes the main eruptive fissure of the 1730–36 eruption of Timanfaya volcano an ideal site for volcano monitoring.

Acknowledgements

This research was supported by the Spanish Minister of Science and Innovation (CGL2008-06345), by the European Union MAC 2007-2013 Transnational Cooperation Program (MAKAVOL (MAC/3/C161)) and by the Cabildo Insular de Tenerife, Spain. We are grateful to Timanfaya National Park for their important logistic collaboration and to Cynthia Tapia for her support in the field work. Constructive reviews by two anonymous reviewers are greatly acknowledged.

References

Ancochea, E., Hernán, F., Cendrero, A., Cantagrel, J.M., Fúster, J.M., Ibarrola, E., Coello, J., 1994. Constructive and destructive episodes in the building of a young Oceanic Island, La Palma, Canary Islands, and genesis of the Caldera de Taburiente. Journal of Volcanology and Geothermal Research 60, 243–262.

Araña, V., Díez, J.L., Ortiz, R., Yuguero, J., 1984. Convection of the geothermal fluids in the Timanfaya volcanic area, Lanzarote, Canary Islands. Bulletin of Volcanology 47, 667–677.

Banda, E., Dañobeitia, J.J., Suriñach, E., Ansorge, J., 1981. Features of crustal structure under Canary Islands. Earth and Planetary Science Letters 55, 11–24.

Banwell, G.M., Parizek, R.R., 1988. Helium-4 and radon-222 concentrations in groundwater and soil gas as indicators of zones of fracture concentration in unexposed rock. Journal of Geophysical Research 93 (B1), 355–366.

Baubron, J.C., Rigo, A., Toutain, J.P., 2002. Soil gas profiles as a tool to characterise active tectonic areas: the Jaut Pass example (Pyrenees, France). Earth and Planetary Science Letters 196, 69–81.

Cardellini, C., Chiodini, G., Frondini, F., 2003. Application of stochastic simulation to CO_2 flux from soil: mapping and quantification of gas release. Journal of Geophysical Research 108 (B9), 2425. http://dx.doi.org/10.1029/2002JB002165.

Carracedo, J.C., Rodriguez, Badiola E., Soler, V., 1992. The 1730–1736 eruption of Lanzarote, Canary Islands: a long, high-magnitude basaltic fissure eruption. Journal of Volcanology and Geothermal Research 53, 239–250.

Cerling, T.E., Solomon, D.K., Quade, J., Bowman, J.R., 1991. On the isotopic composition of carbon in soil carbon dioxide. Geochimica et Cosmochimica Acta 55, 3403–3405.

D'Alessandro, W., Parello, F., 1997. Soil gas prospection of He, ^{222}Rn and CO_2: Vulcano Porto area, Aeolian Islands, Italy. Applied Geochemistry 12, 213–224.

Dañobeitia, J.J., Canales, J.P., 2000. Magmatic underplating in the Canary Archipelago. Journal of Volcanology and Geothermal Research 103, 27–41.

Deutsch, C.V., Journel, A.G., 1998. GSLIB. Geostatistical Software Library and Users Guide. Applied Geostatistics Series. Oxford University Press, New York Oxford (369 pp.).

Dogan, T., Mori, T., Tsunomori, F., Notsu, K., 2007. Soil H_2 and CO_2 surveys at several active faults in Japan. Pure and Applied Geophysics 164, 2449–2463.

Etiope, G., Martinelli, G., 2002. Migration of carrier and trace gases in the geosphere: an overview. Physics of the Earth and Planetary Interiors 129, 185–204.

García, A., 1983. Modelos corticales a partir de sondeos magnetotelúricos. Aplicación a zonas volcánicas activas. Ph.D. Thesis, Complutense University of Madrid, 129 pp. (in Spanish).

Giammanco, S., Gurrieri, S., Valenza, M., 1995. Soil CO_2 degassing on Mt. Etna (Sicily) during the period 1989–1993: discrimination between climatic and volcanic influences. Bulletin of Volcanology 57, 52–60.

Giammanco, S., Gurrieri, S., Valenza, M., 2006. Fault-controlled soil CO_2 degassing and shallow magma bodies: summit and lower east rift of Kilauea Volcano (Hawaii), 1997. Pure and Applied Geophysics 163, 853–867.

Giammanco, S., Sims, K.W.W., Neri, M., 2007. Measurements of ^{220}Rn and ^{222}Rn and CO_2 emissions in soil and fumarole gases on Mt. Etna volcano (Italy): implications for gas transport and shallow ground fracture. Geochemistry, Geophysics, Geosystems 8 (10). http://dx.doi.org/10.1029/2007GC001644.

Gluekauf, E., 1946. A microanalysis of helium and neon contents of air. Proceedings of the Royal Society of London Series A 185, 98–119.

González, P.J., Fernández, J., 2011. Error estimation in multitemporal InSAR deformation time series, with application to Lanzarote, Canary Islands. Journal of Geophysical Research 116, B10404. http://dx.doi.org/10.1029/2011JB008412.

Graham, D.W., 2002. Noble gas isotope geochemistry of mid-ocean ridge and ocean island basalts; characterization of mantle source reservoirs. In: Noble Gases in Geochemistry and Cosmochemistry. In: Porcelli, D., Wieler, R., Ballentine, C. (Eds.), Reviews in Mineralogy and Geochemistry. Mineral. Soc. Amer., Washington, D.C., pp. 247–318.

Guillou, H., Carracedo, J.C., Pérez-Torado, F., Rodriguez-Badiola, E., 1996. K-Ar ages and magnetic stratigraphy of a hotspot induced, fast grown oceanic island: El Hierro, Canary Islands. Journal of Volcanology and Geothermal Research 73, 141–155.

Hernández, P.A., Pérez, N.M., Salazar, J.M.L., Sato, M., Notsu, K., Wakita, H., 2000. Soil gas CO_2, CH_4, and H_2 distribution in and around Las Cañadas caldera, Tenerife, Canary Islands, Spain. Journal of Volcanology and Geothermal Research 103, 425–438.

Hernández, P.A., Pérez, N.M., Salazar, J.M.L., Reimer, M., Notsu, K., Wakita, H., 2004. Radon and helium in soil gases at Cañadas caldera, Tenerife, Canary Islands, Spain. Journal of Volcanology and Geothermal Research 131, 59–76.

Hernández, P.A., Padilla, G., Padrón, E., Pérez, N.M., Calvo, D., Nolasco, D., Melián, G., Barrancos, J., Dionis, S., Rodríguez, F., Sumino, H., 2012. Analysis of long- and short-term temporal variations of the diffuse CO2 emission from Timanfaya volcano, Lanzarote, Canary Islands. Applied Geochemistry 27, 2486–2499. http://dx.doi.org/10.1016/j.apgeochem.2012.08.008.

Hong, W.-L., Yang, T.F., Walia, V., Lin, S.-J., Fu, C.-C., Chen, Y.-G., Sano, Y., Chen, C.-H., Wen, K.-L., 2010. Nitrogen as the carrier gas for helium emission along an active fault in NW Taiwan. Applied Geochemistry 25, 593–601.

Immè, G., La Delfa, S., Lo Nigro, S., Morellia, D., Patanè, G., 2006. Soil radon concentration and volcanic activity of Mt. Etna before and after the 2002 eruption. Radiation Measurements 41, 241–245.

Javoy, M., Pineau, F., Ilyama, I., 1978. Experimental determination of the isotopic fractionation between gaseous CO_2 and carbon dissolved in tholeitic magma. Contributions to Mineralogy and Petrology 67, 35–39.

King, C.-K., King, B.-S., Evans, W.C., Zang, W., 1996. Spatial radon anomalies on active faults in California. Applied Geochemistry 11, 497–510.

Lan, T.F., Yang, T.F., Lee, H.-F., Chen, Y.-G., Chen, C.-H., Song, S.-R., Tsao, S., 2007. Compositions and flux of soil gas in Liu-Huang-Ku hydrothermal area, northern Taiwan. Journal of Volcanology and Geothermal Research 165, 32–45.

Lombardi, S., Voltattorni, N., 2010. Rn, He and CO_2 soil gas geochemistry for the study of active and inactive faults. Applied Geochemistry 25, 1206–1220. http://dx.doi.org/10.1016/j.apgeochem.2010.05.006.

Lombardi, S., Di Filippo, M., Zantedeschi, L., 1984. Helium in Phlegraean Fields soil gases: July 20th–26th–September 19th–25th, 1983. Bulletin of Volcanology 47–2, 259–265.

Marinoni, L.B., Pasquaré, G., 1994. Tectonic evolution of the emergent part of a volcanic ocean island: Lanzarote, Canary Islands. Tectonophysics 239, 111–135.

Martín, M.C., Ahijado, A., De la Nuez, J., Quesada, M.L., Steinitz, G., Vulkan, U., Eff-Darwich, A., 2003. Radon survey at La Palma Island (Canary Islands): first results. Vulcânica 1, 113–116.

Marty, B., 1995. Nitrogen content of the mantle inferred from N_2–Ar correlation in oceanic basalts. Nature 377, 326–329.

Morgan, W.J., 1971. Convection plumes in the lower mantle. Nature 230, 42–44.

Neri, M., Giammanco, S., Ferrera, E., Patanè, G., Zanon, V., 2011. Spatial distribution of soil radon as a tool to recognize active faulting on an active volcano: the example of Mt. Etna (Italy). Journal of Environmental Radioactivity 102, 863–870.

Ortiz, R., Araña, V., Astiz, M., García, A., 1986. Magnetotelluric study of the Teide (Tenerife) and Timanfaya (Lanzarote) volcanic areas. Journal of Volcanology and Geothermal Research 30, 357–377.

Padilla, G., Hernández, P.A., Padrón, E., Barrancos, J., Melián, G., Dionis, S., Rodríguez, F., Nolasco, D., Calvo, D., Hernández, I., Peraza, M.D., Pérez, N.M., 2012. Soil gas ^{222}Rn and volcanic activity at El Hierro (Canary Islands) before and after the 2011 submarine eruption. Geophysical Research Abstracts 14, EGU2012–13473.

Padrón, E. 2008. Emisión difusa de dióxido de carbono y otros volátiles en el volcán Cumbre Vieja, La Palma, Islas Canarias. Ph.D. Thesis, University of La Laguna, 499 pp. (in spanish).

Padrón, E., López, D.L., Magaña, M.I., Marrero, R., Pérez, N.M., 2003. Diffuse degassing and relation to structural flow path at Ahuachapán geothermal field, El Salvador. Geothermal Resources Council Transactions 27, 325–330.

Padrón, E., Pérez, N.M., Hernández, P.A., Sumino, H., Melián, G., Barrancos, J., Nolasco, D., Padilla, G., 2012. Helium emisión at Cumbre Vieja volcano, La Palma, Canary Islands. Chemical Geology 312–313, 138–147.

Pandey, G.N., Rasintek, M., Katz, D.L., 1974. Diffusion of fluids through porous media with implication in petroleum geology. American Association of Petroleum Geologists Bulletin 58 (2), 291–303.

Pérez, N.M., Sturchio, N.C., Williams, S.N., Carracedo, J.C., Coello, A., 1992. Geochemical characteristics of the volcanic-hidrothermal gases in Teide, Timanfaya, Taburiente and Teneguía volcanoes, Canary Islands, Spain. Actas III Congreso Geológico de España, 1, pp. 463–467.

Pérez, N.M., Wakita, H., Nakai, S., Sano, Y., Williams, S.N., 1994. ^{3}He/^{4}He isotopic ratios in volcanic hydrothermal discharges from the Canary Islands, Spain: implications on the origin of the volcanic activity. Mineralogical Magazine 58A, 709–710.

Pérez, N.M., Hernández, P.A., Padrón, E., Melián, G., Marrero, R., Padilla, G., Barrancos, J., Nolasco, D., 2007. Precursory subsurface ^{222}Rn and ^{220}Rn degassing signatures of the 2004 seismic crisis at Tenerife, Canary Islands. Pure and Applied Geophysics 164, 2431–2448.

Pérez, N.M., Hernández, Igarashi, G., Trujillo, I., Nakai, S., Sumino, H., Wakita, H., 2008. Searching and detecting earthquake geochemical precursors in CO_2-rich groundwaters from Galicia, Spain. Geochemical Journal 42, 75–83.

Pogorski, L.A., Quirt, G.S., 1981. Helium emanometry in exploration for hydrocarbons, Part I. In: Gottlieb, B.M. (Ed.), Unconventional Methods in Exploration for Petroleum and Natural Gas II. Southern Methodist University Press, Dallas, pp. 136–149.

Reddy, D.V., Sukhija, B.S., Nagabhushanam, P., Reddy, G.K., Kumar, D., Lachassagne, P., 2006. Soil gas radon emanometry: a tool for delineation of fractures for groundwater in granitic terrains. Journal of Hydrology 329, 186–195.

Sinclair, A.J., 1974. Selection of thresholds in geochemical data using probability graphs. Journal of Geochemical Exploration 3, 129–149.

Stolper, E., Holloway, J.R., 1988. Experimental determination of the solubility of carbon dioxide in molten basalt at low pressure. Earth and Planetary Science Letters 87, 397–408.

Trolier, M., White, J.W.C., Tans, P.P., Masarie, K.A., Gemery, P.A., 1996. Monitoring the isotopic composition of atmospheric CO_2: measurements from the NOAA Global Air Sampling Network. Journal of Geophysical Research 101 (D20), 25897–25916. http://dx.doi.org/10.1029/96JD02363.

Walia, V., Su, T.C., Fu, C.C., Yang, T.F., 2005. Spatial variations of radon and helium concentrations in soil–gas across the Shan-Chiao fault, NorthernTaiwan. Radiation Measurements 40, 513–516.

Walia, V., Lin, S.J., Fu, C.C., Yang, T.F., Hong, W.-L., Wen, K.-L., Chen, C.-H., 2010. Soil–gas monitoring: a tool for fault delineation studies along Hsinhua Fault (Tainan), Southern Taiwan. Applied Geochemistry 25, 602–607.

Yang, T.F., Chou, C.Y., Chen, C.-H., Chyi, L.L., Jiang, J.H., 2003. Exhalation of radon and its carrier gases in SW Taiwan. Radiation Measurements 36, 425–429.

Zimmer, M., Erzinger, J., 2003. Continuous H_2O, CO_2, ^{222}Rn and temperature measurements on Merapi Volcano Indonesia. Journal of Volcanology and Geothermal Research 125, 25–38.

Bull Volcanol (2015) 77:28
DOI 10.1007/s00445-015-0914-2

RESEARCH ARTICLE

Dynamics of diffuse carbon dioxide emissions from Cumbre Vieja volcano, La Palma, Canary Islands

Eleazar Padrón · Nemesio M. Pérez · Fátima Rodríguez · Gladys Melián · Pedro A. Hernández · Hirochika Sumino · Germán Padilla · José Barrancos · Samara Dionis · Kenji Notsu · David Calvo

Received: 5 December 2014 / Accepted: 23 February 2015

Abstract We report herein the results of 13 soil CO_2 efflux surveys at Cumbre Vieja volcano, La Palma Island, the most active basaltic volcano in the Canary Islands. The CO_2 efflux measurements were undertaken using the accumulation chamber method between 2001 and 2013 to constrain the total CO_2 output from the studied area and to evaluate occasional CO_2 efflux surveys as a volcanic surveillance tool for Cumbre Vieja. Soil CO_2 efflux values ranged from non-detectable up to 2442 g m^{-2} $days^{-1}$, with the highest values observed in the south, where the last volcanic eruption took place (Teneguía, 1971). Isotopic analyses of soil gas carbon dioxide suggest an organic origin as the main contribution to the CO_2 efflux, with a very small magmatic gas component observed at the southern part of the volcano. Total biogenic and magmatic combined CO_2 emission rates showed a high temporal variability, ranging between 320 and 1544 t $days^{-1}$ and averaging 1147 t $days^{-1}$ over the 220-km^2 region. Two significant increases in the CO_2 emission observed in 2011 and 2013 were likely caused by an enhanced magmatic endogenous contribution revealed by significant changes in the $^3He/^4He$ ratio in a CO_2-rich cold spring. The relatively stable emission rate presented in this work defines the background CO_2 emission range for Cumbre Vieja during a volcanic quiescence period.

Keywords Diffuse degassing · CO_2 · Cumbre Vieja · Volcanic activity · $^3He/^4He$

Editorial responsibility: P. Wallace

N. M. Pérez · G. Melián · P. A. Hernández · G. Padilla · J. Barrancos
Enviromental Research Division, Instituto Tecnológico y de Energías Renovables (ITER), 38611 Granadilla, Santa Cruz de Tenerife, Spain
e-mail: eleazar@iter.es

E. Padrón · N. M. Pérez · F. Rodríguez · G. Melián · P. A. Hernández · G. Padilla · J. Barrancos · S. Dionis · D. Calvo
Instituto Volcanológico de Canarias (INVOLCAN), Antiguo Hotel Taoro, Parque Taoro, 22, 38400 Puerto de La Cruz, Tenerife, Spain

H. Sumino
Geochemical Research Center, Graduate School of Science, The University of Tokyo, 7-3-1 Hongo, Bunkyo-ku, Tokyo 113-0033, Japan

K. Notsu
Center for Integrated Research and Education of Natural Hazards, Shizuoka University, Shizuoka 422-8529, Japan

Present Address:
E. Padrón (✉)
Enviromental Research Division, Instituto Tecnológico y de Energías Renovables (ITER), 38611 Granadilla, Santa Cruz de Tenerife, Spain
e-mail: eleazar@iter.es

Published online: 07 March 2015

Introduction

Many studies on volcanic gas emissions report that large amounts of CO_2 are released during periods of quiescence and not only as visible emanations such as fumaroles, hot springs, or plume degassing from active craters but also as diffuse soil emanations from the flanks of the volcano (Baubron et al 1990; Allard et al 1991; Chiodini et al 1996; Gerlach et al. 2001; Salazar et al. 2001; Hernández et al. 2001a, 2003, 2006, 2012a, b; Padrón et al. 2012a; Pérez et al. 2013). Results from diffuse CO_2 degassing studies allow computation of CO_2 output and can be used to identify active structural features (faults and fractures) and potential sites of future eruptions (Giammanco et al. 1998a, b, 2006; Frondini et al. 2004; McGee et al. 2006). Changes in diffuse CO_2 emission rates may also provide important information for volcanic surveillance and seismotectonic monitoring (Hernández et al. 2001a; Granieri et al. 2006; Salazar et al. 2002; Carapezza et al. 2004; Padrón et al. 2008; Pérez et al. 2012, 2013; Padilla et al. 2013; Arpa et al. 2013).

After water vapor CO_2 is the main gas species in basaltic magmas (Barnes et al. 1988). Because of its low solubility in silicate melts at low and moderate pressures (Stolper and Holloway 1988; Pan et al. 1991) it is a good tracer to detect subsurface magma degassing. Possible sources of CO_2 at the surface of volcanoes include thermal degradation of organic material, metamorphism of marine carbonate rocks, and degassing of mantle-derived magma (Barnes et al. 1978). Changes in CO_2 efflux may provide important information about subsurface magma movement. Since the spatial distribution of diffuse CO_2 emissions and overall emission rates may increase extraordinarily before a volcanic eruption (Hernández et al. 2001a, b; Melián et al. 2014), it is very important to map surface CO_2 efflux anomalies and determine the total output of this gas prior to volcanic activity, in order to have a better understanding during future volcanic events.

We present in this work the results of intensive soil CO_2 emission surveys carried out between 2001 and 2013 at Cumbre Vieja volcano. The main goals of this study are to study the spatial distribution of CO_2 efflux anomalies and estimate the total diffuse CO_2 output to the atmosphere and its relation to the level of volcanic activity.

Tectonics and geological setting

La Palma Island, the fifth longest (706 km^2) and the second highest elevation (2423 m asl) of the Canary Islands, is located at the northwestern end of the archipelago (Fig. 1). Subaerial volcanic activity on La Palma started ~2.0 My ago (Ancoechea et al. 1994; Carracedo et al. 1998). La Palma is elongated along a N-S direction and can be separated into two distinct units: the older Seamount Series (4–2.9 Ma) and a younger subaerial complex known as Coberta Series (Staudigel et al. 1986). The Coberta series covers most of the island, consisting of the older Taburiente series (2–0.6 Ma), which forms the major shield volcano at the north of La Palma island, and Cumbre Vieja volcano, formed by younger lavas (0.6–0 Ma) (Ancoechea et al. 1994). The center of La Palma is dominated by the Taburiente caldera, a spectacular eroded depression that exposes

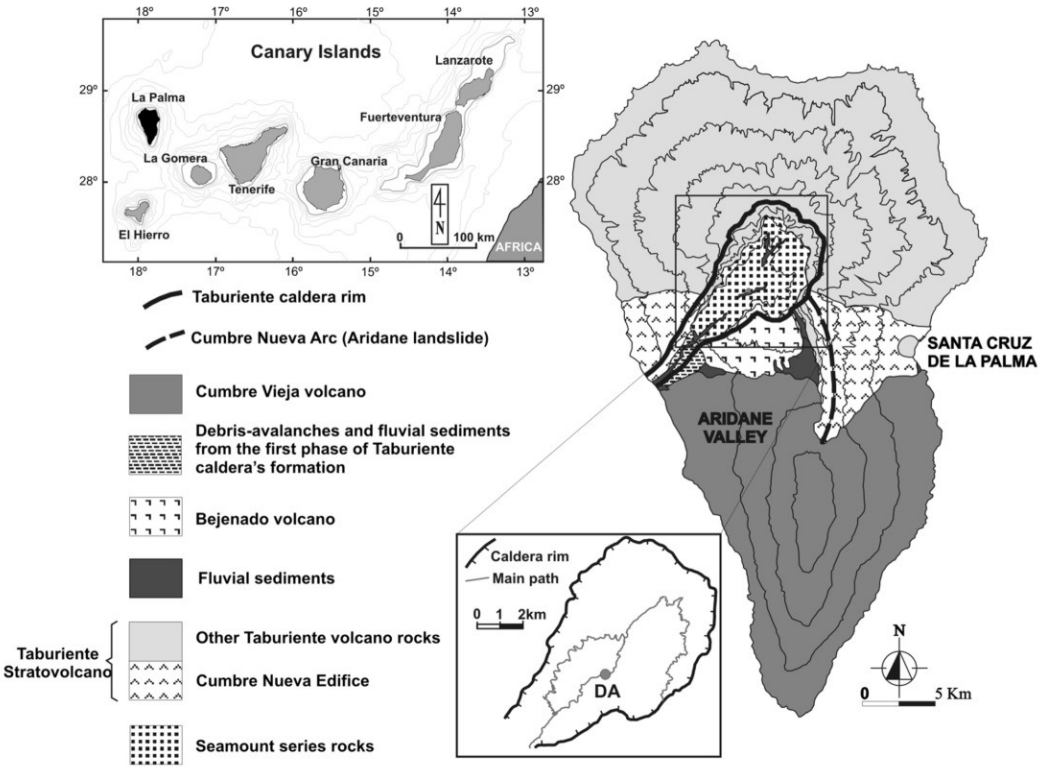

Fig. 1 Geographic location and simplified geologic map of La Palma Island (modified from Navarro 1993). DA shows the location of the Dos Aguas cold spring in Taburiente caldera

the submarine stratigraphy of the island (Ancoechea et al. 1994) formed after a collapse of the western flank of the Cumbre Nueva edifice (Fig. 1). Volcanic activity in the last 123 ka has taken place exclusively at the southern part of the island, where Cumbre Vieja volcano, the most active basaltic volcano in the Canaries, has been constructed. Cumbre Vieja volcano, which has been likened to a Hawaiian-style rift zone (Ancoechea et al. 1994; Carracedo 1996; Day et al 1999), includes a main north–south rift zone 20 km long and up to 1950 m in elevation and covers 220 km^2 with vents located also at the northwest and northeast (Fig. 2). Historical lavas are associated with the Cumbre Vieja volcanic ridge where many cinder cones are exposed. The most recent volcanic eruption was Teneguía in 1971 (Fig. 2) that produced highly alkalic basaltic and basanitic lavas. Most of the eruptions have been strombolian and phreato-strombolian. Recent studies on olivine phenocrysts from lavas on La Palma reveal interaction between recycled oceanic lithosphere, depleted mantle, and a high-$^3He/^4He$ component (mantle plume) (Day and Hilton 2011).

In the last 15 years, there has been much interest in Cumbre Vieja volcano because the 1949 volcanic eruption near the summit may have been accompanied by development of a west-facing normal fault system along the crest of the volcano and is considered to be the first surface rupture along a developing zone of flank instability (Day et al. 1999; Ward and Day 2001). Recent studies of González et al. (2010) indicate that ongoing creep beneath the western flank of Cumbre Vieja tends to stabilize the flank through reorganization with a decrease of gravitational potential forces.

The only known visible gas emanation on La Palma Island is a CO_2-rich bubbling cold spring in Taburiente caldera (Dos Aguas, DA in Fig. 1). Gas from this cold spring has the highest $^3He/^4He$ ratio measured in the Canary Islands, ranging from 9.5 to 9.95 R_A (Pérez et al. 1994; Hilton et al. 2000; Padrón et al. 2012b), where R_A is the atmospheric $^3He/^4He$ ratio (1.384×10^{-6}, Clarke et al. 1976). This value is higher than those measured in any phenocrysts or geothermal gas samples in the archipelago (Pérez et al. 1994; Hilton et al. 2000; Day and Hilton 2011).

Nowadays, there are no visible gas emissions from fumaroles or hot springs at Cumbre Vieja. However, recent studies indicated that the main N-S volcanic rift of Cumbre Vieja represents an area of enhanced permeability for deep gas migration that is a preferential route for degassing, where significant amounts of non-reactive gases (helium) escape to the atmosphere (Padrón et al. 2012b).

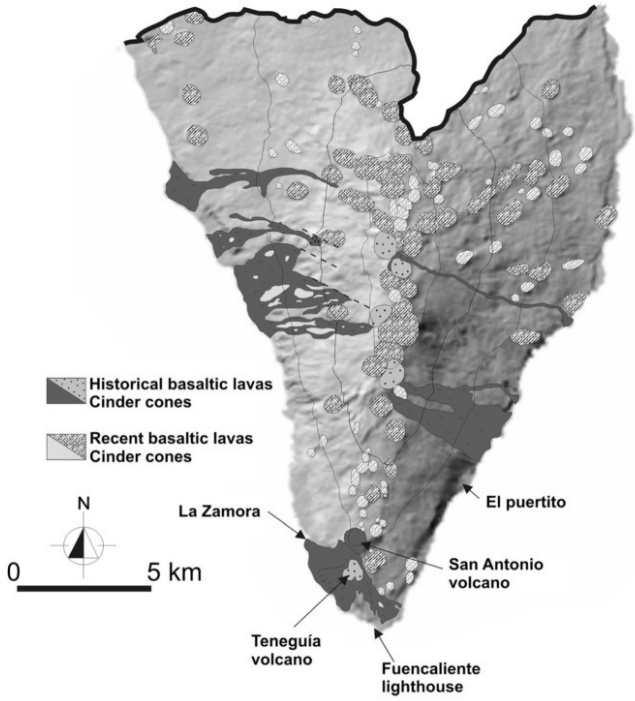

Fig. 2 Shaded relief map of Cumbre Vieja volcano

Procedures and methods

Diffuse CO_2 emission surveys were performed in summer under ideal weather conditions (calm and dry) each year from 2001 to 2013. Stable dry conditions help to eliminate variations in soil gas emissions during the measurements. About 570 sampling sites were selected for each survey to obtain a homogeneous distribution (Fig. 3a), after taking into consideration the local geology, structure, and accessibility. The soil CO_2 efflux measurement sites covered the Cumbre Vieja volcano area and its margins with a spacing about 500 m or less.

Measurements of soil CO_2 efflux were performed in situ by means of a portable non-dispersive infrared (NDIR) CO_2 analyzer LICOR LI-800, equipped with a 2000-ppm optical path. The instrument was used following the accumulation chamber method (Parkinson 1981; Chiodini et al. 1998). The internal diameter and height of the chamber used was 0.2 and 0.097 m. Each CO_2 efflux measurement started when the open side of the chamber was placed on the soil surface. A pump allowed the chamber air to circulate through the NDIR spectrophotometer and then back into the chamber. The analyzer was interfaced with a hand size computer running a data acquisition software. To verify the performances and the reliability of this method, several calibration tests were made in the laboratory and the accuracy was estimated to be 10 %. Additionally, soil temperatures were measured at each sampling site by inserting a type-K thermocouple probe at 40 cm depth.

The measured CO_2 efflux data were used to construct spatial distribution maps of diffuse CO_2 emissions using the sequential Gaussian simulation (sGs) module within the *sgsim* program of the GSLIB software (Deutsch and Journel 1998; Cardellini et al. 2003). The sGs procedure is composed of the following steps: (1) Normal score transformation of the original data, (2) experimental variogram computation of the normal score transformed data, (3) variogram model assignation using spherical models, (4) sequential Gaussian simulation of N equiprobable realizations, and (5) backtransforming the normal score data into simulated values of the original variable. The sGs procedure allows one to both interpolate the soil CO_2 efflux at un-sampled sites, to estimate total diffuse emissions of carbon dioxide for the entire studied area, and to assess uncertainty on the diffuse emissions estimate. The experimental variograms were fitted with spherical models in all the surveys, using a consistent nugget effect of ~0.7 and a range between 2000 and 5000 m.

Soil gas samples were collected at 143, 57, and 42 sites with relatively high CO_2 efflux (Fig. 3b) during the 2001, 2002, and 2010 surveys, respectively. The gas was collected at a depth of 40–50 cm using a metal probe and a syringe and then stored in glass vials. The CO_2 content and its carbon isotope composition were analyzed in the laboratory by a micro-GC VARIAN CP-2002 and a Finnigan MAT Delta S mass spectrometer (for 2001 and 2002 surveys) and Thermo Finnigan MAT 253 (for the 2010 survey), respectively. The

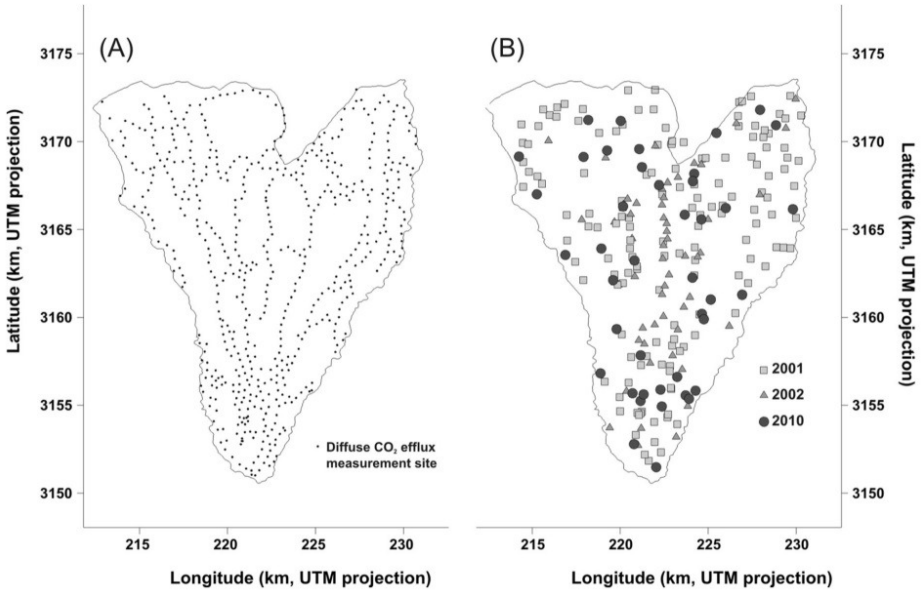

Fig. 3 Location of the sampling points selected **a** for the diffuse CO_2 efflux measurements and **b** for chemical and isotopic analysis of the soil CO_2 at Cumbre Vieja

$^{13}C/^{12}C$ ratio is given as $\delta^{13}C$ values with respect to VPBD standard with an uncertainty of 0.1‰.

Additionally, $^{3}He/^{4}He$ ratios and $\delta^{13}C$-CO_2 were analyzed in the gas from the Dos Aguas CO_2-rich bubbling cold spring (see location in Fig. 1). The gas was sampled once in 2007, 2008, and 2011 and three times in 2012. The collected gas was channeled using a funnel and obligated to flow through a lead-glass bottle using a syringe connected to the other end of the sample bottle. Helium isotope analysis was carried out in all samples following the method described by Sumino et al. (2001). Air standards were measured frequently during analyses to determine sensitivities of the mass spectrometer. The correction factor for helium isotope ratios was determined by measurement of an inter-laboratory helium standard named HESJ with recommended $^{3}He/^{4}He$ ratio of 20.63 0.10 R_A (Matsuda et al. 2002). The carbon isotopic composition was analyzed by means of a Thermo Finnigan MAT 253 mass spectrometer and the CO_2 by a micro-GC VARIAN CP-2002.

Results and discussion

The CO_2 efflux results for each survey are summarized in Table 1. The efflux values ranged from non-detectable to 2442 g m^{-2} $days^{-1}$ with a median of 1.8 g m^{-2} $days^{-1}$. The $\delta^{13}C(CO_2)$ values for the soil gas ranged from −35.1 to −1.5 ‰, suggesting different carbon sources, with an average value of −25.7‰ that falls just within the usual range for CO_2 of a biogenic origin. The respective soil CO_2 concentrations ranged from 0.02 to 10.1 mol.%. The ranges of $\delta^{13}C(CO_2)$ values from the three surveys showed slight differences, with some gas collected in 2002 having heavier $\delta^{13}C(CO_2)$ values (up to −1.5 ‰). These differences might be related sampling grid differences at each survey. The average $\delta^{13}C$-CO_2 value increased over the 3 years: −27.9 ‰ (2001), −23.7‰ (2002), and −16.5‰ (2010).

Statistical results

We applied the Kolmogorov–Smirnov test (Zar 1984) to the original and the log-transformed flux data for each survey to measure the deviation between the actual distribution and that expected for a normal distribution. At 0.05 significance level, none of the original or log-transformed data were determined to be drawn from a normally distributed population.

To check whether the log-transformed data comes from mixed polymodal distributions, the probability-plot technique (Tennant and White 1959; Sinclair 1974) was applied to all CO_2 efflux data sets (Fig. 4). This technique is based on the recognition of inflection points along a curve produced by plotting cumulative percentile flux data on a log-normal scale. One inflection point was found for data from all surveys and allowed us to distinguish two modes of degassing: normal I and normal II. The two distinct populations are here referred to as background (commonly derived from biogenic CO_2 emission) and peak (mainly deep-seated CO_2 degassing), respectively. Table 2 summarizes the results from the probability-plot technique. Normal I or background emissions represent 98.2 % of the total data, which seems to indicate a main biogenic origin for the CO_2 emission at Cumbre Vieja. Only ~1 % of the total data are present in the normal II or peak population, which suggests limited CO_2 emissions from deep-seated sources at Cumbre Vieja.

Table 1 Statistical results of soil CO_2 efflux measured in the 2001–2013 period surveys and $\delta^{13}C$ (CO_2) in the 2001, 2002, and 2010 surveys

Year	Soil CO_2 efflux (g m^{-2} day^{-1})				CO_2 output (t day^{-1})[a]	$\delta^{13}C$ (CO_2) (‰ vs. PDB)				Soil CO_2 concentration (mol.%)		
	No. samples	Min.	Max.	Median		No. samples	Min.	Max.	Median	Min.	Max.	Median
2001	621	<0.5	1461	3.2	1348 89	143	−35.1	−11.5	−28.8	0.02	1.29	0.21
2002	619	<0.5	1250	1.4	950 68	57	−33.4	−1.5	−23.7	0.77	10.1	0.24
2003	611	<0.5	1915	1.8	1253 111	–	–	–	–	–	–	–
2004	555	<0.5	1171	1.8	990 79	–	–	–	–	–	–	–
2005	560	<0.5	872	1.6	1169 110	–	–	–	–	–	–	–
2006	599	<0.5	1294	1.1	1060 139	–	–	–	–	–	–	–
2007	531	<0.5	252	2.4	992 44	–	–	–	–	–	–	–
2008	505	<0.5	103	1.8	807 92	–	–	–	–	–	–	–
2009	548	<0.5	1404	0.9	657 55	–	–	–	–	–	–	–
2010	550	<0.5	878	0.9	748 71	42	−21.2	−8.8	−16.9	0.05	0.62	0.14
2011	572	<0.5	75	3.6	1544 81	–	–	–	–	–	–	–
2012	565	<0.5	558	0.7	320 31	–	–	–	–	–	–	–
2013	583	<0.5	2442	1.9	1538 160	–	–	–	–	–	–	–

[a] The CO_2 output uncertainty is represented as 1 standard deviation (1σ) of 100 sGs equiprobable realizations

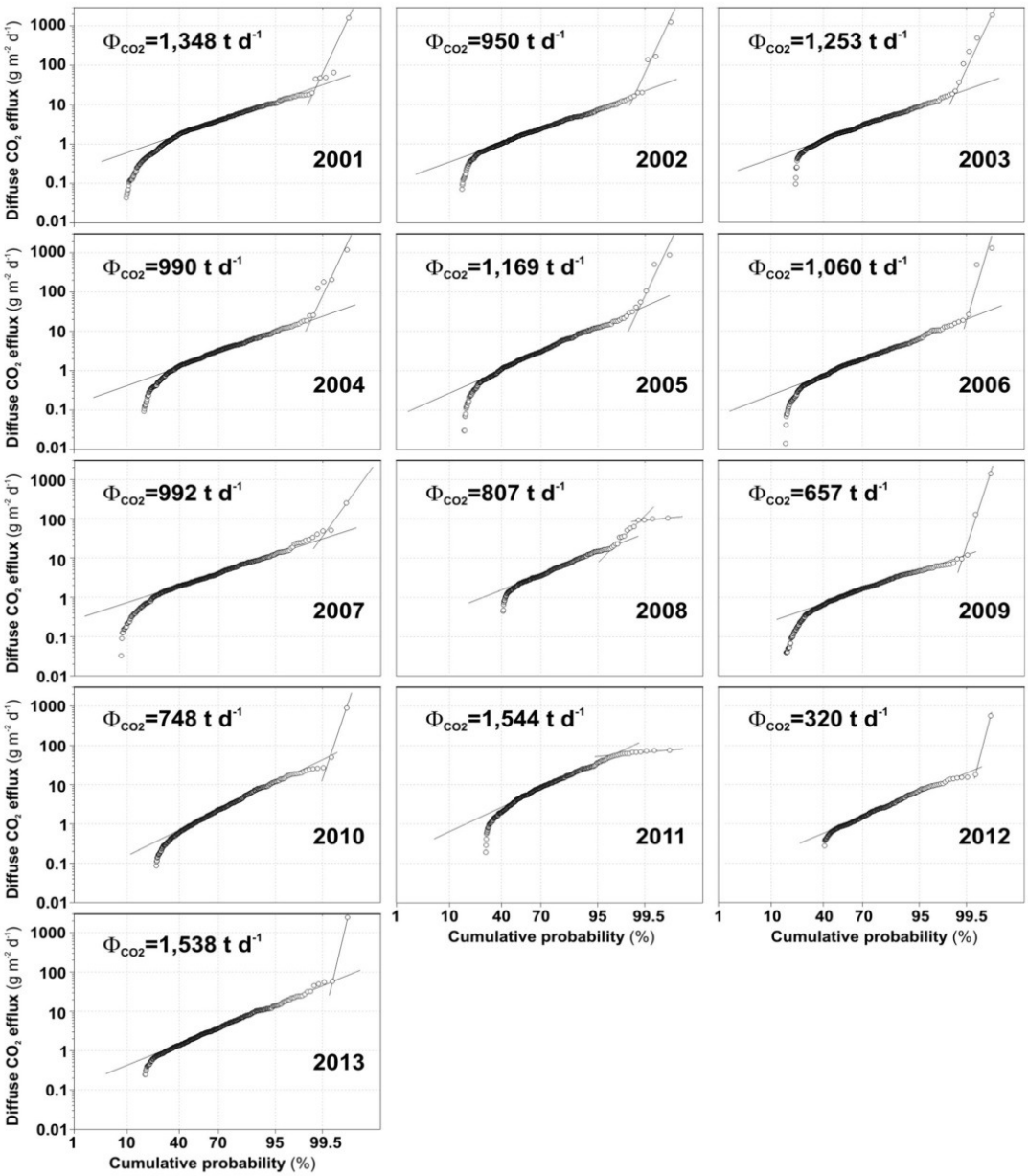

Fig. 4 Yearly cumulative frequency plots (*x*-axis, *probability scale*) of the diffuse CO_2 efflux data (*y*-axis, *Log scale*) in the period 2001–2013. The total diffuse CO_2 emissions (Φ_{CO_2}) calculated for each year are also displayed in the plot

To better delineate subtleties in the peak log-normal population, we used the probability-plot method on the entire data set (7448 diffuse CO_2 efflux measurements) (Fig. 5). The resulting plot shows four inflection points, indicating three populations of flux values: normal I or background, II or intermediate and III or peak. The mean populations are ~1.4, 50.0, and 1400 g m^{-2} days^{-1}, with 98.7, 1.04, and 0.26 %. The intermediate values are only visible in the probability-plot

Table 2 Statistical summary of the probability plots of the different data sets

Year	Probability-plot technique			
	Mean normal I (g m^{-2} day^{-1})	Mean normal II (g m^{-2} day^{-1})	% normal I	% normal II
2001	2.4	138.2	99.4	0.6
2002	1.3	175.0	99.5	0.5
2003	1.7	384.7	99.3	0.7
2004	1.9	221.0	99.0	1.0
2005	0.9	85.0	99.3	0.7
2006	1.1	98.5	99.3	0.7
2007	2.4	27.0	97.4	2.6
2008	2.0	102.9	97.7	0.7
2009	1.0	60.8	99.5	0.5
2010	0.9	21.9	96.9	3.1
2011	4.0	68.5	99.0	1.0
2012	0.8	49.0	99.0	1.0
2013	1.9	58.2	99.7	0.3

analysis of the entire data set. Advection might be the responsible transport mechanism to explain the observed relatively high CO_2 efflux values, whereas background CO_2 efflux values could be mainly characterized by biogenic CO_2 which is mainly transported by diffusion.

Spatial and temporal distribution of CO_2 efflux at Cumbre Vieja

Soil CO_2 efflux measurements at Cumbre Vieja exhibited high spatial variability (Fig. 6). In most of the surveys, CO_2 efflux values ranging from 15 to 25 g m^{-2} $days^{-1}$ were measured at the north end of Cumbre Vieja, around the surface contact with Cumbre Nueva ridge. This area is characterized by a wet climate and is mainly vegetated by pine forests and heaths. Pine forest can be found also along both sides of the N-S volcanic rift of Cumbre Vieja, where CO_2 efflux values from 5 to 20 g m^{-2} $days^{-1}$ were measured in all the surveys. The maximum flux values (>800 g m^{-2} $days^{-1}$) were measured in the summit of Teneguía cinder cone, except during the 2007, 2008, 2011, and 2012 surveys. This sampling site showed important soil temperature values, ranging between 90 and 130 °C at 40 cm depth in the study period. The rest of the soil temperature values seemed to be modulated by ambient temperature values. It is important to point out that the high flux anomaly at Teneguía cinder cone is the result of only one site, and its emission value was strongly disturbed on windy days. Repeated diffuse CO_2 measurements at this point over the study period (2001–2013) form the peak population in Fig. 5. This anomalous CO_2 emission might be caused by residual degassing of volatiles from stored magma bodies beneath the southern part of the volcano that were responsible of the volcanic eruption of Teneguía.

Other relatively high CO_2 efflux values (up to 150 g m^{-2} $days^{-1}$) were measured in nearly all surveys at three sites at the southern coast of Cumbre Vieja, El Puertito, La Zamora, and Fuencaliente lighthouse, close to Teneguía volcano (Fig. 2). These sites are poorly vegetated beach areas and surroundings, and the elevated emissions suggest a non-biogenic, deep-seated origin for the CO_2. Fluxes at these three sites represent the intermediate population in Fig. 5.

The observed strong structural-spatial correlation in the emission of inert gases (helium) observed in Cumbre

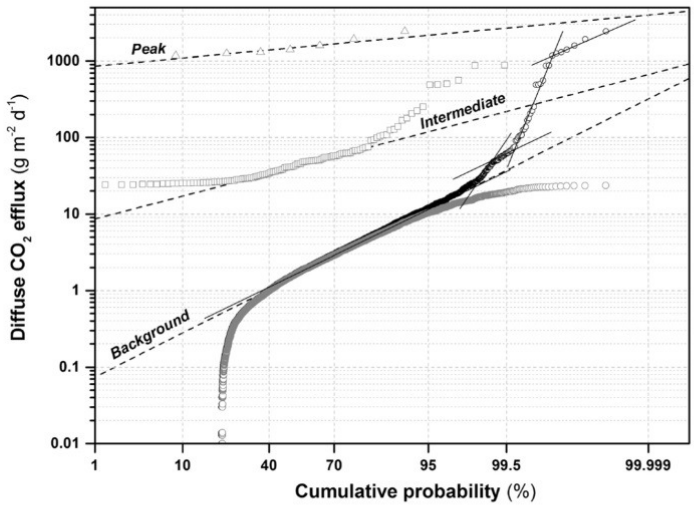

Fig. 5 Cumulative frequency plot of all diffuse CO_2 efflux data sets from this study. The intercepts of the *solid black lines* are interpreted as threshold values that separate different populations of emissions. The separated populations are shown as *open gray circles* (background), *squares* (intermediate), and *triangles* (peak). *Dashed lines* indicate the fitting lines of background, intermediate, and peak log-normal populations

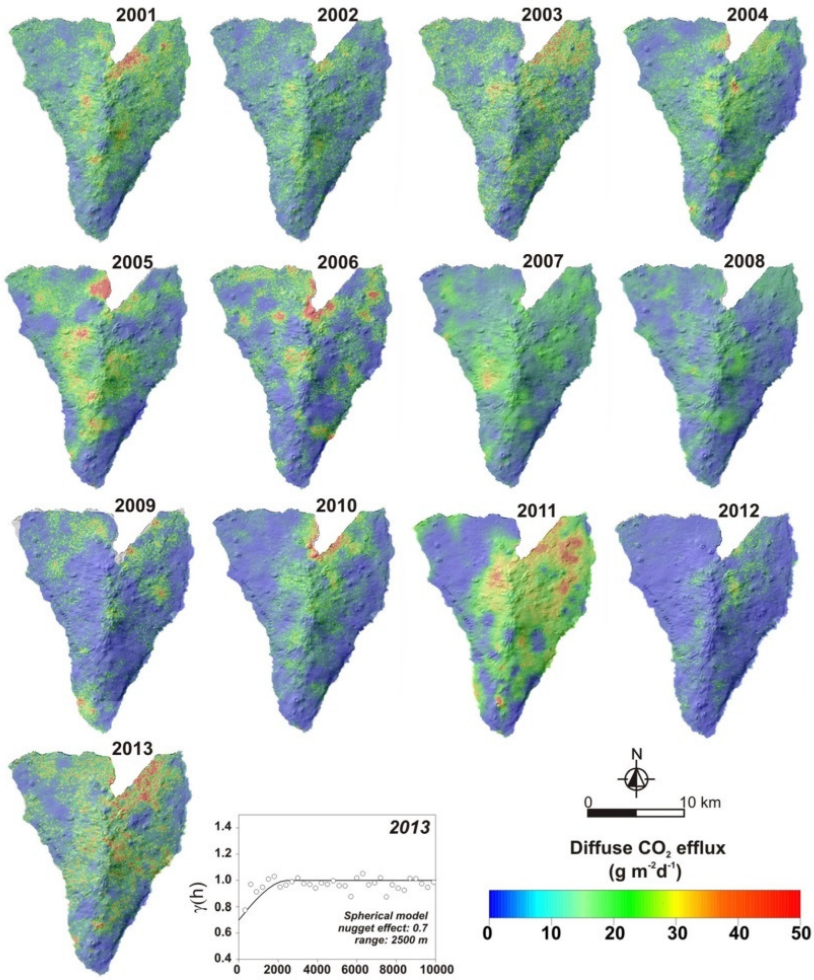

Fig. 6 Spatial distribution of diffuse CO_2 efflux on Cumbre Vieja volcano, based on sequential Gaussian simulations for the 13 surveys. The experimental and the modeled variogram used by sequential Gaussian simulation to construct the spatial distribution of the 2013 survey are also shown

Vieja by Padrón et al. (2012b) and the absence of such correlation in the CO_2 emission, support the interpretation that any reactive gases (as CO_2, SO_2, H_2S) released from depth by the volcanic system of Cumbre Vieja undergo chemical reactions or are almost completely dissolved in water during their rise. This observation is also supported by the chemical composition of groundwater extracted in the few existing vertical or horizontal wells at Cumbre Vieja (Veeger 1991; Pérez et al. 1996). CO_2 is transported to the ocean by groundwater circulation towards the southern coast of the island following the main structural N-S rift zone of Cumbre Vieja. The groundwater flows preferentially along N-S direction due to the geometry of dikes beneath Cumbre Vieja (Padrón et al. 2012b). Since most of the highest diffuse CO_2 emission values were measured at the southern part of Cumbre Vieja, Teneguía volcano, and surrounding areas, we carried out a more detailed CO_2 diffuse emission survey during the summer of 2005. A total of 241 sampling points covered 6.2 km^2 and included the sites with the highest CO_2 efflux values. As an approximation, we considered deep-seated CO_2 as the main contributor to the total CO_2 efflux at this area. The probability plot of the diffuse CO_2 emission data (Fig. 7a) shows two overlapping populations. Background efflux represented 95.2 % of the data, with a mean below the detection limit of the instrument (<0.5 g m^{-2} $days^{-1}$), and the peak population represented 3.4 % of the data, with a mean of 237 g m^{-2} $days^{-1}$. The low efflux for the background population supports the hypothesis of negligible biogenic contribution to the diffuse CO_2 emission at these sites. Figure 7 shows the average flux map from 100 sGs simulations composed of

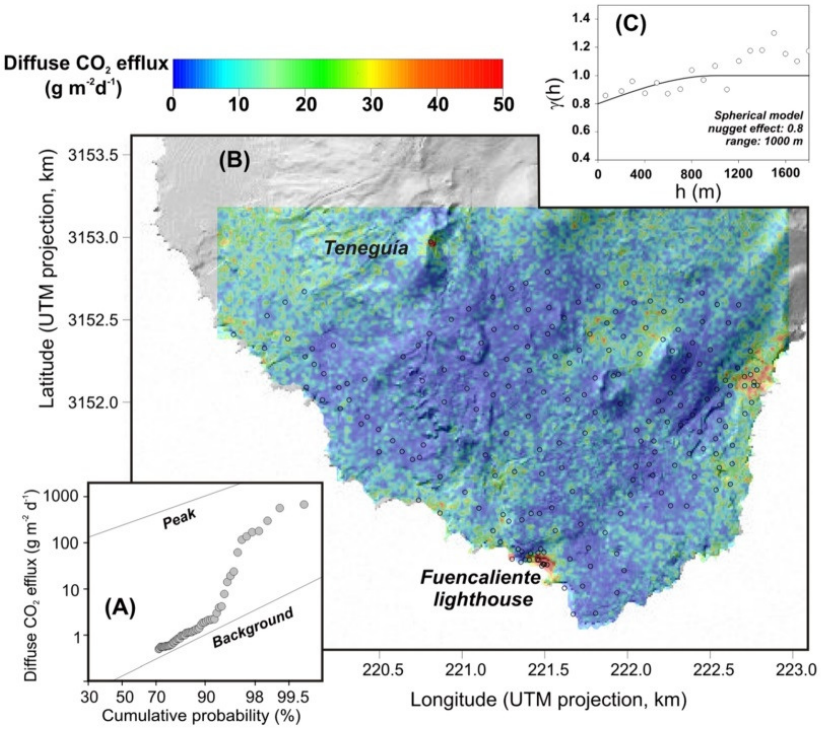

Fig. 7 **a** Cumulative frequency plot of diffuse CO_2 efflux data and **b** spatial distribution of diffuse CO_2 efflux from the southern part of Cumbre Vieja volcano. *Open circles* indicate the location of the measuring sites. **c** Experimental and the modeled variogram used by sequential Gaussian simulation to construct the spatial distribution

15,961 cells with a size of 20×20 m. The highest diffuse CO_2 emission values were measured at Teneguía cinder cone (870 g m^{-2} $days^{-1}$) and in the coast area around Fuencaliente lighthouse (up to 674 g m^{-2} $days^{-1}$).

Total diffuse CO_2 emissions

To estimate the total diffuse CO_2 output in metric tons per day released from Cumbre Vieja edifice (220 km^2) for each survey, we ran sGs simulations of 24,070 cells (100×100 m) and the average of 100 simulations to estimate the total output with 1 standard deviation uncertainty. The average and standard deviation for each survey are shown in Table 1 and plotted in Fig. 8. The mean flux of the background populations was assumed to be a representative cut-off value with a confidence level of one standard deviation (σ). This mean value (mean of the 50 percentile values of the 13 probability plots, i.e., 1.7 g m^{-2} $days^{-1}$) is similar to background values for other volcanic systems in the Canary Islands with similar soils, vegetation and climate conditions (e.g., El Hierro: 1.4 g m^{-2} $days^{-1}$; Melián et al. 2014), and slightly higher than Timanfaya in Lanzarote Island (0.4 g m^{-2} $days^{-1}$; Hernández et al. 2012a, b). Given the studied area of 220 km^2, a total CO_2 output of 374 t $days^{-1}$ is calculated as background emission, with -1σ of 132 t $days^{-1}$ and $+1\sigma$ of 1254 t $days^{-1}$ (mean of the 16 and 84 percentile values of the probability plots, respectively; Sinclair 1974). If we increase the confidence limits of the background range up to 95 % using 2σ from the mean, the upper limit of the background emission would be ~1.495 t $days^{-1}$.

Results shown in Fig. 8 depict stable emissions around 1100 t $days^{-1}$ in the first five surveys, followed by a downward trend that was broken by sudden increases in emissions during 2011 and 2013. Most of the emission estimations in the study period are entirely within the range defined for background emissions. The 2011 and 2013 studies were the only surveys with mean values slightly above background. It should be noted that in 2011, when the highest total CO_2 emission was estimated, the maximum emission value measured was the lowest and was not measured at Teneguía cinder cone, likely due to atmospheric disturbances (windy weather); however, the median diffuse emission value was the highest of all years (3.6 g m^{-2} $days^{-1}$, Table 1). Recent diffuse degassing studies carried out during a volcanic unrest period on the neighboring island of El Hierro have demonstrated that low CO_2 emission values (in the range 1–20 g m^{-2} $days^{-1}$) can be slightly increased by endogenous degassing (Pérez et al. 2012; Melián et al. 2014). These observations suggest that we cannot exclude the possibility that an endogenous component is responsible for this increase in the background emission

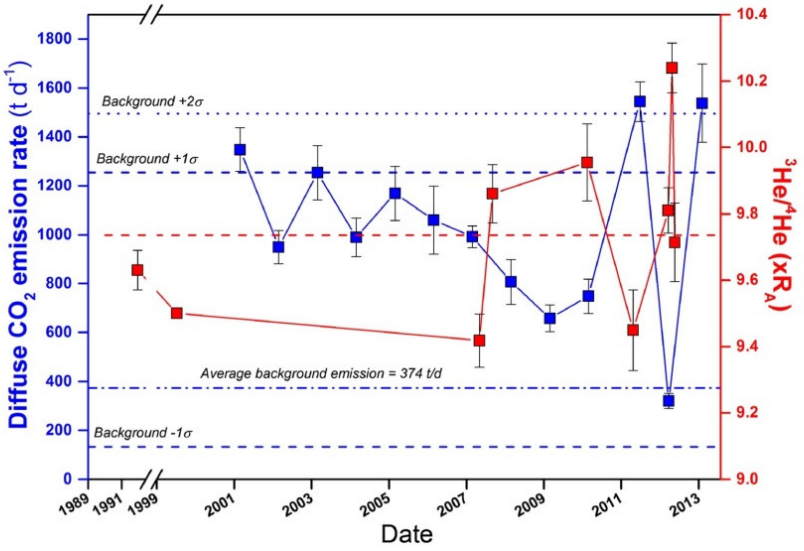

Fig. 8 Plot showing annual estimates of the total diffuse CO_2 output released from Cumbre Vieja volcano since 2001 (*blue squares*) and changes in the $^3He/^4He$ ratio measured in gas from the Dos Aguas cold spring (*red squares*). *Red dashed line* indicates the average $^3He/^4He$ ratio during the study period. Uncertainties with reported $^3He/^4He$ ratios are 1 sigma, including error of the measured raw $^3He/^4He$ ratio, that of measured raw $^3He/^4He$ ratio of HESJ, and that on the recommended $^3He/^4He$ ratio of HESJ. Data from Pérez et al. (1994), Hilton et al. (2000), and Padrón et al. (2012a) are shown in their respective sampling dates: 1991, 1999, and 2010, respectively

values and, thus in the total emission. In the case of the detailed survey performed at the southern part of the volcano in 2005, the total CO_2 output was 51.1 6 t $days^{-1}$, compared with the total diffuse CO_2 output from the entire volcano, which was estimated at 1169 110 t $days^{-1}$ in 2005. We consider this amount as the main deep contribution to the total output, indicating that a maximum of ~4 % of the total diffuse CO_2 output is released from a deep source at Cumbre Vieja volcano during volcanic quiescence.

Compared with other diffuse CO_2 emission rates published worldwide (Burton et al. 2013), the emissions from Cumbre Vieja are some of the lowest per unit area (1.5–7.0 t $days^{-1}$ km^2) and support the idea that the volcano is undergoing quiescence. According to the five-stage evolutionary model proposed by Notsu et al. (2006), Cumbre Vieja is exhibiting stage I behavior, in which plume or diffuse degassing of volcanic gas is very low because magma is present only at a significant depth.

Figure 8 also shows the temporal evolution of the $^3He/^4He$ ratio measured in Dos Aguas cold spring from 1991 to 2012. Table 3 shows all the published $^3He/^4He$ data including the new results reported in this work. The helium isotope composition of the bubbling gas emission at Dos Aguas indicates an important mantle contribution with values ranging around an average of 9.73 R_A (red dashed line in Fig. 7).

Significant increases from 2007 to 2010 and from 2011 to 2012 were observed. Diffuse CO_2 increases observed in 2011 and 2013 seem to be preceded by an increase in the $^3He/^4He$ observed in Dos Aguas. The $CO_2/^3He$ measured in the bubbling gases of this cold spring (0.5–1.7 10^{10}; Hilton et al. 2000; Padrón et al. 2012b) are within the range found in typical mantle environments (1–10 10^9, Marty and Jambon 1987) and reasonably contain a significant CO_2 component from the present magmatic source of Cumbre Vieja. Assuming that the measured $CO_2/^3He$ ratio in this cold spring is applicable for the whole island, as was suggested previously by Hilton et al. (2000), the rise in the ^3He emission would suggest corresponding increases in the deep-seated CO_2 release. We conclude that enhanced endogenous contributions were responsible for the higher CO_2 emission values in 2011 and 2013, with a delayed response of about 1 year.

Assuming that crustal helium does not significantly contribute to the observed $^3He/^4He$ ratios in Dos Aguas and following the model proposed by Sano et al. (1985) and Padrón et al. (2012b), $^3He/^4He$ ratios in Dos Aguas can be explained by a mixing model of atmospheric-type, MORB-type and plume-type helium, and the fraction of helium from each reservoir can be calculated following a simple mass balance. Table 3 summarizes the estimated amounts of atmospheric-type ($^3He/^4He$=1 R_A and $^4He/^{20}Ne$=0.318), MORB-type ($^3He/^4He$=8 R_A and $^4He/^{20}Ne$=1000), and plume-type ($^3He/^4He$ ~35 R_A and

Table 3 Results of the $^3He/^4He$ and $^4He/^{20}Ne$ ratios measured in Dos Aguas cold spring

Sampling date	$^3He/^4He$ (xR_A)	$^4He/^{20}Ne$	$^3He/^4He$ corr. (xR_A)	Atm. He (%)	MORB He (%)	Plume He (%)	$\delta\ ^{13}C(CO_2)$ (‰ vs. VPDB)	$CO_2/^3He$ ($\times10^{10}$)
15 Dec 1991[a]	9.63 0.06	50	9.68 0.06	0.6	93.3	6.1	–	–
13 Dec 1999[a]	9.5	–	–	–	–	–	–	1.7
07 Oct 2007	9.40 0.08	119.1	9.42 0.08	0.2	94.6	5.2	–	–
07 Feb 2008	9.82 0.09	78.3	9.86 0.09	0.4	92.9	6.7	–	–
20 Jul 2010[a]	9.95 0.12	181	9.96 0.12	0.1	92.7	7.2	−3.58	0.50
28 Sept 2011	9.43 0.12	169.1	9.45 0.12	0.2	94.5	5.3	−3.19	0.59
24 Aug 2012	9.80 0.07	212.3	9.81 0.07	0.1	93.3	6.6	–	–
29 Sept 2012	10.04 0.07	14.9	10.24 0.07	2.1	90.0	8.0	−2.86	0.57
24Oct 2012	9.70 0.12	215.7	9.71 0.12	0.1	93.6	6.2	−3.71	0.73

Uncertainties with reported $^3He/^4He$ ratios are 1 sigma, including error of the measured raw $^3He/^4He$ ratio, that of measured raw $^3He/^4He$ ratio of HESJ, and that on the recommended $^3He/^4He$ ratio of HESJ. Errors on concentrations are estimated to be 10 % based on reproducibility of noble gas sensitivity of the mass spectrometer during repeated air standard analyses

Atm. percentage of helium from atmospheric, *MORB* percentage of helium from MORB, *plume He* percentage of helium from mantle plume

[a] Data from Pérez et al. (1994), Hilton et al. (2000), Padrón et al. (2012a, b)

$^4He/^{20}Ne$=1000) helium released by Dos Aguas cold spring, using the following equations:

$$\left(^3He/^4He\right)_i = \left(^3He/^4He\right)_a \times A + \left(^3He/^4He\right)_m \times M + \left(^3He/^4He\right)_p \times P$$

$$\frac{1}{\left(^4He/^{20}Ne\right)_i} = \frac{A}{\left(^4He/^{20}Ne\right)_a} + \frac{M}{\left(^4He/^{20}Ne\right)_m} + \frac{P}{\left(^4He/^{20}Ne\right)_p}$$

$$A + M + P = 1$$

where subscripts *i*, *a*, *m*, and *p* indicates the sample, atmospheric, MORB type, and plume type, respectively, and *A*, *M*, and *P* are the fraction of helium from atmospheric, MORB, and mantle plume, respectively. The calculations reveal a small but persistent component of plume-type helium, which suggests a component from the deep mantle, in accordance with the hot-spot model proposed earlier for the Canaries (Pérez et al. 1994; Carracedo et al. 1998). In Fig. 9, $^3He/^4He$ ratios are plotted against $^4He/^{20}Ne$ ratios for the Dos Aguas gas. As indicated by the mixing lines between atmospheric and mantle-derived helium, the Dos Aguas samples plotted above the canonical mid-ocean ridge basalt (MORB, 8 1 R_A, Graham 2002). A slight contribution of plume-type helium is observed at all the samples, which reached a maximum value in September 2012 (~8 %, Table 3).

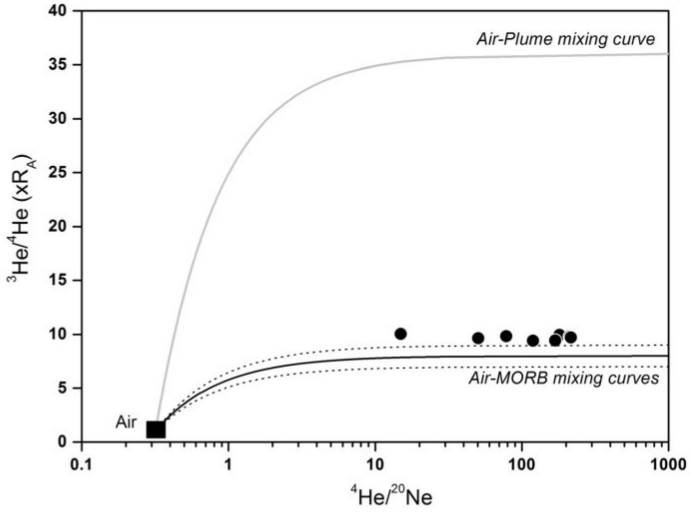

Fig. 9 $^3He/^4He$ vs. $^4He/^{20}Ne$ diagram for gas from the Dos Aguas cold spring. The curves indicate mixing relationships between endogenous end-members having an assumed $^4He/^{20}Ne$ ratio of 1000 and different $^3He/^4He$ ratios. *Black and dotted lines* indicate the mixing line between air and the canonical range of a MORB-type helium (8 1 R_A, Graham 2002). *Gray line* indicates the mixing line between air and plume-type helium (~35 R_A, Sano et al. 1985)

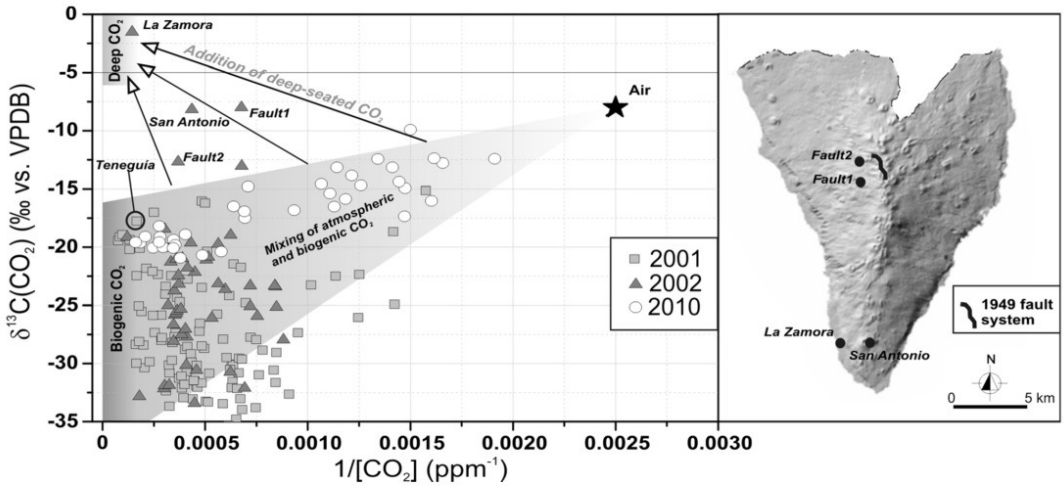

Fig. 10 *Left*, correlation diagrams between $\delta^{13}C(CO_2)$ and $1/[CO_2]$ (ppm^{-1}) from the 2001, 2002, and 2010 surveys. The degraded shaded area from the atmospheric to the biogenic end-member represents samples affected by mixing of atmospheric and biogenic CO_2. The result from the soil CO_2 in Teneguía cinder cone is indicated. *Right*, location of the samples with the more obvious endogenous CO_2 contribution: La Zamora site, San Antonio volcano, and two sites close to the normal fault system originated in the 1949 eruption (faults 1 and 2) (Day et al. 1999)

Origin of CO_2

To investigate the origin of the soil CO_2 at Cumbre Vieja, a binary diagram of the $\delta^{13}C(CO_2)$ vs. $1/[CO_2]$ was constructed with two geochemical end-members (Fig. 10): air, characterized by $\delta^{13}C(CO_2)=-8.0‰$ and $[CO_2]=400$ ppm and biogenic CO_2. To construct the range of the biogenic end-member, we have taken into account that biogenic CO_2 in the soil can be up to +4.4‰ heavier than the soil-respired CO_2 produced by roots, owing to diffusion induced isotopic fractionation (Cerling et al. 1991). Since the isotopic composition of soil organic matter is less than −20‰ (Craig 1953), the isotopic composition for the biogenic soil CO_2 was defined ≤15.6‰. The addition of deep-seated CO_2 (which includes mantle-derived CO_2 and metamorphism of marine carbonate rocks) would produce trends that lie along the arrows shown in Fig. 10, towards $\delta^{13}C(CO_2)$ ≥8‰ (Javoy et al. 1978; Barnes et al. 1988) and $[CO_2]$ ~100 %.

Figure 10 indicates that most of the sampling sites contain CO_2 composed by different degrees of mixing between atmospheric and biogenic CO_2. Soil CO_2 sampled where the high flux anomaly at Teneguía cinder cone was measured (Teneguía sample in Fig. 10), showed $\delta^{13}C(CO_2)=-17.7‰$, and $[CO_2]=0.17$ %. Due to the low $\delta^{13}C$-CO_2 values, the high CO_2 emissions at Teneguía cannot be explained solely on the origin of the gas and indicate an important advective (likely convective), component in the flux, because of the high soil temperature measured. The samples with the more obvious endogenous CO_2 contribution were sampled in 2002 (solid triangles plotted above the area of mixing between atmospheric and biogenic CO_2). Their location is depicted in Fig. 10: La Zamora site, San Antonio volcano, and two sites close to the normal fault system that was formed during the 1949 eruption (Day et al. 1999), named as faults 1 and 2 in Fig. 10. The $\delta^{13}C$-CO_2 value of −1.5‰ at La Zamora with $[CO_2]=10.1$ mol.% showed the heavier isotopic composition. The isotopic composition of the CO_2 at this site can be explained by diffuse fractionation of magmatic CO_2 with an original non-fractionated value approximately −5.9‰ (Cerling et al. 1991). Finally, the presence of significant enrichments in the deep component of the CO_2 in the

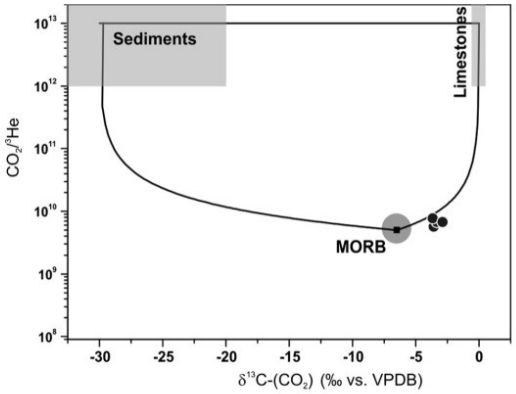

Fig. 11 Plot showing $CO_2/^3He$ vs. $\delta^{13}C(CO_2)$ for gas from the Dos Aguas spring, following the model of Sano and Marty (1995). The curves indicate sedimentary rock-mantle-marine limestone mixing relationships

sites close to the 1949 eruption (−8.0 and −12.7‰) could be explained by residual emission of volatiles from source magmatic bodies, released preferentially through the fracture zone. A more detailed survey would be necessary to confirm this hypothesis. The other anomalously high CO_2 emission values observed at El Puertito and Fuencaliente lighthouse (Fig. 2), showed values of −19.0 and −8.8‰, respectively, which suggests a slight deep contribution in the CO_2 emission.

To investigate the origin of the CO_2 released in Dos Aguas cold spring, we plotted the $\delta^{13}C(CO_2)$ vs. $CO_2/^3He$ ratios, with the following assumed end-member compositions (Sano and Marty 1995): $(CO_2/^3He)_{mantle} = 5 \times 10^9$, $(CO_2/^3He)_{limestone} = 10^{13}$, $(CO_2/^3He)_{sediments} = 10^{13}$, $\delta^{13}C(CO_2)_{mantle} = -6.5‰$, $\delta^{13}C(CO_2)_{limestones} = 0‰$, and $\delta^{13}C(CO_2)_{sediments} = -30‰$. The four gas samples from Dos Aguas plot close to the mantle end-member, along the mantle-crust (limestones) mixing trend in Fig. 11. Using the mass balance proposed by Sano and Marty (1995), an important contribution of mantle carbon, in the range 20–29 %, have been estimated in Dos Aguas. Similarly, we calculate ~10 % mantle CO_2 for gas from La Zamora and Fuencaliente lighthouse sites. To calculate the mantle component at this site, we have assumed a similar $^3He/^4He$ ratio for both, measured by Padrón et al. (2012b) in Fuencaliente lighthouse (~1.084 R_A). Under this assumption, we can conclude that approximately 10 % of the anomalous diffuse CO_2 emission observed at several sites along the southern coast of Cumbre Vieja (La Zamora, Fuancaliente lighthouse, and El Puertito in Fig. 2) are derived by mantle degassing.

Conclusions

The diffuse CO_2 emissions and the isotopic composition of the soil CO_2 reported here indicate the presence of different CO_2 sources that contribute to the release of this gas from Cumbre Vieja. Biological processes such as degradation of organic matter are the main source of CO_2 at Cumbre Vieja with a slight contribution of deep-seated CO_2. Our results suggest that this endogenous CO_2 is released diffusively at several sites along the southern coast of the volcano. At these sites, an important component of mantle CO_2 (~10 %) is present. Owing to the main organic origin in the CO_2 released through the Cumbre Vieja soils, estimating the deep-seated fraction is difficult. This fraction amounted to around 51 t $days^{-1}$ in the southern part of Cumbre Vieja, an area with almost negligible biogenic contribution, and where the highest CO_2 efflux values were measured. This amount indicates that only ~4 % of the total diffuse CO_2 output should be considered to be released from a deep source during volcanic quiescence periods.

Significant increases in the CO_2 emission rate from Cumbre Vieja were observed in 2011 and 2013, which might be related to inputs of deep-seated CO_2 as observed by important increases in the magmatic component of helium measured in Dos Aguas cold spring, 1 year before the high CO_2 emission rates estimated. The CO_2-rich Dos Aguas cold spring shows ~25 % of CO_2 derived directly forms mantle degassing and represents an important site to monitor changes in the volcanic activity of Cumbre Vieja. The results reported here for Cumbre Vieja, together with the recent results observed in El Hierro by Pérez et al. (2012) and Melián et al. (2014), demonstrate that low CO_2 efflux measurements are also useful for volcanic surveillance programs, since the emission rate responds also to changes in the deep CO_2 contribution.

The spatial distribution of diffuse CO_2 efflux from Cumbre Vieja volcano showed that relatively high values were measured at the northern end of Cumbre Vieja, and at both sides of the N-S volcanic rift, in areas characterized by wet climate and a strong development of vegetation. The maximum diffuse emission values were repeatedly measured in the summit of Teneguía cinder cone, where the last eruption took place at Cumbre Vieja. Enhanced endogenous contributions of deep-seated CO_2 might have been responsible for the higher CO_2 emission values in 2011 and 2013, which likely occurred with a delayed response of about 1 year. The observed secular variations on the total output of diffuse CO_2 emission observed in the rest of the surveys do not seem to be related with physical-chemical changes on the volcanic system of Cumbre Vieja and might be controlled by meteorological conditions, which can affect strongly to the CO_2 concentrations and, in consequence, its fluxes (Maljanen et al. 2002), as has been observed in other volcanic areas (Viveiros et al. 2008; Hernández et al. 2012a, b).

Acknowledgments The authors wish to thank A. Alfaya, L. Fuentes, M. Brito, A. Concepción, A. Mena, R. Delgado, T. Cabrera, S. Vargas, M.D. Peraza, and G. López for their help during the fieldwork. Funds provided by projects ALERTA and ALERTA II (financially supported by INTERREG IIIB Azores-Canaries-Madeira), PI2001/025 (financially supported by Dirección General de Universidades e Investigación, Canary Islands Government), MAKAVOL (MAC/3/C161) by the European Union MAC2007–2013 Transnational Cooperation Program, ProID20100160 by Canarian Agency for Research, Innovation and Information Society (Canary Island Government) and by Cabildo Insular de Tenerife and Cabildo Insular de La Palma supported this work. We also thank the municipality of Fuencaliente for logistical support.

References

Allard P, Carbonelle J, Dajlevic D, Le Bronec J, Morel P, Robe MC, Maurenas JM, Faivre-Pierret R, Martins D, Sabroux JC, Zettwoog P (1991) Eruptive and diffuse emissions of CO_2 from Mount Edna. Nature 351:387–391

Ancochea E, Hernán F, Cendrero A, Cantragrel JM, Fúster JM, Ibarrola E, Coello J (1994) Constructive and destructive episodes in the building of a young Oceanic Island, La Palma, Canary Islands, and genesis of the Caldera de Taburiente. J Volcanol Geotherm Res 60:243–262

Arpa MC, Hernández PA, Padrón E, Reniva P, Padilla GD, Bariso E, Melián GV, Barrancos J, Nolasco D, Calvo D, Pérez NM, Solidum RU (2013) Geochemical evidence of magma intrusion inferred from diffuse CO_2 emissions and fumarole plume chemistry: the 2010–2011 volcanic unrest at Taal volcano, Philippines. Bull Volcanol 75:747. doi:10.1007/s00445-013-0747-9

Barnes I, Irwin WP, White DE (1978) Global distribution of carbon dioxide discharges and major zones of seismicity. US Geol Surv Water Res Investig 78–39:1–12

Barnes I, Evans WC, White D (1988) The role of mantle CO_2 in volcanism. Appl Geochem 3:281–285

Baubron JC, Allard P, Toutain JP (1990) Diffuse volcanic emissions of carbon dioxide from Vulcano Island (Italy). Nature 344:51–53

Burton MR, Sawyer GM, Granieri D (2013) Deep carbon emission from volcanoes. Rev Mineral Geochem 75:323–354

Carapezza ML, Inguaggiato S, Brusca L, Longo M (2004) Geochemical precursors of the activity of an open-conduit volcano: the Stromboli 2002–2003 eruptive events. Geophys Res Lett 31:L07620

Cardellini C, Chiodini G, Frondini F (2003) Application of stochastic simulation to CO_2 flux from soil: mapping and quantification of gas release. J Geophys Res 108:2425. doi:10.1029/2002JB002165

Carracedo JC (1996) A simple model for the genesis of large gravitational landslide hazards in the Canary Islands. In: McGuire WJ, Jones AP, Neuberg J (eds) Volcano instability on earth and other planets. Geol Soc Spec Pub110:125–135

Carracedo JC, Day S, Guillou H, Rodríguez-Badiola E, Canas JA, Pérez-Torrado FJ (1998) Hotspot volcanism close to a passive continental margin: the Canary Islands. Geol Mag 135:591–604

Cerling TE, Solomon DK, Quade J, Bowman JR (1991) On the isotopic composition of carbon in soil carbon dioxide. Geochim Cosmochim Acta 55:3403–3405

Chiodini G, Frondini F, Raco B (1996) Diffuse emission of CO_2 from the Fossa crater, Vulcano Island (Italy). Bull Volcanol 58:41–50

Chiodini G, Cioni R, Guidi M, Raco B, Marini L (1998) Soil CO_2 flux measurements in volcanic and geothermal areas. Appl Geochem 13:543–552

Clarke WB, Jenkins WB, Top Z (1976) Determination of tritium by mass spectrometric measurement of ^{3}He. Int J Appl Radiat Isot 27:515–522. doi:10.1016/0020-708X(76)90082-X

Craig H (1953) The geochemistry of the stable carbon isotope. Geochim Cosmochim Acta 3:53–92

Day JMD, Hilton DR (2011) Origin of ^{3}He/^{4}He ratios in HIMU-type basalts constrained from Canary Island lavas. Earth Planet Sci Lett 305:226–234

Day SJ, Carracedo JC, Guillou H, Gravestock P (1999) Recent structural evolution of the Cumbre Vieja volcano, Canary Islands: volcanic rift zones reconfiguration as a precursor to volcano flank instability? J Volcanol Geotherm Res 94:135–167

Deutsch CV, Journel AG (1998) GSLIB: Geostatistical Software Library and Users Guide, 2nd ed. Oxford U

Frondini F, Chiodini G, Caliro S, Cardelini C, Granieri D, Ventura G (2004) Diffuse CO_2 degassing at Vesuvio, Italy. Bull Volcanol 66:642–651

Gerlach TM, Doukas MP, McGee KA, Kessler R (2001) Soil efflux and total emission rates of magmatic CO_2 at the Horseshoe Lake tree kill, Mammoth Mountain, California, 1995–1999. Chem Geol 177:101–116

Giammanco S, Gurrieri S, Valenza M (1998a) Anomalous soil CO_2 degassing in relation to faults and eruptive fissures on Mount Etna (Sicily, Italy). Bull Volcanol 69:252–259

Giammanco S, Inguaggiato S, Valenza M (1998b) Soil and fumarole gases of Mount Edna: geochemistry and relations with volcanic activity. J Volcanol Geotherm Res 81:297–310

Giammanco S, Gurrieri S, Valenza M (2006) Fault-controlled soil CO_2 degassing and shallow magma bodies: summit and lower east rift of Kilauea volcano (Hawaii), 1997. Pure Appl Geophys 163:853–867

González PJ, Tiampo KF, Camacho AG, Fernández J (2010) Shallow flank deformation at Cumbre Vieja volcano (Canary Islands): implications on the stability of steep-sided volcano flanks at oceanic islands. Earth Planet Sci Lett 297:545–557. doi:10.1016/j.epsl.2010.07.006

Graham DW (2002) Noble gases in MORB and OIB: observational constraints for the characterization of mantle source reservoirs. Rev Mineral Geochem 46:247–318

Granieri D, Carapezza ML, Chiodini G, Avino R, Caliro S, Ranaldi M, Ricci T, Tarchini L (2006) Correlated increase in CO_2 fumarolic content and diffuse emission from La Fossa crater (Vulcano, Italy): evidence of volcanic unrest or increasing gas release from a stationary deep magma body? Geophys Res Lett 33:L13316

Hernández PA, Notsu K, Salazar JM, Mori T, Natale G, Okada H, Virgili G, Shimoike Y, Sato M, Pérez NM (2001a) Carbon dioxide degassing by advective flow from Usu volcano, Japan. Science 292:83–86

Hernández PA, Salazar JM, Shimoike Y, Mori T, Notsu K, Pérez NM (2001b) Diffuse emission of CO_2 from Miyakejima volcano, Japan. Chem Geol 177:175–185

Hernández PA, Notsu K, Tsurumi M, Mori T, Ohno M, Shimoike Y, Salazar J, Pérez N (2003) Carbon dioxide emissions from soils at Hakkoda, north Japan. J Geophys Res 108(B4):2210

Hernández PA, Notsu K, Okada H, Mori T, Sato M, Barahona F, Pérez NM (2006) Diffuse emission of CO_2 from Showa-Shinzan, Hokkaido, Japan: a sign of volcanic dome degassing. Pure appl geophys 163:869–881

Hernández PA, Padilla G, Padrón E, Pérez NM, Calvo D, Nolasco D, Melián G, Barrancos J, Dionis S, Rodríguez F, Sumino H (2012a) Analysis of long- and short-term temporal variations of the diffuse CO_2 emission from Timanfaya volcano, Lanzarote, Canary Islands. Appl Geochem 27(12):2486–2499. doi:10.1016/j.apgeochem.2012.08.008

Hernández PA, Pérez NM, Fridriksson T, Egbert J, Ilyinskaya E, Thárhallsson A, Ívarsson G, Gíslason G, Gunnarsson I, Jónsson B, Padrón E, Melián G, Mori T, Notsu K (2012b) Diffuse volcanic degassing and thermal energy release from Hengill volcanic system, Iceland. Bull Volcanol 74:2435–2448. doi:10.1007/s00445-012-0673-2

Hilton DR, MacPherson CG, Elliot TR (2000) Helium isotope ratios in mafic phenocrysts and geothermal fluids from La Palma, the Canary Islands (Spain): Implications for HIMU mantle sources. Geochim Cosmochim Acta 64(12):2119–2132

Javoy M, Pineau F, Ilyama I (1978) Experimental determination of the isotopic fractionation between gaseous CO_2 and carbon dissolved in tholeitic magma. Contrib Mineral Petrol 67:35–39

Maljanen M, Martikainen PJ, Aaltonen H, Silvola J (2002) Short-term variation in fluxes of carbon dioxide, nitrous oxide and methane in cultivated and forested organic boreal soils. Soil Biol Biochem 34:577–584

Marty B, Jambon A (1987) C/^{3}He in volatile fluxes from the solid Earth: implications for carbon geodynamics. Earth Planet Sci Lett 83:16–26

Matsuda J, Matsumoto T, Sumino H, Nagao K, Yamamoto J, Miura Y, Kaneoka I, Takahata N, Sano Y (2002) The ^{3}He/^{4}He ratio of the new internal He Standard of Japan (HESJ). Geochem J 36:191–195

McGee KA, Sutton AJ, Elias T, Doukas MP, Gerlach TM (2006) Puhimau thermal area: a window into the upper east rift zone of Kilahuea volcano, Hawaii? Pure Appl Geophys 163:837–851

Melián G, Hernández PA, Padrón E, Pérez NM, Barrancos J, Padilla G, Dionis S, Rodríguez F, Calvo D (2014) Spatial and temporal variations of diffuse CO_2 degassing at El Hierro volcanic system: relation to the 2011–2012 submarine eruption. J Geophys Res 119(9):6976–6991

Navarro JM (1993) Avance del Plan Hidrológico Insular. Conserjería de Obras Publicas Vivienda y Aguas. 242 pp

Notsu K, Mori T, Chanchah Do Vale S, Kagi H, Ito T (2006) Monitoring quiescent volcanoes by diffuse CO_2 degassing: case study of Mt. Fuji, Japan. Pure Appl Geophys 163:825–835

Padilla G, Hernández P, Pérez NM, Pereda E, Padrón E, Melián G, Barrancos J, Rodríguez F, Dionis S, Calvo D, Herrera M, Strauch W, Muñoz A (2013) Anomalous Diffuse CO_2 Emissions at the Masaya Volcano (Nicaragua) Related to Seismic-Volcanic Unrest. Pure Appl Geophys 1–14. doi:10.1007/s00024-013-0756-9

Padrón E, Melián G, Marrero R, Nolasco D, Barrancos J, Padilla G, Hernández PA, Pérez NM (2008) Changes in the diffuse CO_2 emission and relation to seismic activity in and around El Hierro, Canary Islands. Pure Appl Geophys 165:95–114. doi:10.1007/978-3-7643-8738-9_7

Padrón E, Hernández PA, Pérez NM, Toulkeridis T, Melián G, Barrancos J, Virgili G, Sumino H, Notsu K (2012a) Fumarole/plume and diffuse CO_2 emission from Sierra Negra caldera, Galapagos archipelago. Bull Volcanol 74:1509–1519. doi:10.1007/s00445-012-0610-4

Padrón E, Pérez NM, Hernández PA, Sumino H, Melián G, Barrancos J, Nolasco D, Padilla G (2012b) Helium emisión at Cumbre Vieja volcano, La Palma, Canary Islands. Chem Geol 312–313:138–147

Pan V, Holloway JR, Hervig RL (1991) The pressure and temperature dependence of carbon dioxide solubility in tholeiitic basalts melts. Geochim Cosmochim Acta 55:1587–1595

Parkinson KJ (1981) An improved method for measuring soil respiration in the field. J Appl Ecol 18:221–228

Pérez NM, Wakita H, Nakai S, Sano Y, Williams SN (1994) $^3He/^4He$ isotopic ratios in volcanic-hydrothermal discharges from the Canary Islands, Spain: implications on the origin of the volcanic activity. Mineral Mag 58A:709–710

Pérez NM, Hanor JS, Means J, Álvarez CE, Hernández Moreno JM (1996) Volcanogenic mercury pollution in the ground water system of La Palma, Canary Islands, Spain. Geogaceta 20(6):1302–1304

Pérez NM, Padilla GD, Padrón E, Hernández PA, Melián G, Barrancos J, Dionis S, Nolasco D, Rodríguez F, Calvo D, Hernández I (2012) Precursory diffuse CO_2 and H_2S emission signatures of the 2011–2012 El Hierro submarine eruption, Canary Islands. Geophys Res Lett 39:L16311. doi:10.1029/2012GL052410

Pérez NM, Hernández PA, Padrón E, Melián G, Nolasco D, Barrancos J, Padilla G, Calvo D, Rodríguez F, Dionis S, Chiodini G (2013) An increasing trend of diffuse CO_2 emission from Teide volcano (Tenerife, Canary Islands): geochemical evidence of magma degassing episodes. J Geol Soc London 170(4):585–592. doi:10.1144/jgs2012-125

Salazar JM, Hernández PA, Pérez NM, Melián G, Álvarez J, Segura F, Notsu K (2001) Diffuse emissions of carbon dioxide from Cerro Negro volcano, Nicaragua, Central America. Geophys Res Lett 28:4275–4278

Salazar JM, Pérez NM, Hernández PA, Soriano T, Barahona F, Olmos R, Cartagena R, López DL, Lima N, Melián G, Padrón E, Galindo I, Notsu K (2002) Precursory diffuse carbon dioxide degassing signatures of recent earthquakes in El Salvador, Central America. Earth Planet Sci Lett 205(1–2):81–89

Sano Y, Marty B (1995) Origin of carbon in fumarolic gas from island arcs. Chem Geol 119:265–274

Sano Y, Urabe A, Wakita H (1985) Chemical and isotopic composition of gases in geothermal fluids in Iceland. Geochem J 19:135–148

Sinclair AJ (1974) Selection of thresholds in geochemical data using probability graphs. J Geochem Explor 3:129–149

Staudigel H, Feraud G, Giannerini G (1986) The history of intrusive activity on the island of La Palma (Canary Islands). J Volcanol Geotherm Res 27:299–322

Stolper E, Holloway JR (1988) Experimental determination of the solubility of carbon dioxide in molten basalt at low pressure. Earth Planet Sci Lett 87:397–408

Sumino H, Nagao K, Notsu K (2001) Highly sensitive and precise measurement of helium isotopes using a mass spectrometer with double collector system. J Mass Spectrom Soc Jpn 492:61–68

Tennant CB, White ML (1959) Study of the distribution of some geochemical data. Econ Geol 54:1281–1290

Veeger AI (1991) Geochemical methods for evaluating the origin and evolution of ground water in volcanic rocks at La Palma Canary Islands, Spain. PhD Thesis, The University of Arizona, 241 pp

Viveiros F, Ferreira T, Cabral Vieira J, Silva C, Gaspar JL (2008) Environmental influences on soil CO_2 degassing at Furnas and Fogo volcanoes (São Miguel Island, Azores archipelago). J Volcanol Geotherm Res 177:883–893

Ward SN, Day S (2001) Cumbre Vieja Volcano—potential collapse and tsunami at La Palma, Canary Islands. Geophys Res Lett 28:3397–3400. doi:10.1029/2001GL013110

Zar JH (1984) Biostatistical Análisis, 2nd edn. Prentice-Hall, Englewood, p 663

Diffusive helium emissions as a precursory sign of volcanic unrest

Eleazar Padrón[1,2]*, Nemesio M. Pérez[1,2], Pedro A. Hernández[1,2], Hirochika Sumino[3], Gladys V. Melián[1,2], José Barrancos[1,2], Dácil Nolasco[1,2], Germán Padilla[1,2], Samara Dionis[1,2], Fátima Rodríguez[1,2], Íñigo Hernández[1,2], David Calvo[1,2], María D. Peraza[1,2], and Keisuke Nagao[3]

[1]Environmental Research Division, Instituto Tecnológico y de Energías Renovables, 38611 Granadilla de Abona, Tenerife, Canary Islands, Spain

[2]Instituto Volcanológico de Canarias (INVOLCAN), 38400 Puerto de la Cruz, Tenerife, Canary Islands, Spain

[3]Geochemical Research Center, Graduate School of Science, University of Tokyo, 7-3-1 Hongo, Bunkyo-ku, Tokyo 113-0033, Japan

ABSTRACT

Significant increases in helium emissions from the soil and $^3He/^4He$ ratios in groundwater on El Hierro Island (Canary Islands, Spain) were observed prior to the 2011–2012 submarine eruption off the coast of the island. The changes of diffusive helium emissions rate were observed one month prior to the submarine eruption onset (12 October 2011) and the major increase preceded increases in seismic energy release during the volcanic unrest. Measured $^3He/^4He$ ratios in groundwaters from a well in El Hierro Island increased from 2–3 R_A to 7.2 R_A (R_A = $^3He/^4He$ ratio in air) 1 month prior to the eruption onset, and reached a peak of 8.2 R_A, indicating a dominant magmatic contribution to the dissolved gases in ground waters. $^3He/^4He$ values and diffusive helium emission studies have been extremely important for forecasting the onset of the volcanic unrest and subsequent volcanic eruption. An aseismic exsolution of magmatic gases from magma bodies beneath El Hierro Island through fractures and vertical permeability structures increased the diffusive helium emission rate prior to episodes of seismic energy release associated with the volcanic unrest.

INTRODUCTION

In the past 20 years, there has been considerable interest in the study of diffuse degassing as a powerful tool in volcano monitoring programs (Allard et al., 1991; Hernández et al., 2001; Carapezza et al., 2004), particularly in those volcanic areas where there are no visible volcanic-hydrothermal gas emissions (plume, fumaroles, hot springs). Historically, soil gas and degassing surveys in volcanic environments have focused mainly on CO_2 because it is, after water vapor, the most abundant gas dissolved in magma (Stolper and Holloway, 1988). Changes in CO_2 flux patterns over time provide important information for monitoring volcanic and seismic activity (Hernández et al., 2001; Carapezza et al., 2004; Pérez and Hernández, 2007). However, magma-derived gases change their original magmatic composition owing to various factors, such as dilution by surface processes, including of a biological and meteorological nature, and solubility-controlled fractionation in groundwaters (Federico et al., 2002; Tassi et al., 2007). The geochemical properties of helium minimize the interaction of this noble gas on its movement toward the Earth's surface, and its isotopic composition is not affected by subsequent chemical reactions (Ozima and Podosek, 2002). It is highly mobile, chemically inert, physically stable, nonbiogenic, sparingly soluble in water under ambient conditions, almost nonadsorbable, and highly diffusive with a diffusion coefficient ~10× that of CO_2 (Jenkins and Cook, 1961). Because of these properties, helium has been studied as a precursor of volcanic eruptions (Thomas and Naughton, 1979; Sano et al., 1984). There are two naturally occurring isotopes of helium, ^3He and ^4He, with an atmospheric $^3He/^4He$ ratio (R_A) of 1.384×10^{-6} (Clarke et al., 1976) and an atmospheric concentration of 5220 ppb (Holland and Emerson, 1990); ^4He is produced from the radioactive decay of ^{238}U, ^{235}U, and ^{232}Th, while nearly all ^3He is primordial in origin, produced by mantle degassing, the most important terrestrial source of ^3He (Graham, 2002). The isotopic composition of helium in fumarolic gases, measured as the $^3He/^4He$ ratio, exhibits significant changes in relation to volcanic activity (Sano et al., 1984; Sano and Fischer, 2013).

El Hierro Island (Fig. 1A), the smallest (278 km^2), youngest, and southwesternmost of the Canary Islands (Spain), does not show any visible volcanic gas emissions, and therefore diffusive degassing studies are an important tool for the volcanic surveillance programs on the island.

Seismo-volcanic unrest began on El Hierro Island in July 2011. It was first characterized by the location of a large number of relatively small earthquakes (M < 2.5) beneath El Hierro at depths between 8 and 15 km (Fig. 1B). In mid- to late September, the seismicity migrated toward the south of the island with an increase in the earthquake magnitudes. On 10 October 2011, a continuous tremor was clearly detected, and a submarine eruption was confirmed in the afternoon of 12 October 2011 by visual observations of a large, light green area off the coast of El Hierro, ~2 km south of the small village of La Restinga in the southernmost part of the island (Fig. 1C). Since then, frequent episodes of turbulent gas emission and foaming and steamy lava fragments were observed at the sea surface. Ibáñez et al. (2012) grouped the seismic sequence into three well-separated spatial clusters and distinct earthquake regimes (phases 1, 2, and 3 in Fig. 1B). Phase 1 (between 1 July and 10 September 2011) was characterized by high earthquake rates and relatively low magnitudes, reflecting the initial intrusion of magma from the upper mantle into the crust. In phase 2 (21 September to 15 October 2011), seismicity migrated to the south with apparently ordinary tectonic activity. The eruption occurred in this phase with a substantial lack of shallow seismicity between 8 km depth and the surface. A new burst of seismicity occurred off the northern coast of El Hierro (phase 3 in Fig. 1B) after 16 October. The significant increase in the number and magnitude recorded during phase 3 culminated in the largest earthquake of the seismic series, an M 4.6 event on 11 November 2011. (The seismic catalog can be found at the Spanish Instituto Geográfico Nacional site: http://www.ign.es/ign/layoutIn/volcaFormularioCatalogo.do.)

METHODS

In summer 2003, the first diffusive helium emission survey of El Hierro Island was performed by analyzing the helium content of soil gas at 473 sampling points located homogeneously across the entire surface of the island. Since the beginning of the recent 2011–2012 seismo-volcanic unrest period at El Hierro, another 14 helium emission surveys have been carried out, with 601 sampling sites. Simultaneously, the $^3He/^4He$ ratio in groundwater has been measured regularly at San Simon well (Fig. 1B), located in the northwest part of the island (27°45′16.6″N, 18°6′24.5″W).

At each sampling site, soil gas samples were collected at 40 cm depth using a stainless steel probe, stored in preevacuated vials, and analyzed for helium concentration within 24 h by means of a quadrupole mass spectrometer (Pfeiffer Omnistar 422). The instrument accuracy of the helium concentration was estimated to be 300 ppb. The soil helium concentration data were used to estimate the diffusive helium flux at each point by means of Fick's law (Etiope and Martinelli, 2002):

$$F_D = D_e \frac{dC}{dz}, \quad (1)$$

*E-mail: eleazar@iter.es.

GEOLOGY, May 2013; v. 41; no. 5; p. 539–542; Data Repository item 2013149 | doi:10.1130/G34027.1 | Published online 18 March 2013

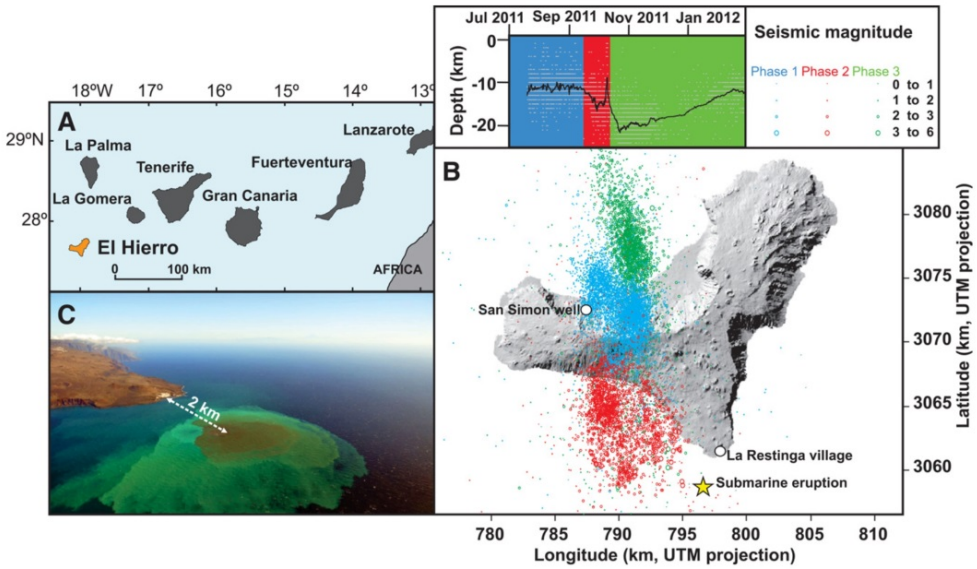

Figure 1. A: Geographic location of El Hierro Island (Canary Islands, Spain). B: Epicenter locations of 12,178 seismic events recorded until 9 February 2012. Different phases of seismicity described by Ibáñez et al. (2012) are displayed in blue, red, and green. Temporal evolution of hypocentral depth of earthquakes is depicted by 100-event moving average (black line). Star indicates location of submarine eruption (UTM—Universal Transverse Mercator). C: Water discoloration south of La Restinga produced by submarine eruption.

where $D_e = n^2 D_m$ is the global diffusion coefficient (m^2/s); dC is the variation of gas concentration (kg/m^3) along the depth dz (m); n is the effective porosity of the medium (%); and D_m is the diffusion coefficient of helium in air (0.7×10^{-4} m^2/s at 25 °C; Pandey et al., 1974). We used an average of 29% for the soil porosity, as measured on Cumbre Vieja volcano (La Palma Island, Canarian archipelago), a similar volcanic system with a comparable age and surface (Padrón et al., 2012). Soil helium efflux data were used to construct spatial distribution maps by sequential Gaussian simulation, sGs (Cardellini et al., 2003), and then to estimate the total helium emission in the entire area of El Hierro Island. The helium output was computed for each sGs realization by summing the products of simulated value of each grid cell by the cell surface in 50 sGs realizations at each survey (Cardellini et al., 2003).

We collected 8 groundwater samples from San Simon well between 28 July 2011 and 11 January 2012 for analysis of $^3He/^4He$ in groundwater. $^3He/^4He$ data were corrected for air-derived contributions following the method described by Craig et al. (1978). A detailed explanation about the helium isotope measurement is available in the GSA Data Repository[1].

RESULTS AND DISCUSSION

Diffusive helium emissions in the 2003 survey amounted for 9 1 kg/d for the entire area of El Hierro Island (Table DR2 in the Data Repository). This value is interpreted as the background helium emission of El Hierro Island in a period of volcanic quiescence, and it is depicted in Figure 2A, which shows both diffusive helium emissions for the entire island and the corrected $^3He/^4He$ ratio for the dissolved gases in the San Simon waters together with the seismic energy released up to 9 February 2012. The diffusive helium emission estimated in the two first surveys was 11 1 kg/d, slightly higher than the background emission measured in 2003. By mid-September, a drastic increase in the 2 geochemical parameters had been observed, several days before the beginning of a significant increase in the seismic activity on the island; helium emission increased from 11 1 kg/d to 24 1 kg/d, and $^3He/^4He$ increased from 2.48 0.07 R_A to 7.3 0.2 R_A. The increase in diffusive helium emissions continued over 2 more surveys, reaching a relative maximum of 30 2 kg/d and preceding the onset of the submarine eruption. The survey in which this maximum value was measured started on 2 October and was completed two days before the onset of the submarine eruption. This emission value continued until the following survey, which finished on 19 October. The $^3He/^4He$ ratio measured in the San Simon waters sampled on 12 October also indicated a relative maximum. After the onset of the eruption, there was a drastic decrease in diffusive helium emissions measured between 20 and 26 October. (Diffusive helium emission and $^3He/^4He$ ratio data are shown in Tables DR1–DR3.)

Assuming that the San Simon water is an indicator of the $^3He/^4He$ ratio of deep-sourced helium during the volcanic unrest period, it is possible to estimate the crustal and mantle fractions of the helium released during the studied period. Significant increases of $^3He/^4He$ ratios in groundwater were reported (from 1–3 R_A to 7.2 R_A; Rodríguez et al., 2012) maintained along the volcanic unrest period at another three groundwater capture points of the island, supporting this assumption. The amount of helium released in the volcanic unrest period was estimated by

[1]GSA Data Repository item 2013149, helium isotope measurement explanation, Table DR1 (soil helium content and diffusive emission flux data), Table DR2 (summary of the diffusive soil helium emission results), Table DR3 (helium isotope ratio data in San Simon groundwater) and Table DR4 (noble gas composition in an atmospheric gas collected by the Toepler pump system), is available online at www.geosociety.org/pubs/ft2013.htm, or on request from editing@geosociety.org or Documents Secretary, GSA, P.O. Box 9140, Boulder, CO 80301, USA.

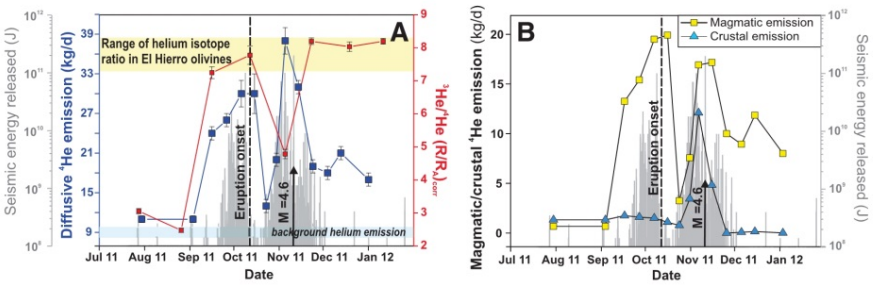

Figure 2. A: Temporal evolution of seismic energy released (gray), diffusive helium emission at entire island (blue squares), and air-corrected ^{3}He/^{4}He ratio in San Simon groundwater (red squares). R_A = atmospheric ^{3}He/^{4}He ratio. Errors on diffusive helium emission values are 1σ of 50 equiprobable realizations by sequential Gaussian simulation. Yellow band represents range of ^{3}He/^{4}He ratios measured on olivine phenocrysts at El Hierro lavas, 7.2–8.2 R_A (Day and Hilton, 2011). B: Temporal evolution of estimated magmatic (yellow squares) and crustal (blue triangles) helium emission during volcano-seismic unrest and seismic energy released (gray bars).

subtracting the background helium emission (~9 kg/d) and resolving the rest to crustal (C) and magmatic (1 – C) fractions based on the ^{3}He/^{4}He ratio of San Simon water interpolated for the date when each helium emission was measured, following the method described by Ballentine et al. (2002) (Table DR2). Figure 2B depicts the evolution of the magmatic and crustal emission rate over the volcanic unrest period. The magmatic helium time series began with <1 kg/d and increased to ~20 kg/d several days before the eruption onset. However, the crustal helium emission remained at ~1 kg/d throughout the volcanic unrest period, except on the survey performed between 2 November and 8 November 2011, when it reached 12 kg/d immediately before the occurrence of the biggest earthquake of the unrest period. Figures 3A and 3B reveal that the density of warm colors is higher prior to the eruption than at the beginning of the unrest period, indicating an increase in helium emissions from 11 1 kg/d to 30 2 kg/d.

Following the submarine eruption, the third phase of seismicity started (Fig. 1B). In this stage, both the temporal evolution of helium emissions and the ^{3}He/^{4}He ratio displayed opposite behaviors; there was an increase in the diffusive helium emission, reaching the absolute maximum of the series (38 2 kg/d) on the survey performed between 2 November and 8 November, and the ^{3}He/^{4}He ratio in the San Simon well groundwaters decreased to 4.8 0.1 R_A in the dissolved gases sampled on 5 November. The discrepancy could not have been due to a delayed response of the ^{3}He/^{4}He ratio observed at San Simon to the change in the ^{3}He/^{4}He ratio of helium supplied to the groundwater system, because the ^{3}He/^{4}He ratio in the San Simon waters increased concurrently with the increase in diffusive helium emissions and seismic activity at the beginning of the first phase, although the distance from the San Simon well to the epicenters during the third seismicity phase was greater than that during the first two phases. In Figure 3C, the density of warm colors is the maximum observed on El Hierro during the survey period between 2 and 8 November. The helium emission anomalies in Figure 3C are located mainly in the north of the island, in agreement with the location of the earthquake epicenters during the sampling period. In the following two surveys (performed on 9–19 November and 20–29 November), the helium emissions dropped to 19 1 kg/d and fluctuated around this value until the last survey, showing excellent agreement with the seismic energy released (see Fig. 2A). Conversely, the ^{3}He/^{4}He ratio measured in the San Simon groundwaters increased to the maximum values measured in the study period and showed a value similar to the maximum ^{3}He/^{4}He ratio measured in phenocrysts from El Hierro lavas; i.e., ~8.2 R_A (Day and Hilton, 2011).

At the beginning of the seismo-volcanic unrest period, magma movement beneath El Hierro Island generated new fracture and microfracture systems, allowing volcanic gases to travel to the surface. Helium could easily ascend from deep areas through structures of high vertical permeability, thereby enhancing the helium content of soil gases. This fact was confirmed by an increase in the amount of mantle-derived gases dissolved in the San Simon waters exhibited by the ^{3}He/^{4}He ratio. The increases in the diffusive helium emission values over the entire island preceded episodes of seismic energy release. Similar results were observed by continuous monitoring of diffuse CO_2 and H_2S emissions by using two different geochemical stations (Pérez et al., 2012). The onset of the submarine eruption produced a sudden release

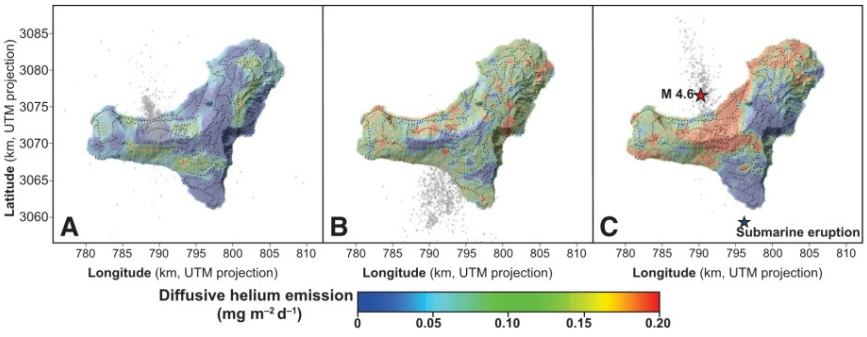

Figure 3. Spatial distribution of diffusive helium emission values (UTM—Universal Transverse Mercator.) Gray dots indicate seismicity in sampling period; black dots indicate sampling sites. A: Measured in first 2011 survey, 25 July through 4 August 2011. B: Measured immediately before occurrence of submarine eruption, 2–10 October 2011. C: Measured immediately before occurrence of largest earthquake of seismo-volcanic unrest period (M 4.6, red star), 2–8 November 2011. Blue star indicates location of submarine eruption.

of volcanic gases, and consequently, a decrease in the volcanic gas pressure of the magma bodies moving beneath the island, reflected by a drastic decrease in the diffusive helium emissions measured between 20 and 26 October 2011. Seismicity in the third phase was more energetic and was preceded by the highest diffusive helium emission value measured in the study period, between 2 and 8 November 2011. Crustal deformation and fracturing in this phase enhanced the release of radiogenic helium produced in the crust and caused a decrease in the $^3He/^4He$ measured at San Simon well groundwaters (Fig. 2). The $^3He/^4He$ ratio seemed to have reached a peak of ~8.2 R_A, indicating a significant mantle-derived contribution to the dissolved gases in the San Simon groundwaters, and diffusive helium emission values of ~17–21 kg/d are still higher than the estimated background.

CONCLUSIONS

High volcanic-gas pressure in a magma surrounded by a less deformed and fractured crust could be responsible for the high magmatic helium emission rate and eventual submarine eruption during the first two phases of activity, whereas the third phase, causing extensive crustal deformation and fracturing, resulted in low gas pressure in the magma and relatively low magmatic helium emission rates. Gases being exsolved from the magmatic melts through fractures and vertical permeability structures generated overpressures sufficient to fracture rocks surrounding the magma, reaching the surface prior to trigger the failure of the rock.

The results presented here demonstrate that higher helium emission rates and isotopic composition preceded the 2011–2012 El Hierro submarine eruption. These results clearly show the critical role that helium can play in the prediction of major volcanic events and the importance of continuous monitoring of this gas in active volcanic regions, mainly when magma migrates aseismically, i.e., silently, toward the surface.

ACKNOWLEDGMENTS

This research was financially supported by project MAKAVOL (MAC/3/C161) of the European Union MAC 2007-2013 Transnational Cooperation Program, and project HELIO (ProID20100158) of the Canary Islands Government, as well as the Cabildo Insular de Tenerife and El Hierro. We thank two anonymous reviewers for their constructive comments and suggestions, and all volunteers for their help during the field work.

REFERENCES CITED

Allard, P., Carbonelle, J., Dajlevic, D., Le Bronec, J., Morel, P., Robe, M.C., Maurenas, J.M., Faivre-Pierret, R., Martins, D., Sabroux, J.C., and Zettwoog, P., 1991, Eruptive and diffuse emissions of CO_2 from Mount Etna: Nature, v. 351, p. 387–391, doi:10.1038/351387a0.

Ballentine, C.J., Burgess, R., and Marty, B., 2002, Tracing fluid origin, transport and interaction in the crust: Reviews in Mineralogy and Geochemistry, v. 47, p. 539–614, doi:10.2138/rmg.2002.47.13.

Carapezza, M.L., Inguaggiato, S., Brusca, L., and Longo, M., 2004, Geochemical precursors of the activity of an open-conduit volcano: The Stromboli 2002–2003 eruptive events: Geophysical Research Letters, v. 31, L07620, doi:10.1029/2004GL019614.

Cardellini, C., Chiodini, G., and Frondini, F., 2003, Application of stochastic simulation to CO_2 flux from soil: Mapping and quantification of gas release: Journal of Geophysical Research, v. 108, 2425, doi:10.1029/2002JB002165.

Clarke, W.B., Jenkins, W.B., and Top, Z., 1976, Determination of tritium by mass spectrometric measurement of ^3He: International Journal of Applied Radiation and Isotopes, v. 27, p. 515–522, doi:10.1016/0020-708X(76)90082-X.

Craig, H., Lupton, J.E., and Horibe, Y., 1978, A mantle helium component in circum Pacific volcanic gases: Hakone, the Marianas, and Mt. Lassen, *in* Alexander, E.C., and Ozima, M., eds., Terrestrial rare gases: Tokyo, Japan Scientific Societies Press, p. 3–16.

Day, J.M.D., and Hilton, D.R., 2011, Origin of $^3He/^4He$ ratios in HIMU-type basalts constrained from Canary Island lavas: Earth and Planetary Science Letters, v. 305, p. 226–234, doi:10.1016/j.epsl.2011.03.006.

Etiope, G., and Martinelli, G., 2002, Migration of carrier and trace gases in the geosphere: An overview: Physics of the Earth and Planetary Interiors, v. 129, p. 185–204, doi:10.1016/S0031-9201(01)00292-8.

Federico, C., Aiuppa, A., Allard, P., Bellomo, S., Jean-Baptiste, P., Parello, F., and Valenza, M., 2002, Magma-derived gas influx and water-rock interactions in the volcanic aquifer of Mt. Vesuvius, Italy: Geochimica et Cosmochimica Acta, v. 66, p. 963–981, doi:10.1016/S0016-7037(01)00813-4.

Graham, D.W., 2002, Noble gas isotope geochemistry of mid-ocean ridge and ocean island basalts: Characterization of mantle source reservoirs: Reviews in Mineralogy and Geochemistry, v. 47, p. 247–317, doi:10.2138/rmg.2002.47.8.

Hernández, P.A., Notsu, K., Salazar, J.M., Mori, T., Natale, G., Okada, H., Virgili, G., Shimoike, Y., Sato, M., and Pérez, N.M., 2001, Carbon dioxide degassing by advective flow from Usu volcano, Japan: Science, v. 292, p. 83–86, doi:10.1126/science.1058450.

Holland, P.W., and Emerson, D.E., 1990, The global helium-4 content of near-surface atmospheric air: Athens, Greece, Theophrastus Publications (GRC), p. 97–109.

Ibáñez, J.M., De Angelis, S., Díaz-Moreno, A., Hernández, P., Alguacil, G., Posadas, A., and Pérez, N., 2012, Insights into the 2011–2012 submarine eruption off the coast of El Hierro (Canary Islands, Spain) from statistical analyses of earthquake activity: Geophysical Journal International, v. 191, p. 659–670, doi:10.1111/j.1365-246X.2012.05629.x.

Jenkins, A.C., and Cook, A., 1961, Argon, helium and the rare gases: History, occurrence and properties: London, Interscience Publishers, 818 p.

Ozima, M., and Podosek, F.A., 2002, Noble gas geochemistry (second edition): Cambridge, UK, Cambridge University Press, 286 p.

Padrón, E., Pérez, N.M., Hernández, P.A., Sumino, H., Melián, G., Barrancos, J., Nolasco, D., and Padilla, G., 2012, Helium emission at Cumbre Vieja volcano, La Palma, Canary Islands: Chemical Geology, v. 312–313, p. 138–147, doi:10.1016/j.chemgeo.2012.04.018.

Pandey, G.N., Rasintek, M., and Katz, D.L., 1974, Diffusion of fluids through porous media with implication in petroleum geology: American Association of Petroleum Geologists Bulletin, v. 58, p. 291–303.

Pérez, N.M., and Hernández, P.A., 2007, Earthquake forecasting research in active volcanic areas by means of diffuse CO_2 emission studies, *in* Sen, P., and Das, N.K., eds., Geochemical precursors for earthquakes: Bangalore, MacMillan India Ltd., p. 94–113.

Pérez, N.M., Padilla, G., Padrón, E., Hernández, P.A., Melián, G.V., Barrancos, J., Dionis, S., Nolasco, D., Rodríguez, F., Calvo, D., and Hernández, I., 2012, Precursory diffuse CO_2 and H_2S emission signatures of the 2011–2012 El Hierro submarine eruption, Canary Islands: Geophysical Research Letters, v. 39, L16311, doi:10.1029/2012GL052410.

Rodríguez, F., and 12 others, 2012, Dissolved gas geochemical signatures of the ground waters related to the 2011 El Hierro magmatic reactivation: Geophysical Research Abstracts, v. 14, p. 11331.

Sano, Y., and Fischer, T., 2013, The analysis and interpretation of noble gases in modern hydrothermal systems, *in* Burnard, P., ed., The noble gases as geochemical tracers: Springer-Verlag Advances in Isotope Geochemistry (in press).

Sano, Y., Nakamura, Y., Wakita, H., Urabe, A., and Tominaga, T., 1984, Helium-3 emission related to volcanic activity: Science, v. 224, p. 150–151, doi:10.1126/science.224.4645.150.

Stolper, E., and Holloway, J.R., 1988, Experimental determination of the solubility of carbon dioxide in molten basalt at low pressure: Earth and Planetary Science Letters, v. 87, p. 397–408, doi:10.1016/0012-821X(88)90004-0.

Tassi, F., Vaselli, O., Capaccioni, B., Montegrossi, G., Barahona, F., and Caprai, A., 2007, Scrubbing process and chemical equilibria controlling the composition of light hydrocarbons in natural gas discharges: An example from the geothermal fields of El Salvador: Geochemistry Geophysics Geosystems, v. 8, Q05008, doi:10.1029/2006GC001487.

Thomas, D.M., and Naughton, J.J., 1979, Helium/carbon dioxide ratios as premonitors of volcanic activity: Science, v. 204, p. 1195–1196, doi:10.1126/science.204.4398.1195.

Manuscript received 8 September 2012
Revised manuscript received 19 November 2012
Manuscript accepted 21 November 2012

Printed in USA

Remote Sensing of Environment 154 (2014) 219–225

Contents lists available at ScienceDirect

Remote Sensing of Environment

journal homepage: www.elsevier.com/locate/rse

Magma emission rates from shallow submarine eruptions using airborne thermal imaging

Pedro A. Hernández [a,b,*], Sonia Calvari [c], Antonio Ramos [b,d], Nemesio M. Pérez [a,b], Antonio Márquez [e], Roberto Quevedo [b,f], José Barrancos [a,b], Eleazar Padrón [a,b], Germán D. Padilla [a,b], Dina López [b,g], Ángel Rodríguez Santana [b,h], Gladys V. Melián [a,b], Samara Dionis [b], Fátima Rodríguez [b], David Calvo [b], Letizia Spampinato [c]

[a] División de Medio Ambiente, ITER, Granadilla de Abona, Tenerife, Canary Islands, Spain
[b] Instituto Volcanológico de Canarias, INVOLCAN, Puerto de la Cruz, Tenerife, Canary Islands, Spain
[c] Istituto Nazionale di Geofisica e Vulcanologia, Obsservatorio Etneo, Sezione di Catania, Catania, Italy
[d] Division of Robotic and Computational Oceanography (SIANI), Facultad de Ciencias del Mar, Universidad de Las Palmas de Gran Canaria, Canary Islands, Spain
[e] Unidad de Helicópteros UTF, Guardia Civil, Zona de Canarias, Tenerife, Canary Islands, Spain
[f] Bionerics Research, Teror-Arucas, Gran Canaria, Canary Islands, Spain
[g] Department of Geological Sciences, OH University, Athens, USA
[h] Departamento de Física, Facultad de Ciencias del Mar, Universidad de Las Palmas de Gran Canaria, Canary Islands, Spain

ARTICLE INFO

Article history:
Received 17 April 2014
Received in revised form 11 August 2014
Accepted 14 August 2014
Available online xxxx

Keywords:
Shallow submarine eruption
Thermal airborne monitoring
Erupted volume
Effusion rate
El Hierro
Canary Islands

ABSTRACT

The effusion rate is the most important parameter to gather when a volcanic eruption occurs, because it controls the way in which a lava body grows, extends and expands, influencing its dimensional properties. Calculation of lava flow volume from thermal images collected by helicopter surveys has been largely used during the last decade for monitoring subaerial effusive eruptions. However, due to the depths where volcanic activity occurs, monitoring submarine volcanic eruptions is a very difficult task. The 2011–2012 submarine volcanic eruption at El Hierro, Canary Islands, has provided a unique and excellent opportunity to monitor eruptive processes occurring on the seabed. The use of a hand-held thermal camera during daily helicopter flights allowed us to estimate for the first time the daily and total erupted magma volumes from a submarine eruption. The volume of magma emitted during this eruption has been estimated at 300 Mm^3, giving an average effusion rate of ~25 $m^3\ s^{-1}$. Thermal imagery by helicopter proved to be a fast, inexpensive, safe and reliable technique of monitoring volcanic eruptions when they occur on the shallow seabed.

1 . Introduction

Volcanoes are widely spread out over the seabed of our planet, being concentrated mainly along mid-ocean ridges. Due to the depths where this volcanic activity occurs, monitoring submarine volcanic eruptions is a very difficult task. There have been only two occasions where a deep (>500 m) submarine eruption has been directly observed, on the West Mata submarine volcano in the northeast Lau Basin, southwest Pacific Ocean (Resing et al., 2011) and at the Monowai submarine volcano, Kermadec arc (Chadwick et al., 2008). Observations of shallow submarine activity have been done at Kilauea and Mauna Loa by scuba divers and remotely operating vehicles, revealing channelized flows and submarine lava tubes (Tribble, 1991), pillows and a large amount of fragmental debris formed by lava quenching when entering the sea (Garcia & Davies, 2001; Moore & Chadwick, 1995; Moore, Phillips, Grigg, Peterson, & Swanson, 1973). However, performing long-term monitoring in such an environment is challenging and expensive, and is normally done for short periods of time and through the use of autonomous ocean bottom systems (Deardorff, Cashman, & Chadwick, 2011). Thus, when a submarine eruption occurs at shallow depths, there is an excellent opportunity to monitor and study the eruptive activity and test new techniques. Typical phenomena associated with shallow submarine eruptions are floating lava fragments, rising water columns, explosions and discoloration of sea water (Deardorff et al., 2011; Nogami, Yoshida, & Osaka, 1993). Therefore, it is possible to guess the eruption point and intensity of volcanic activity from the color tone, shade and dimensions of the discoloration area (Nogami et al., 1993).

When dealing with a volcanic eruption, the effusion rate and Time Averaged Discharge Rate (TADR) are the most important parameters to measure, because they control the way in which a lava body grows, extends and expands, influencing its dimensional properties, such as length, width, thickness, volume and/or area (Harris, Dehn, & Calvari,

* Corresponding author at: Instituto Volcanológico de Canarias, INVOLCAN, Puerto de la Cruz, Tenerife, Canary Islands, Spain.
E-mail address: phdez@iter.es (P.A. Hernández).

http://dx.doi.org/10.1016/j.rse.2014.08.027
0034-4257/

2007). Calculation of lava flow volume and TADR from thermal images collected by helicopter surveys has been widely used during the last decade for monitoring subaerial effusive eruptions at Etna and Stromboli (Italy), Kilauea (Hawaii, USA), and other volcanoes (Spampinato, Calvari, Oppenheimer, & Boschi, 2011). Other authors (Harris et al., 2005) developed a useful routine to calculate TADR from thermal helicopter surveys during the 2002–03 eruption of Stromboli. However, when lava flows spread under the sea, calculations are more complex.

The recent submarine eruption at El Hierro Island in the Canaries started on October 12, 2011, and has offered an excellent opportunity to monitor the volcanic activity and apply novel methodologies for the detection and understanding of the eruptive process. Thermal surveys of the sea surface heated by the emission of lava, fragmented ejecta, and hydrothermal fluids, have been performed on a regular basis to estimate the erupted volume and to correlate the temporal variation of the surface measured temperatures with the level of activity, mainly based on the seismicity. This study presents the first estimates of emitted magma volume from a submarine volcano during a long period of observation by means of thermal surveys from a helicopter.

The Canary Islands consist of an east–west trending volcanic chain of seven islands, with El Hierro being located at the south westernmost end of the archipelago (Fig. 1). With an area of 268 km^2 and a maximum altitude of 1501 m above sea level, El Hierro has a characteristic trilobed shape. It is the youngest of the Canary Islands, with the oldest subaerial rocks dated at 1.12 Ma, and is believed to be near the present hotspot location (Guillou, Carracedo, Pérez Torrado, & Badiola, 1996; Hoernle, Tilton, & Schmincke, 1991). The island is truncated to the north by a large escarpment (Fig. 1), as the result of a gravitational collapse of El Golfo volcano about 130,000 years ago; other smaller collapse features are present on the island (Masson et al., 2002). The subaerial portion of the volcano, which consists of Quaternary lava flows and tuffs capped by numerous cinder cones, contains the greatest concentration of young vents in the Canary Islands (Becerra, Guillén, & Dóniz, 2007). Recent volcanic activity occurred along radial directions, focusing mainly along the three volcanic ridges bearing NE, S and SW with respect to the El Golfo depression (Fig. 1). Morphometric analyses of the volcanic cones that form these ridges (Gee, Watts, Masson, & Mitchell, 2001) reveal several monogenetic structures, indicative of the occurrence of low-volume eruptions with predominantly effusive character. The submarine extension of the S-Ridge, in contrast, is defined by a 38 km long, narrow ridge curving gently to the southwest and extending to a depth of 3700 m (Gee et al., 2001). El Hierro had no confirmed eruptions during the last 500 years; some uncertainty exists about a possible event in 1793 (Hernández Pacheco, 1982). Based on a thermobarometric and petrologic study (Stroncik, Klügel, & Hansteen, 2009) of basanites that erupted from young volcanic cones along the submarine portions of the three El Hierro rift zones (NE-Ridge, NW-Ridge and S-Ridge) to reconstruct magma plumbing and storage beneath the island, the authors concluded that the plumbing system beneath El Hierro rather resembles the magma storage systems beneath Madeira and La Palma islands, indicating that small, intermittent magma chambers might be a common feature of oceanic islands fed by plumes with relatively low fluxes, which results in only limited and periodic magma supply.

On July 19, 2011, the two seismic stations of the National Geographical Institute (IGN) deployed at El Hierro recorded the start of some unusual low magnitude seismic activity ($M < 2.5$) at depths between 8 and 15 km, indicating the start of volcanic unrest. During the first two months, seismic activity was concentrated mainly to the north of El Hierro. From mid-September, seismicity began to migrate southwards (Ibáñez et al., 2012). After almost three months of intense seismic activity, on October 10, 2011, at 05:15 (UTC), seismicity changed from discrete earthquakes to continuous tremor (Ibáñez et al., 2012). An underwater eruption was confirmed on October 12, 2011 by visual observations off the coast of El Hierro, about 2 km south of the small village of La Restinga, when a brown patch of warm water appeared on the sea surface.

Since the start of the submarine eruption, a large water discoloration area was observed on the sea surface most of the time (Fig. 2a), from light-green to dark-brown in color, due to the intense discharge of high temperature hydrothermal fluids, magmatic gases, and volcanic ash (Nogami, 2004). More than 12,000 seismic events occurred during the whole eruption, with the largest of magnitude 4.6 recorded on

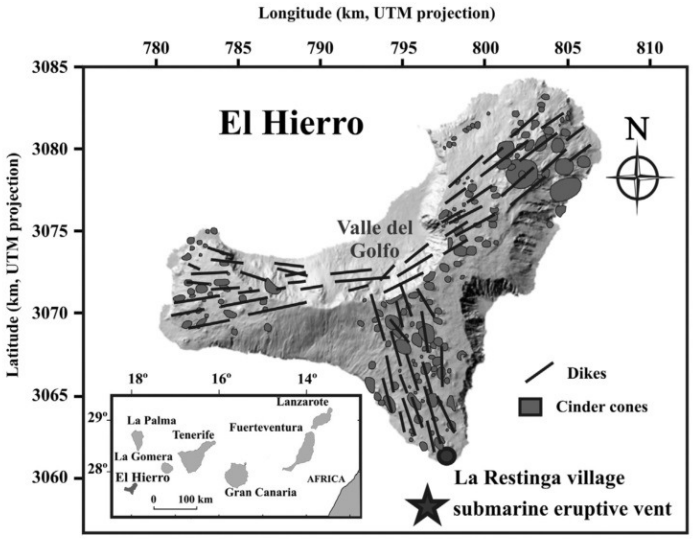

Fig. 1. Location of El Hierro Island and simplified volcano-structural map of the island (modified from Navarro & Soler, 1994). Star indicates the location of the submarine eruption. For bathymetry see Rivera et al. (2013).

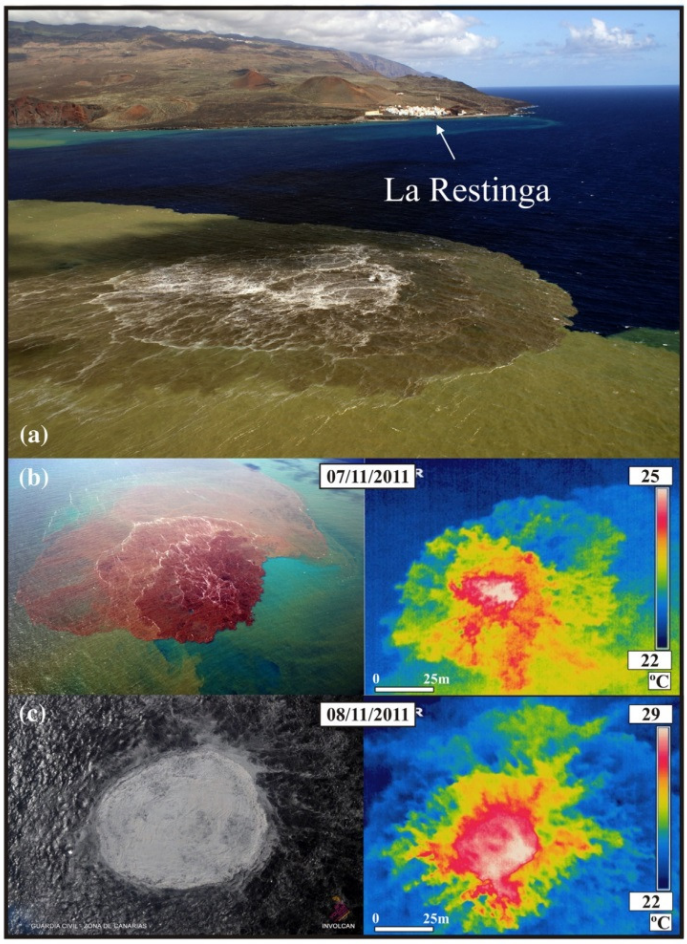

Fig. 2. (a) Aerial picture of the discolored sea water surface where submarine eruption occurred; (b) thermal infrared image of the discolored seawater area over the eruption site taken on November 7, 2011; (c) thermal infrared image of the discolored seawater area over the eruption site taken on November 8, 2011.

November 11 (Ibáñez et al., 2012). Throughout December 2011 and January 2012, the seismicity gradually declined, and the eruption subsided, with earthquake rates returning close to background levels, and tremors considerably reduced in amplitude (Ibáñez et al., 2012).

Preliminary petrological analysis of the "Restingolite" pyroclasts produced during the first stages of the eruption that were found floating on the sea surface evidenced the presence of rhyolite–basanite composite mingled pyroclasts (Gimeno, Aulinas, & Gisbert, 2012; Longpré, Klügel, Diehl, & Stix, in press), and indicated that the eruption tapped a source in the upper mantle. More recent and detailed petrological analysis of lava samples has revealed that at least two distinct magmas initially supplied from reservoirs in the mantle underwent hybridization at 15–25 km depth, with magma mixing occurring during the period of pre-eruptive seismicity and continuing for weeks after the eruption onset (Sagiya et al., 2012). GPS measurements indicated inflation directly beneath El Hierro between August and late September 2011, which is in good agreement with the epicentral location of seismicity over the same period (Sagiya et al., 2012). Multi-sensor interferometric analysis of 27 space borne radar images (González et al., 2013) revealed two spatially distinct shallow (crustal) magma reservoirs, a deeper central source (9.5 4.0 km) and a shallower magma reservoir to the west of the southern rift (4.5 2.0 km). Before the occurrence of the submarine eruption on October 12, an increase of diffuse CO_2 emission as well as radon recorded at different geochemical stations (Padilla et al., 2013; Pérez et al., 2012) together with an increase in the total diffuse soil He emission (Padrón et al., 2013) occurred as a response to stress/strain changes at depth.

2 . Materials and methods

Thermal images were collected by means of a hand-held FLIR Thermal Camera P65. The camera consists of an uncooled microbolometer with a thermal sensitivity of 0.05 °C (50/60 Hz 50 mK at 30 °C) sensitive to the 7.5–13 μm spectral range. A total of 76,000 pixels provide real-time, 16-bit thermal images. The field of view/min focus distance is 19° × 14°/0.3 m with a spatial resolution (IFOV) of 1.1 mrad (0.3 m^2 of maximum ground resolution). Ground spatial resolution GSR = tan(IFOV) ∗ altitude, [305, 460, 610 m] GSR [33,5 cm, 50,6 cm and

67,1 cm]. Internal calibration and atmospheric correction based on user input for reflected ambient temperature, distance, relative humidity, atmospheric transmission, and external optics, allow the FLIR built-in software to calculate realistic source temperatures. The accuracy of the instrument (% of reading) is 2 °C or 2%. The camera can record radiometric images according to different dynamic ranges of temperature (see flir.com for details). During the collection of thermal images at the sea surface we used the lowest temperature range (−40 °C to +55 °C) for detection of low temperature values.

Erupted magma volumes were calculated from 19 October 2011 to 28 February 2012 by means of thermal imaging of a brown patch of warm seawater observed in front of La Restinga (Fig. 2a). During this period, we carried out thermal surveys every time we had the availability of a helicopter, allowing a total of 21 thermal surveys (Fig. 2b and c). Images were recorded taking care to avoid solar reflection (with cloudy weather) or at times of the day without direct sunlight (Pinkerton, James, & Jones, 2002). Air temperature and humidity were measured in situ during every flight with a hand-held digital thermometer–hygrometer before thermal image collection, and distance from the target was measured via the altimeter of the helicopter. Thermal images of the sea surface were collected as perpendicular as possible to the sea surface in order to avoid atmospheric attenuation of source radiation (Spampinato et al., 2011). During thermal surveys, digital photos were also collected in order to compare the temperature distribution with the features observed at the sea surface. Since apparent temperatures are sensitive to viewing distance, thermal surveys from the helicopter were always carried out at three fixed altitudes over the eruption spot, ~305, ~460 and ~610 m. Since the size of the pixel depends on distance from the helicopter to the target, first we calculated the area (pixels) with a temperature value equal or higher than the normal sea water temperature and later we transformed pixels to meters taking into account the distance to the target. Considering the type of activity being viewed, the pixel sizes (0.4 to 0.9 m), and the fact that we avoided conditions with direct sun on the sea surface, effects of solar reflection can be neglected, but images might still be affected by volcanic gas and ash in the atmosphere (Dehn, Dean, Engle, & Izbekov, 2002; Pinkerton et al., 2002; Spampinato, Calvari, Oppenheimer, & Lodato, 2008; Spampinato et al., 2011).

The erupted volume of lava and pyroclastic was calculated on the basis of the temperature difference (heat flux exponential reduction) between the seawater contained within the dark patch visible at the sea surface ($T_{surface}$), and the boiling temperature of seawater next to the eruptive vent.

Constraints on the characteristics of this submarine volcano resulted in a heat flux plume that was derived from a model which produced the convective heat flux in a seawater column at each time step and depth of the crater. Thus, upward heat convection was modeled in 2D and time as a heat plume forced by the difference of the boiling temperature of the water surrounding the hot crater vent at each depth (considered for the simulations of 1 m^2), and the anomalous Sea Surface Temperature ($T_{camera} - T_{surrounding\ seawater}$) reported during the event (from 19 October 2011 to 28 February 2012). Results included different temperatures at different depths and horizontal position. Heat flux simulations (Fig. 4) were computed for each day on "Energy 2D" software (Xie, 2012). The boundary conditions included T at the sea surface, the crater depth, boiling temperature at this depth, density of seawater, heat capacity and kinematic viscosity for each day. The 2D shape of the plume was idealized as an inverted truncated cone of a fixed radius r of the crater (1 m^2) and a variable radius R_i obtained from the thermal anomaly length at the sea surface. The energy released from the source is propagated and stored in the water column in the inverted truncated cone. The total energy released per day is given by the integral of the energy transferred at a different depth within the volume of the cone and it is expressed by Eq. (1):

$$\sum Qi = \sum [W_0 * e - (K * Z_i)] * \left\{ \rho * C_e * \left[1/3 * \pi * Z_i * \left(R^2 + r^2 + rR \right) \right] \right\} * 86400 \qquad (1)$$

where Qi (J) is the accumulated energy released during one day and stored in the water column, w_0 (J s^{-1}) is the instantaneous energy released per s at the source decreasing exponentially with increasing depth, and K the exponential decay constant of the heat flux variation with depth obtained by the Energy 2D simulator and plotted in Fig. 5 for 100 m, 200 m and 300 m depth; ρ is the density of the seawater (considered constant at 1020 kg m^{-3}), C_e is the specific heat (considered constant at 4020 J kg^{-1} K^{-1}), Z_i the crater depth (m) and 86,400 s to convert the heat flux (J s^{-1}) to J d^{-1} to report the heat energy released to the water column daily. Based on calculated Qi values, to compute the lava volume that erupted daily for the whole eruptive event, we used a model (Calvari et al., 2010; Harris et al., 1998; Pinkerton et al., 2002) that was successfully applied to Stromboli for the portion of the lava flow field spreading below sea level, following the equation:

$$V_l\left(m^3\right) = \left(\frac{Q_i \times \Delta T_{sw}}{(d_l \times C_l \times \Delta T_l)} \right) \qquad (2)$$

where V_l is the calculated erupted volume (m^3), ΔT_{sw} the temperature difference between initial lava temperature (1373 K) and boiling temperature of sea water at the depth of the eruptive vent, d_l the density of lava (2500 kg m^{-3}), C_l the heat capacity of lava (1225 J kg^{-1} K^{-1}), and ΔT_l the decrease in temperature by the lava. We have considered

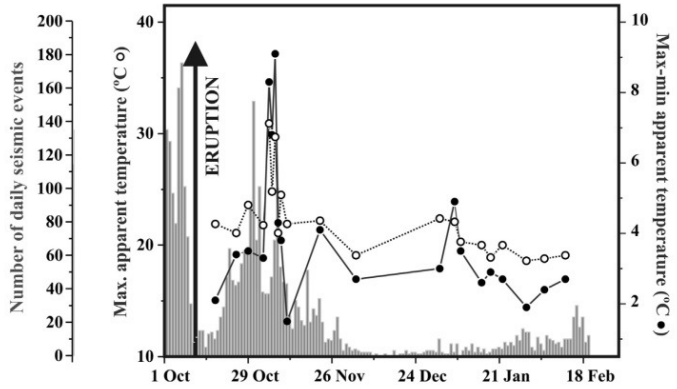

Fig. 3. Temporal evolution of maximum apparent temperatures (open circles) and difference between maximum and minimum apparent temperatures (black circles) measured at the seawater surface. Daily seismic events are indicated with light gray bars (source IGN).

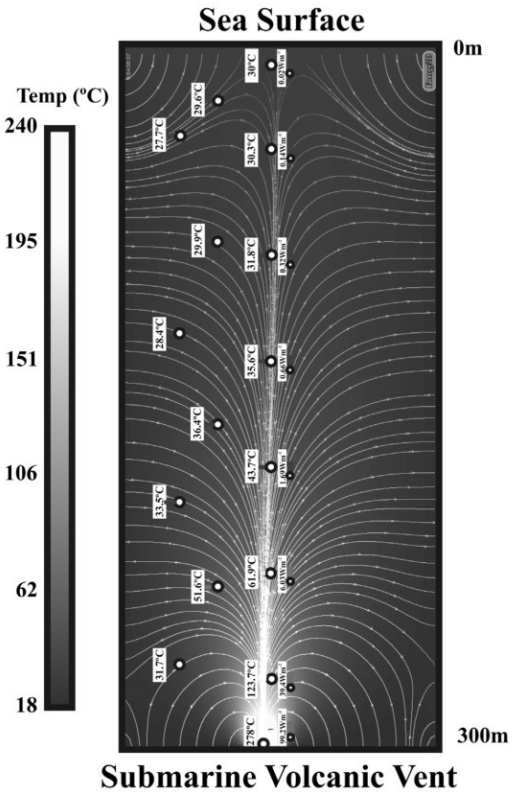

Fig. 4. Heat flux simulation computed for 300 m depth crater with "Energy 2D" software.

the volume of the discolored area as a closed system having homogeneous temperature, and for simplicity the composition of the lava typical of basalt (Calvari et al., 2010; Harris et al., 1998).

3 . Results and discussion

Analyses of thermal images carried out almost daily from a helicopter of the sea surface where the discolored area appeared were performed using FLIR R&D software which allowed us to correct the IR images for distance, humidity and air temperature recorded during each flight and to estimate apparent temperatures. After correction, maximum sea water temperatures within the discolored area ranged from 18.6 °C to 30.9 °C, compared with sea surface temperature of 18–20 °C outside the eruption site. Maximum apparent temperatures obtained from thermal images of the sea surface showed interesting changes during the period of observation (Fig. 3). Thermal surveys started on October 18, just a few days after the appearance of the discolored area on the sea surface on October 12, 2011, and have been updated to 12 February 2012. The first and most important peak in Fig. 3 was probably caused by strong emission of lava and release of hot hydrothermal fluids from the widening vent during the initial phase of the eruption. Eruptive activity between 5 and 10 November 2011 (Fig. 2b and c) coincided with the occurrence of (i) large explosive "bubbles" at the sea surface, some potentially as high as 25 m on November 5, and (ii) the largest earthquake (M = 4.6) on November 11 (Ibáñez et al., 2012). This activity caused a sudden increase in the maximum apparent temperature measured at the sea surface, which reached its peak on November 5 (Fig. 3). Apparent maximum temperatures dropped after November 8, reaching nearly stable values afterwards until mid-January 2012. This increase occurred simultaneously with a change in the seismic activity pattern (Ibáñez et al., 2012), and was marked by stronger explosive activity revealed by a greater amount of floating balloons on the sea surface. Apparent temperature differences between the sea water within and outside the discolored area ranged from 1.5 °C to 9.1 °C, with a maximum observed on November 7, 2011. This value was measured during the onset of volcanic activity (November 5–10), indicating a larger discharge of magma and hydrothermal fluids, accompanied by a marked increase in visible explosive activity at the sea surface.

To estimate the erupted volume of lava flow and pyroclastic, we measured the surface area of heated seawater, depth of the submarine volcanic cone (lava effusion spot) and temperature of seawater not affected by the eruption. During each thermal survey, tens of thermal images were recorded and analyzed to select those most representative of the area affected by warm seawater over the submarine eruption spot. For the 21 thermal infrared surveys, pixels containing temperatures that exceeded normal seawater temperatures were selected, allowing us to calculate the area of anomalous heating. Fig. 2a shows a thermal infrared image of the seawater surface at the eruption site, taken on November 11 2011, a few days after the onset of the submarine volcanic activity. After computing total seawater volumes and depths of the submarine volcanic cone, Eq. (2) was used to estimate the daily erupted volumes (see Material and methods section).

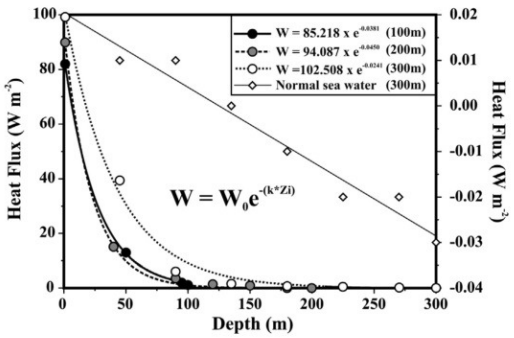

Fig. 5. Heat flux variations with depth obtained with the "Energy 2D simulator" for 100 m, 200 m and 300 m depths. Simulation for normal sea water temperature is also shown.

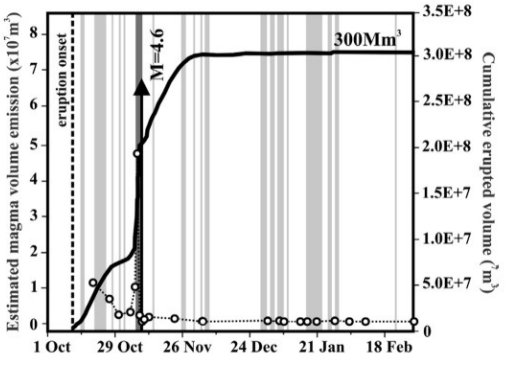

Fig. 6. Temporal evolution of estimated magma volume emission (white circles) and cumulative erupted volume (solid black line) during the period of study. Light gray bars indicate formation of a patch with brown color and floating rocks. The dark gray bar indicates the days with stronger eruptive activity (bubbling columns at the sea surface).

Fig. 6 shows the estimated erupted volumes for the 21 thermal surveys. The plotted values are just single estimates obtained during each survey, and do not represent the total emitted magma volume. In order to reconstruct the submarine eruptive thermal behavior and estimate the total erupted volume, a graphical interpolation was done between each survey, to obtain the cumulative erupted magma volume (black line in Fig. 6). On this basis we obtained a total erupted volume of lava flows and pyroclastic of 300×10^6 m^3 during the period of study (October 18, 2011–February 12, 2012), resulting in a TADR of ~25 m^3 s^{-1}. This volume, although roughly estimated, is very close to the total accumulated volume of 329×10^6 non-dense rock equivalent m^3 estimated by the IEO using bathymetric surveys (Rivera et al., 2013). These similar volume estimations suggest that the lava flows that erupted during the submarine eruption at El Hierro were very fluid due to their composition and most of the heat released was used to heat the surrounding seawater (Applegarth, Pinkerton, James, & Calvari, 2010; Hon, Kauahikaua, Denlinger, & Mackay, 1994). However, this averaged TADR value is not representative of the effusion rate during the eruption. Effusion rates usually vary during the course of most basaltic eruptions, with rates rising rapidly to a peak soon after the onset of an eruption (waxing flow) and then decreasing exponentially afterwards (waning flow) (Wadge, 1981; Wright, Blake, Harris, & Rothery, 2001). In a simple elastic model of subvolcanic magma storage, effusion rates decline exponentially as a result of the release of stored elastic strain energy from the magma reservoir during viscous flow along the eruptive conduit (Wadge, 1981). For this reason, the eruption rate (when calculated for the entire eruptive episode) will be unrepresentative of the effusion rate at most times during the eruption (Wright et al., 2001). It is well known that the explosivity of magma is largely caused by the exsolution of dissolved volatiles, and hence volatile exsolution is an important means for increasing the rate of magma emission. Any process that lowers the density of part of the magma column increases the average density contrast between wall rock and magma. This will tend to accelerate the upward movement of the vesiculated portion of the flow (Wadge, 1981). During the submarine eruption at El Hierro, similar behavior was observed, with a sharp increase of the magma effusion rate a few days after the onset of the eruption and with the highest calculated effusion rates obtained while the most important degassing events occurred. As magma moves to the surface, it expends energy on opening cracks by forcing intrusions, cooling and increasing viscosity. Assuming that the upper extremities of the cracks are probably filled with exsolved gases rather than cohesive magma, these gases did not have sufficient heat content to raise the temperature of the host rock very much and although the eruption had begun the upward velocity was inhibited by heat loss to the walls (Wadge, 1981). For this reason, the effusion rate increases as the initially cold walls of the conduit approach thermal equilibrium with the magma flux (Applegarth et al., 2010). In other words, waning flow is usually the dominant part of a basaltic eruption, and reflects the steady release of stored energy from the volcanic system as a whole. Several authors (González et al., 2013; Longpré et al., in press) reported that during the El Hierro eruption, magma storage occurred within the brittle/elastic upper crust. This magma storage involves transfer of elastic strain energy to the reservoir rocks, most of which is released again as magma leaves the system, though some will be released through brittle fracture and fissure formation. The energy is transferred through pressure from the reservoir rocks to the magma. If the elastic response during eruption is perfect and the bulk modulus of the rocks is constant, then this pressure will decline exponentially (Wadge, 1981; Wright et al., 2001).

Fig. 6 displays two mean peaks in the curve of the erupted volume. The first peak was recorded at the start of the survey on October 18, six days after eruption onset and due to the intense explosive activity during the early stages of the eruption; with a maximum of ~152×10^6 m^3 erupted magma averaged over 24 h on October 19, 2011. The thermal measurement reached a climax between 5 and 7 November 2011, corresponding to a maximum of ~656×10^6 m^3 erupted magma averaged over 24 h on November 7, 2011. This output is much smaller than that reported for Mauna Loa (Hawaii, USA) eruptions (Wadge, 1981), similar to subaerial basaltic eruptions of Kilauea (Hawaii, USA) (Wright et al., 2001), Etna (Italy) (Calvari, Neri, & Pinkerton, 2003; Wadge, 1981), Iceland (Thordarson & Larsen, 2007), the East Pacific Rise (Sinton et al., 2002) and the Galapagos Spreading Center (Colman et al., 2012), and Tolbachik (Russia; http://en.ria.ru/russia/20121211/178066660.html) volcanoes, and extremely large if compared to Stromboli and other Etna volcanic eruptions (Italy) (Calvari et al., 2005, 2010; Harris, Steffke, Calvari, & Spampinato, 2011; Kilburn & Lopes, 1988). The maximum erupted magma volume is very close to the peak volcanic tremor, suggesting that it was produced by both strong explosive activity, building up a submarine cinder cone, and vigorous lava output, typically recorded during the initial phases of fissure eruptions (Calvari et al., 2005, 2010; Harris et al., 2011; Kilburn & Lopes, 1988). A third smaller peak was recorded on 7 January 2012 that corresponds to a volume of 2.6×10^6 m^3 averaged over the 24 h. Direct observations of the sea surface suggest that significant explosive activity was occurring at the eruption vents. Given that the third peak in erupted magma volume at El Hierro occurred after two months of eruption, we consider feasible the possibility of a small batch of gas-rich magma entering the system as reliable.

From mid-July to mid-September 2011, a steady inflation occurred at the center of the island (González et al., 2013; Sagiya et al., 2012), produced by the intrusion of ~13×10^6 m^3 of magma at a depth of ~5 km. From mid-September until the start of the submarine eruption in October 12, a greater deformation was due to ~21×10^6 m^3 of magma at a depth of 1–2 km. No significant deformation was observed until the beginning of November 2011, when a slow subsidence was recorded. Other authors (Ibáñez et al., 2012) reported the occurrence of an initial intrusion of magma from the upper mantle into the crust during the first months of volcanic unrest. Both geodetic and seismic interpretations (González et al., 2013; Ibáñez et al., 2012; Sagiya et al., 2012) support the hypothesis that the observed deflationary trend throughout November 2011 was associated with depressurization underneath the Moho. The existence of interconnected magma pockets between ~12 and 35 km depth beneath El Hierro (Stroncik et al., 2009) may have favored new magma migration along zones of structural weakness.

The 2011–2012 submarine eruption at El Hierro has been a unique opportunity to monitor for the first time the volume of lava spreading over the sea bottom on the basis of thermal data collected from a helicopter. Our thermal data, together with seismicity and visual observations, have allowed us to reconstruct the temporal evolution of the eruption and to estimate the total magma volume emitted during the submarine eruption. Aerial thermal images have proven to be an easy method to use, efficient and reliable in producing results during a volcanic crisis, and relatively inexpensive when compared to bathymetric surveys. In addition, the TADR and erupted magma volume results obtained by thermal imagery allowed us to keep the El Hierro submarine eruption constantly monitored. This technique produced regular estimates of erupted magma that, although interpolated for the days when surveys were missing, gave a total erupted volume within 10% of that obtained by bathymetric surveys.

Acknowledgments

This research was financially supported by the projects MAKAVOL (MAC/3/C161) from the European Union MAC 2007–2013 Transnational Cooperation Program as well as from the Cabildo Insular de Tenerife. We are also grateful to the staff of El Hierro airport (AENA) for providing logistical support. The authors acknowledge the tremendous help of UATF crews during the flights. Memoriam: Lieutenant Marcos Antonio BENITO, Helicopter Pilot Unit, UALEON, dead in act of service in august

2014. We would like to thank the reviewers for critical review of the manuscript, their suggestions and the technical and scientific advice.

Author contributions

P.A.H. and N.M.P. designed the surveys. P.A.H., S.C. and A.R. wrote the paper. P.A.H., S.C., A.R., N.M.P., R.Q., D.L., J.B. G.P. and L.S. carried out the modeling. P.A.H., N.M.P., A.M., J.B., E.P., G.P., G.V.M., S.D., F.R. and D.C. carried out the field measurements. All authors contributed to the interpretation and manuscript editing.

References

Applegarth, L. J., Pinkerton, H., James, M. R., & Calvari, S. (2010). Lava flow superposition: The reactivation of flow units in compound flow fields. *Journal of Volcanology and Geothermal Research*, *194*, 100–106.

Becerra, R., Guillén, C., & Dóniz, J. (2007). Erupción basáltica fisural al NE del volcán monogénico de Orchilla, El Hierro, Canarias Caracteres geomorfológicos En Lario. In G. J y Silva (Ed.), *Contribuciones al estudio del período cuaternario, Aequa, Ávila* (pp. 133–134) (in spanish).

Calvari, S., Lodato, L., Steffke, A., Cristaldi, A., Harris, A. J. L., Spampinato, L., et al. (2010). The 2007 Stromboli flank eruption: chronology of the events, and effusion rate measurements from thermal images and satellite data. *Journal of Geophysical Research*, *115*(B4), B04201.

Calvari, S., Neri, M., & Pinkerton, H. (2003). Effusion rate estimations during the 1999 summit eruption on Mt Etna, and growth of two distinct lava flow fields. *Journal of Volcanology and Geothermal Research*, *119*, 107–123.

Calvari, S., Spampinato, L., Lodato, L., Harris, A. J. L., Patrick, M. R., Dehn, J., et al. (2005). Chronology and complex volcanic processes during the 2002–2003 flank eruption at Stromboli volcano (Italy) reconstructed from direct observations and surveys with a handheld thermal camera. *Journal of Geophysical Research*, *110*, B02201.

Chadwick, W. W., Wright, I. C., Jr., Schwarz-Schampera, U., Hyvernaud, O., Reymond, D., & de Ronde, C. E. J. (2008). Cyclic eruptions and sector collapses at Monowai submarine volcano, Kermadec arc: 1998–2007. *Geochemistry, Geophysics, Geosystems*, *9*(10), Q10014. http://dx.doi.org/10.1029/2008gc002113.

Colman, A., Sinton, J. M., White, S. M., McClinton, J. T., Bowles, J. A., Rubin, K. H., et al. (2012). Effects of variable magma supply on mid-ocean ridge eruptions: Constraints from mapped lava flow fields along the Galápagos Spreading Center. *Geochemistry, Geophysics, Geosystems*, *13*, Q08014. http://dx.doi.org/10.1029/2012GC004163.

Deardorff, N. D., Cashman, K. V., & Chadwick, W. W., Jr. (2011). Observations of eruptive plume dynamics and pyroclastic deposits from submarine explosive eruptions at NW Rota-1, Mariana arc. *Journal of Volcanology and Geothermal Research*, *202*, 47–59.

Dehn, J., Dean, K. G., Engle, K., & Izbekov, P. (2002). Thermal precursors in satellite images of the 1999 eruption of Shishaldin Volcano. *Bulletin of Volcanology*, *64*, 525–534.

Garcia, M.O., & Davies, M. G. (2001). Submarine growth and internal structure of ocean island volcanoes based on submarine observations of Mauna Loa volcano, Hawaii. *Geology*, *29*, 163–166.

Gee, M. J. R., Watts, A. B., Masson, D.G., & Mitchell, N. C. (2001). Landslides and the evolution of El Hierro in the Canary Islands. *Marine Geology*, *177*, 271–293.

Gimeno, D., Aulinas, M., & Gisbert, G. (2012). Geochemical characterization of the initial phase of El Hierro eruption. *Minerals Magazine*, *76*(6), 1761.

González, P. J., Samsonov, S. V., Pepe, S., Tiampo, K. F., Tizzani, P., Casu, F., et al. (2013). Magma storage and migration associated with the 2011–2012 El Hierro eruption: Implications for crustal magmatic systems at oceanic island volcanoes. *Journal of Geophysical Research*, *118*, 4361–4377.

Guillou, H., Carracedo, J. C., Pérez Torrado, F. J., & Badiola, E. R. (1996). K–Ar ages and magnetic stratigraphy of a hotspot-induced, fast grown oceanic island: El Hierro, Canary Islands. *Journal of Volcanology and Geothermal Research*, *73*, 141–155.

Harris, A. J. L., Dehn, J., & Calvari, S. (2007). Lava effusion rate definition, measurement and operational requirements: A review. *Bulletin of Volcanology*, *70*, 1–22.

Harris, A. J. L., Dehn, J., Patrick, M., Calvari, S., Ripepe, M., & Lodato, L. (2005). Lava effusion rates from hand-held thermal infrared imagery: An example from the June 2003 effusive activity at Stromboli. *Bulletin of Volcanology*, *68*, 107–117.

Harris, A. J. L., Flynn, L. P., Keszthelyi, L., Mouginis-Mark, P. J., Rowland, S. K., & Resing, J. A. (1998). Calculation of lava effusion rates from Landsat TM data. *Bulletin of Volcanology*, *60*, 52–71.

Harris, A. J. L., Steffke, A., Calvari, S., & Spampinato, L. (2011). Thirty years of satellite-derived lava discharge rates at Etna: Implications for steady volumetric output. *Journal of Geophysical Research*, *116*, B08204.

Hernández Pacheco, A. (1982). Geochemical characterization of the initial phase of El Hierro eruption. *Estudios Geológicos*, *38*, 15–25 (in spanish).

Hoernle, K., Tilton, G., & Schmincke, H. U. (1991). Sr–Nd–Pb isotopic evolution of Gran Canaria: Evidence for shallow enriched mantle beneath the Canary Islands. *Earth and Planetary Science Letters*, *106*, 44–63.

Hon, K., Kauahikaua, J., Denlinger, R., & Mackay, K. (1994). Emplacement and inflation of pahoehoe sheet flows: Observations and measurements of active lava flows on Kilauea Volcano, Hawaii. *Geological Society of America Bulletin*, *106*, 351–370.

Ibáñez, J. M., De Angelis, S., Díaz-Moreno, A., Hernández, P. A., Alguacil, G., Posadas, A., et al. (2012). Insights into the 2011–2012 submarine eruption off the coast of El Hierro (Canary Islands, Spain) from statistical analysis of earthquake activity. *Geophysical Journal International*, *2*, 659–670.

Kilburn, C. R. J., & Lopes, R. M. C. (1988). The growth of AA lava flow fields on Mount Etna, Sicily. *Journal of Geophysical Research*, *93*(B12), 14759–14772.

Longpré, M.A., Klügel, A., Diehl, A., & Stix, J. (2014s). Mixing in mantle magma reservoirs prior to and during the 2011–2012 eruption at El Hierro, Canary Islands. *Geology*. http://dx.doi.org/10.1130/G351651 (in press).

Masson, D.G., Watts, A. B., Geea, M. J. R., Urgeles, R., Mitchell, N. C., Le Bas, T. P., et al. (2002). Slope failures on the flanks of the western Canary Islands. *Earth-Science Reviews*, *57*(1–2), 1–35.

Moore, J. G., & Chadwick, W. W. (1995). Offshore geology of Mauna Loa and adjacent areas, Hawaii. In J. M. Rhodes, & J. P. Lockwood (Eds.), *Mauna Loa revealed: Structure, composition, history, and hazards*. Washington, D.C.: American Geophysical Union http://dx.doi.org/10.1029/GM092p0021.

Moore, J. G., Phillips, R. L., Grigg, R. W., Peterson, D. W., & Swanson, D. A. (1973). Flow of lava into the sea, 1969–1971, Kilauea Volcano, Hawaii. *Geological Society of America Bulletin*, *84*, 537–546.

Navarro, J. M., & Soler, C. (1994). *El agua en El Hierro, Resumen del Avance del Plan Hidrológico Public Cabildo de El Hierro Con OP Gob Canarias.* , 1–59 (in Spanish).

Nogami, K. (2004). Relationship in chemical composition between mother solution and allophane-like aluminosilicate precipitate through neutralization of acid hydrothermal water by seawater. *Earth and Planetary Science Letters*, *56*(4), 457–462.

Nogami, K., Yoshida, M., & Osaka, J. (1993). Chemical composition of discolored seawater around Satsuma-Iwojima, Kagoshima, Japan. *Bulletin Volcanologique Society of Japan*, *38*(3), 71–77.

Padilla, G., Hernández, P. A., Padrón, E., Barrancos, J., Pérez, N. M., Melián, G., et al. (2013). Soil gas radon emissions and volcanic activity at El Hierro (Canary Islands): The 2011–2012 submarine eruption. *Geochemistry Geophysics Geosystems*, *14*(2), 432–447.

Padrón, E., Pérez, N. M., Hernández, P. A., Sumino, H., Melián, G., Barrancos, J., et al. (2013). Diffusive helium emissions as a precursory sign of volcanic unrest. *Geology*, *41*, 539–542.

Pérez, N. M., Padilla, G. D., Padrón, E., Hernández, P. A., Melián, G. V., Barrancos, J., et al. (2012). Precursory diffuse CO_2 and H_2S emission signatures of the 2011–2012 El Hierro submarine eruption: Canary Islands. *Geophysical Research Letters*, *39*, L16311.

Pinkerton, H., James, M., & Jones, A. (2002). Surface temperature measurements of active lava flows on Kilauea Volcano, Hawaii. *Journal of Volcanology and Geothermal Research*, *113*, 159–176.

Resing, J., Rubin, K. H., Embley, R., Lupton, J., Baker, E. T., Dziak, R., et al. (2011). Active submarine eruption of boninite in the northeastern Lau Basin. *Nature Geoscience*, *4*, 799–806. http://dx.doi.org/10.1038/NGEO1275.

Rivera, J., Lastras, G., Canals, M., Acosta, J., Arrese, B., Hermida, N., et al. (2013). Construction of an oceanic island: Insights from the El Hierro (Canary Islands) 2011–2012 submarine volcanic eruption. *Geology*, *41*, 355–358.

Sagiya, T., Barrancos, J., Calvo, D., Padrón, E., Padilla, G., Hernández, P. A., et al. (2012). *Crustal deformation during the 2011 volcanic crisis of El Hierro, Canary Islands, revealed by continuous GPS observation. EGU Reference Shelf*, *14*, EGU.

Sinton, J., Bergmanis, E., Rubin, K., Batiza, R., Gregg, T. K. P., Gronvold, K., et al. (2002). Volcanic eruptions on mid-ocean ridges: New evidence from the superfast spreading East Pacific Rise, 17°–19°S. *Journal of Geophysical Research*, *107*(B6), 2115. http://dx.doi.org/10.1029/2000JB000090.

Spampinato, L., Calvari, S., Oppenheimer, C., & Boschi, E. (2011). Volcano surveillance using infrared cameras. *Earth-Science Reviews*, *106*, 63–91.

Spampinato, L., Calvari, S., Oppenheimer, C., & Lodato, L. (2008). Shallow magma transport for the 2002–3 Mt Etna eruption inferred from thermal infrared surveys. *Journal of Volcanology and Geothermal Research*, *177*(2), 301–312.

Stroncik, N. A., Klügel, A., & Hansteen, T. H. (2009). The magmatic plumbing system beneath El Hierro (Canary Islands): Constraints from phenocrysts and naturally quenched basaltic glasses in submarine rocks. *Control Mining Petroleum*, *157*(5), 593–607.

Thordarson, T., & Larsen, G. (2007). Volcanism in Iceland in historical time: Volcano types, eruption styles and eruptive history. *Journal of Geodynamics*, *43*, 118–152.

Tribble, G. W. (1991). Underwater observations of active lava flows from Kilauea volcano, Hawaii. *Geology*, *19*, 633–636.

Wadge, G. (1981). The variation of magma discharge during basaltic eruption. *Journal of Volcanology and Geothermal Research*, *11*, 139–168.

Wright, R., Blake, S., Harris, A. J. L., & Rothery, D. A. (2001). A simple explanation for the space-based calculation of lava eruption rates. *Earth and Planetary Science Letters*, *192*, 223–233.

Xie, C. (2012). Interactive heat transfer simulations for everyone. *The Physics Teacher*, *50*(4), 237–240.